High-Throughput Optimization of Layered Oxide Cathodes for Sodium-Ion Batteries

Shipeng Jia

A thesis submitted to McGill University
in partial fulfillment of requirements of the degree of
Doctor of Philosophy
at

Department of Chemistry, McGill University
Montreal, Quebec, Canada
July 2024

"Mystery upon mystery—the gateway to all wonders!"

——Lao Tzu <TaoTe Ching>

"玄之又玄，众妙之门"

——老子《道德经》

To the ones I love, whose presence has made this journey possible

致我挚爱之人，你们的陪伴使这段旅程成为可能。

Table of Contents

Abstract

Energy and environmental challenges are critical impediments to sustainable progress, underscored by the UN's 2050 carbon neutrality goal. The rapid growth of electronic devices, electric vehicles, and energy storage systems necessitates efficient, resource-abundant, and environmentally compatible energy storage materials. While lithium-ion batteries (LIBs) have emerged as a key solution for electric transportation, their reliance on scarce lithium and costly, toxic cobalt poses supply chain risks and environmental concerns. In contrast, sodium-ion batteries (SIBs) offer a promising alternative with sustainable raw materials. Layered oxides, particularly those incorporating Fe and Mn, show potential due to their excellent electrochemical performance, sustainability, and abundant resources. However, challenges like poor air stability, long-term cycling issues, and transition metal dissolution hinder their competitiveness against LIBs.

This thesis explores layered oxide materials with sustainable transition metals using high-throughput (HTP) methodologies. The study systematically investigates the Na-Mn-Fe-O system, revealing wide solid solutions and identifying over 50 single-phase materials. Extensive doping studies involving 52 selected elements across the periodic table uncover novel materials with high capacities and excellent cycling performance. An accelerated aging protocol validates an effective method to screen for air stability, complemented by advanced machine learning methods. Systematic doping provides insights into enhancing and tuning electrochemical performance, air stability, anionic redox, and transition metal dissolution, aiming toward rational material design.

By leveraging cutting-edge high-throughput methodologies and advanced machine learning techniques, this thesis not only elucidates sodium-ion battery complexities but also accelerates the development of sustainable energy storage solutions under growing energy demands.

Résumé

Les défis énergétiques et environnementaux sont des obstacles critiques au développement durable, soulignés par l'objectif de neutralité de carbone de l'ONU pour 2050. La croissance rapide de l’utilisation d’appareils électroniques, de véhicules électriques et de systèmes de stockage d'énergie nécessite des matériaux de stockage d'énergie efficaces, abondants et compatibles avec l'environnement. Bien que les batteries lithium-ion aient émergé comme une solution clé pour le transport par véhicule électrique, leur dépendance au lithium qui est rare et au cobalt qui est coûteux et toxique pose des risques pour l’approvisionnement et entraine des préoccupations environnementales. En revanche, les batteries sodium-ion offrent une alternative prometteuse avec des matières premières durables. Les oxydes lamellaires, en particulier ceux incorporant le Fe et le Mn, montrent un potentiel en raison de leur excellente performance électrochimique, de leur durabilité et de l’abondance du fer et du manganèse. Cependant, des défis tels que la faible stabilité à l'air, les problèmes de cyclage à long terme et la dissolution des métaux de transition entravent leur compétitivité par rapport aux batteries au lithium.

Cette thèse explore les matériaux d'oxyde lamellaire avec des métaux de transition écologiquement durables en utilisant des méthodologies à haut débit. Cette étude examine systématiquement le système Na-Mn-Fe-O, révélant de larges solutions solides et identifiant plus de 50 matériaux à phase unique. Des études de dopage approfondies impliquant 52 éléments sélectionnés à travers le tableau périodique découvrent de nouveaux matériaux avec des capacités de charge élevées et une excellente performance de cyclage. Un protocole de dégradation accéléré s’avère comme étant une méthode efficace pour évaluer la stabilité à l'air, agrémenté par des méthodes avancées d'apprentissage automatique. Le dopage systématique fournit des informations sur l'amélioration

et l'ajustement de la performance électrochimique, de la stabilité à l'air, de l'activité anionique et de la dissolution des métaux de transition, visant à une conception rationnelle de matériaux.

En tirant parti des méthodologies de pointe à haut débit et des techniques avancées d'apprentissage automatique, cette thèse élucide non seulement les complexités des batteries sodium-ion mais accélère également le développement de solutions de stockage d'énergie durables face à la demande énergétique croissante.

Acknowledgements

I am profoundly grateful to everyone who has supported, advised, and accompanied me throughout my Ph.D. journey. Completing this extensive five-year study and research at the Department of Chemistry at McGill University has been a significant achievement, and I owe this success to the many individuals who have contributed to my growth and development.

First and foremost, I extend my deepest appreciation to my Ph.D. supervisor, Prof. Eric McCalla. His vast knowledge, innovative ideas, and unwavering support have been a constant source of inspiration and motivation. From our first conversation about the blueprint of my projects to the final steps of this journey, his mentorship has always been invaluable and important to me. It has been an honor and a pleasure to be part of his lab, team, and student. The memories and lessons learned will remain significant throughout my life, guiding me in both my future studies, work and personal endeavors.

I am also deeply grateful to my committee members, Prof. Janie Mauzeroll and Prof. Scott Bohle. Their constructive comments, insightful feedback, and steadfast support have been crucial in shaping my research and academic development. I also extend my heartfelt thanks to Prof. Dima Perepichka, my first-year supervisor, who provided essential guidance and support during my initial transition to Canada. Furthermore, I would like to express my gratitude to the professors who have educated and mentored me during my graduate courses: Prof. Mark Andrews, Prof. Matthew Harrington, Prof. Audrey Moores, and Prof. Ian Butler. Their teachings have equipped me with the knowledge and skills necessary for my academic research and professional growth. A special thanks goes to Chantal Marotte, the Graduate Administrator, whose assistance and support have made navigating the Ph.D. program much smoother and more enjoyable. I also want to acknowledge the instructors I worked with as a teaching assistant—Mitchell, Danielle, Sandra, and Badawy—who helped me develop better teaching abilities and provided valuable mentorship.

I am grateful for the collaboration with Sang Bok Ma from Samsung and Wendy Zhou, Erin Perry, Shinichi Kumakura, Valentin Saibi, and Hunho Kwak from Umicore. These industrial collaborations have enriched my understanding of industrial R&D and project management, and I cherish the time spent working on these innovative projects, which culminated in the achievement of two patents. I also acknowledge the financial support and scholarships that funded my Ph.D. studies: the FRQNT Scholarship, Molson and Hilton Hart Fellowship, Alexander McFee Memorial Award, Clark Science Executive Leadership Scholarship, Chinese Government Award for Outstanding Self-Financed Students Abroad, M.A. Whitehead Prize, Pall Dissertation Award, and ECS Canada Section Student Award. I am thankful for the recognition and honors from these esteemed organizations, which have enabled me to pursue my research with dedication and focus.

Moreover, I express my heartfelt gratitude to my group members, who have been my teammates, colleagues, and second family: Antranik (and his wife Tamar), Michel, Michelle, Alex, Ethan, Sarish, Sofina, Rui, Nooshin, Marzieh, Michael, Marc, Jean-Danick, Stephanie, Antoine, Elliot, Parisa, and Janie; and the undergraduates Victor, Danielle, Yixuan, Zijin, and Elissa. The camaraderie, support, and shared experiences with my group members have been invaluable, and I am deeply appreciative of the bonds we have formed. I also thank my friends—Lida Tan, Jingtan Han, Chenghao Liu, Antranik, Tamar, Yaoti Cheng, and Jiaxiang Lu—for the wonderful moments and for making my life colorful. Their friendship and encouragement have been a source of joy and strength throughout my Ph.D. journey.

Lastly, I express my deepest love and gratitude to my family for their unwavering support under any circumstances, especially during the COVID period when I couldn't visit home frequently. I dedicate this thesis to my beloved parents, Xiangwen Jia and Huimin Yang, who taught me resilience and provided both emotional and financial support to complete my Ph.D. at McGill. Their love, sacrifices, and encouragement have been the foundation of my success. Thank you all from the bottom of my heart. As time passes, I hope to always cherish the moment of finishing this thesis and look forward to the next chapter of my future with optimism and excitement.

Author Contributions and Publication

The projects detailed in this thesis were conducted under the supervision of Prof. **Eric McCalla,** who conceived the overarching research goals, provided critical guidance, and played a pivotal role in the experimental design. He also contributed to the writing of the manuscripts and provided thorough revisions.

Chapter 2

*Shipeng Jia, Jonathan Counsell, Michel Adamič, Antranik Jonderian, and Eric McCalla**

Conceived and designed the experiments: **S. Jia** and **M. Adamič**; Implemented the experiments: **S. Jia** and **M. Adamič**; Performed high-throughput X-ray photoelectron spectroscopy and data analysis: **J. Counsell**; SEM analysis: **A. Jonderian**; Data analysis and interpretation, manuscript writing: **S. Jia**; Revisions and comments: **J. Counsell** and **M. Adamič**.

Chapter 3

*Shipeng Jia, Elissa Yao, Rui Peng, Antranik Jonderian, Marzieh Abdolhosseini, and Eric McCalla**

Conceived and designed the experiments: **S. Jia**; Implemented the experiments: **S. Jia, E. Yao**, and **R. Peng**; Data collection: **S. Jia**, **E. Yao**, **R. Peng**, and **M. Abdolhosseini**; SEM analysis: **A. Jonderian**; Bond valence calculation: **A. Jonderian** and **S. Jia**; Data analysis and interpretation, manuscript writing: **S. Jia**; Revisions and comments: **E. Yao** and **M. Abdolhosseini**.

Chapter 4

*Shipeng Jia, Marzieh Abdolhosseini, Chenghao Liu, Antranik Jonderian, Yixuan Li, Hunho Kwak, Shinichi Kumakura, James Michael Sieffert, Maddison Eisnor, and Eric McCalla**

Conceived and designed the experiments: **S. Jia**; Data collection: **S. Jia**, **M. Abdolhosseini**, and **Y. Li**; Machine learning implementation: **S. Jia** and **C. Liu**; SEM analysis: **A. Jonderian**; X-ray absorption spectroscopy sample preparation and analysis: **S. Jia**, **Y. Li**, **J. M. Sieffert**, and **M. Eisnor**; Revisions and comments: **H. Kwak** and **S. Kumakura**.

Publication List:

Research work reproduced in this thesis from Chapter 2 to Chapter 4:

(1) Jia, S.; Counsell, J.; Adamič, M.; Jonderian, A.; McCalla, E. High-Throughput Design of Na–Fe–Mn–O Cathodes for Na-Ion Batteries. *Journal of Materials Chemistry A* **2021**, *10* (1), 251–265.

(2) Jia, S.; Yao, E.; Peng, R.; Jonderian, A.; Abdolhosseini, M.; McCalla, E. Chemical Speed Dating: The Impact of 52 Dopants in Na–Mn–O Cathodes. *Chemistry of Materials* **2022**, *34* (24), 11047–11061.

(3) Jia, S.; Abdolhosseini, M.; Liu, C.; Jonderian, A.; Li, Y.; Kwak, H.; Kumakura, S.; Sieffert, J. M.; Eisnor, M.; McCalla, E. Stabilization of Na-Ion Cathode Surfaces: Combinatorial Experiments with Insights from Machine Learning Models. *Advanced Energy and Sustainability Research* **2024** 2400051.

Other publications during author's Ph. D. period:

(4) Jonderian, A.†; **Jia, S.**†; Yoon, G.; Cozea, V.; Galabi, N.; Ma, S.; McCalla, E. Accelerated Development of High Voltage Li-Ion Cathodes. *Advanced Energy Materials* **2022**, *12* (40). † Contributed equally.

(5) McCalla, E.; Parmaklis, M.; Rehman, S.; Anderson, E.; **Jia, S.**; Hebert, A.; Potts, K.; Jonderian, A.; Adhikari, T.; Adamič, M. Combinatorial Methods in Advanced Battery Materials Design. *Canadian Journal of Chemistry* **2022**, *100* (2), 132–143.

(6) Johari, N. S. M.; Jonderian, A.; **Jia, S.**; Cozea, V.; Yao, E.; Syed; Ahmad, N.; McCalla, E. High-Throughput Development of Na2ZnSiO4-Based Hybrid Electrolytes for Sodium-Ion Batteries. *Journal of power sources* **2022**, *541*, 231706–231706.

(7) Jonderian, A.; Anderson, E.; Peng, R.; Xu, P.; **Jia, S.**; Cozea, V.; McCalla, E. Suite of High-Throughput Experiments for Screening Solid Electrolytes for Li Batteries. *Journal of The Electrochemical Society* **2022**, *169* (5), 050504–050504.

(8) McCalla, E.; **Jia, S.** Topology to Improve Battery Technology. *Nature Sustainability* **2021**. *5*, 181–182

(9) Sieffert, J. M.; Lang, C. J.; Bazylevych, S.; **Jia, S.**; McCalla, E. The Nb–Ti–W–O System as Safe High-Power Anodes for Li-Ion Batteries. *Journal of Materials Chemistry A* **2024**, *12* (3), 1429–1437.

(10) Jonderian. A; Rehman, S.; Gormley, M.; **Jia, S.**; Ma, S.; Kwon, G.; McCalla, E. Pioneering Combinatorial Investigation to Unlock the Potential of Lithium Borosilicate Glasses as Solid Electrolytes. *ACS Applied Energy Materials* **2024**.

(11) Abdolhosseini, A.; **Jia, S.**; Sieffert, M.; Eisnor, M.; Kumakura, S.; McCalla, E. Systematic Exploration of the Benefits of Ni Substitution in Na–Fe–Mn–O Cathodes. *Advanced Sustainable Systems* **2024**, 2400296.

(12) **Jia, S.**; Kumakura, S.; McCalla, E. Unravelling Air/Moisture Stability of Cathode Materials in Sodium Ion Batteries: Characterization, Rational Design, and Perspectives. *Energy & Environmental Science* **2024**, *17*, 4343-4389.

Contributions to Original knowledge

Addressing the emerging and rapidly increasing demand for energy storage materials in sodium-ion batteries, we demonstrated an innovative high-throughput workflow, showcasing several significant contributions of the original knowledge of sodium-ion battery technology:

1. **Development of a high-throughput optimization methodology:** A novel high-throughput methodology, encompassing synthesis and characterization, was developed. This approach enables the rapid evaluation and screening of potential cathode materials, overcoming the limitations of traditional trial-and-error research. It significantly accelerates the discovery and optimization process by 64 times, reducing energy consumption and waste.
2. **Discovery of novel materials:** We identified over 50 single-phase layered oxide materials and revealed large solid-solution regions within the Na-Mn-Fe-O pseudoternary system, most of which are reported here for the first time. High-throughput doping studies uncovered several new dopants, expanding the range of doping options for layered oxides.
3. **Insights into Composition-Structure-Property relationships:** We addressed several critical cathode properties that influence practical applications and commercialization. New accelerated aging protocols were proposed to study air/moisture stability, crucial for battery production. We identified that doping dramatically improved the structural retention from 0% to 99%. Additionally, we discovered the correlation between anionic redox behavior and bond valence mismatch, demonstrating that modifying the ionic-covalence bond nature of metal-oxygen octahedra can trigger reversible anionic redox, boosting high-voltage capacity. Furthermore, we investigated transition metal dissolution, identifying dopants like B, Li, and

Cu that stabilize the surface and suppress dissolution, enhancing long-term cycling and safety of the battery materials.

4. **Resolution of literature conflicts and confusions:** We resolved several discrepancies and confusions in the literature. We identified a phase stability map for the Na-Mn-Fe-O system, clarifying proper structures and compositions while easily identifying impurities. Our comprehensive XPS studies provided reliable peak assignments through comparative analysis, offering guidance for further peak fitting. Our studies on air stability and transition metal dissolution offered a clear comparative analysis of various doping effects, addressing the lack of quantification and comparison in previous research.
5. **Comprehensive performance database and machine learning approaches:** This thesis examined over one thousand cathode materials, producing thousands of X-ray diffraction patterns and battery test data. The research generated a comprehensive database of the electrochemical properties of various cathode materials, serving as a valuable resource for future research and development. The integration of machine learning techniques refined the understanding of complex relationships between material properties and performance, providing insights into air stability mechanisms and accelerating the discovery of optimal material compositions.

These contributions collectively push the boundaries of current knowledge, offering new paradigms and methodologies for the advancement of sodium-ion battery technologies.

List of Figures

List of Tables

List of Abbreviations

BV	Bond valence
BVM	Bond valence mismatch
CE	Coulombic efficiency
CEI	Cathode electrolyte interphase
CFSE	Crystal field stabilization energy
CFT	Crystal field theory
CJTD	Co-operative Jahn-Teller distortion
CV	Cyclic voltammetry
DFT	Density functional theory
EES	Energy storage system
ESW	Electrochemical stability window
EV	Electric vehicle
EXAFS	Extended X-ray absorption fine structure
FEC	Fluoroethylene carbonate
GoF	Goodness-of-fit
HOMO	Highest occupied molecular orbital
HTP	High throughput
ICE	Internal combustion engine
ICP-OES	Inductively coupled plasma optical emission spectroscopy
J-T	Jahn-Teller
LIB	Lithium-ion battery
LUMO	lowest unoccupied molecular orbital
M	Metal/dopant
ML	Machine learning
NFMO	Sodium iron manganese oxide
NMO	Sodium manganese oxide
NMP	N-Methyl-2-pyrrolidon
OCV	Open-circuit voltage

OSSE	Octahedral-site stabilization energy
PBA	Prussian blue analogs
PCA	Principal component analysis
PLSR	Partial least square regression
PVDF	Polyvinylidene fluoride
RH	Relative humidity
RMSECV	Root mean squared error of cross-validation
R-S	Randles–Ševčík
SEI	Solid electrolyte interphase
SEM	Scanning electron microscope
SIB	Sodium-ion battery
TGA	Thermogravimetric analysis
TM	Transition metal
t-SNE	t-Distributed stochastic neighbor embedding
V2G	Vehicle-to-grid
XANES	X-ray absorption near edge structure
XAS	X-ray absorption spectroscopy
XPS	X-ray photoelectron spectroscopy
XRD	X-ray diffraction

Chapter 1 Introduction

1.1 Battery technologies and electrification

Energy storage technology has played a pivotal role in the advancement of human civilization since the discovery of fire, which harnessed chemical energy and marked a crucial milestone in our development. Today, our pursuit of advanced energy storage technologies continues unabated, driven by the need to manage and store energy effectively to meet diverse consumption demands.[1–3] Furthermore, these technologies are instrumental in capturing and storing renewable energy from sources such as solar and wind[4], thereby contributing significantly to global sustainable development goals[5], as illustrated in **Figure 1.1**.

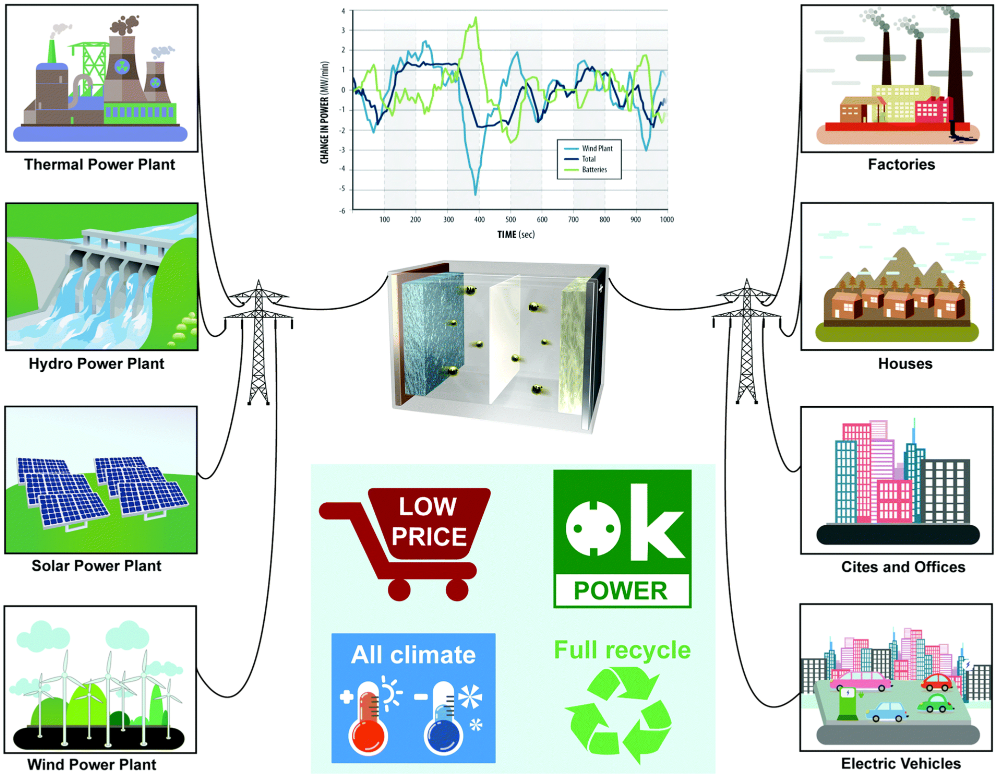

Figure 1.1 Key roles of sodium-ion batteries (SIBs) in sustainable development of grid and electricity applications. Inset, real data of wind-energy battery storage systems. Reproduced with permission from ref. [4].

Conversely, climate change has profoundly impacted human life, leading to a rise in the frequency and intensity of extreme weather events.[6–8] In 2023, devastating wildfires in Canada caused considerable economic losses, destroying 7.76 million hectares of forest cover—a figure surpassing the cumulative loss of the previous six years combined.[9] These fires released approximately 3 billion tons of carbon dioxide into the atmosphere, nearly four times the global aviation emissions recorded in 2022.[10] These environmental crises underscore the urgent imperative for emission control and robust environmental protection measures. Therefore, the development of efficient and sustainable energy storage technologies is critical not only for meeting energy demands but also for mitigating the adverse effects of climate change.

1.1.1 Electric vehicles

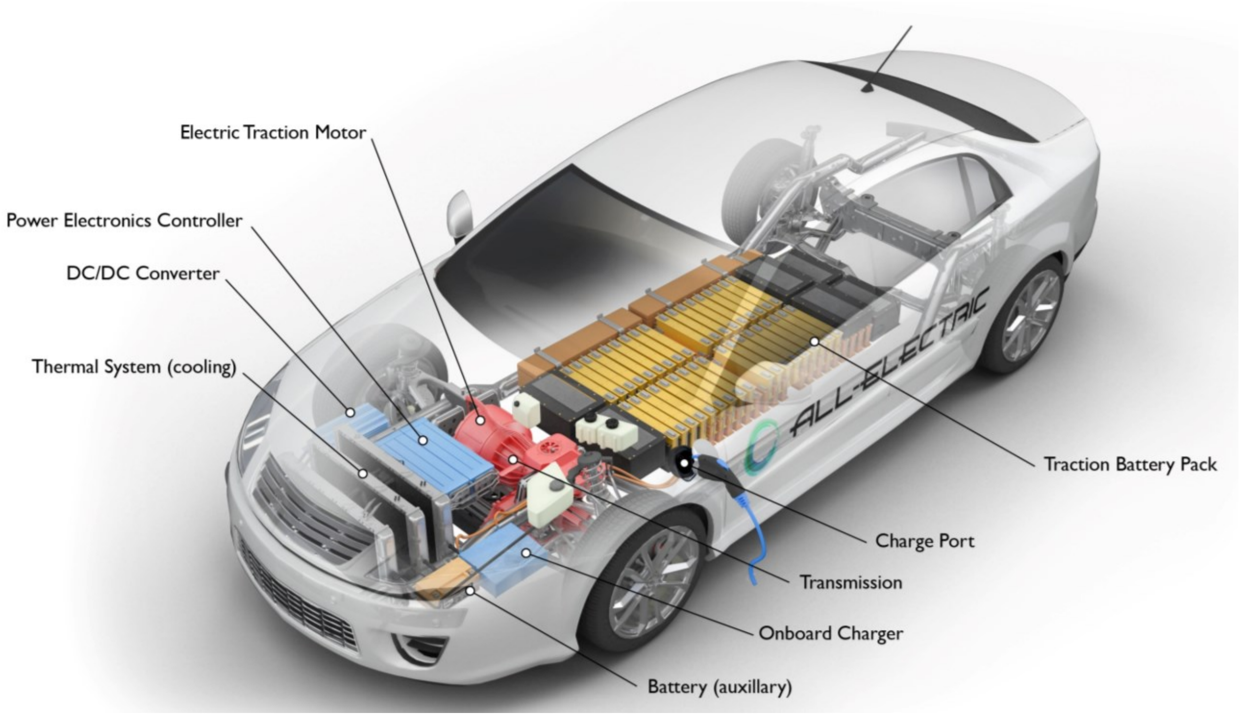

Figure 1.2 *The schematic illustration of key components and structure of an all-electric car. Reproduced with permission from ref.* [11].

In recent decades, the rapid growth of consumer electronics, electric vehicles (EVs), and energy storage systems has positioned lithium-ion batteries at the forefront due to their high energy density and conversion efficiency.[12] EVs significantly reduce pollution and carbon emissions compared to internal combustion engine (ICE) vehicles.[13] Electric motors exhibit a remarkable energy conversion efficiency of over 77% from the grid to the wheel (see **Figure 1.2**), while ICE vehicles achieve only 12-30% efficiency from gasoline to the wheel.[12,14–16]

According to the International Energy Agency (IEA), electric car sales reached approximately 14 million units in 2023, accounting for 18% of total car sales, with China contributing to 60% of these sales.[17,18] The transportation sector is responsible for 29% of total greenhouse gas emissions in the U.S., with over 94% of fuel consumption derived from petroleum.[19] Increasing the electrification of transport vehicles can significantly reduce direct greenhouse gas emissions, provided that the electricity used is generated from renewable energy sources like hydro, wind, and solar power. According to the Canada Energy Regulator's 2023 Global Net-Zero Scenario[20–22], achieving 100% zero-emission vehicle sales by 2035 is projected to meet the net-zero greenhouse gas emissions target by 2050. Consequently, the ongoing environmental crisis and the implementation of urgent policy measures are expected to further accelerate the electrification of passenger vehicles and expand the demand for battery markets. Simultaneously, the sustainability of battery usage must be carefully considered to avoid precipitating another energy crisis.

1.1.2 Energy storage system

Currently, lithium-ion batteries dominate over 90% of energy-storage applications in the global grid market, playing a crucial role in balancing peak and valley electricity demands and enhancing grid resilience.[23] Given the intermittent nature of renewable energy sources, energy storage systems (ESS) are essential for stabilizing the grid and reducing energy curtailment.[4] Industrial-level ESS can store energy during periods of off-peak period for future use, while home-level ESS can integrate with solar panels to store daytime solar energy for nighttime use. Additionally, some electric vehicle companies offer vehicle-to-grid (V2G) technology, which allows EV batteries to supply power back to the grid, further advancing the application of battery packs in EVs.[24]

Energy storage systems are designed to address electricity storage needs at capacities of MWh, which are substantial enough to support renewable energy integration and smart grid demands.[25] These large-scale battery systems must meet several key objectives: cost efficiency, environmental sustainability, high reliability, and robustness.[26,27] Compared to EV batteries, ESS can be less critical regarding energy density and module size, allowing sodium-ion batteries to offer cost advantages over lithium-ion batteries. However, several additional criteria are essential for ESS. Batteries must exhibit excellent rate performance and long-term cycling capabilities to accommodate various operational patterns. A low self-discharge rate is also beneficial for long-term storage applications. End-users should see tangible benefits, such as cost savings or income generation, from investing in ESS, making cost control a crucial factor for practical applications. The resilience and safety of ESS, particularly those used in residential settings, must be ensured to protect consumers. Furthermore, these massive ESS and battery packs should ideally be sustainable and recyclable at the end of their life cycle to prevent significant pollution and toxicity issues.[28] In summary, the development and implementation of advanced ESS, are vital for the effective integration of renewable energy sources and the enhancement of grid stability. These systems must balance performance, cost, and sustainability to meet the growing demands of the modern energy landscape.

1.1.3 Lithium demand and strategic analysis

As shown in **Figure 1.3**, a significant shift towards energy storage systems and transportation will substantially increase the demand for lithium batteries, projecting over 3000 GWh per year by 2030—more than four times the demand in 2023.[29] This surge will result in the energy storage systems and transportation sectors comprising over 90% of the total demand for global battery applications. Concurrently, McKinsey & Company has warned of a potential lithium carbonate shortage, estimating a deficit of approximately 55% or 1772 kilo tons by 2030 (see **Figure 1.4**), based on the current supply chain and mining resources.[30] This indicates an ongoing conflict between rising energy demands and the limitations of battery supply chains.

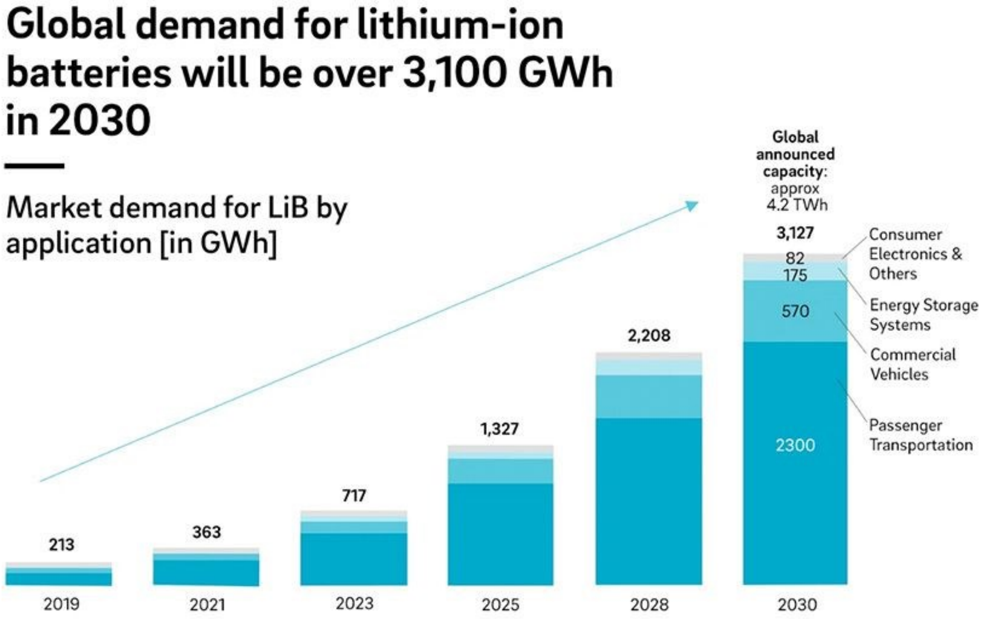

__Figure 1.3__ Global annual demand for Li-ion batteries predicted until 2030. Sources: Avicenne, Fraunhofer, HIS Markit, Interviews with market participants, Roland Berger. Reproduced with permission from ref. [29].

However, the extensive use of LIB presents challenges related to lithium resources. Global lithium reserves are estimated at 98 million tons[31], with recoverable reserves at 26 million tons. While the theoretical lithium reserves may suffice for LIB production, most lithium resources are concentrated in high-altitude plateau salt lakes, complicating extraction and potentially damaging local ecosystems.[32,33] The uneven distribution of lithium reserves also threatens the stable development and reliability of the battery industry, with the majority of these reserves located in the "Lithium Triangle"—Chile, Argentina, and Bolivia—which accounts for half of the global lithium reserves[34]. Rapid expansion in lithium extraction consumes significant water resources—approximately 1,900 tons of water per ton of lithium[34]. For instance, in Chile's Salar de Atacama, 65% of the local water supply is used for lithium extraction, leading to serious environmental impacts on soil, water, and air quality.[34] Therefore, the sustainability issues associated with the lithium mining industry must be carefully considered for future large-scale battery deployment.

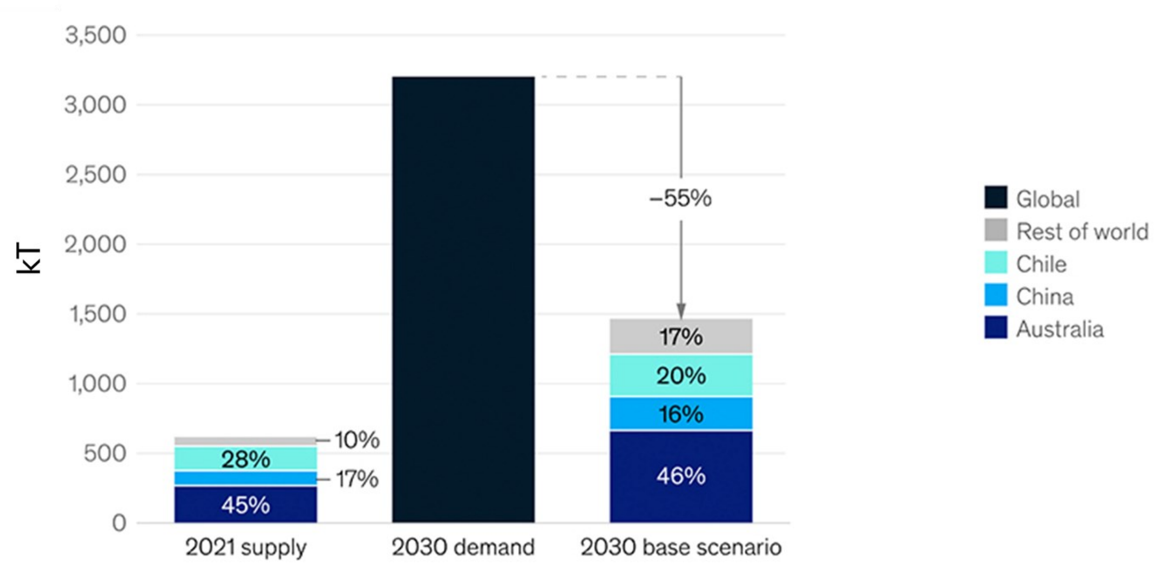

Figure 1.4 *Lithium carbonate global equivalent demand 2030, supply 2021 and 2023 by country. Source: McKinsey MineSpans, 2022. Reproduced with permission from ref.* [30].

In contrast, sodium is abundant and shares chemical properties with lithium, making sodium-ion batteries a viable alternative to lithium-ion battery systems. SIBs offer advantages such as lower cost, sustainable properties with various transition metal selections, and highly tunable electrochemical properties.[35–37] However, achieving comparable battery performance in terms of energy density and lifecycle remains a challenge. It is crucial to emphasize that an inefficient or short-lasting battery cannot be considered environmentally friendly. Therefore, my research aims to advance the development of sustainable sodium-ion batteries through high-throughput methodologies, thereby facilitating their widespread adoption as alternatives or supplements to lithium-ion batteries. SIBs represent a promising technology to meet the increasing demand for energy storage solutions.

1.1.4 Comparison between LIBs and SIBs

The history and development of LIBs and SIBs are closely intertwined, as both technologies share similar chemical properties as alkali metals. The key events for LIBs and SIBs are highlighted in **Figure 1.5**. The intercalation chemistry of alkali metals was first demonstrated in graphite by K. Fredenhagen et al. in 1926.[38] This breakthrough was followed by the first report of alkali metal intercalation into layered dichalcogenides as hosts by Rüdorff and Sick in 1959.[39,40] These foundational studies laid the groundwork for the use of layered materials in battery applications.

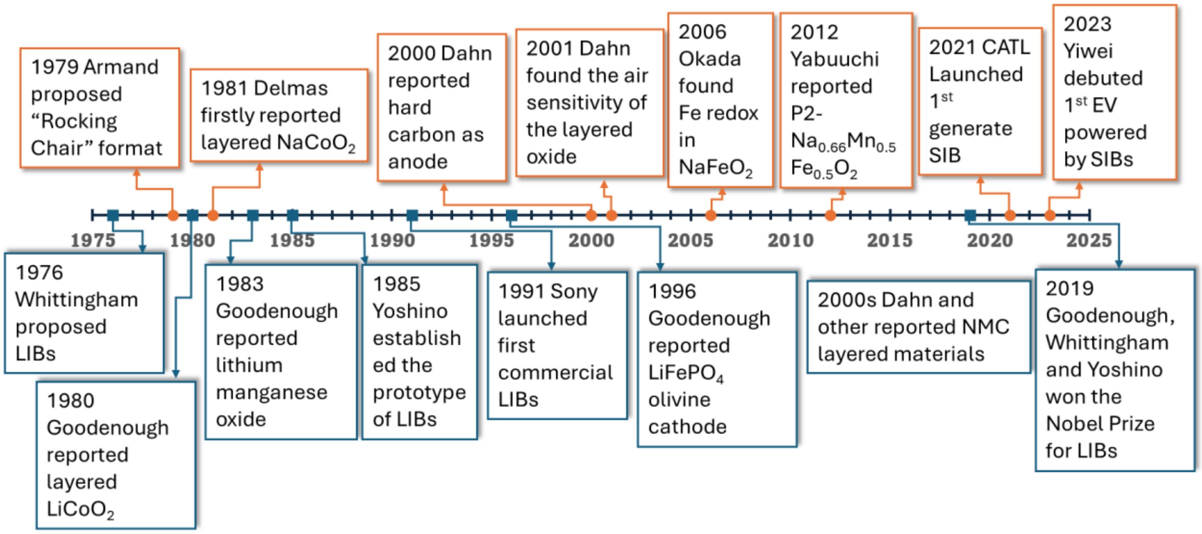

Figure 1.5 *The timeline of the key events for SIBs (up) and LIBs (down) development.*

In 1976, American scientist M.S. Whittingham et al. investigated the electrochemical intercalation behavior of Li^+ and Na^+ ions into TiS_2, using it as a cathode with alkali metals as anodes.[41] This research marked the beginning of the era of Li/Na-ion batteries. Whittingham discovered that Li_xTiS_2 could reversibly insert $x = 1$ of Li^+ ions into the TiS_2 layers with a voltage of about 2.0 V, while Na_xTiS_2 exhibited less energy density, accommodating only 0.8 Na ions per formula unit within its layered structure[42], as demonstrated in **Figure 1.6**. Whittingham also envisioned this ambient-temperature battery being used for electric vehicle propulsion. In 1979, French scientist Michel Armand proposed the concept of the "Rocking Chair" battery[43], which emphasized the high reversibility of Li/Na-ion rechargeable batteries. In 1980, John Goodenough synthesized Li_xCoO_2 as a cathode material[44], achieving an open-circuit voltage of 3.7 V, nearly double that of TiS_2. In the following year, Delmas reported Na_xCoO_2 as an analogous material[45], becoming one of the pioneers in SIB development. Up to this point, the development of Li and Na-ion batteries had progressed synchronously.

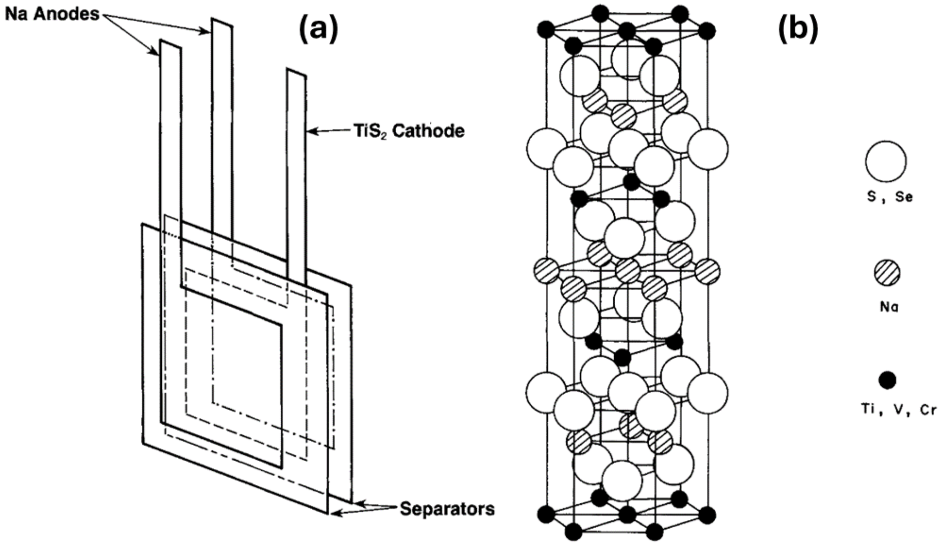

Figure 1.6 *(a) Schematic construction prototype design of prismatic Na-TiS_2 battery. Reproduced with permission from ref.* [46]*. (b) Crystal structure of layered $Na_{0.8}TiS_2$ ($Na_{0.8}MX_2$). Reproduced with permission from ref.* [47]*.*

However, from the 1980s onward, significant attention shifted towards lithium-ion batteries, particularly after Sony's commercialization of the first lithium-ion battery in 1991. Several factors may contribute to this divergence:

a) Radius: The ionic radius of Li^+ is smaller than that of Na^+, which leads to better compatibility with host materials and higher charge capacities for Li^+ storage.

b) Energy density: SIBs typically operate at voltages below 3 V, whereas LIBs can achieve higher voltages (around 3.7 V), resulting in greater energy density for Li-ion batteries.

c) Safety: Both battery types initially used metal anodes, but sodium metal, being more reactive, is harder to handle even with a modern glove box and more dangerous than lithium metal.

d) Suitable anode: The commercialization success of lithium-ion batteries was bolstered by the use of carbon anodes, such as graphite, which is unsuitable for the larger radius Na^+ ion. This issue was addressed in 2000 when Jeff Dahn et al. discovered that hard carbon could effectively store Na^+ ions[48].

Therefore, while the early development of Li and Na-ion batteries was parallel, practical challenges and material properties led to a greater focus on lithium-ion technology. However, recent advancements in sodium-ion battery technology, particularly the use of hard carbon anodes, suggest a promising future for SIBs as a complementary or alternative energy storage solution.

The resurgence of sodium-ion batteries began in the 2010s, with the number of papers published between 2010-2013 nearly equaling the total number of papers published previously. As the battery market rapidly expanded, researchers and some companies started to revisit SIBs, recognizing their potential alongside the success of LIBs in electronic devices and the emerging fields of electric vehicles and energy storage systems. The maturity of LIB technology encouraged researchers to explore and discover new battery materials beyond LIB. Additionally, increasing concerns about sustainability and climate change have driven the development of green and eco-friendly battery alternatives.

Table 1.1 *Comparison of chemical and physical properties between Li and Na.*[49–52]

Properties	**Li**	**Na**
Atomic mass [g mol^{-1}]	6.94	22.99
Electron configuration	[He]2s^1	[Ne]3s^1
Shannon radius [Å]	0.76	1.02
Stokes radius (PC) [Å]	4.8	4.6
Molar conductivity in $AClO_4$ (PC) [S cm^2 mol^{-1}]	6.54	7.16
De-solvation energy (PC) [kJ mol^{-1}]	218.0	157.3
Standard electrode potential [V]	-3.04	-2.71
Melting point [°C]	180.5	97.7
Density [g cm^{-3}]	0.534	0.971
First ionization energy [kJ mol^{-1}]	520.2	495.8
Theoretical gravimetric capacity [mAh g^{-1}]	3861	1165
Theoretical volumetric capacity [mAh g^{-1}]	2062	1131
Abundance in the earth's crust [mg kg^{-1}]	20	23600
Cost of carbonate [USD kmol^{-1}]	740-4400	39

Building on the wealth of knowledge accumulated from LIB research, three primary types of cathode materials have garnered significant attention in the development of SIBs: layered oxides, polyanion compounds, and Prussian blue analogs (PBAs). In 2012, Yabuuchi et al. demonstrated the potential of $Na_{0.66}Mn_{0.5}Fe_{0.5}O_2$, a layered oxide made with earth-abundant Mn and Fe contribute to a high specific capacity of 190 mAh/g.[53] This discovery highlighted the feasibility of utilizing abundant elements in battery materials. In 2013, Goodenough et al. reported on Prussian white, which exhibited excellent rate capability, further expanding the scope of viable materials for SIBs.[54] The ongoing discovery of new materials, particularly layered oxides, has broadened the range of elemental compositions available for optimizing electrochemical performance and other key properties. This progress has sparked significant interest from industry players such as Faradion, Tiamat, CATL, and HiNa, who are actively contributing to the accelerated development of SIBs.

Table 1.1 summaries various physical and chemical properties of Li and Na. Currently, SIBs demonstrate comparable electrochemical performance to certain types of LIBs, such as spinel $LiMn_2O_4$. This highlights the potential of SIBs as the next generation of battery technology, offering several extra promising advantages over LIBs:

a) Abundance and Environmental Friendliness: Sodium is over 1000 times more abundant than lithium, widely distributed, environmentally friendly, and lower in cost.

b) Diverse Transition Metal Selections: Layered oxides in SIBs can incorporate various transition metals (Ti, V, Cr, Mn, Fe, Co, Ni, and Cu), allowing for extensive combinatorial studies to optimize battery materials.

c) Smaller Stokes Radius and De-Solvation Energy: Although Na ions have a larger Shannon ionic radius, which reduces its mobility in cathode materials, its Stokes radius and de-solvation energy in the electrolyte can be smaller.[52] This suggests that SIBs can operate with lower concentrated electrolytes without compromise electrolyte performance.

d) Cost-Effective Current Collectors: Unlike lithium, sodium does not react with aluminum foil, enabling the use of aluminum for both cathode and anode current collectors in SIBs, which reduces production costs.

e) Design Flexibility: SIBs permit the application of cathode and anode materials on both sides of a single aluminum foil, such as a bipolar electrode structure, enabling the creation of high-voltage battery stacks and offering design flexibility.

f) Improved Safety and Temperature Tolerance: SIBs generally exhibit better safety and tolerance to wider temperatures compared to LIBs[55,56], enhancing overall battery reliability and safety in various applications.

Based on these opportunities and challenges, this thesis will concentrate on optimizing SIB materials to improve their electrochemical performance and enhance their various chemical and physical properties. By exploring and refining the characteristics of SIB materials, this work aims to contribute to the advancement and commercialization of high-energy sodium-ion battery technology in the context of future energy storage applications.

1.2 Principles of sodium-ion batteries

The operation of sodium-ion batteries is fundamentally based on intercalation chemistry and the "rocking chair" mechanism, as pioneered by Whittingham[41] and Armand[43]. As shown in **Figure 1.7**, during the charging process, sodium ions are extracted from the cathode and intercalated into the anode through an ion-conductive electrolyte, which is soaked in a polymer separator and acts as an electronic insulator. During discharge, the process reverses: sodium ions move back to the cathode from the anode, facilitating energy conversion. This cyclical movement of sodium ions between the electrodes allows for efficient energy storage and retrieval.

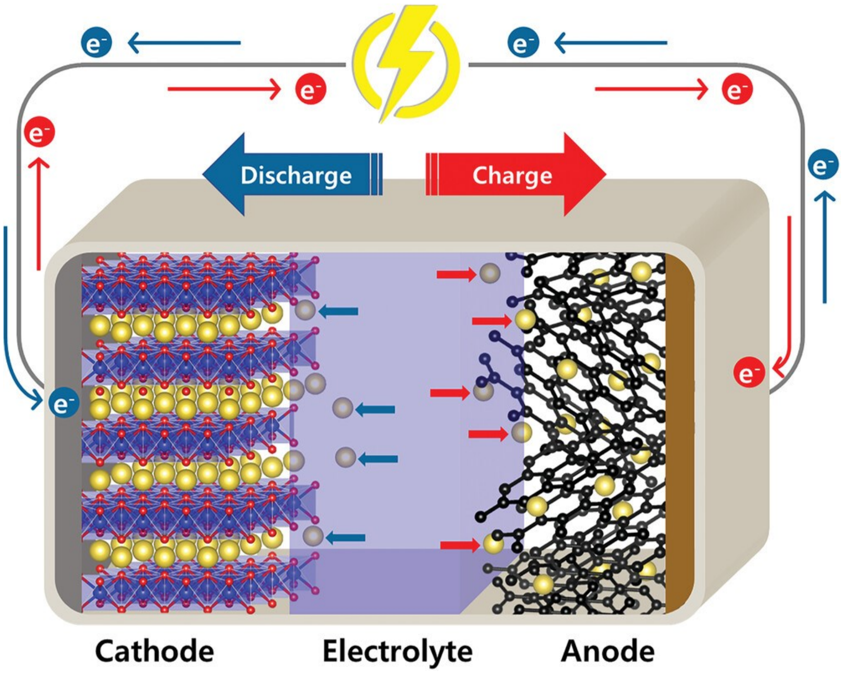

Figure 1.7 *A schematic illustration of a sodium-ion battery showcases a layered oxide as the positive electrode (labelled cathode, its role during discharge) and hard carbon as the negative electrode (labelled anode, its role during discharge). Reproduced with permission from ref.* [57].

1.2.1 Electrochemical principles

As proposed in the early 1970s, the initial battery design utilized TiS_2 as the cathode and Li/Na metal as the anode. In this setup (see **Figure 1.6**), the anode serves as the source of Li/Na ions, which must first be discharged. The Li/Na ions then intercalate into the layered TiS_2 structure, forming Na_xTiS_2 (refer to Eq. 1-1 and 1-2 below). However, researchers soon identified a significant drawback of using Li/Na metal as the anode: it tends to form dendrites after repeated cycling. During the charging process, Li^+/Na^+ ions are reduced and electrochemically deposited onto the metallic anode. However, non-uniform ionic flux, electric field gradients, and thermodynamic instabilities at the electrolyte-electrode interface can lead to the formation and accumulation of dendrites.[60] These dendrites can penetrate the separator, causing short circuits and posing safety hazards during long-term usage. To address this issue, it was proposed that the cathode should be pre-lithiated/sodiated to eliminate the dependence on alkali metals in their metallic form.

Cathode: $$TiS_2 + xNa^+ + xe^- \leftrightarrow Na_xTiS_2$$ *Eq. 1-1*

Anode: $$Na \leftrightarrow Na^+ + e^-$$ *Eq. 1-2*

Therefore, as illustrated in **Figure 1.7**, the modern model of sodium-ion batteries incorporates intercalation hosts for both the cathode and anode to prevent sodium metal deposition and dendrite formation. In the example shown, the cathode is composed of layered transition metal oxides (Na_xTMO_2), while the anode is hard carbon, which has a higher degree of disorder compared to graphite used in lithium-ion batteries. The redox reactions at the electrodes during battery discharge are depicted in the equations below. The reverse reactions occur during the charging process.

Cathode: $$Na_{1-x}TMO_2 + xNa^+ + xe^- \leftrightarrow NaTMO_2$$ *Eq. 1-3*

Anode: $$Na_xC_y \leftrightarrow yC + xNa^+ + xe^-$$ *Eq. 1-4*

Total reaction: $$Na_{1-x}TMO_2 + Na_xC_y \leftrightarrow NaTMO_2 + yC$$ *Eq. 1-5*

During the operation of sodium-ion batteries, electrical energy is first converted into chemical energy during the charging process. Specifically, sodium ions de-intercalate from the cathode and shuttle through the electrolyte to intercalate into the anode. Concurrently, the electrochemical potential of the cathode increases as it loses electrons through the external circuit. The opposite process occurs during discharge, where chemical energy is converted back into electrical energy and delivered to the external circuit. The energy and electrochemical potential of the battery can be better understood with the assistance of an energy diagram of the battery components. In this diagram, the cathode ($NaTMO_2$) is positioned at a lower electron energy (higher voltage), and the anode (hard carbon) is positioned at a higher electron energy (lower voltage). The initial electrochemical potential difference, known as the open circuit voltage (V_{oc}), typically ranges from 2 to 3 V versus Na/Na^+. Upon charging, the Fermi energy of the cathode decreases as it loses electrons and sodium de-intercalates. Concurrently, the transition metal (TM) in $NaTMO_2$ is oxidized, reaching a high electrochemical potential (~4.3V vs Na/Na^+). However, at higher voltages, the anion (O^{2-}) can also undergo oxidation to form O^-, a process known as anionic redox.[58]

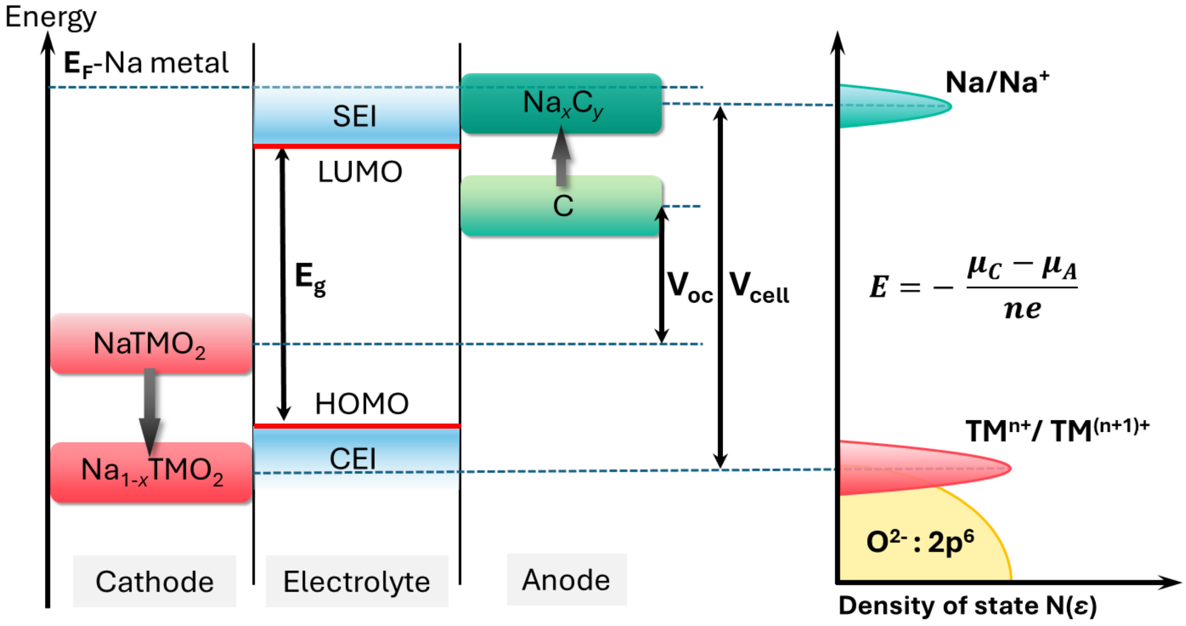

Figure 1.8 *Schematic energy diagram of the cathode, the electrolyte, and the anode. The gray arrow showcases the relative energy movement after charging.*

Conversely, the anode's electrochemical potential decreases (~0.1 V vs Na/Na^+). The overall cell voltage (V_{cell}) is also influenced by the voltage window (E_g) of the electrolyte, determined by the energy gap between the highest occupied molecular orbital (HOMO) and the lowest unoccupied molecular orbital (LUMO). Ideally, battery operation should be limited within the electrochemical potential range between the LUMO and HOMO.

However, in practice, the cell voltage can exceed this range, which results in electrolyte decomposition and creates interphases that can suppress further electrolyte decomposition.[35] These interphases are known as the cathode electrolyte interphase (CEI) at the cathode and the solid electrolyte interphase (SEI) at the anode. The function of these interphases, particularly the SEI, is crucial as they passivate side reactions of the electrolyte and extend the voltage range.[59] An ideal interphase should be an electronic insulator with high sodium-ion conductivity. Additionally, it should possess good mechanical properties to maintain the uniformity of active particles, prevent the exfoliation of hard carbon, and suppress dendrite formation.[60] However, unfavorable SEI formation can increase internal resistance, consume sodium ions, and accelerate cell degradation. Thus, comprehending and optimizing these diverse battery components are vital and intricate tasks for improving the performance, safety, and longevity of sodium-ion batteries.

1.2.2 Concepts and terminologies for battery

During the electrochemical testing of sodium-ion batteries, it is essential to clarify certain concepts and terminologies to better understand the principles of these batteries.

Voltage:

- **Electromotive Potential (E):**

  The electrochemical reaction combines the chemical redox reactions occurring at the cathode and anode. The relationship between the Gibbs free energy of the redox reaction and the converted electrochemical potential under standard conditions is given by:

$$\Delta G_{(T,p)} = -n_e F E$$

where n_e is the number of electrons transferred during the electrode reaction, **F** is Faraday's constant (**F** = 96485 C/mol); E is the standard electromotive potential, theoretically representing the maximum limit of electrical energy converted from chemical energy.

- **Open-Circuit Voltage (V_{oc}):**

  V_{oc} is the voltage differential between the cathode and anode in the absence of any load or external current, and it is generally lower than the electromotive potential E.

- **Working or Operating voltage (V_w):**

  This refers to the actual voltage during battery operation under load. Due to internal resistance, the working voltage is invariably lower than V_{oc}. It fluctuates with the current and depth of discharge during operation and must overcome both ohmic and polarization resistances:

$$V_w = E - iR_i = E - i(R_\Omega + R_f)$$

- **Cut-off Voltage:**

  The cut-off voltage delineates the permissible range for charging and discharging the battery, thereby preventing over-charging or over-discharging. Exceeding the cut-off voltage can induce irreversible reactions, rapid battery degradation, and safety risks. In practical applications, the cut-off voltage is confined to a narrower range compared to laboratory conditions to mitigate these issues.

Charge capacity:

- **Theoretical Capacity (C_0):**

  The theoretical capacity represents the maximum amount of charge that can be provided by the electrode material, calculated using Faraday's law. Although charge is measured in

Coulombs, it is more commonly described in terms of current integrated over time (1 mAh = 3.6 C). The theoretical capacity is given by:

$$C_0 = \frac{F \times n_e}{M_w \times 3600} = \frac{26.8 \times n_e}{M_w}$$

For instance, the molecular weight (***M_w***) of $NaMnO_2$ is 110 g/mol. If it fully charges to MnO_2 and transfers one equivalent electron, the theoretical capacity of $NaMnO_2$ is 244 mAh/g.

- **Actual Capacity (*C* or *Q*):**

  The actual capacity denotes the real charge passing through the electrode during operation. In this thesis, this value will be calculated from cyclic voltammetry (CV) data. The actual capacity is determined by integrating the current over time:

$$C = \int_0^t I dt$$

  where ***I*** is the charge/discharge current pass through the battery as function of time ***t***.

- **Specific Capacity (*C_m*):**

  The specific capacity of the active material is obtained by normalizing the actual capacity with the mass of the active material (or the cell). Thus, the units are mAh/g for mass-specific capacity and mAh/L for volume-specific capacity:

$$C_m = \frac{C}{m}$$

- **Rate Capacity:**

  The rate capacity is determined by charging and discharging the battery at a specific current density. This metric reflects the rate performance of the battery, which is particularly important for applications requiring fast charging or high power during use. Increased current density often results in decreased capacities due to kinetic limitations from ion transport and charge transfer. Specifically, the rate of Na-ion diffusion through electrode materials and the electrolyte may be insufficient to keep pace with increasing current density, resulting in concentration polarization. Additionally, inadequate electronic conductivity within the electrodes can introduce greater resistance at high current densities, thereby compromising the rate performance.

- **Nominal or Rated Capacity:**

  The nominal capacity, typically specified by the manufacturer, describes the specific capacity under designated operating conditions, such as current density and temperature.

Energy and Power:

- **Theoretical Energy (W_0):**

  The theoretical energy represents the ideal scenario during battery discharge, where the voltage remains at the electromotive potential ***E*** with 100% Faraday charge conversion. The unit is typically expressed in watt-hours (Wh):

$$W_0 = C_0 E$$

- **Actual Energy (W):**

  In real-world situations, the current ***I*** and the working voltage V_w vary over time ***t***. Therefore, the actual energy ***W*** is calculated as:

$$W = \int_0^t V_W I dt$$

  Once the capacity ***C*** over the time ***t*** is obtained, the actual energy can also be calculated using the average voltage. However, this equation is often used to calculate the average voltage instead. We use this equation to calculate the average voltage after the cell operates at cyclic voltammetry:

$$W = V_{avg.}C$$

- **Specific Energy or Energy Density (*W_m* or *W_v*):**

  Energy density is a crucial metric for battery performance as it is proportional to both capacity and voltage. It is used to compare various active materials or battery packs. It is calculated by dividing the energy by the mass or volume of the active material or battery pack, with units of Wh/kg or Wh/L.

$$W_m = \frac{V_{avg}C}{m} \ or \ W_V = \frac{V_{avg}C}{V}$$

- **Theoretical Power (*P_0*):**

  Cell power expresses the rate of energy or work output over time, which is crucial for applications such as electric vehicles. Theoretical power can be calculated as:

$$P_0 = \frac{W_0}{t} = \frac{C_0 E}{t} = IE$$

- **Actual Power (*P*):**

  Actual power is obtained using real-time voltage and current, such as instantaneous power. At high current densities, the polarization resistance R_f may increase, which can compromise the actual power:

$$P = IV_w = I(E - I(R_{\Omega} + R_f))$$

Cycling:

- **Charge or Discharge Rate:**

  The charge/discharge rate is utilized to evaluate the rate performance of the battery. During galvanostatic (constant current) testing, it is often denoted as the C-rate, where 1C represents the current density that fully charges the battery in one hour. Typically, 1C is defined by the current density required to achieve theoretical capacity. For example, for $NaMnO_2$, 1C corresponds to 244 mA/g.

- **Coulombic efficiency (CE):**

  CE describes the efficiency of the charge and discharge process. Ideally, CE should be a value very close to, but less than, 100%, indicating that all the charge is generated from reversible faradic current. However, irreversible processes such as solid-electrolyte interphase (SEI) formation, electrolyte decomposition, and overpotential can result in a lower CE. It is important to note that CE is calculated by dividing the discharge capacity by the charge capacity from the preceding half cycle.

$$CE = \frac{C^{Discharge}}{C^{Charge}} \times 100\%$$

- **Capacity Retention or Cyclability:**

  Capacity retention is calculated by dividing the discharge capacity at a specific cycle *n* by the discharge capacity at the 1st or 2nd cycle, depending on the cyclic conditions. In practical applications, the cycle life is determined when the capacity retention decays to 80%. In this thesis, we optimized various factors, including compositions and doping, to influence the capacity retention of the cathode materials:

$$Capacity\ retention = \frac{C_n^{Discharge}}{C_{\mathrm{1st\ or\ 2nd}}^{Discharge}}$$

- **Galvanostatic (Constant Current) Measurements:**

  For battery measurement, a common method involves applying a constant current during charging and allowing the battery to discharge at the same constant current. The voltage within cut-off voltages is measured as a function of time throughout this process, as shown in **Figure 1.9**. As previously mentioned, the C-rate is used to determine the scan rate, which is a critical parameter in battery testing. Typically, a 0.1C (or C/10) rate is considered a slow charge/discharge rate, which means the battery is expected to be charged in about 10 h for a half cycle. This slow rate is used to analyze various electrochemical properties and determine the battery's capacity with high accuracy. On the other hand, a 1C rate or higher is often considered a fast charge rate, and it is used to evaluate the rate performance of the battery. This involves charging or discharging the battery in one hour or less. By testing the battery at different C-rates, researchers can gain comprehensive insights into its performance characteristics, including capacity retention, rate capability, and cycle life. The derivative of the charge-voltage curve, known as the ***dQ/dV*** curve, can be used to analyze redox peaks and material activity as a function of voltage, similar to a CV curve.

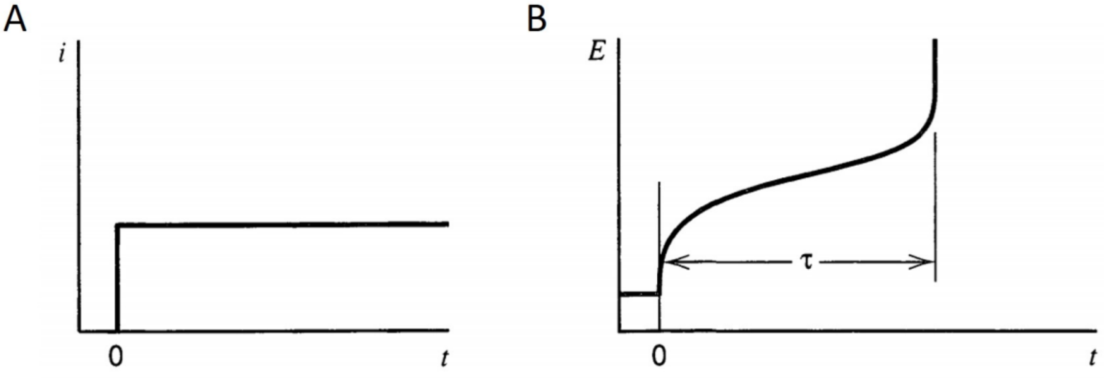

Figure 1.9 *Galvanostatic measurement (A) constant current applied to the battery. (B) The voltage profile as a function of time. Reproduced with permission from ref.* [61].

- **Cyclic Voltammetry (CV) Measurements:**

  CV often applies a linear voltage scan to charge and discharge the battery, as shown in **Figure 1.10**. During this process, the response current is recorded, allowing for the plotting of the CV curve (voltage vs. current). A pair of peaks in the CV curve indicates a redox process, which is typically associated with a transition metal redox reaction coupled with the Na^+ (de-)intercalation.

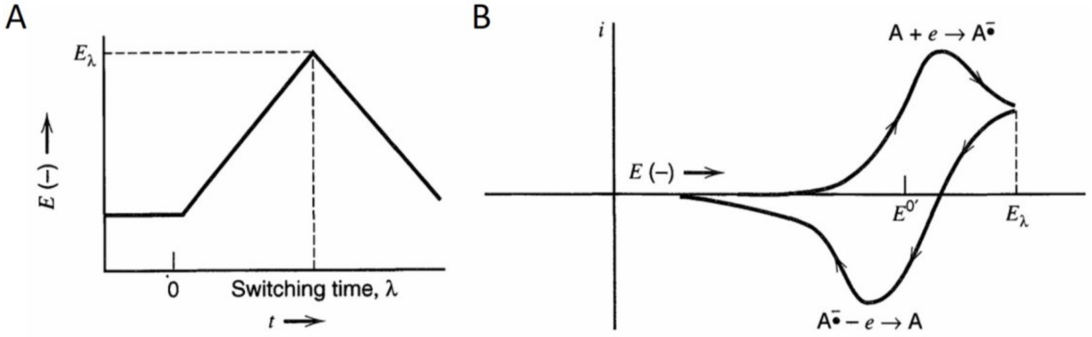

Figure 1.10 *Cyclic voltammetry measurement. (A) The forward and reverse linear voltage scan. (B) The CV curve obtained from the voltage scan and the response current. Reproduced with permission from ref.* [61].

In an ideal electrochemical process, the charge peak potential will be slightly higher than the equilibrium electrochemical potential, while the discharge peak voltage will be slightly lower. The difference between the peak of the cathodic (reduction) and anodic (oxidation) currents can be used to estimate the reversibility of the redox process. A narrower difference between these peak voltages indicates higher reversibility of the redox process. In this thesis, cyclic voltammetry (CV) analysis is employed. A scan rate of 0.1V/h from 1.5 V to 4.3 V is selected to calculate various electrochemical properties.

Moreover, the current in the CV curve is influenced by the scan rate and the diffusion coefficients according to the Randles–Ševčík (R-S) theory[61]. According to this theory, the peak current ($\boldsymbol{i_p}$) is directly proportional to the square root of the scan rate ($\boldsymbol{v}$), the concentration of the electroactive species, and the diffusion coefficient ($\boldsymbol{D}$). The constant $\boldsymbol{A}$ and $\boldsymbol{c}$ are the area of the electrode and concentration of electroactive species. The Randles–Ševčík equation is expressed as:

$$i_p = (2.69 \times 10^5) n^{3/2} A D^{1/2} c v^{1/2}$$

By measuring the peak current under various scan rates, the Na^+ diffusion coefficient can be estimated. Several key criteria should be considered when applying this equation.[61] It is essential that the process being measured is electrochemically reversible and that the electrochemical reaction is primarily diffusion-controlled. The linear relationship between $\boldsymbol{i_p}$ and $\boldsymbol{v}^{1/2}$ must be experimentally verified to obtain a meaningful diffusion coefficient ($\boldsymbol{D}$), which should remain constant under diffusion-controlled conditions. This information is crucial for understanding the mass transport properties of the electrochemical reactions and the performance of the battery materials. In **Chapter 3**, we applied R-S equation to study the Na^+ diffusion coefficient affected by various dopants.

1.2.3 Battery components (electrolyte and anode)

During battery operation, it is crucial to maintain strict separation between the cathode and anode with a separator to prevent short circuits. Additionally, a polar aprotic organic electrolyte containing Na salts ensures ionic conductivity while insulating electrons. Each component of the battery must function cohesively to achieve both high performance and safety. In the following sections, we will provide a concise overview of key battery components, including the electrolyte and anode. A detailed introduction to cathode materials will be presented in Section 1.3.

Electrolyte:

The electrolyte is pivotal in connecting the cathode and anode, ensuring efficient ion channel formation to maintain separation and establish potential differences. It forms interphases with the electrodes to facilitate solid-liquid ion transport and ensure interfacial stability. Additionally, the electrolyte plays a critical role in facilitating fast charging, ensuring safety, minimizing self-discharge, and extending battery life cycle.[62] Typically, the electrolyte system consists of a sodium salt as the ion carrier dissolved in an organic polar aprotic solvent, often supplemented with additives for stabilization. Overall, an excellent electrolyte must meet the following criteria:

a) **High Ionic Conductivity and Electron Insulation:** Ensuring high ionic conductivity and effective electron insulation is crucial for the efficient transfer of Na^+ within the liquid electrolyte, particularly for fast charging. Electron insulation helps prevent short circuits and self-discharge. Low de-solvation energy and viscosity enable rapid Na^+ transport within solvent fractions. Ionic conductivities in organic liquid electrolytes (OLEs) typically range from 1 to 10 mS/cm.

b) Wide Range of Physical Properties: A low melting point and high boiling point provide the electrolyte with versatile temperature-dependent properties. A high boiling point indicates low volatility, high polarity, and high solubility for sodium salts, ensuring stability over a wide temperature range. A low melting point signifies low viscosity, excellent electrode wettability, and enhanced battery performance at lower temperatures.

c) Chemical and Electrochemical Stability: Excellent chemical and electrochemical stability is essential for ensuring compatibility with electrodes and preventing redox decomposition. A wide electrochemical stability window contributes to long-term battery stability and safety.

d) Thermal Stability and Flammability: Thermal stability and flammability are significant concerns for OLEs. Future solutions may involve additives to suppress combustion, non-flammable electrolyte, and solid electrolytes to mitigate these risks.

e) Cost-effectiveness and Toxicity: Cost-effectiveness is a key advantage of most OLEs, although toxicity, especially in fluorine-based sodium salts, should be carefully considered and managed.

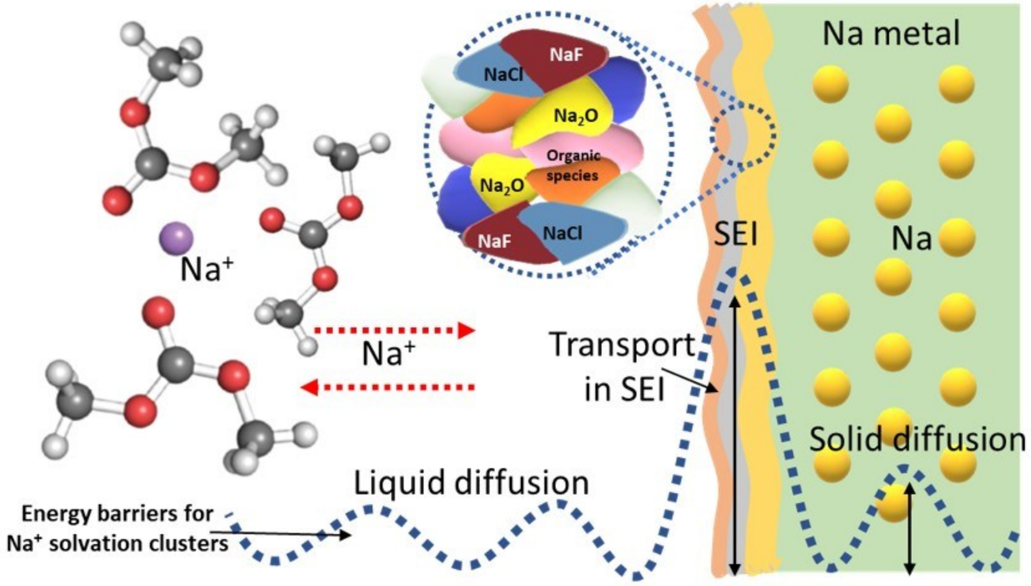

Figure 1.11 *Scheme illustrates Na$^+$ solvation clusters and transport. Solid electrolyte interphase formation at the surface of the anode. Reproduced with permission from ref.* [59].

Common organic solvents used as electrolytes include ester-based and ether-based solvents (see **Table 1.2**).[62] Ester-based solvents are widely adopted in SIBs and LIBs, known for their high oxidation voltages, reaching up to 4.3V. Key examples of ester-based solvents include propylene carbonate (PC) and ethylene carbonate (EC). These cyclic carbonates typically exhibit high dielectric constants, facilitating the dissociation of sodium salts while maintaining relatively low viscosity. EC has a higher melting point (36.4 °C), necessitating blending with other OLEs. EC is also capable of forming a dense SEI layer, thereby increasing the electrochemical voltage window (see **Figure 1.11**).

Table 1.2 *Common organic solvents for liquid electrolytes in SIBs.*[62–65]

Solvent	Chemical Structure	Molecular weight (g mol^{-1})	Density (g cm^{-3})	Melting point (°C)	Viscosity (25 °C) (cP)	Dielectric constant (25 °C)
Propylene carbonate (PC)	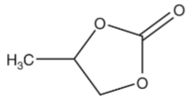	102.09	1.204	-49.2	2.35	64.92
Ethylene carbonate (EC)	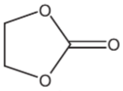	88.06	1.321	36.4	2.1	89.78 (48 °C)
Dimethyl carbonate (DMC)	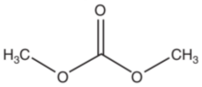	90.8	1.069	4.6	0.59 (20 °C)	3.107
Dimethoxy-methane (DME)	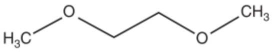	90.12	0.867	-58	0.46	7.18
1,3-dioxolane (DOL)	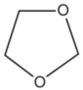	74.08	0.531	-95	0.531	7.13
Tetrahydrofuran (THF)		72.11	0.89	-108	0.53 (20 °C)	7.58
Fluoroethylene carbonate (FEC)	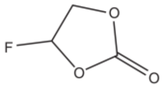	106.05	1.41	18	2.23	Additive

In contrast, PC has a lower melting point (-48.8 °C), making it suitable for a broader range of operating temperatures. While PC is known to intercalate into graphite and exfoliate its structure in LIBs, it is stable against hard carbon in SIBs, making it one of the most common solvent choices for SIBs.[63,64] Ether-based solvents, such as dimethoxymethane (DME), 1,3-dioxolane (DOL), and tetrahydrofuran (THF), are noted for their better chemical stability against reduction at the anode. They tend to form thin and dense SEI layers, especially exhibiting good compatibility with sodium metal. However, these solvents are less stable at higher voltages in the cathode, making them more suitable for low-voltage cathode applications.[65]

To achieve better electrolyte properties that meet the aforementioned criteria, researchers have found that combining or mixing solvents can address the shortcomings of individual solvents. Common solvent combinations include EC/PC, PC/DMC, and EC/PC/DME, among others.[63]

Additionally, the use of additives can significantly enhance electrolyte performance in various ways[62]:

a) **Film Formation Additives:** These improve the stability of the Solid Electrolyte Interface (SEI) and Cathode Electrolyte Interface (CEI).

b) **Flame Retardant Additives:** These reduce the risk of combustion.

c) **Overcharge Protection Additives:** These additives act sacrificially to protect the battery during overcharge conditions.

A notable example of an effective additive is fluoroethylene carbonate (FEC)[66]. Adding 2% FEC can prevent the decomposition of solvents like PC by sacrificing itself and forming an SEI layer at around 0.7V, which benefits long-term cycling. However, excessive use of FEC can result in a thicker SEI layer, increased electrolyte polarity, and reduced Na^+ conductivity. Moreover, optimizing a combination of various solvents and additives can be complex but highly beneficial for improving battery performance. Although not covered in this thesis, high-throughput screening and optimization of different solvents and electrolytes present an interesting avenue for further research in sodium-ion batteries.

Sodium salts used in electrolytes consist of Na^+ ions paired with large-size anion groups. These salts must exhibit several key properties: high solubility in OLEs, chemical and electrochemical stability, excellent thermal stability, cost-effectiveness, environmental friendliness, and low toxicity.[65] Sodium salts are generally categorized into inorganic and organic types. Common inorganic sodium salts include $NaClO_4$, $NaBF_4$, and $NaPF_6$. Organic sodium salts include $NaSO_3CF_3$ (NaOTf), $Na[(FSO_2)_2N]$ (NaFSI), and $Na[(CF_3SO_2)_2N]$ (NaTFSI). Among these, $NaClO_4$ is widely regarded as one of the most effective sodium salts. It boasts high ionic conductivity (6.4 mS/cm), excellent thermal stability (M_p 468 °C), high voltage stability, and compatibility with both sodium metal and hard carbon electrodes.[63] Moreover, $NaClO_4$ is cost-effective. However, due to the high oxidation state of chlorine (+7), handling and storage of $NaClO_4$ must be approached with extreme caution to avoid risks of explosion.[64]

In this thesis, we have adopted an electrolyte system consisting of 1 mol/L $NaClO_4$ in propylene carbonate (PC) with a 2% fluoroethylene carbonate (FEC) additive. This formulation is one of the most common and straightforward electrolyte systems. It has demonstrated excellent performance in high-throughput studies for evaluating cathode materials.[67] Furthermore, this system can serve as a representative model for other studies, providing a valuable reference for similar research endeavors.

Anode:

The development of anode materials, particularly graphite, has been a crucial aspect in realizing the commercialization of LIBs. Consequently, research on anode candidates for SIBs is another vital area of focus for facilitating commercialization. Recent studies have identified several main anode candidates[60], which can be categorized into carbon-based layered materials, Ti-based materials, organic-based materials, and alloys, as shown in **Figure 1.12**.

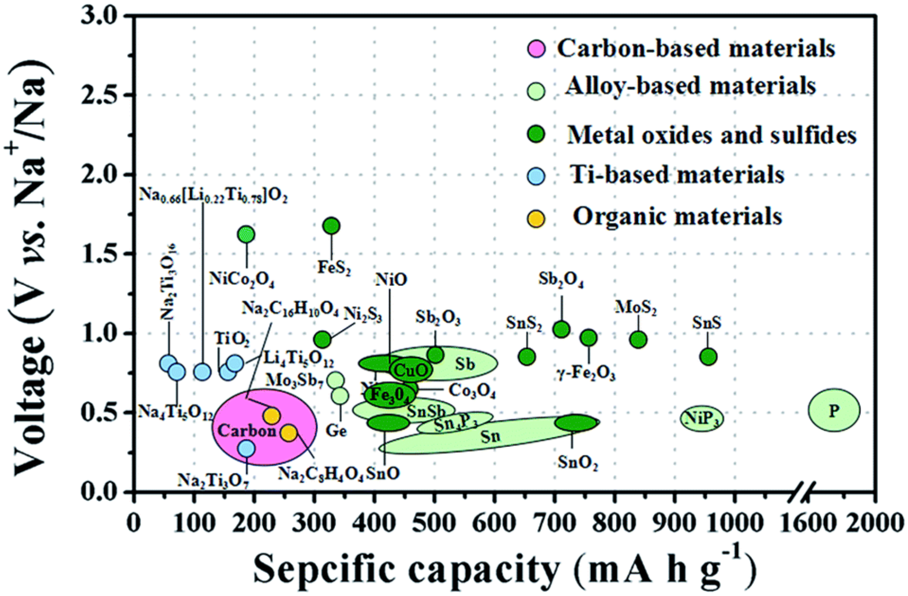

Figure 1.12 *Specific capacity-voltage chart for reported anode materials for SIBs. Reproduced with permission from ref.* [60].

Carbon-based anodes are highly promising due to their low redox potential, excellent electron conductivity, and low cost.[48] Despite their potential, they face challenges such as low first-cycle coulombic efficiency and limited cyclability that need to be addressed. Improving the structural design and surface modification of carbon-based anodes could help in overcoming these issues and enhancing their overall performance. Ti-based anodes, on the other hand, exhibit excellent air stability. The Ti^{3+}/Ti^{4+} redox couple operates at typically low voltages (approximately 0-2 V, depending on the structure).[68] These anodes are known for their superior long-term cycling performance and electrochemical stability. Further research into optimizing the crystalline structure and particle size of Ti-based materials could lead to even better performance metrics.[69] Organic anodes offer numerous advantages, including abundance, cost-effectiveness, and ease of chemical synthesis.[70] Their voltage window and stability can be chemically tuned to meet specific requirements. However, the primary challenge is their tendency to dissolve in organic electrolytes during long-term operation.[71] Developing novel polymerization techniques and cross-linking strategies could mitigate these dissolution issues, making organic-based anodes more viable.[72] Alloy anodes generally provide higher capacity at low voltage and excellent conductivity. Nevertheless, the volume changes that occur during alloy formation can lead to electrode failure and safety concerns.[73] Incorporating nanostructured alloys and using flexible binder materials could help address these volume expansion problems.[74] Overall, while these anode materials show promise, significant research is still needed to overcome the challenges they present for the commercialization of SIBs. Advances in material science, coupled with innovative engineering solutions, will be essential in developing anodes that are both efficient and commercially viable.

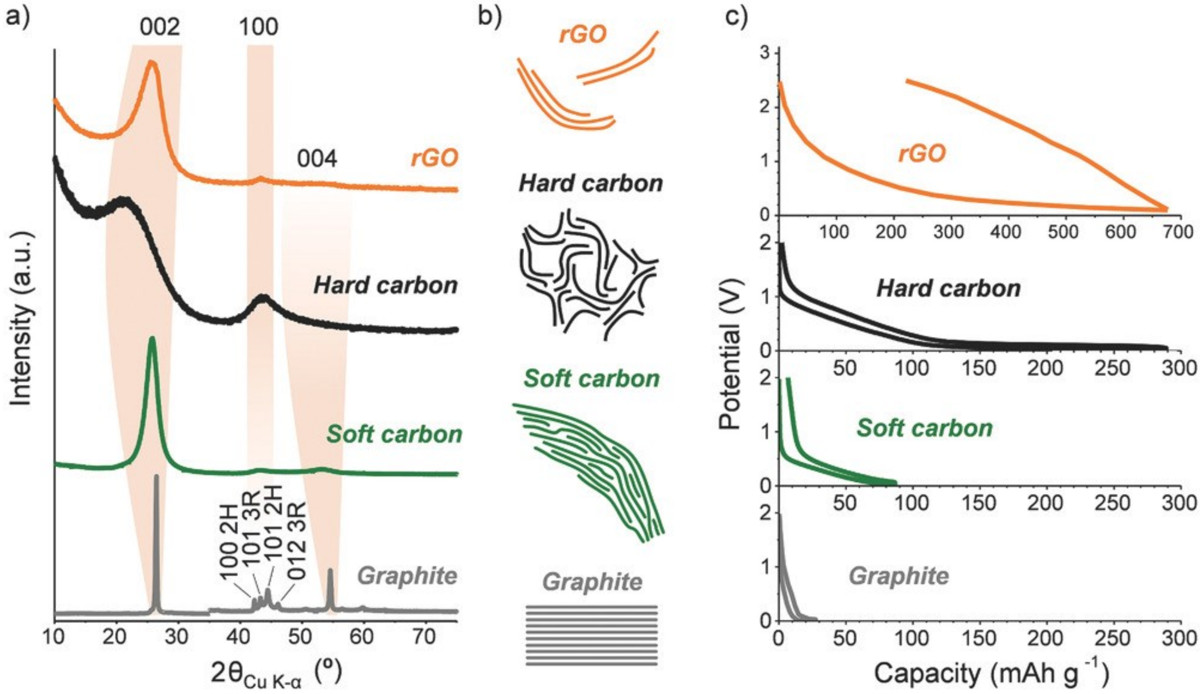

Figure 1.13 *Comparison between various carbon-based anodes - graphite, soft carbon, hard carbon, and reduced graphene oxide (rGO) (a) XRD patterns. (b) Graphical representation. (c) Capacity-voltage profiles at the second cycle in sodium half cell. Reproduced with permission from ref.* [75].

Since carbon-based anodes are among the most promising candidates, we present a brief discussion on their properties and potential. Hard carbon, characterized by a high degree of disorder, has been found to accommodate Na^+ at low voltages with a high capacity of about 300 mAh/g. This was first reported by Dahn et al., who used glucose as a precursor.[48] The exact mechanism of Na^+ storage in hard carbon remains unclear due to its disordered structural nature. However, several proposed steps—adsorption, intercalation, and filling—are used to explain Na^+ storage behavior across a voltage range from 2 V to 0.1 V[75–77]. As shown in **Figure 1.13**, the electrochemical storage behavior of Na^+ in various carbon-based materials varies significantly depending on their crystallinity and morphology.[75] Although graphite shows excellent Li storage in LIBs, its application for Na^+ storage remains challenging.[78] Na^+ is thermodynamically unfavorable for reversible insertion into graphite. Interestingly, despite Na ion's larger ionic radius compared to Li ion, other larger alkali metal ions such as K^+, Rb^+, and Cs^+ can still insert into graphite.[79] First-principles computations by Goddard et al. have shown that Na^+ insertion into graphite has a positive Gibbs free energy, indicating its unfavorable nature.[80] Additionally, the relatively low surface area of graphite limits its capacity for Na^+ storage. Graphene, with its high surface area, demonstrates high capacity through the Na^+ adsorption process, but it suffers from low reversibility. Hard carbon, which combines a high surface area with a high degree of disorder, appears to be a better choice for SIB anodes. However, the synthesis and morphology control of amorphous carbon remain challenging. Various reports indicate that different precursors and sintering temperatures lead to varied electrochemical properties.[60,75,76]

In this thesis, we utilized Na metal as the anode in a half-cell test. The use of Na metal as an anode is a straightforward approach and often regarded as an ideal choice due to its high theoretical capacity of 1166 mAh/g, inherent electronic conductivity, and low redox potential.[60] However, the formation of a stable solid electrolyte interphase (SEI) layer is critical for Na metal anodes to mitigate electrolyte reduction at low potentials and suppress dendrite formation. To address these challenges, we employed 2% fluoroethylene carbonate (FEC) as an additive to promote the formation of a uniform and dense SEI layer on the Na metal surface[66], effectively mitigating these detrimental effects. While using Na metal as the anode provides valuable insights into our cathodes, further studies on full-cell properties are crucial for the commercialization of SIBs based on high-throughput studies. Future research will also focus on incorporating anode materials to enhance their full battery performance. Investigating the interactions between different cell components under real-world conditions will also be critical to ensuring the safety and efficiency of SIBs.

1.3 Cathode materials for SIBs

1.3.1 Overview of cathode classes

Cathode materials are critical components in sodium-ion batteries, significantly influencing the voltage, specific capacity, and overall cost of the batteries. Since the initial report on $NaCoO_2$ layered oxide materials[45], a diverse range of materials has been explored for use as cathodes. These materials often feature a Na-X-M configuration that stabilizes the intercalation chemistry necessary for effective sodium storage. In this configuration, Na-X denotes the bonding with Na^+, facilitating the conductivity and transport of Na^+ within the lattice structure. The metal component, M—typically a 3d transition metal—is responsible for the redox reactions by undergoing changes in oxidation states, which in turn determines the electrochemical potential of the cathode material. X generally represents an anion or anionic group that facilitates electron withdrawal and forms ionic bonds to connect both Na^+ and M^{n+}, with high electronegativity anions like O^{2-} or S^{2-} being preferred.[81] Based on the variety of Na-X-M configurations and structures, cathode materials can be categorized into several types[28]: layered oxide (Na_xMO_2), polyanion ($Na_xM_2(XO_4)_3$), Prussian blue analogues ($Na_xM_2(CN)_6$). The diverse structural configurations of these cathode materials offer various electrochemical properties, making them suitable for different applications. Continued research and development in this area are essential to optimize these materials for better performance, stability, and cost-effectiveness in SIBs.

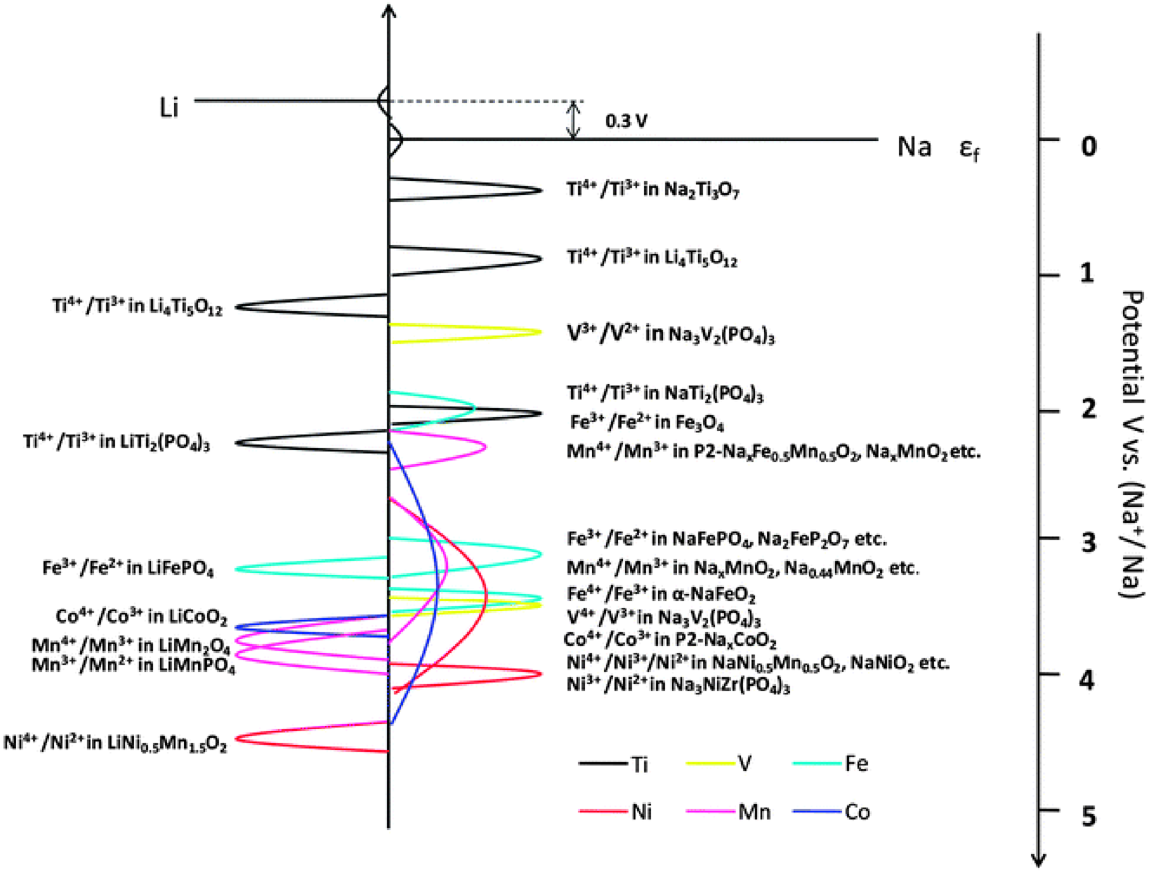

Figure 1.14 *Comprehensive comparison of electrode potentials for various transition metals in SIBs and LIBs. Reproduced with permission from ref.* [82].

To increase the energy density of cathode materials, it is crucial to achieve higher specific capacity and higher voltage. Enhancing the specific capacity of the cathode involves ensuring that the effective Na/(NaXM) ratio has a higher molecular weight ratio, meaning a greater proportion of Na can be removed. However, a significant challenge in intercalation chemistry arises when large amounts of Na are removed: the Vac(Na)-X-M structure (Vac: vacancy) must remain stable to prevent phase transitions that can decrease the reversibility of the process.[3,35,54]

Improving the voltage of the cathode generally involves increasing the ionic nature of the X-M bonding, which effectively lowers the Fermi level of the transition metal electrons, as illustrated in **Figure 1.8**. Generally, the greater the difference in electronegativity between X and M, the higher the voltage.[83,84] For instance, transitioning from $NaTiS_2$ to $NaCoO_2$ increases the voltage from approximately 1.5 V to around 3.0 V. Polyanion materials, which have strong electron-withdrawing inductive effect, exhibit higher voltages compared to oxides; for example, $NaTi_2(PO_4)_3$ (~2 V) has a higher voltage than $NaTiO_2$ (~1 V).[82]

Additionally, high-valence redox couples exhibit higher voltages; for example, Fe^{3+}/Fe^{4+} has a higher redox potential than Fe^{2+}/Fe^{3+} due to the loss of an additional electron. The anion X also plays a crucial role in stabilizing the high-valence M necessary for high-voltage redox reactions.[85] For example, Fe^{4+} in a layered structure may suffer from lower octahedral-site stabilization energy (OSSE), potentially leading to a transition into a tetrahedral site and subsequent transition metal migration into Na^+ layer.[81] Another method to increase the voltage in layered oxides involves anionic redox reactions, or oxygen redox, where O^{2-} can be oxidized to O^- at voltages above 4.0 V. However, stabilizing such high-voltage anionic redox reactions remains challenging.[86] Achieving higher energy density in cathode materials requires a delicate balance between increasing specific capacity and redox pairs engineering. Continued research in this area is critical for developing next-generation SIBs with superior energy densities and operational stability.

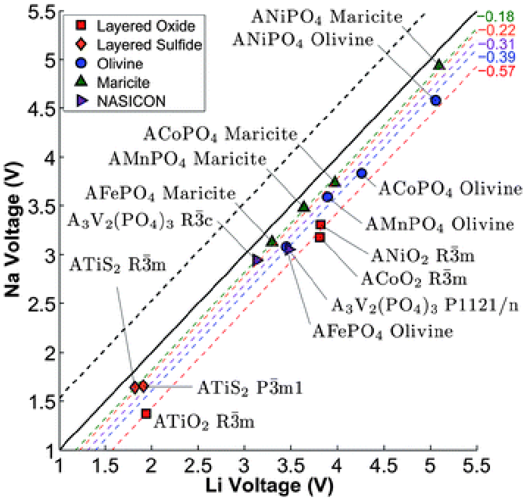

Figure 1.15 *Calculated Na voltage vs. calculated Li voltage for different structures. Reproduced with permission from ref.* [87].

Overall, compared to the cathode materials for LIBs, those for SIBs tend to have similar or slightly lower specific capacities but often suffer from lower voltage.[88] One obvious reason for this is that the Na^+/Na redox couple has an anode potential about 0.3V lower than that of Li^+/Li. Additionally, the larger ionic radius of Na^+ compared to Li^+ often results in lower energy gain from Na^+ intercalation into the host structure. For instance, in layered oxides, Na^+ tends to form weaker interactions with O^{2-} compared to Li^+. This is evident when comparing the formation enthalpies of more stable Li_2O (-598.73 kJ/mol) and Na_2O (-417.95 kJ/mol), which share the same crystal structure but significantly differ in stability.[87] Consequently, a hypothetical Na-O battery forming Na_2O would have about 1 V lower voltage than its Li-O counterpart. As shown in **Figure 1.15**, density functional theory (DFT) calculations indicate that Na-based cathodes generally exhibit voltages lower by about 0.18 V to 0.57 V compared to their Li-based counterparts.[87] Therefore, increasing the voltage of Na cathode materials is crucial for improving the energy density to make SIBs more competitive with LIBs.

Herein, we summarize various types of cathode materials for sodium-ion batteries, highlighting their structures, electrochemical properties, and potential for further development. This overview includes layered oxides, polyanion compounds, and Prussian blue analogs, providing a comprehensive understanding of the current landscape and future directions in SIB cathode research. A comparative analysis of these materials, along with radar charts illustrating various properties, is shown in **Figure 1.16**. The oxides exhibit superior overall properties compared to the other two types of materials.

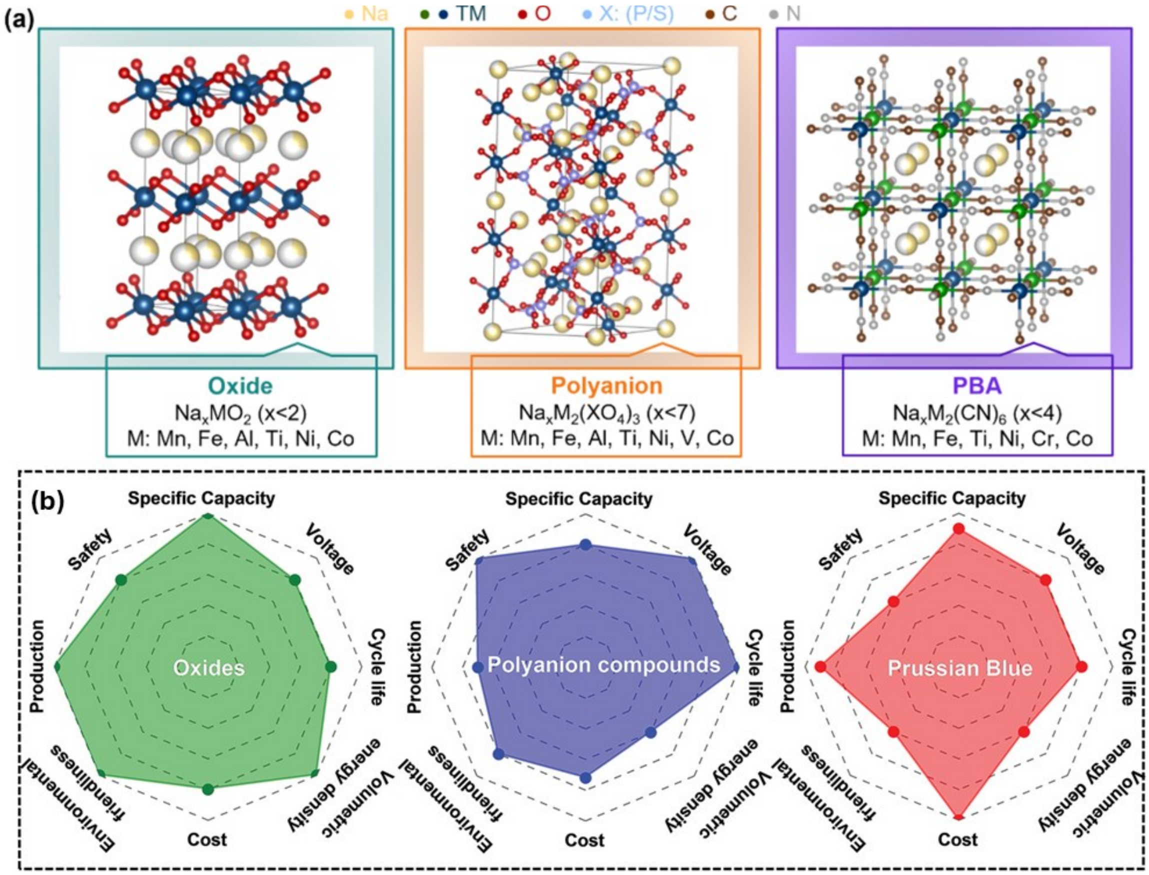

***Figure 1.16** Comparison of the three main types of cathode materials in SIBs, oxides, polyanion, and Prussian blue. (a) The representative structures. (b) Radar charts of various properties. Reproduced with permission from refs.* [89,90].

The summary of reported materials, presented in **Figure 1.17**, indicates that oxides generally achieve high specific capacities and volumetric energy densities. This makes them highly attractive for applications with limited volume like EVs. On the other hand, polyanion materials are known for their high voltage and excellent cycle life, making them suitable for applications where long-term stability is crucial. Prussian blue analogs, while showing medium properties across various metrics, offer significant advantages in cost control, potentially lowering the overall cost of SIBs. Notably, each type of cathode material has its unique strengths and challenges. Layered oxides, known for their superior overall performance and high tunability due to a wide range of compositional options, show the most promise. In this context, we discuss the detailed background and design principles of these layered oxides.

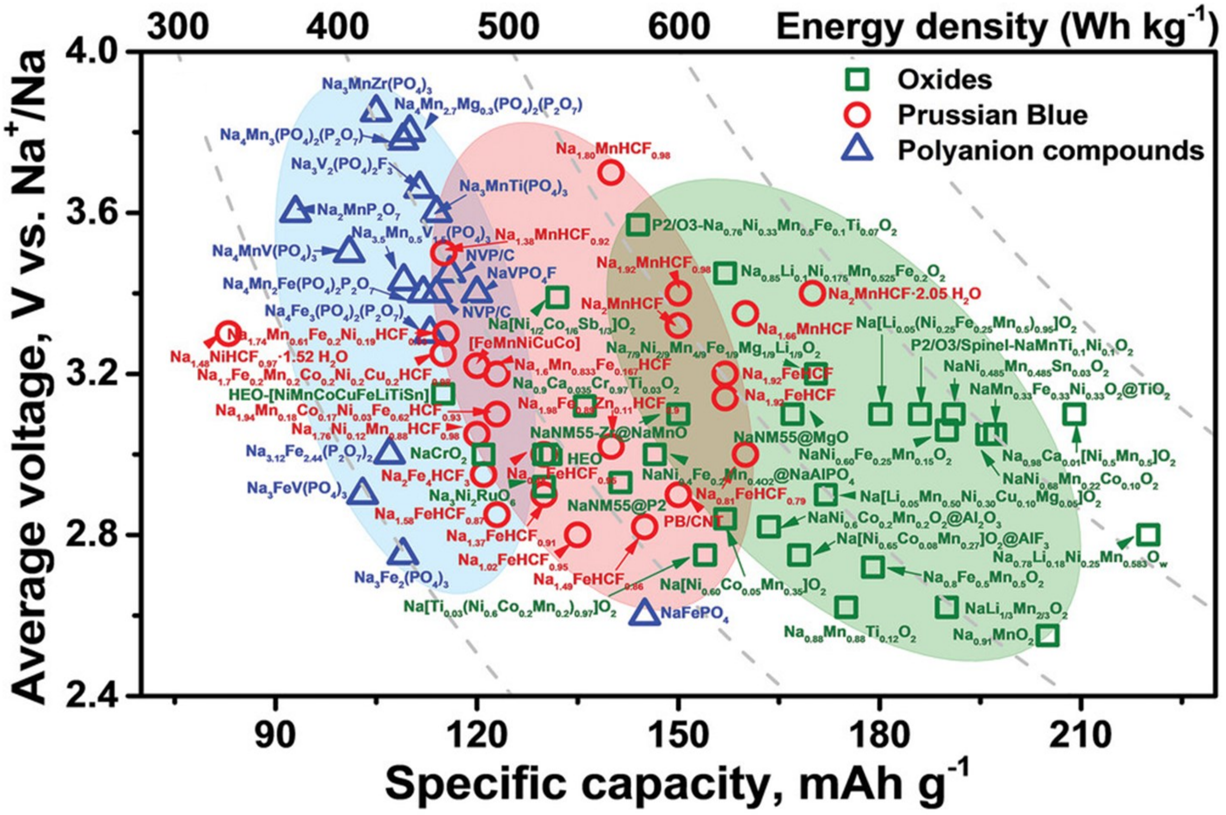

Figure 1.17 Specific capacity, average voltage, and energy density of reported materials categorized into three main types of cathode materials. Reproduced with permission from ref. [90]*.*

1.3.2 Layered oxides

The layered oxides are among the first types of cathode materials investigated for SIBs. Based on intercalation chemistry, their chemical formula can be written as Na_xTMO_2 , where TM represents a transition metal or a combination of metals, and *x* indicates the sodium content, theoretically ranging from $0 \leqslant x \leqslant 1$. The structure of layered oxides consists of layers of transition metal oxide in octahedral TMO_6 configurations, with sodium layers in between. Based on stacking patterns and sodium chemical environments, layered materials can be categorized into four common configurations: O3, O2, P3, and P2, as shown in **Figure 1.18**. This notation was first introduced by Delmas.[45] The letters “O” or “P” represent the sodium chemical environment, either in "octahedral" or "prismatic." The subsequent number indicates the minimum number of units required to repeat the lattice structure into crystals. As shown in **Figure 1.18**, the oxygen positions on the ***ab*** plane can be categorized into A, B, C positions. The combinations of different stacking pattern based on oxygen positions can derive different phases including three layers: O3 (AB/CA/BC), P3 (AB/BC/CA), and two layers: P2 (AB/BA), and O2 (AB/AC).

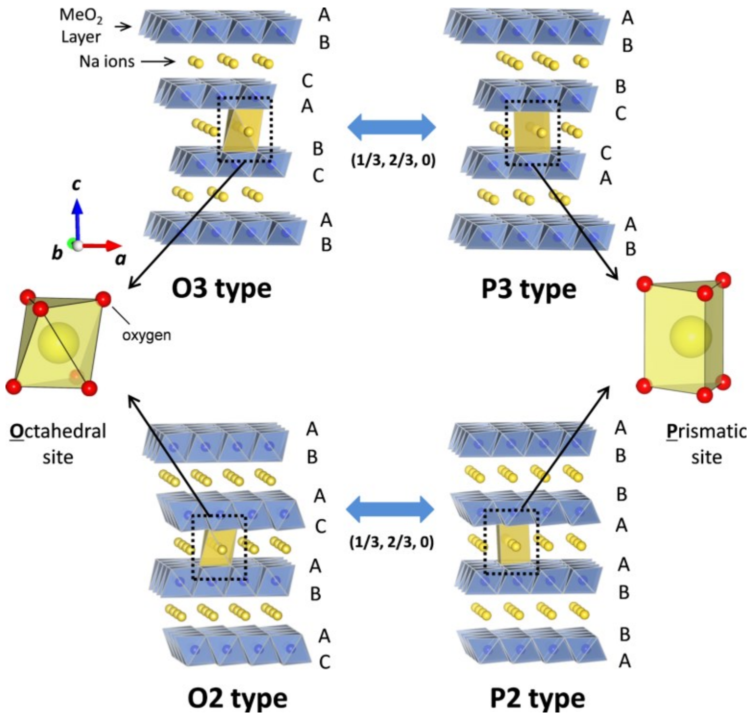

Figure 1.18 *Various phases for layered oxides according to different stacking patterns and* Na^+ *environment—O3, P3, P2, O2. The phase transformations that are possible between O3 and P3, and between O2 and P2 are shown. Reproduced with permission from ref.* [49].

The most common and stable phases are P2 ($0.50 < x < 0.7$, typical $x = 0.67$) and O3 ($0.8 < x < 1.0$, typical $x = 1.0$). P3 materials are usually sub-stable, synthesized at lower temperatures. O2 is generally unstable, typically obtained during the electrochemical charging of P2 materials after a phase transition. The identification of these crystal structures can be achieved using X-ray diffraction (XRD), and the space groups of P2, O3, and P3 materials are $P6_3/mmc$, $R\bar{3}m$, and $R3m$, respectively. In the space group coordinates, the ***ab*** plane represents the TM layer, where one TM ion is surrounded by six TM ions, forming a honeycomb configuration. The ***c***-axis denotes the stacking direction. In the unit cell, the lattice parameter should be $a = b$ and is mostly determined by TM size, while lattice parameter c is primarily determined by Na content but also influenced by TM size.

During charging, Na^+ ions are removed from the Na layer, causing an increase in lattice parameter ***c*** due to reduced interslab attraction from O-Na-O and increased repulsion from O^{2-}-O^{2-} ions. Unlike TiS_2 layered materials, which use van der Waals forces to maintain layer distance, oxides exhibit stronger electronegativity, meaning that some amount of Na must remain in the layers to prevent structural collapse. Consequently, structure distortion may occur, indicated by a prime sign (') to denote distorted layered oxides. The space groups of P'2, O'3, and P'3 change to $Cmcm$, $C2/m$, and $P2_1/m$, respectively, indicating orthorhombic or monoclinic structures. Furthermore, phase transitions can occur between O3-P3 and P2-O2 through slab gliding, as shown in **Figure 1.18**. However, the transition between P2 and O3 is electrochemically unfavorable because it requires the rotation of TMO_2 slabs, achievable only during high-temperature sintering.

For electrochemical performance, P2 materials often demonstrate superior properties compared to O3 materials, with higher specific capacities, better rate performance, and longer cyclability.[91] This difference can largely be attributed to the distinct Na^+ environments and diffusion paths in these structures.[49] In P-type oxides, Na^+ ions reside in prismatic environments with 6 oxygen atoms, and the O^{2-} ions from the neighboring TM slabs overlap in the ***c*** direction. To mitigate this overlap, the vertical distance or Na^+ spacing in P-type materials is greater than in O-type materials, which promotes higher ionic conductivity. Moreover, in P-type materials, Na^+ ions can hop horizontally from one prismatic NaO_6 site to another, as shown in **Figure 1.19**.

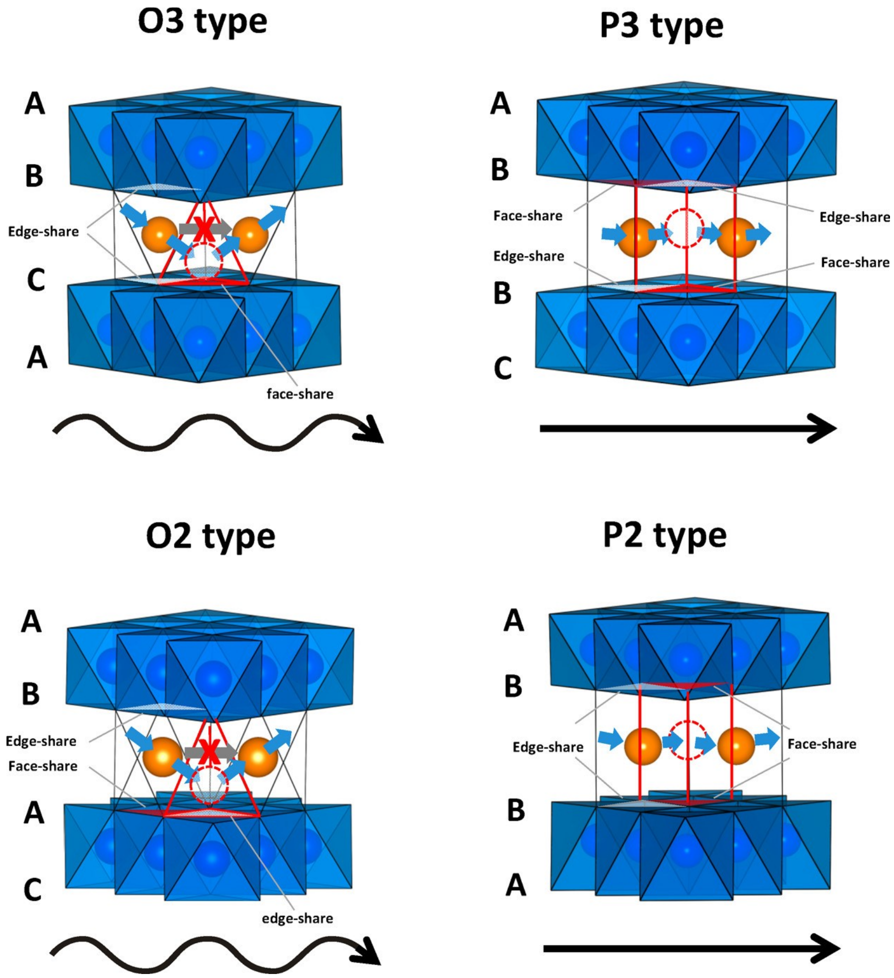

***Figure 1.19** Na migration paths in different layered phases. Reproduced with permission from ref.* [92].

In contrast, O-type materials require Na^+ ions to hop from octahedral sites to neighboring tetrahedral sites to diffuse, which involves a higher energy barrier. Despite this, O3 materials have some advantages, such as higher sodium content, which can be beneficial for making full cells with hard carbon anodes. On the other hand, Na-deficient P2 materials typically require pre-sodiation to be used effectively in full cells. This need for pre-sodiation in P2 materials can be an additional step in the battery fabrication process, potentially complicating their commercialization. However, the intrinsic electrochemical benefits of P2 materials, such as enhanced ionic conductivity and favorable Na^+ diffusion paths, make them highly promising candidates for high-performance sodium-ion batteries.

In summary, while O3 materials have the advantage of higher sodium content, P2 materials offer superior electrochemical performance due to their more favorable Na^+ environments and diffusion pathways. This makes P2 materials particularly suitable for applications where high specific capacity and excellent rate performance are critical. In this thesis, we have systematically studied and compared P2 and O3 structures in **Chapter 2**, and further optimization is mostly focused on P2 material in later chapters.

Compared to the layered oxides for LIBs, the layered oxides for SIBs have more diverse options for TM selections. For Na_xTMO_2 layered materials, reported TMs include Ti[68], V[93], Cr[94], Mn[95], Fe[96], Co[97], and Ni[98]. The voltages of various transition metals, as demonstrated in **Figure 1.14**, indicate that the order of increased voltage roughly follows the 3d metal order with increased d electrons and mildly increased electronegativity. During the charge and discharge processes of these layered materials, a common phenomenon is the formation of several plateaus, which correspond to various phase transitions. The reasons for these plateaus are often complex and multifaceted. For instance, in LIBs layered oxides, the voltage profile is rather smooth and continuous. However, the larger Na^+ radius in SIBs can trigger more complex phase transitions during the (de)-intercalation process. Each plateau should correspond to one peak in the CV measurement, indicating a fast Na^+ diffusion process at this configuration. Researchers often use energy barrier concepts to interpret each process.[41,47,82] Each configuration has one diffusion energy barrier at a certain voltage or Na content, and the transition for each structural configuration will correspond to various diffusion energy barriers. This results in multiple plateaus in the voltage profile or CV curves, each representing a different phase transition with its unique diffusion characteristics.[28]

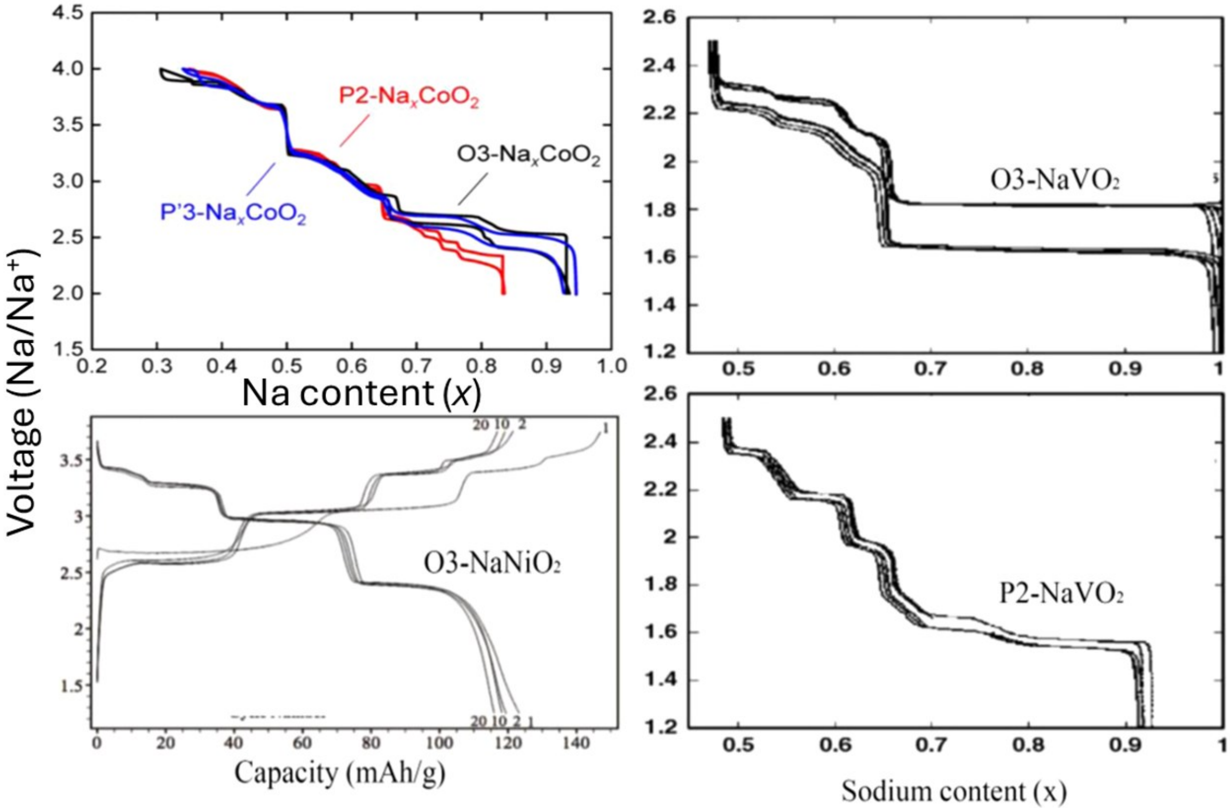

***Figure 1.20** Charge and discharge profile for various 3d TM layered oxides. Reproduced with permission from ref. [99].*

Among various 3d transition metals, Mn and Fe stand out due to their earth abundance, cost-effectiveness, non-toxicity, and environmental friendliness. Consequently, Mn and Fe-based layered oxides have garnered significant attention, particularly since the first report of $Na_xMn_{0.5}Fe_{0.5}O_2$ by Yabuuchi et al[53]. The voltage profile for $NaMnO_2$ shows a series of phase transitions with several voltage plateaus, with the largest plateau at 2.4V attributed to the

Mn^{3+}/Mn^{4+} redox process (see **Figure 1.21**a). Despite an initial high discharge capacity of approximately 185 mAh/g, degradation occurs rapidly after further cycling. In contrast, $NaFeO_2$ can only remove about 0.4 Na^+ from the structure through the Fe^{3+}/Fe^{4+} redox process, exhibiting a relatively smooth voltage profile but also experiencing a fast capacity decay from 80 mAh/g to 51 mAh/g within the first 8 cycles (see **Figure 1.21**b). Interestingly, combining Mn and Fe to form P2-$Na_{0.66}Mn_{0.5}Fe_{0.5}O_2$ significantly improves both capacity and cyclability, achieving about 190 mAh/g with 78% retention after 30 cycles as shown in **Figure 1.21**.

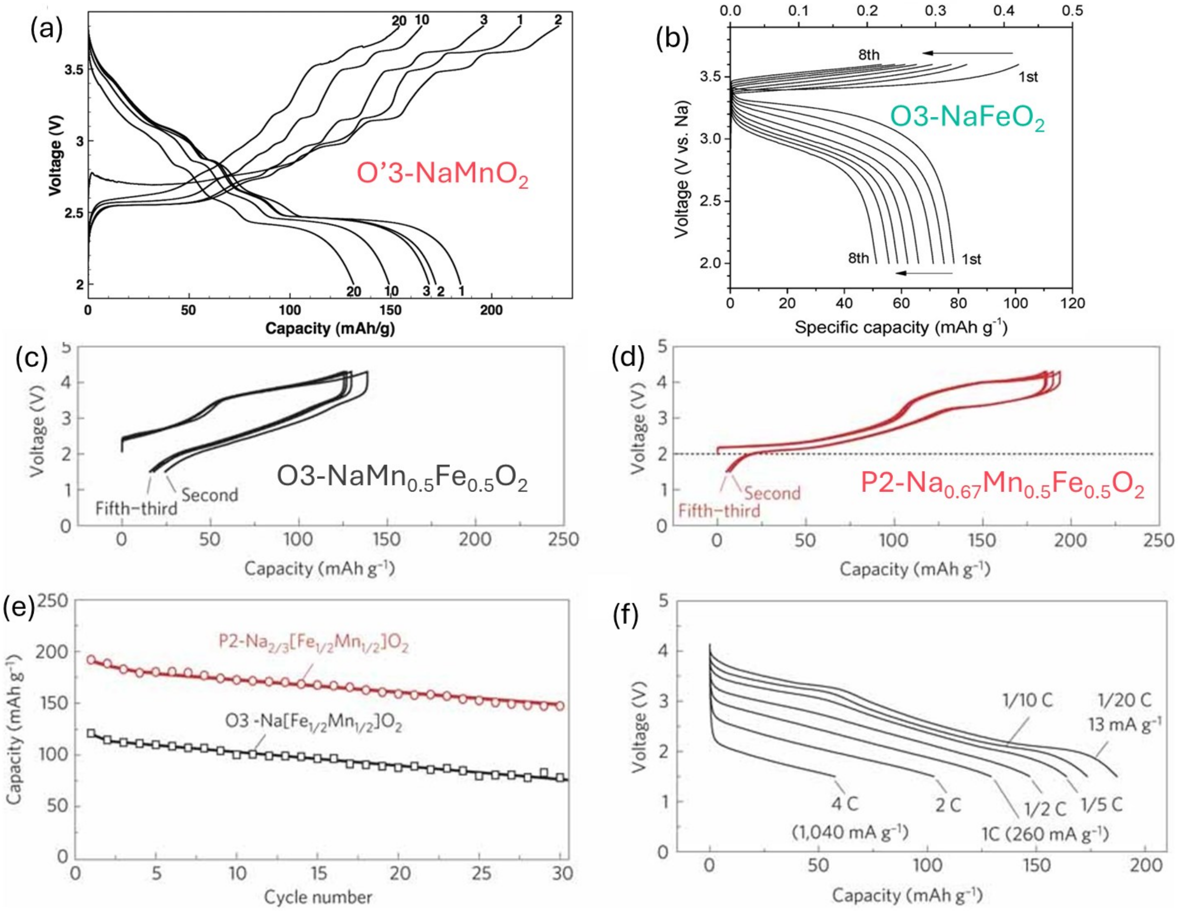

Figure 1.21 *Charge and discharge voltage profile of (a) O'3-*$NaMnO_2$*, (b) O3-*$NaFeO_2$*, (c) O3-*$NaMn_{0.5}Fe_{0.5}O_2$*, and (d) P2-*$Na_{0.67}Mn_{0.5}Fe_{0.5}O_2$*. (e) The capacity retention of P2 and O3 materials. (f) The rate performance at various current density, where 1C = 260 mA/g. Reproduced with permission from refs.* [53,100,101].

The improvement from combining transition metals is not unique to the Mn-Fe system but is also observed in other systems such as $Na_{0.66}Mn_{2/3}Ni_{1/3}O_2$[102], $NaNi_{0.5}Ti_{0.5}O_2$[103], and $NaMn_{1/3}Fe_{1/3}Ni_{1/3}O_2$[104]. More reported materials support the notion that combining transition metals often results in better electrochemical performance than single-metal systems, as each metal contributes its unique properties to enhance the overall performance. For instance, Zhao et al. reported high-entropy layered cathode materials that incorporate nine different elements into the transition metal layer[105], $NaNi_{0.12}Cu_{0.12}Mg_{0.12}Fe_{0.15}Co_{0.15}Mn_{0.1}Ti_{0.1}Sn_{0.1}Sb_{0.04}O_2$. This indicates the high tunability and compatibility of combining transition metals in the TM layer. However, the complexity of these combinations is considerable, and rational design of high-entropy materials is challenging. Therefore, combinatorial studies are imperative to identify the function of each element, driving the application of high-throughput studies to tackle the intricacies of combination trials. A combinatorial approach allows for a more efficient exploration of the vast compositional space, enabling the identification of optimal compositions and properties more rapidly than traditional trial-and-error methods. The high-throughput studies in this thesis intends to reveal insights into the synergistic effects of different transition metals, ultimately leading to the development of more robust and efficient cathode materials for sodium-ion batteries.

1.3.3 Synthesis methods

Various common synthesis methods are summarized in **Table 1.3**. In this thesis, we adopted the sol-gel method[106] to achieve high-throughput synthesis. By preparing various metals into a 2M solution precursor and adjusting the volume of each component, diverse compositions can be synthesized in a high-throughput manner. Additionally, the combined solutions achieve excellent metal mixing with the aid of a chelating agent, such as citric acid, which ensures uniform distribution and effective incorporation of the metals into the final product.[67,107] This approach not only enhances the efficiency of the synthesis process but also improves the quality and consistency of the resulting materials.

Table 1.3 *Common synthesis methods for cathode materials.*

Synthesis method	Advantages	Shortcomings	Applicable Conditions
Solid-state synthesis	Simple operation, easy control, short process, low cost	Limited uniformity, requires fine precursors, longer and higher temperature sintering	Suitable for both lab research and industrial production
Sol-gel method	Excellent uniformity and consistency, low cost, energy-saving	Chelating agent burnout may leave carbon residue, inert sintering conditions required	Soluble precursors required; fast for lab research but limited scalability for industrial production
Co-precipitation	Well-mixed, excellent morphology control	Multiple conditions to manage (concentration, pH, stirring), generates waste	Soluble precursors required; applicable for both lab research and industrial production
Hydrothermal /Solvothermal method	Rapid reaction, low synthesis temperature, may not require sintering	Difficult to control crystallinity, relatively low yield	Requires an autoclave; suitable for chemical reactions at low temperatures (often below 300 °C)
Spray drying process	Fast reaction, high uniformity	Requires spray dryer, needs fine and consistent precursors	Not suitable for large-scale production

1.4 Challenges and issues of layered oxides

In this section, we will discuss several existing challenges and issues in the development of layered oxides, which are critical aspects influencing the electrochemical performance and commercialization of these materials in sodium-ion batteries. These challenges include Jahn-Teller distortion, phase transitions during cycling, TM migration and dissolution, and air/moisture stability. These issues are addressed in subsequent chapters, where we employ high-throughput methodologies to improve cathode properties.

1.4.1 Jahn-Teller distortion

In 1937, H. A. Jahn and E. Teller first reported that in symmetric nonlinear molecules, if the ground state of the system has more than one degenerate level, there will be spontaneous distortion, thereby eliminating the degeneracy.[108] For MO_6 octahedra, Jahn-Teller (J-T) distortion can occur with certain transition metals that have an odd number of electrons in the $\boldsymbol{e_g}$ orbitals, especially Mn^{3+}. This phenomenon is significant in the context of sodium-ion batteries because it can directly impact the structural and electrochemical stability of the cathode materials. Despite the promising potential of Mn-based layered oxides, the Mn^{3+} J-T distortion poses a significant issue, particularly affecting structural stability and long-term cycling performance.

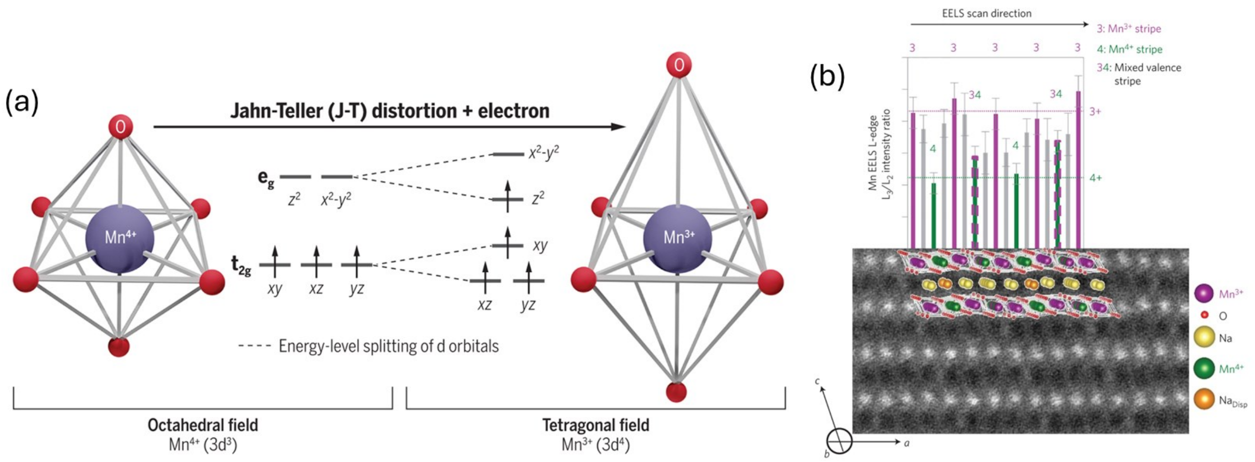

Figure 1.22 *(a) Scheme of Jahn-Teller distortion of* Mn^{3+}*. (b) STEM image along [010] of* $Na_{5/8}MnO_2$ *with periodic J-T distortion of Mn* ***ab*** *plane. Reproduced with permission from refs.*[109,110]*.*

As illustrated in **Figure 1.22**, the J-T distortion of Mn^{3+} manifests as elongated bonds along the z-axis, splitting the $\boldsymbol{e_g}$ orbital into $\boldsymbol{d_{z^2}}$ and $\boldsymbol{d_{x^2-y^2}}$ to accommodate the odd electron with lower overall energy.[109] This results in an anisotropic expansion of the lattice, which can lead to a gradual breakdown of the crystal structure over repeated charge and discharge cycles. Cedar et al. utilized scanning transmission electron microscopy (STEM) to visualize and identify the J-T distortion in $Na_{5/8}MnO_2$. Their work provided direct evidence of the structural changes associated with J-T distortion, highlighting the need for strategies to mitigate these effects.[110]

Currently, the prevailing opinion on J-T distortion is negative due to its impact on structural distortion. This leads to multiple peaks in CV curves and several plateaus in voltage profiles, indicating a less stable and efficient energy storage process. Consequently, these materials are often considered less suitable for long-term cycling and practical applications. Addressing J-T distortion remains a critical challenge in the development of stable, high-performance SIBs.[111,112] In later chapters, we will explore potential strategies to overcome these challenges, leveraging high-throughput methodologies to identify and optimize suitable materials.

1.4.2 Phase transition

Phase transitions during cycling are a crucial aspect of electrochemical analysis for material development. Phase transition is a broad term that refers to the structural or configurational changes of cathode materials during cycling. One type of phase transition involves structural changes, such as P3-O3 and P2-O2 transitions at high voltage. As shown in **Figure 1.18**, these structural changes require slab gliding, which is unfavorable for maintaining structural stability over repeated cycling. Another type of phase transition involves configurational changes, such as lattice distortion (P2-P’2) and Na/vacancy ordering. As mentioned above, the J-T effect of the Mn^{3+}/Mn^{4+} redox couple can trigger lattice distortion during cycling. Kumakura et al.[113] investigated the effect of cooperative J-T distortion on the electrochemistry of P’2-$Na_{2/3}MnO_2$. As shown in **Figure 1.23**, several plateaus (or peaks in *dQ/dV* curves) highlight the complexity of phase transitions, which were elucidated by in-situ XRD. The P’2 phase initially underwent several sub-phase transitions before changing to an OP4 structure (a mixed O and P structure), which is not favorable for practical use.

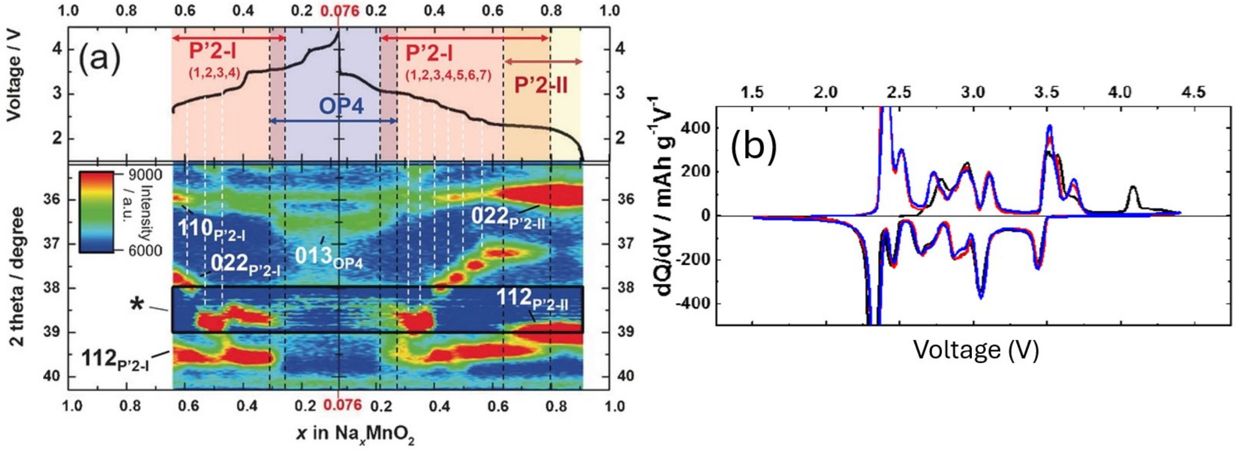

Figure 1.23 *Phase transition of P'2-$Na_{2/3}MnO_2$ (a) Voltage profile and in situ XRD. (b) dQ/dV curve. Reproduced with permission from ref.* [113].

Additionally, due to the large Na^+ radius and Na^+-Na^+ repulsion, Na^+ ions tend to occupy positions with lower diffusion energy first during the intercalation process. This often leads to Na/vacancy ordering, which strongly correlates with Na content, such as x=1/3, 1/2, and 2/3. As shown in **Figure 1.20**, this phenomenon is commonly observed in single TM systems, where high symmetry from TM^n/TM^{n+1} charge ordering can trigger configurational transitions.

However, it has been found that composition engineering, involving multiple TM systems and doping, can suppress or delay these phase transitions.[57,112] In later chapters, we will discuss this strategy via high-throughput studies. For example, we found that 5% Fe substitution can suppress phase transitions and smooth the CV curve. Additionally, in **Chapter 3** *in situ* XRD has shown that Ga doping can suppress phase transitions, maintaining the P2 phase during cycling between 1.5 V and 4.3 V. These findings emphasize the importance of continued research and innovation in rational materials engineering in SIBs.

1.4.3 Transition metal dissolution

The phenomenon of transition metal dissolution has been reported, particularly during cycling at high voltages, where TMs can dissolve into the electrolyte.[91] This dissolution is strongly correlated with the stability of TMs within their octahedral environments. Several factors can trigger this unwanted process. During the investigation of $NaFeO_2$ and $NaCrO_2$, it was found that Fe or Cr can migrate to the Na^+ layer, occupying tetrahedral sites at high voltages when Na content is low.[114–116]. While this migration can be somewhat reversible, higher voltages exacerbate the TM migration, making it irreversible. This can partially contribute to the fast degradation of $NaFeO_2$ cycling, as shown in **Figure 1.21**b. If these processes occur on the particle surface, TMs from the unstable surface will dissolve into the electrolyte and can subsequently deposit onto the anode. Additionally, Manthiram et al. discovered that the J-T effect can also promote TM dissolution, especially for Mn^{3+}. They found that Mn^{3+} is particularly sensitive to acids, such as HF formed from $NaPF_6$, which can accelerate Mn^{3+} dissolution.[109] TM dissolution is crucial for TM stability at high voltage, long-term cycling, and safety concerns.

Several strategies to address TM dissolution consist of coating, doping, and electrolyte engineering. These methods are designed to stabilize the TMs and enhance the overall performance and lifespan of the battery. In **Chapter 4**, we will further explore how doping can mitigate TM dissolution, highlighting its effectiveness in improving surface stability of the particles. These solutions are essential for enhancing the durability and commercial viability of layered oxide cathode materials in SIBs.

1.4.4 Air/moisture stability

Air stability of cathode materials is critical in sodium-ion battery manufacturing and research. Certain materials are reported to degrade after a few hours to days of air exposure, compromising the reliability and reproducibility of experiments.[117–119] This necessitates meticulous storage and handling in gloveboxes, slowing research and increasing costs. Industrially, air stability impacts every stage of the battery production: synthesis, storage, transportation, electrode preparation, and assembly, as shown in **Figure 1.24**. High-moisture environments during post-treatments and long-distance shipping further complicate matters. Air-sensitive materials require handling in argon gloveboxes or ultra-dry rooms, escalating manufacturing costs. While sodium-ion batteries are cost-effective in terms of raw materials compared to lithium-ion batteries[120], stringent air protection measures can negate this advantage, making them less economically viable[118,119,121].

Carbon dioxide and water vapor, despite low concentrations, significantly contribute to degradation. Sodium carbonate forms on particle surfaces from reactions between lattice Na^+ ions and carbon dioxide. Water accelerates Na^+ dissolution through Na^+/H^+ exchange, leading to hydrated phases or structural transitions.[122] Oxygen can oxidize low-valence transition metals, though its involvement is not consistent.[123] Air-induced degradation mechanisms involve complex interactions at the interface or nano-scale. Moreover, alkaline residues on cathode particles can decompose polyvinylidene fluoride (PVDF) binders, increasing slurry viscosity and affecting electrode film uniformity.[124,125] This residue can also corrode aluminum current collectors. Air-aging defects in manufacturing may not manifest early, making them difficult to detect through routine methods. These defects, such as minor PVDF decomposition or aluminum corrosion, can lead to battery failure later, reducing battery lifespan and posing safety risks.

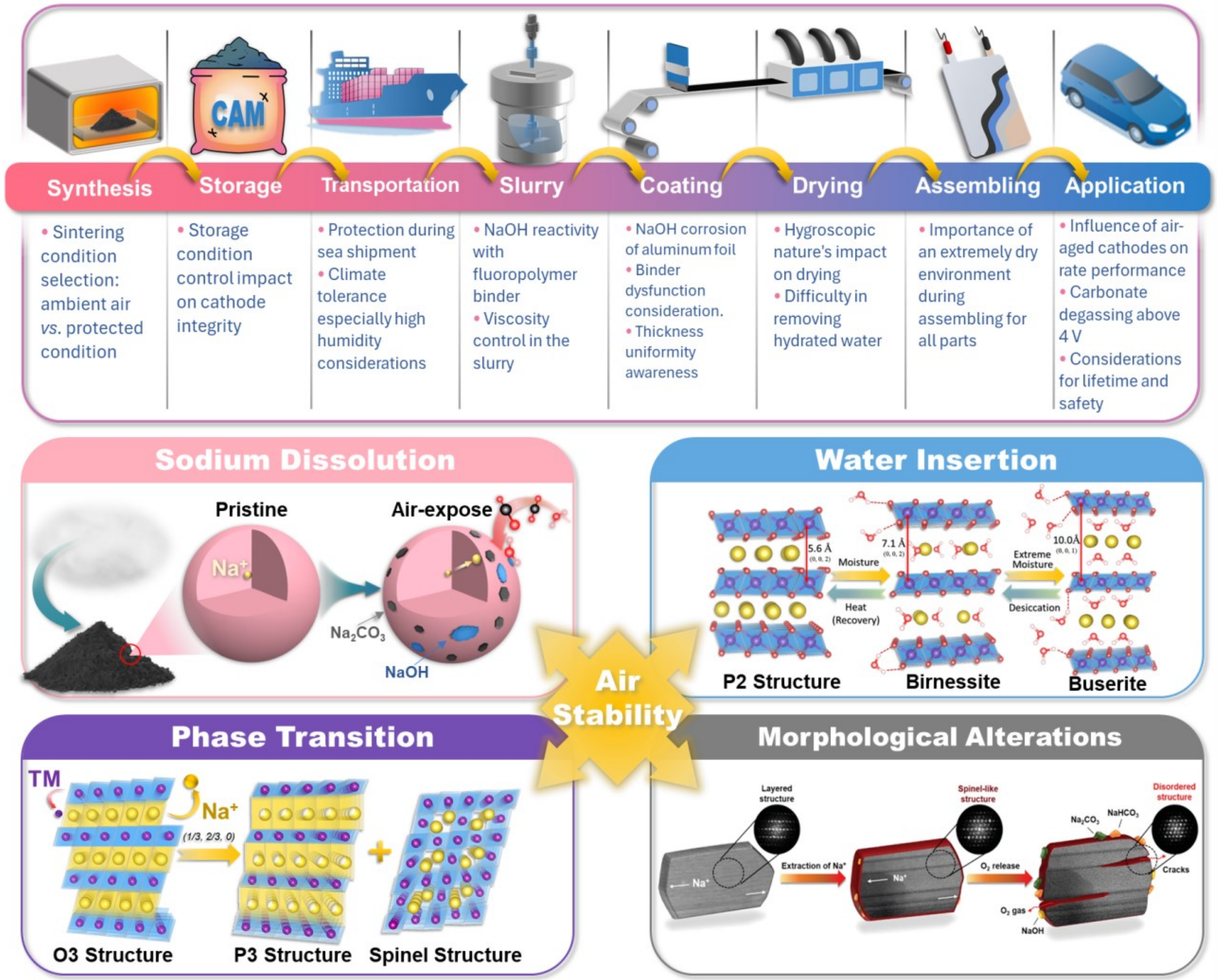

Figure 1.24 *Scheme illustrates the critical role of air/moisture stability across all aspects of battery manufacturing and the four main degradation effects. Reproduced with permission from ref.* [118].

As shown in **Figure 1.24**, there are mainly four effects from the air/moisture reaction with cathode materials.

(1) Sodium dissolution on cathode particles forms compounds like NaOH, Na_2CO_3, $Na_2CO_3 \cdot H_2O$, and $NaHCO_3$, influenced by humidity and composition. Na_2CO_3 increases cathode impedance, hinders Na^+ diffusion, and decomposes at ~4 V, releasing CO_2 and raising safety concerns.

(2) Water molecules from air can insert into the cathode structure, expanding layers and disrupting crystallinity, especially in P2-type materials.

(3) Significant sodium loss during air exposure can lead to phase transitions and structural collapse, forming transition metal oxides and disordered structures.

(4) Air exposure also causes surface cracking and particle brittleness, reducing capacity and cyclability, which negatively impacts the electrochemical performance.

Mitigating these air-induced degradation effects is crucial for enhancing the performance, stability, and safety of sodium-ion batteries. In later chapters, we address the critical property of air/moisture stability by examining both surface and bulk chemistry using HTP-XPS and HTP-XRD after aging. Additionally, we applied machine learning algorithms to demonstrate the insights and the possibility to predict air stability based on thousands of XRD patterns studied.

1.5 Characterization techniques for battery development

In this section, we overview and summarize the fundamental knowledge about key characterization techniques used for battery development and employed in this thesis.

1.5.1 X-ray diffraction (XRD)

The X-ray diffraction (XRD) technique is a widely applied method for analyzing phase composition and identifying lattice structures.[126] Typically, X-ray diffractometers contain three main components: an X-ray tube, a sample holder, and an X-ray detector. The fundamental principle of XRD is based on Bragg's equation, as shown below:

$$2d \sin\theta = n\lambda$$

where ***n*** is the order of diffraction, ***λ*** is the X-ray wavelength, ***θ*** is the Bragg's angle, and d is the distance between atomic planes. The scattering angle, 2***θ***, between the incident and reflected X-rays, and is often used as the X-axis in XRD scan patterns, with the corresponding diffraction intensity on the Y-axis. Therefore, lattice information ***d*** values can be calculated from the scattering angle 2***θ*** of scattering peaks. Two examples of XRD simulated from the crystal structures of P2 and O3 materials are provided for reference (see **Figure 1.25**).

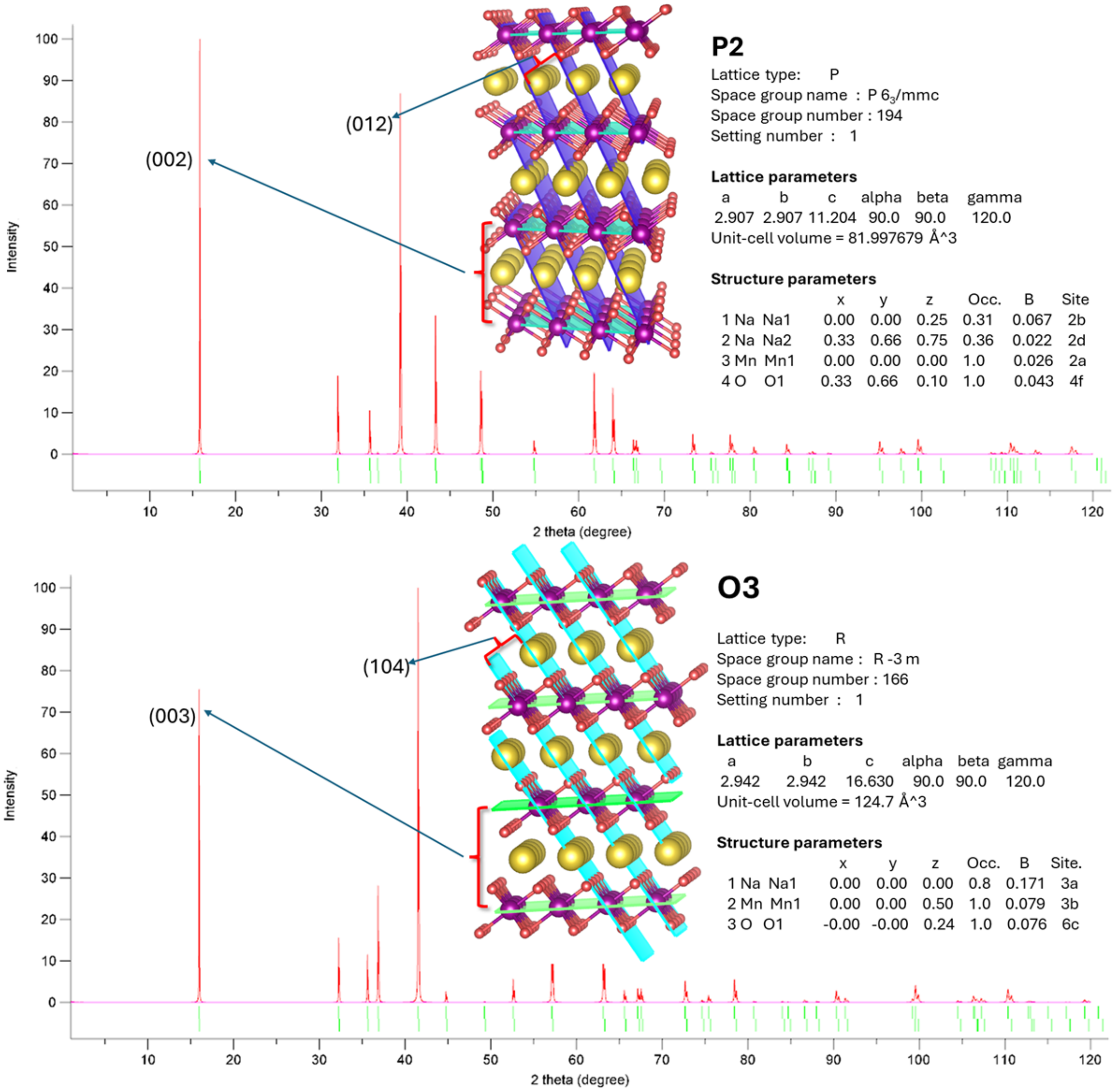

P2

Lattice type: P
Space group name : P 6_3/mmc
Space group number : 194
Setting number : 1

Lattice parameters

a	b	c	alpha	beta	gamma
2.907	2.907	11.204	90.0	90.0	120.0

Unit-cell volume = 81.997679 Å^3

Structure parameters

			x	y	z	Occ.	B	Site
1	Na	Na1	0.00	0.00	0.25	0.31	0.067	2b
2	Na	Na2	0.33	0.66	0.75	0.36	0.022	2d
3	Mn	Mn1	0.00	0.00	0.00	1.0	0.026	2a
4	O	O1	0.33	0.66	0.10	1.0	0.043	4f

O3

Lattice type: R
Space group name : R -3 m
Space group number : 166
Setting number : 1

Lattice parameters

a	b	c	alpha	beta	gamma
2.942	2.942	16.630	90.0	90.0	120.0

Unit-cell volume = 124.7 Å^3

Structure parameters

			x	y	z	Occ.	B	Site.
1	Na	Na1	0.00	0.00	0.00	0.8	0.171	3a
2	Mn	Mn1	0.00	0.00	0.50	1.0	0.079	3b
3	O	O1	-0.00	-0.00	0.24	1.0	0.076	6c

Figure 1.25 *XRD patterns and lattice information of P2 (up) and O3 (bottom) layered oxides.*

As shown **Figure 1.26** there are two modes of XRD setup: reflection mode and transmission mode. In this thesis, we applied the transmission mode using Mo Kα radiation for high-throughput XRD detection.[107] Compared to the more common Cu Kα radiation, Mo Kα offers several advantages: (1) Mo has a smaller wavelength ($\lambda = 0.70926$ Å for $K\alpha_1$) than Cu $K\alpha_1$ ($\lambda = 1.54051$ Å), providing stronger energy to penetrate the sample for transmission setup; (2) Mo Kα's smaller wavelength shortens the scan range and accelerates detection times (4°–30° instead of 10°–70° for Cu radiation); (3) Mo has low fluorescence with 3d transition metals, resulting in low background noise.

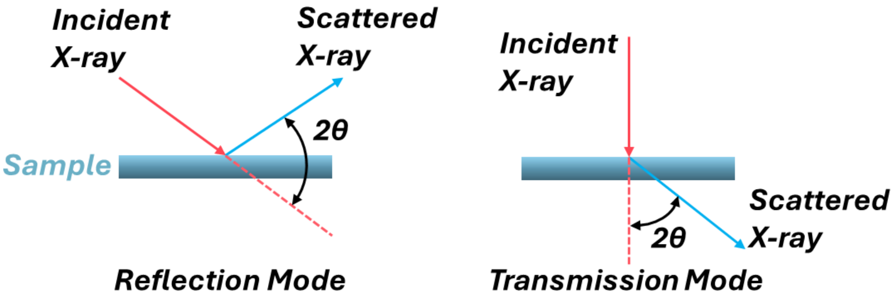

__Figure 1.26__ Two XRD setup: reflection mode (left) and transmission mode (right).

To gain further information from the XRD patterns, fitting is often applied. One of the most renowned algorithms is the Rietveld refinement, detailed in reference sources.[127] The principle of the Rietveld method is to minimize the residual difference between the calculated profile from the proposed lattice and the observed data from the XRD scan, by modifying three components: peak position, peak intensity, and peak shape:

$$M = \sum_i W_i \left\{ y_i^{obs} - \frac{1}{c} y_i^{calc} \right\}^2$$

Several figures of merit quantify the refinement quality, such as the weighted profile residual $\boldsymbol{R_{wp}}$, expected profile residual $\boldsymbol{R_{exp}}$ (depending on the instrument), and the goodness of fit χ^2. Since $\boldsymbol{R_p}$

varies with instrument type and X-ray source, this thesis adopts the goodness of fit χ^2. A perfect fit has a χ^2 value of 1, but in practice, a χ^2 below 2 is considered excellent.

$$\chi^2 = \sum_{i}^{n} \frac{(Y_i^{obs} - Y_i^{calc})^2}{n - p} = (\frac{R_{wp}}{R_{exp}})$$

XRD is crucial in battery material development, providing essential insights into phase composition and lattice structures. In this thesis, we employed HTP-XRD to rapidly and effectively investigate structural information. Additionally, we applied HTP-XRD in accelerated aging tests to detect the air stability of cathode materials. This approach enabled us to swiftly identify changes in structural integrity and composition, which are vital for understanding and enhancing the durability and performance of sodium-ion batteries.

1.5.2 X-ray photoelectron spectroscopy (XPS)

XPS is a powerful technique widely used to investigate the surface chemistry of solid-state materials. It leverages the photoelectric effect to identify elemental composition and relative concentration.[128] XPS is particularly sensitive to the oxidation states and chemical environments of elements, providing detailed insights into the electronic structure and density of states in materials.[129] The fundamental principle of XPS involves using a low-energy incident X-ray, typically Al Kα with E_{photon} = 1486.7 eV, to excite core electrons in the elements on the sample surface under extreme vacuum. This excitation causes the transfer of E_{photon} into binding energy via the photoelectric effect, with the remaining energy converting into kinetic energy. By measuring the kinetic energy, the binding energy can be determined ($E_{binding} = E_{photon} - E_{kinetic}$), which is unique to specific elements and their chemical states.

In **Chapter 2**, we applied high-throughput XPS to analyze the surface chemistry of a series of materials with various compositions and phases. This comprehensive analysis allowed us to identify carbonate species and excess sodium on the surface after air aging, providing valuable information about the air stability and degradation mechanisms of these materials. Furthermore, we conducted XPS profiling with Ar^+ etching to examine the surface reconstruction of particles after cycling, specifically looking at transition metal dissolution and its impact on material performance. Overall, XPS is an essential, surface-sensitive tool for battery material development. It provides crucial insights into the chemical states and transformations occurring on the material's surface, which are vital for understanding and improving battery performance and stability.

1.5.3 X-ray absorption spectroscopy (XAS)

XAS has been instrumental in battery material development by determining the oxidation states and coordination structures of transition metals.[130] Unlike XPS, which primarily probes surface characteristics, XAS uses high-energy X-ray radiation from synchrotron facilities to penetrate the bulk of samples, providing insights into both bulk oxidation states and local geometric chemical structures. By finely tuning the X-ray energy using a crystalline monochromator, XAS selectively excites the core electrons of specific elements (see **Figure 1.27**). The resulting absorption spectra are divided into two key regions: X-ray absorption near edge structure (XANES) and extended X-ray absorption fine structure (EXAFS).[131,132] XANES involves the excitation of core electrons to unoccupied states, providing crucial information about the electron structures of transition metals and allowing for the measurement of oxidation states. In contrast, EXAFS provides insights into local fine structures, including bond lengths and geometric arrangements.

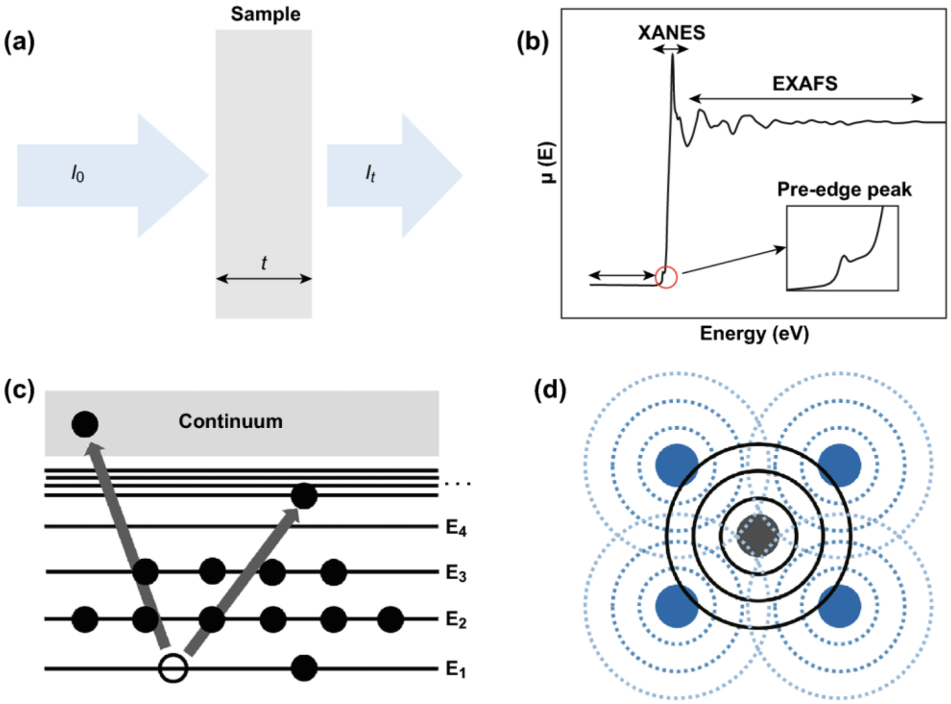

Figure 1.27 *(a) Schematic of XAS setup. (b) The representative XAS scan with XANES and EXAFS regions. (c) Electron energy diagram after X-ray absorption and excitation. (d) Interference pattern created by neighbor atoms to analysis local structure. Reproduced with permission from ref.* [133].

In **Chapter 3**, we included ex-situ XANES to study the anionic redox behavior of cathode materials at different voltages, identifying that Mn redox is not involved at high voltage capacity and, instead, oxygen redox contributes to this capacity. In **Chapter 4**, we used EXAFS to investigate local structural alterations after air aging. Overall, XAS demonstrates powerful capabilities in detecting oxidation states and local structures, making it a valuable tool for battery material development. By providing detailed information about the bulk properties of materials, XAS complements other techniques and contributes to a comprehensive understanding of the factors influencing battery performance and stability. This integrated approach is essential for advancing the development of more durable and efficient batteries.

1.6 High throughput methodology

The complexity of material design necessitates HTP methodologies for accelerated material screening and property optimization. Traditional trial-and-error approaches significantly limit new material discovery. This thesis presents pioneering HTP studies focused on developing cathode materials for sodium-ion batteries, building on several foundational works.

One of the earliest demonstrations of HTP electrochemical methods was developed by M. D. Ward et al., showcasing modified electrode materials[134]. Watanabe et al. demonstrated combinatorial synthesis and XRD characterization of $LiCo_{1-x}Mn_xO_2$, achieving a throughput of 16 samples.[135] J. R. Dahn reported several combinatorial syntheses and electrochemical tests, significantly advancing HTP methodologies.[136–138] Additionally, numerous HTP computation and machine learning studies have explored voltage, energy density, and new electrode materials and electrolytes.[139] Despite these advancements, a comprehensive HTP approach to investigate a wide array of materials remains lacking, and a gap persists between experimental and theoretical work. Sanchez-Lengeling et al. further proposed the machine learning-aided robotics route for novel material discovery.[140] G. Ceder et al. achieved and showcased an autonomous lab for material discovery powered by active learning, obtaining 41 novel inorganic compounds in 17 days of continuous operation.[141] Recently, McCalla et al. developed a series of HTP studies for battery material research, including cathodes, anodes, and solid electrolytes[142–145], demonstrating high effectiveness and promising results. K. Potts et al. systematically investigated HTP systems applied to developing cathodes for lithium-ion batteries.[146] Following this, T. Adhikari et al. adopted Na metal as an anode and demonstrated the potential of applying HTP methods for sodium-ion batteries.[67]

In this thesis, we demonstrated a series of pioneering works to apply HTP methods to investigate several properties of the cathode materials and new material discovery for SIBs. By leveraging HTP techniques, we aim to bridge the gap between experimental and data-driven research, ultimately accelerating the development of advanced SIB technologies. By incorporating advanced characterizations and machine learning algorithms, we have enhanced our ability to investigate material properties and optimization, thus reducing the time and resources required for pattern identification and material discovery. These innovative approaches have the potential to transform the field of battery research, leading to more efficient and cost-effective energy storage solutions.

1.7 Motivation and structure of the thesis

Building upon the context established in **Chapter 1**, this thesis aims to advance sodium-ion batteries, with a particular emphasis on the pivotal role of cathode materials. Several critical challenges for cathodes are addressed, such as preventing Jahn-Teller distortions, phase transitions, and transition metal dissolution, as well as improving air/moisture stability. These challenges form the foundation for the thesis, which seeks to systematically investigate and optimize layered cathodes for sodium-ion batteries using high-throughput methodologies. In parallel, the thesis aims to develop effective strategies to address these challenges, paving the way for the commercialization of sodium-ion batteries.

Chapter 2 establishes the high-throughput methodologies employed in this work, demonstrating the feasibility of integrating high-throughput synthesis and characterization techniques. The exploration of the environmentally benign Na-Fe-Mn-O pseudoternary system provides critical insights into the relationships between composition and material properties.

Chapter 3 expands on doping strategies for designing high-manganese cathodes, systematically evaluating the effects of dopants on phase stability, rate performance, anionic redox activity, and air stability. A novel accelerated protocol is introduced, enabling a systematic investigation of air stability.

Chapter 4 delves into more complex Fe-Mn-based systems incorporating various dopants, with a focus on addressing surface stability issues, including transition metal dissolution and air stability. The chapter explores the underlying mechanisms of these detrimental effects and identifies dopants that significantly enhance surface stability. Furthermore, machine learning algorithms are applied to XRD patterns to uncover latent factors, providing valuable insights into designing air-stable layered oxide materials.

Chapter 5 presents the key findings, discussing design principles for layered oxide cathodes derived from the high-throughput studies. Additionally, it presents perspectives on future work, emphasizing the integration of artificial intelligence, machine learning, and automation into high-throughput methodologies to further accelerate the screening and development of energy storage materials.

1.8 Reference

(1) Liu, C.; Li, F.; Ma, L.-P.; Cheng, H.-M. Advanced Materials for Energy Storage. *Advanced Materials* **2010**, *22* (8), E28–E62.

(2) Zhang, C.; Wei, Y.-L.; Cao, P.-F.; Lin, M.-C. Energy Storage System: Current Studies on Batteries and Power Condition System. *Renewable and Sustainable Energy Reviews* **2018**, *82*, 3091–3106.

(3) Goodenough, J. B. Energy Storage Materials: A Perspective. *Energy Storage Materials* **2015**, *1*, 158–161.

(4) Liu, T.; Zhang, Y.; Jiang, Z.; Zeng, X.; Ji, J.; Li, Z.; Gao, X.; Sun, M.; Lin, Z.; Ling, M.; Zheng, J.; Liang, C. Exploring Competitive Features of Stationary Sodium Ion Batteries for Electrochemical Energy Storage. *Energy & Environmental Science* **2019**, *12* (5), 1512–1533.

(5) *Sustainable Development Goals*. UNDP. https://www.undp.org/sustainable-development-goals (accessed 2024-07-12).

(6) US EPA, O. *Climate Change Indicators: Weather and Climate*. https://www.epa.gov/climate-indicators/weather-climate (accessed 2024-07-12).

(7) Singh, B. K.; Delgado-Baquerizo, M.; Egidi, E.; Guirado, E.; Leach, J. E.; Liu, H.; Trivedi, P. Climate Change Impacts on Plant Pathogens, Food Security and Paths Forward. *Nature Reviews Microbiology* **2023**, *21* (10), 640–656.

(8) Yuan, X.; Wang, Y.; Ji, P.; Wu, P.; Sheffield, J.; Otkin, J. A. A Global Transition to Flash Droughts under Climate Change. *Science* **2023**, *380* (6641), 187–191.

(9) MacCarthy, J.; Tyukavina, A.; Weisse, M.; Harris, N. *Canada's Record-breaking 2023 Wildfires Released Nearly 4 Times More Carbon than Global Aviation*. https://www.wri.org/insights/canada-wildfire-emissions (accessed 2024-07-12).

(10) *CO2 emissions in aviation in the Net Zero Scenario, 2000-2030 – Charts – Data & Statistics*. IEA. https://www.iea.org/data-and-statistics/charts/co2-emissions-in-aviation-in-the-net-zero-scenario-2000-2030 (accessed 2024-07-12).

(11) *Alternative Fuels Data Center: How Do All-Electric Cars Work?* https://afdc.energy.gov/vehicles/how-do-all-electric-cars-work (accessed 2024-07-11).

(12) Thomas, J. Drive Cycle Powertrain Efficiencies and Trends Derived from EPA Vehicle Dynamometer Results. *SAE International Journal of Passenger Cars—Mechanical Systems* **2014**, *7* (4), 1374–1384.

(13) *ICE Vehicles vs. Electric Vehicles | Elasto Proxy*. https://www.elastoproxy.com/ice-vehicles-vs-electric-vehicles/ (accessed 2024-07-12).

(14) Rhodes, K.; Kok, D.; Sohoni, P.; Perry, E.; Kraska, M.; Wallace, M. Estimation of the Effects of Auxiliary Electrical Loads on Hybrid Electric Vehicle Fuel Economy; 2017; pp 2017-01–1155.

(15) Carlson, R. B.; Wishart, J.; Stutenberg, K. On-Road and Dynamometer Evaluation of Vehicle Auxiliary Loads. *SAE International Journal of Fuels and Lubricants* **2016**, *9* (1), 260–268.

(16) Lohse-Busch, H.; Duoba, M.; Rask, E.; Stutenberg, K.; Gowri, V.; Slezak, L.; Anderson, D. Ambient Temperature (20°F, 72°F and 95°F) Impact on Fuel and Energy Consumption for Several Conventional Vehicles, Hybrid and Plug-In Hybrid Electric Vehicles and Battery Electric Vehicle; 2013; pp 2013-01–1462.

(17) *Trends in electric cars – Global EV Outlook 2024 – Analysis*. IEA. https://www.iea.org/reports/global-ev-outlook-2024/trends-in-electric-cars (accessed 2024-07-12).

(18) *Global EV Outlook 2024 – Analysis*. IEA. https://www.iea.org/reports/global-ev-outlook-2024 (accessed 2024-07-12).

(19) US EPA, O. *Sources of Greenhouse Gas Emissions*. https://www.epa.gov/ghgemissions/sources-greenhouse-gas-emissions (accessed 2024-07-12).

(20) Canada, S. *Net-zero emissions by 2050*. https://www.canada.ca/en/services/environment/weather/climatechange/climate-plan/net-zero-emissions-2050.html (accessed 2024-07-12).

(21) Canada, T. *Canada's Zero-Emission vehicle sales targets*. AHSB 17484854. https://tc.canada.ca/en/road-transportation/innovative-technologies/zero-emission-vehicles/canada-s-zero-emission-vehicle-sales-targets (accessed 2024-07-12).

(22) Government of Canada, C. E. R. *CER – Market Snapshot: Zero emission vehicles now account for over 10% of all new vehicles in Canada*. https://www.cer-rec.gc.ca/en/data-analysis/energy-markets/market-snapshots/2024/market-snapshot-zero-emission-vehicles-now-account-for-over-10-percent-of-all-new-vehicles-in-canada.html (accessed 2024-07-12).

(23) *Could replacing lithium with salt solve the battery crisis?*. euronews. https://www.euronews.com/green/2022/02/09/we-re-facing-a-lithium-battery-crisis-what-are-the-alternatives (accessed 2024-07-12).

(24) *V2G and the Powersnack^{TM}: How does it work?* https://witricity.com/media/blog/v2g-and-the-powersnack-how-does-it-work (accessed 2024-07-12).

(25) Chen, H.; Cong, T. N.; Yang, W.; Tan, C.; Li, Y.; Ding, Y. Progress in Electrical Energy Storage System: A Critical Review. *Progress in Natural Science* **2009**, *19* (3), 291–312.

(26) Zhang, C.; Wei, Y.-L.; Cao, P.-F.; Lin, M.-C. Energy Storage System: Current Studies on Batteries and Power Condition System. *Renewable and Sustainable Energy Reviews* **2018**, *82*, 3091–3106.

(27) Yang, Y.; Bremner, S.; Menictas, C.; Kay, M. Battery Energy Storage System Size Determination in Renewable Energy Systems: A Review. *Renewable and Sustainable Energy Reviews* **2018**, *91*, 109–125.

(28) Hirsh, H. S.; Li, Y.; Tan, D. H. S.; Zhang, M.; Zhao, E.; Meng, Y. S. Sodium-Ion Batteries Paving the Way for Grid Energy Storage. *Advanced Energy Materials* **2020**, *10* (32), 2001274.

(29) Bernhart, W. *Rising demand for lithium-ion batteries may lead to shortages in raw material supply*. Roland Berger. https://www.mynewsdesk.com/rolandberger/pressreleases/rising-demand-for-lithium-ion-batteries-may-lead-to-shortages-in-raw-material-supply-3173780 (accessed 2024-07-11).

(30) Fleischmann, J.; Schaufuss, P. *Lithium-ion battery demand forecast for 2030 | McKinsey*. Battery 2030: Resilient, sustainable, and circular. https://www.mckinsey.com/industries/automotive-and-assembly/our-insights/battery-2030-resilient-sustainable-and-circular (accessed 2024-07-07).

(31) *Lithium facts*. Canada Natural Resources. https://natural-resources.canada.ca/our-natural-resources/minerals-mining/mining-data-statistics-and-analysis/minerals-metals-facts/lithium-facts/24009 (accessed 2024-07-12).

(32) Vera, M. L.; Torres, W. R.; Galli, C. I.; Chagnes, A.; Flexer, V. Environmental Impact of Direct Lithium Extraction from Brines. *Nature Reviews Earth & Environment* **2023**, *4* (3), 149–165.

(33) Kaunda, R. B. Potential Environmental Impacts of Lithium Mining. *Journal of Energy & Natural Resources Law* **2020**, *38* (3), 237–244.

(34) Ahmad, S. The Lithium Triangle: Where Chile Argentina, and Bolivia Meet. *Harvard International Review* **2020**, *41* (1), 51–53.

(35) Slater, M. D.; Kim, D.; Lee, E.; Johnson, C. S. Sodium-Ion Batteries. *Advanced Functional Materials* **2013**, *23* (8), 947–958.

(36) Delmas, C. Sodium and Sodium-Ion Batteries: 50 Years of Research. *Advanced Energy Materials* **2018**, *8* (17), 1703137.

(37) Hwang, J.-Y.; Myung, S.-T.; Sun, Y.-K. Sodium-Ion Batteries: Present and Future. *Chemical Society Reviews* **2017**, *46* (12), 3529–3614.

(38) Fredenhagen, K.; Cadenbach, G. Die Bindung von Kalium durch Kohlenstoff. *Zeitschrift für anorganische und allgemeine Chemie* **1926**, *158* (1), 249–263.

(39) Rüdorff, W. Einlagerungsverbindungen mit Alkali- und Erdalkalimetallen. *Angewandte Chemie* **1959**, *71* (15–16), 487–491.

(40) Rüdorff, W.; Sick, H. H. Einlagerungsverbindungen von Alkali- Und Erdalkalimetallen in Molybdän- Und Wolframdisulfid. *Angewandte Chemie* **1959**, *71* (3), 127–127.

(41) Whittingham, M. S. Electrical Energy Storage and Intercalation Chemistry. *Science* **1976**, *192* (4244), 1126–1127.

(42) Silbernagel, B. G.; Whittingham, M. S. The Physical Properties of the NaxTiS2 Intercalation Compounds: A Synthetic and NMR Study. *Materials Research Bulletin* **1976**, *11* (1), 29–36.

(43) Armand, M. B. Intercalation Electrodes. In *Materials for Advanced Batteries*; Murphy, D. W., Broadhead, J., Steele, B. C. H., Eds.; Springer US: Boston, MA, 1980; pp 145–161.

(44) Mizushima, K.; Jones, P. C.; Wiseman, P. J.; Goodenough, J. B. LixCoO2 (0<x<-1): A New Cathode Material for Batteries of High Energy Density. *Materials Research Bulletin* **1980**, *15* (6), 783–789.

(45) Delmas, C.; Braconnier, J.-J.; Fouassier, C.; Hagenmuller, P. Electrochemical Intercalation of Sodium in NaxCoO2 Bronzes. *Solid State Ionics* **1981**, *3–4*, 165–169.

(46) Newman, G. H.; Klemann, L. P. Ambient Temperature Cycling of an Na - TiS2 Cell. *Journal of the Electrochemical Society* **1980**, *127* (10), 2097.

(47) Whittingham, M. S. Chemistry of Intercalation Compounds: Metal Guests in Chalcogenide Hosts. *Progress in Solid State Chemistry* **1978**, *12* (1), 41–99.

(48) Stevens, D. A.; Dahn, J. R. High Capacity Anode Materials for Rechargeable Sodium-Ion Batteries. *Journal of the Electrochemical Society* **2000**, *147* (4), 1271.

(49) Yabuuchi, N.; Kubota, K.; Dahbi, M.; Komaba, S. Research Development on Sodium-Ion Batteries. *Chemical Reviews* **2014**, *114* (23), 11636–11682.

(50) Shannon, R. D. Revised Effective Ionic Radii and Systematic Studies of Interatomic Distances in Halides and Chalcogenides. *Acta Crystallographica Section A* **1976**, *32* (5), 751–767.

(51) Kuratani, K.; Uemura, N.; Senoh, H.; Takeshita, H. T.; Kiyobayashi, T. Conductivity, Viscosity and Density of MClO4 (M = Li and Na) Dissolved in Propylene Carbonate and γ-Butyrolactone at High Concentrations. *Journal of Power Sources* **2013**, *223*, 175–182.

(52) Okoshi, M.; Yamada, Y.; Yamada, A.; Nakai, H. Theoretical Analysis on De-Solvation of Lithium, Sodium, and Magnesium Cations to Organic Electrolyte Solvents. *Journal of the Electrochemical Society* **2013**, *160* (11), A2160.

(53) Yabuuchi, N.; Kajiyama, M.; Iwatate, J.; Nishikawa, H.; Hitomi, S.; Okuyama, R.; Usui, R.; Yamada, Y.; Komaba, S. P2-Type Nax[Fe1/2Mn1/2]O2 Made from Earth-Abundant Elements for Rechargeable Na Batteries. *Nature Materials* **2012**, *11* (6), 512–517.

(54) Wang, L.; Lu, Y.; Liu, J.; Xu, M.; Cheng, J.; Zhang, D.; Goodenough, J. B. A Superior Low-Cost Cathode for a Na-Ion Battery. *Angewandte Chemie International Edition* **2013**, *52* (7), 1964–1967.

(55) Mukai, K.; Inoue, T.; Kato, Y.; Shirai, S. Superior Low-Temperature Power and Cycle Performances of Na-Ion Battery over Li-Ion Battery. *ACS Omega* **2017**, *2* (3), 864–872.

(56) Wang, M.; Wang, Q.; Ding, X.; Wang, Y.; Xin, Y.; Singh, P.; Wu, F.; Gao, H. The Prospect and Challenges of Sodium-Ion Batteries for Low-Temperature Conditions. *Interdisciplinary Materials* **2022**, *1* (3), 373–395.

(57) Singh, A. N.; Islam, M.; Meena, A.; Faizan, M.; Han, D.; Bathula, C.; Hajibabaei, A.; Anand, R.; Nam, K.-W. Unleashing the Potential of Sodium-Ion Batteries: Current State and Future Directions for Sustainable Energy Storage. *Advanced Functional Materials* **2023**, *33* (46), 2304617.

(58) Wu, Q.; Zhang, T.; Geng, J.; Gao, S.; Ma, H.; Li, F. Anionic Redox Chemistry for Sodium-Ion Batteries: Mechanisms, Advances, and Challenges. *Energy Fuels* **2022**, *36* (15), 8081–8095.

(59) Vineeth, S. K.; Soni, C. B.; Sun, Y.; Kumar, V.; Seh, Z. W. Implications of Na-Ion Solvation on Na Anode–Electrolyte Interphase. *Trends in Chemistry* **2022**, *4* (1), 48–59.

(60) Kang, H.; Liu, Y.; Cao, K.; Zhao, Y.; Jiao, L.; Wang, Y.; Yuan, H. Update on Anode Materials for Na-Ion Batteries. *Journal of Materials Chemistry A* **2015**, *3* (35), 17899–17913.

(61) Bard, A. J.; Faulkner, L. R.; White, H. S. *Electrochemical Methods: Fundamentals and Applications*; John Wiley & Sons, 2022.

(62) Ji, X.; Hou, H.; Zou, G. *Sodium-Ion Batteries: Technologies and Applications*; John Wiley & Sons, 2023.

(63) Ponrouch, A.; Monti, D.; Boschin, A.; Steen, B.; Johansson, P.; R. Palacín, M. Non-Aqueous Electrolytes for Sodium-Ion Batteries. *Journal of Materials Chemistry A* **2015**, *3* (1), 22–42.

(64) Che, H.; Chen, S.; Xie, Y.; Wang, H.; Amine, K.; Liao, X.-Z.; Ma, Z.-F. Electrolyte Design Strategies and Research Progress for Room-Temperature Sodium-Ion Batteries. *Energy & Environmental Science* **2017**, *10* (5), 1075–1101.

(65) Huang, Y.; Zhao, L.; Li, L.; Xie, M.; Wu, F.; Chen, R. Electrolytes and Electrolyte/Electrode Interfaces in Sodium-Ion Batteries: From Scientific Research to Practical Application. *Advanced Materials* **2019**, *31* (21), 1808393.

(66) Komaba, S.; Ishikawa, T.; Yabuuchi, N.; Murata, W.; Ito, A.; Ohsawa, Y. Fluorinated Ethylene Carbonate as Electrolyte Additive for Rechargeable Na Batteries. *ACS Applied Materials & Interfaces* **2011**, *3* (11), 4165–4168.

(67) Adhikari, T.; Hebert, A.; Adamič, M.; Yao, J.; Potts, K.; McCalla, E. Development of High-Throughput Methods for Sodium-Ion Battery Cathodes. *ACS Combinatorial Science.* **2020**, *22* (6), 311–318.

(68) Wu, D.; Li, X.; Xu, B.; Twu, N.; Liu, L.; Ceder, G. NaTiO 2 : A Layered Anode Material for Sodium-Ion Batteries. *Energy & Environmental Science* **2015**, *8* (1), 195–202.

(69) Lou, S.; Zhao, Y.; Wang, J.; Yin, G.; Du, C.; Sun, X. Ti-Based Oxide Anode Materials for Advanced Electrochemical Energy Storage: Lithium/Sodium Ion Batteries and Hybrid Pseudocapacitors. *Small* **2019**, *15* (52), 1904740.

(70) Zhang, H.; Gao, Y.; Liu, X.-H.; Yang, Z.; He, X.-X.; Li, L.; Qiao, Y.; Chen, W.-H.; Zeng, R.-H.; Wang, Y.; Chou, S.-L. Organic Cathode Materials for Sodium-Ion Batteries: From Fundamental Research to Potential Commercial Application. *Advanced Functional Materials* **2022**, *32* (4), 2107718.

(71) Luo, C.; Shea, J. J.; Huang, J. A Carboxylate Group-Based Organic Anode for Sustainable and Stable Sodium Ion Batteries. *Journal of Power Sources* **2020**, *453*, 227904.

(72) Zhao, Q.; Lu, Y.; Chen, J. Advanced Organic Electrode Materials for Rechargeable Sodium-Ion Batteries. *Advanced Energy Materials* **2017**, *7* (8), 1601792.

(73) Lao, M.; Zhang, Y.; Luo, W.; Yan, Q.; Sun, W.; Dou, S. X. Alloy-Based Anode Materials toward Advanced Sodium-Ion Batteries. *Advanced Materials* **2017**, *29* (48), 1700622.

(74) Zheng, S.-M.; Tian, Y.-R.; Liu, Y.-X.; Wang, S.; Hu, C.-Q.; Wang, B.; Wang, K.-M. Alloy Anodes for Sodium-Ion Batteries. *Rare Metals.* **2021**, *40* (2), 272–289.

(75) Saurel, D.; Orayech, B.; Xiao, B.; Carriazo, D.; Li, X.; Rojo, T. From Charge Storage Mechanism to Performance: A Roadmap toward High Specific Energy Sodium-Ion Batteries through Carbon Anode Optimization. *Advanced Energy Materials* **2018**, *8* (17), 1703268.

(76) Chen, D.; Zhang, W.; Luo, K.; Song, Y.; Zhong, Y.; Liu, Y.; Wang, G.; Zhong, B.; Wu, Z.; Guo, X. Hard Carbon for Sodium Storage: Mechanism and Optimization Strategies toward Commercialization. *Energy & Environmental Science* **2021**, *14* (4), 2244–2262.

(77) Komaba, S.; Murata, W.; Ishikawa, T.; Yabuuchi, N.; Ozeki, T.; Nakayama, T.; Ogata, A.; Gotoh, K.; Fujiwara, K. Electrochemical Na Insertion and Solid Electrolyte Interphase for Hard-Carbon Electrodes and Application to Na-Ion Batteries. *Advanced Functional Materials* **2011**, *21* (20), 3859–3867.

(78) Caragiu, M.; Finberg, S. Alkali Metal Adsorption on Graphite: A Review. *Journal of Physics: Condensed Matter* **2005**, *17* (35), R995.

(79) Li, Y.; Lu, Y.; Adelhelm, P.; Titirici, M.-M.; Hu, Y.-S. Intercalation Chemistry of Graphite: Alkali Metal Ions and Beyond. *Chemical Society Reviews* **2019**, *48* (17), 4655–4687.

(80) Liu, Y.; Merinov, B. V.; Goddard, W. A. Origin of Low Sodium Capacity in Graphite and Generally Weak Substrate Binding of Na and Mg among Alkali and Alkaline Earth Metals. *Proceedings of the National Academy of Sciences* **2016**, *113* (14), 3735.

(81) Manthiram, A. A Reflection on Lithium-Ion Battery Cathode Chemistry. *Nature Communications* **2020**, *11* (1), 1550.

(82) Pan, H.; Hu, Y.-S.; Chen, L. Room-Temperature Stationary Sodium-Ion Batteries for Large-Scale Electric Energy Storage. *Energy & Environmental Science* **2013**, *6* (8), 2338–2360.

(83) Melot, B. C.; Tarascon, J.-M. Design and Preparation of Materials for Advanced Electrochemical Storage. *Accounts of Chemical Research* **2013**, *46* (5), 1226–1238.

(84) Goodenough, J. B.; Kim, Y. Challenges for Rechargeable Li Batteries. *Chemistry of Materials* **2010**, *22* (3), 587–603.

(85) Li, H.; Xu, M.; Zhang, Z.; Lai, Y.; Ma, J. Engineering of Polyanion Type Cathode Materials for Sodium-Ion Batteries: Toward Higher Energy/Power Density. *Advanced Functional Materials* **2020**, *30* (28), 2000473.

(86) Zhang, X.; Qiao, Y.; Guo, S.; Jiang, K.; Xu, S.; Xu, H.; Wang, P.; He, P.; Zhou, H. Manganese-Based Na-Rich Materials Boost Anionic Redox in High-Performance Layered Cathodes for Sodium-Ion Batteries. *Advanced Materials* **2019**, *31* (27), 1807770.

(87) Ping Ong, S.; L. Chevrier, V.; Hautier, G.; Jain, A.; Moore, C.; Kim, S.; Ma, X.; Ceder, G. Voltage, Stability and Diffusion Barrier Differences between Sodium-Ion and Lithium-Ion Intercalation Materials. *Energy & Environmental Science* **2011**, *4* (9), 3680–3688.

(88) Chayambuka, K.; Mulder, G.; Danilov, D. L.; Notten, P. H. L. From Li-Ion Batteries toward Na-Ion Chemistries: Challenges and Opportunities. *Advanced Energy Materials* **2020**, *10* (38), 2001310.

(89) Sayahpour, B.; Hirsh, H.; Parab, S.; Nguyen, L. H. B.; Zhang, M.; Meng, Y. S. Perspective: Design of Cathode Materials for Sustainable Sodium-Ion Batteries. *MRS Energy & Sustainability* **2022**, *9* (2), 183–197.

(90) Liang, X.; Hwang, J.-Y.; Sun, Y.-K. Practical Cathodes for Sodium-Ion Batteries: Who Will Take The Crown? *Advanced Energy Materials* **2023**, *13* (37), 2301975.

(91) Kubota, K.; Kumakura, S.; Yoda, Y.; Kuroki, K.; Komaba, S. Electrochemistry and Solid-State Chemistry of NaMeO2 (Me = 3d Transition Metals). *Advanced Energy Materials* **2018**, *8* (17), 1703415.

(92) Yabuuchi, N.; Kubota, K.; Dahbi, M.; Komaba, S. Research Development on Sodium-Ion Batteries. *Chemical Reviews* **2014**, *114* (23), 11636–11682.

(93) Didier, C.; Guignard, M.; Denage, C.; Szajwaj, O.; Ito, S.; Saadoune, I.; Darriet, J.; Delmas, C. Electrochemical Na-Deintercalation from NaVO2. *Electrochemical and Solid-State Letters* **2011**, *14* (5), A75.

(94) Yu, C.-Y.; Park, J.-S.; Jung, H.-G.; Chung, K.-Y.; Aurbach, D.; Sun, Y.-K.; Myung, S.-T. NaCrO 2 Cathode for High-Rate Sodium-Ion Batteries. *Energy & Environmental Science* **2015**, *8* (7), 2019–2026.

(95) Billaud, J.; Clément, R. J.; Armstrong, A. R.; Canales-Vázquez, J.; Rozier, P.; Grey, C. P.; Bruce, P. G. β-NaMnO2: A High-Performance Cathode for Sodium-Ion Batteries. *Journal of the American Chemical Society* **2014**, *136* (49), 17243–17248.

(96) Zhao, J.; Zhao, L.; Dimov, N.; Okada, S.; Nishida, T. Electrochemical and Thermal Properties of α-NaFeO2 Cathode for Na-Ion Batteries. *Journal of the Electrochemical Society* **2013**, *160* (5), A3077.

(97) Samin, N. K.; Roshidah, R.; Kamarudin, N.; Kamarulzaman, N. Synthesis and Battery Studies of Sodium Cobalt Oxides, NaCoO2 Cathodes. *Advanced Materials Research* **2012**, *545*, 185–189.

(98) Wang, L.; Wang, J.; Zhang, X.; Ren, Y.; Zuo, P.; Yin, G.; Wang, J. Unravelling the Origin of Irreversible Capacity Loss in NaNiO2 for High Voltage Sodium Ion Batteries. *Nano Energy* **2017**, *34*, 215–223.

(99) Su, H.; Jaffer, S.; Yu, H. Transition Metal Oxides for Sodium-Ion Batteries. *Energy Storage Materials* **2016**, *5*, 116–131.

(100) Ma, X.; Chen, H.; Ceder, G. Electrochemical Properties of Monoclinic NaMnO2. *Journal of the Electrochemical Society* **2011**, *158* (12), A1307.

(101) Lee, E.; Brown, D. E.; Alp, E. E.; Ren, Y.; Lu, J.; Woo, J.-J.; Johnson, C. S. New Insights into the Performance Degradation of Fe-Based Layered Oxides in Sodium-Ion Batteries: Instability of Fe3+/Fe4+ Redox in α-NaFeO2. *Chemistry of Materials* **2015**, *27* (19), 6755–6764.

(102) Kataoka, R.; Taguchi, N.; Tada, K.; Machida, A.; Takeichi, N. Improving Electrochemical Activity of P2-Type Na2/3Mn2/3Ni1/3O2 by Controlling Its Crystallinity. *Batteries & Supercaps* **2023**, *6* (2), e202200462.

(103) Maletti, S.; Sarapulova, A.; Schökel, A.; Mikhailova, D. Operando Studies on the NaNi0.5Ti0.5O2 Cathode for Na-Ion Batteries: Elucidating Titanium as a Structure Stabilizer. *ACS Applied Materials & Interfaces* **2019**, *11* (37), 33923–33930.

(104) Li, Z.; Yu, Y.; Zhang, T.; Wong, D.; Schulz, C.; Zhang, N.; Ning, D.; Li, Q.; Zhang, J.; Liu, X. Tuning Electronegativity-Difference Configuration to Construct Non-Bonded O 2p Orbitals for Reversible Anionic Redox in O3-Type Cathode. *Advanced Functional Materials n/a* (n/a), 2404797.

(105) Zhao, C.; Ding, F.; Lu, Y.; Chen, L.; Hu, Y.-S. High-Entropy Layered Oxide Cathodes for Sodium-Ion Batteries. *Angewandte Chemie International Edition* **2020**, *59* (1), 264–269.

(106) Hench, L. L.; West, J. K. The Sol-Gel Process. *Chemical Reviews* **1990**, *90* (1), 33–72.

(107) McCalla, E.; Parmaklis, M.; Rehman, S.; Anderson, E.; Jia, S.; Hebert, A.; Potts, K.; Jonderian, A.; Adhikari, T.; Adamič, M. Combinatorial Methods in Advanced Battery Materials Design. *Canadian Journal of chemistry* **2022**, *100* (2), 132–143.

(108) Sturge, M. D. The Jahn-Teller Effect in Solids*. In *Solid State Physics*; Seitz, F., Turnbull, D., Ehrenreich, H., Eds.; Academic Press, 1968; Vol. 20, pp 91–211.

(109) Asl, H. Y.; Manthiram, A. Reining in Dissolved Transition-Metal Ions. *Science* **2020**, *369* (6500), 140–141.

(110) Li, X.; Ma, X.; Su, D.; Liu, L.; Chisnell, R.; Ong, S. P.; Chen, H.; Toumar, A.; Idrobo, J.-C.; Lei, Y.; Bai, J.; Wang, F.; Lynn, J. W.; Lee, Y. S.; Ceder, G. Direct Visualization of the Jahn–Teller Effect Coupled to Na Ordering in Na5/8MnO2. *Nature Materials* **2014**, *13* (6), 586–592.

(111) Hou, P.; Dong, M.; Lin, Z.; Sun, Z.; Gong, M.; Li, F.; Xu, X. Alleviating the Jahn–Teller Distortion of P3-Type Manganese-Based Cathodes by Compositionally Graded Structure for Sodium-Ion Batteries. *ACS Sustainable Chemistry & Engineering* **2023**, *11* (29), 10785–10794.

(112) Fang, H.; Ji, H.; Zhai, J.; Wang, C.; Zhu, C.; Chen, G.; Chu, M.; Zhang, T.; Ma, Z.; Zhao, W.; Ji, W.; Xiao, Y. Mitigating Jahn–Teller Effect in Layered Cathode Material Via Interstitial Doping for High-Performance Sodium-Ion Batteries. *Small* **2023**, *19* (35), 2301360.

(113) Kumakura, S.; Tahara, Y.; Kubota, K.; Chihara, K.; Komaba, S. Sodium and Manganese Stoichiometry of P2-Type Na2/3MnO2. *Angewandte Chemie International Edition* **2016**, *55* (41), 12760–12763.

(114) Li, Y.; Gao, Y.; Wang, X.; Shen, X.; Kong, Q.; Yu, R.; Lu, G.; Wang, Z.; Chen, L. Iron Migration and Oxygen Oxidation during Sodium Extraction from NaFeO2. *Nano Energy* **2018**, *47*, 519–526.

(115) Yabuuchi, N.; Yoshida, H.; Komaba, S. Crystal Structures and Electrode Performance of Alpha-NaFeO2 for Rechargeable Sodium Batteries. *Electrochemistry* **2012**, *80* (10), 716–719.

(116) Kubota, K.; Ikeuchi, I.; Nakayama, T.; Takei, C.; Yabuuchi, N.; Shiiba, H.; Nakayama, M.; Komaba, S. New Insight into Structural Evolution in Layered NaCrO2 during Electrochemical Sodium Extraction. *Journal of Physical Chemistry C* **2015**, *119* (1), 166–175.

(117) Yao, H.-R.; Zheng, L.; Xin, S.; Guo, Y.-G. Air-Stability of Sodium-Based Layered-Oxide Cathode Materials. *Science China Chemistry* **2022**, *65* (6), 1076–1087.

(118) Jia, S.; Kumakura, S.; McCalla, E. Unravelling Air/Moisture Stability of Cathode Materials in Sodium Ion Batteries: Characterization, Rational Design, and Perspectives. *Energy & Environmental Science* **2024**, *17* (13), 4343–4389.

(119) Zhang, R.; Yang, S.; Li, H.; Zhai, T.; Li, H. Air Sensitivity of Electrode Materials in Li/Na Ion Batteries: Issues and Strategies. *InfoMat* **2022**, *4* (6), e12305.

(120) Duffner, F.; Kronemeyer, N.; Tübke, J.; Leker, J.; Winter, M.; Schmuch, R. Post-Lithium-Ion Battery Cell Production and Its Compatibility with Lithium-Ion Cell Production Infrastructure. *Nature Energy* **2021**, *6* (2), 123–134.

(121) Liu, Y.-F.; Han, K.; Peng, D.-N.; Kong, L.-Y.; Su, Y.; Li, H.-W.; Hu, H.-Y.; Li, J.-Y.; Wang, H.-R.; Fu, Z.-Q.; Ma, Q.; Zhu, Y.-F.; Tang, R.-R.; Chou, S.-L.; Xiao, Y.; Wu, X.-W. Layered Oxide Cathodes for Sodium-Ion Batteries: From Air Stability, Interface Chemistry to Phase Transition. *InfoMat* **2023**, *5* (6), e12422.

(122) Zuo, W.; Qiu, J.; Liu, X.; Ren, F.; Liu, H.; He, H.; Luo, C.; Li, J.; Ortiz, G. F.; Duan, H.; Liu, J.; Wang, M.-S.; Li, Y.; Fu, R.; Yang, Y. The Stability of P2-Layered Sodium Transition Metal Oxides in Ambient Atmospheres. *Nature communications* **2020**, *11* (1), 3544.

(123) Duffort, V.; Talaie, E.; Black, R.; Nazar, L. F. Uptake of CO2 in Layered P2-Na0.67Mn0.5Fe0.5O2: Insertion of Carbonate Anions. *Chemistry of Materials* **2015**, *27* (7), 2515–2524.

(124) Seong, W. M.; Kim, Y.; Manthiram, A. Impact of Residual Lithium on the Adoption of High-Nickel Layered Oxide Cathodes for Lithium-Ion Batteries. *Chemistry of Materials* **2020**, *32* (22), 9479–9489.

(125) Kubota, K.; Komaba, S. Review—Practical Issues and Future Perspective for Na-Ion Batteries. *Journal of the Electrochemical Society* **2015**, *162* (14), A2538.

(126) Bunaciu, A. A.; Udriştioiu, E. gabriela; Aboul-Enein, H. Y. X-Ray Diffraction: Instrumentation and Applications. *Critical Reviews in Analytical Chemistry* **2015**, *45* (4), 289–299.

(127) Rietveld, H. M. A Profile Refinement Method for Nuclear and Magnetic Structures. *Journal of Applied Crystallography* **1969**, *2* (2), 65–71.

(128) Seah, M. P. The Quantitative Analysis of Surfaces by XPS: A Review. *Surface and Interface Analysis* **1980**, *2* (6), 222–239.

(129) Shutthanandan, V.; Nandasiri, M.; Zheng, J.; Engelhard, M. H.; Xu, W.; Thevuthasan, S.; Murugesan, V. Applications of XPS in the Characterization of Battery Materials. *Journal of Electron Spectroscopy and Related Phenomena* **2019**, *231*, 2–10.

(130) Bak, S.-M.; Shadike, Z.; Lin, R.; Yu, X.; Yang, X.-Q. In Situ/Operando Synchrotron-Based X-Ray Techniques for Lithium-Ion Battery Research. *NPG Asia Materials* **2018**, *10* (7), 563–580.

(131) Lamberti, C.; van Bokhoven, J. A. Introduction: Historical Perspective on XAS. In *X-Ray Absorption and X-Ray Emission Spectroscopy*; John Wiley & Sons, Ltd, 2016; pp 1–21.

(132) Yano, J.; Yachandra, V. K. X-Ray Absorption Spectroscopy. *Photosynthesis Research* **2009**, *102* (2), 241–254.

(133) Wang, M.; Árnadóttir, L.; Xu, Z. J.; Feng, Z. In Situ X-Ray Absorption Spectroscopy Studies of Nanoscale Electrocatalysts. *Nano-Micro Letters.* **2019**, *11* (1), 47.

(134) Sullivan, M. G.; Utomo, H.; Fagan, P. J.; Ward, M. D. Automated Electrochemical Analysis with Combinatorial Electrode Arrays. *Analytical chemistry* **1999**, *71* (19), 4369–4375.

(135) Yanase, I.; Ohtaki, T.; Watanabe, M. Application of Combinatorial Process to LiCo1−XMnXO2 (0≦*X*≦0.2) Powder Synthesis. *Solid State Ionics* **2002**, *151* (1), 189–196.

(136) McCalla, E.; Rowe, A. W.; Brown, C. R.; Hacquebard, L. R. P.; Dahn, J. R. How Phase Transformations during Cooling Affect Li-Mn-Ni-O Positive Electrodes in Lithium Ion Batteries. *Journal of the Electrochemical Society* **2013**, *160* (8), A1134.

(137) Fleischauer, M. D.; Hatchard, T. D.; Rockwell, G. P.; Topple, J. M.; Trussler, S.; Jericho, S. K.; Jericho, M. H.; Dahn, J. R. Design and Testing of a 64-Channel Combinatorial Electrochemical Cell. *Journal of the Electrochemical Society* **2003**, *150* (11), A1465.

(138) Dahn, J. R.; Mar, R. E.; Abouzeid, A. Combinatorial Study of Sn1 − xCox (0 < x < 0.6) and [Sn0.55Co0.45] 1 − yCy (0 < y < 0.5) Alloy Negative Electrode Materials for Li-Ion Batteries. *Journal of the Electrochemical Society* **2005**, *153* (2), A361.

(139) Ling, S.-G.; Gao, J.; Xiao, R.-J.; Chen, L.-Q. High-Throughput Theoretical Design of Lithium Battery Materials*. *Chinese Physics B* **2015**, *25* (1), 018208.

(140) Sanchez-Lengeling, B.; Aspuru-Guzik, A. Inverse Molecular Design Using Machine Learning: Generative Models for Matter Engineering. *Science* **2018**, *361* (6400), 360–365.

(141) Szymanski, N. J.; Rendy, B.; Fei, Y.; Kumar, R. E.; He, T.; Milsted, D.; McDermott, M. J.; Gallant, M.; Cubuk, E. D.; Merchant, A.; Kim, H.; Jain, A.; Bartel, C. J.; Persson, K.; Zeng, Y.; Ceder, G. An Autonomous Laboratory for the Accelerated Synthesis of Novel Materials. *Nature* **2023**, *624* (7990), 86–91.

(142) Michael Sieffert, J.; J. Lang, C.; Bazylevych, S.; Jia, S.; McCalla, E. The Nb–Ti–W–O System as Safe High-Power Anodes for Li-Ion Batteries. *Journal of Materials Chemistry A* **2024**, *12* (3), 1429–1437.

(143) McCalla, E. Semiautomated Experiments to Accelerate the Design of Advanced Battery Materials: Combining Speed, Low Cost, and Adaptability. *ACS Engineering Au* **2023**, *3* (6), 391–402.

(144) Johari, N. S. M.; Jonderian, A.; Jia, S.; Cozea, V.; Yao, E.; Adnan, S. B. R. S.; Ahmad, N.; McCalla, E. High-Throughput Development of Na2ZnSiO4-Based Hybrid Electrolytes for Sodium-Ion Batteries. *Journal of Power Sources* **2022**, *541*, 231706.

(145) Jonderian, A.; Jia, S.; Yoon, G.; Cozea, V. T.; Galabi, N. Z.; Ma, S. B.; McCalla, E. Accelerated Development of High Voltage Li-Ion Cathodes. *Advanced Energy Materials* **2022**, *12* (40), 2201704.

(146) Potts, K. P.; Grignon, E.; McCalla, E. Accelerated Screening of High-Energy Lithium-Ion Battery Cathodes. *ACS Applied Energy Materials* **2019**, *2* (12), 8388–8393.

Chapter 2 High-Throughput Design of Na-Fe-Mn-O Cathodes for Na-Ion Batteries

In **Chapter 1**, we delineated the promising layered oxide cathode materials for sodium-ion batteries, but also described the challenges posed by complex systems and the lack of rational design strategies. **Chapter 2** builds on this by presenting the first systematic study of an entire pseudoternary system critical to Na-ion battery cathodes. This work demonstrates the feasibility of using high-throughput methodologies to advance research in sodium-ion batteries. We selected the Na-Fe-Mn-O system specifically for its environmentally friendly and excellent electrochemical characteristics. Given that sodium is abundant and both iron and manganese are environmentally benign, our focus on developing cost-effective, non-toxic materials holds significant promise for large-scale grid storage technology, where the use of lithium-ion batteries may not be practical. However, existing literature has left certain questions unanswered, and some compositions underexplored, with even conflicting findings across various papers. These issues particularly necessitate a comprehensive high-throughput study to provide clarity and resolve inconsistencies. Through an extensive data-driven investigation, we have addressed the complexities of this pseudoternary system, uncovering correlations between electrochemical properties, structure, composition, and other characteristics. This study not only clarifies previous ambiguities but also sets the stage for future advancements in high-throughput methodologies and data-driven research.

Chapter 2 is adapted with permission from "Jia, S.; Counsell, J.; Adamič, M.; Jonderian, A.; McCalla, E. High-Throughput Design of Na–Fe–Mn–O Cathodes for Na-Ion Batteries. *Journal of Materials Chemistry A* **2021**, *10* (1), 251–265."

2.1 Abstract

Sodium-ion batteries are considered to be environmentally favourable alternatives to lithium-ion batteries, particularly in the extremely large-scale application of grid storage, given the abundance of Na. However, to date, the battery performance has not been competitive, and promising Na-Fe-Mn-O materials have been plagued by poor stability in air and unsatisfactory long-term cycling. Herein, high-throughput methods are used to systematically screen the entire pseudo-ternary system. The resulting phase diagram shows significant solid solution regions for 3 important layered-oxide phases: P2, P3 and O3. While only a few compositions were previously studied, we identified over 50 single-phase materials of potential interest for battery materials. The results help explain contradictions in the literature and resolve decisively the locations of each of these phases. The phase mappings were also interpreted within the context of the recently developed cationic potential approach, and we extend the approach to P3 materials for the first time and find that cationic potential cannot be used to distinguish all P2 and P3 materials. High-throughput XPS is used on aged samples to determine stability in air and demonstrates that the stability with both carbon dioxide and moisture is very sensitive to composition and structure (stability changes by an order of magnitude within the Na-Fe-Mn-O system). Importantly, the understudied P3 and Mn-rich P2 regions show better stability in air. High-throughput electrochemistry shows that the Mn-rich P2 material also shows the highest first discharge capacity of 206 mAh/g and excellent specific energy of 504 Wh/kg. The findings herein therefore provide many insights of importance for the further development of these promising and challenging materials.

2.2 Introduction

The battery plays a pivotal role in the storage, transfer, release, and usage of electric energy. With the wide application of Li-ion batteries, the huge demand for electric vehicles, and large-scale energy storage, there are more and more concerns about the sustainability of Li-ion batteries. Na-ion batteries, by contrast, could be the key to break the crisis by utilizing cheaper and environmentally friendly materials. Among them, sodium layered oxides are important cathode materials with good sodium mobilities and high specific capacities[1]. Layered transition metal oxides Na_xMO_2 where M are mixtures of transition metals are constituted of layers of MO_6 octahedra to preserve 2D transport channels for Na in the layers between the MO_6 layers as illustrated in **Figure 2.1**.[2] For metal selections, M can be widely varied including: Fe[3], Mn[4], Co[5, 6], Cr[7], Ni[6], Ti[8], V[9] and their combinations[10-13]. Interestingly, binary or ternary transition metal systems show better battery performance than materials with only a single transition metal[14], which makes composition studies imperative. Moreover, during cathode material design, metal combinations can achieve tunable properties with structure, electrochemical performance, and cycling stability. Herein, we focus on the Na-Fe-Mn-O system only, as a wide variety of compositions are possible and, as discussed extensively throughout, the resulting structural and electrochemical properties vary dramatically within the pseudoternary system.

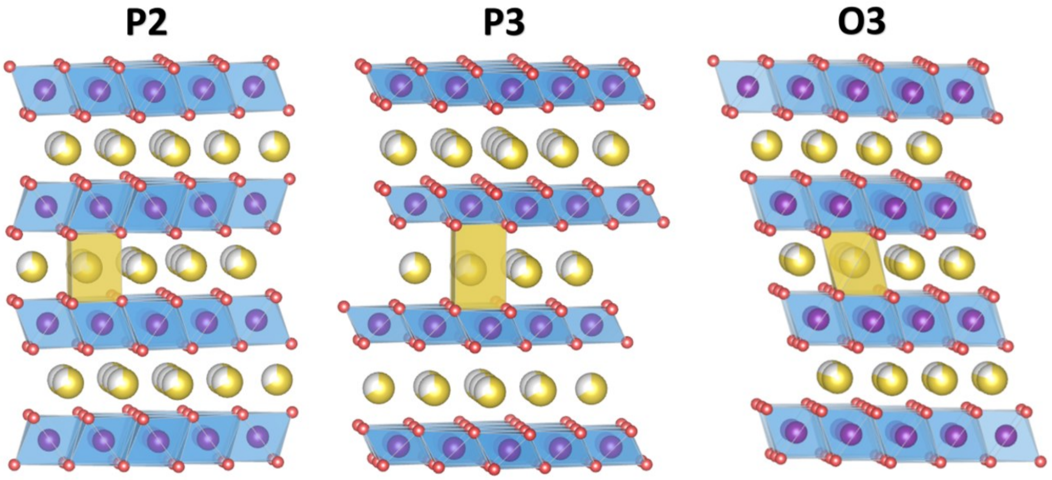

Figure 2.1 *Structures of the 3 phases discussed extensively here: P2, P3 and O3. The polyhedra shown are* MO_2 *where M is a mixture of Fe and Mn (purple spheres). The Na ions are shown in yellow while oxygen ions are red, for all structures the occupation of the Na layer is 2/3. The P3 structure is based on the results of our Rietveld refinement performed herein.*

Due to the larger Na-ion radius, Na layered oxide can be stabilized into two main groups. According to the notation developed by Delmas *et al.*[15], P and O are used to represent the primary two layered structures based on the Na environment either in prismatic (P) or octahedral (O) sites, while a number is used to indicate the number of layers in the z-direction that must be stacked to obtain a repeating unit. P2, P3, and O3 are the most common layered structures for the cathode materials in Na-ion batteries as illustrated in **Figure 2.1**. Importantly, all three of these structures have been reported previously in the Na-Fe-Mn-O system as shown in **Figure 2.2a**[11, 16-27], but at only a few compositions: four P2, one P3, and five O3 compositions (including one that was not phase pure and resulted in great confusion in the literature as discussed and resolved further herein). **Figure 2.2c** shows our findings here, revealing that all 3 solid solutions are far larger than previously suspected in the literature, this alone justifies the use of high-throughput methods to study this system. The further importance of this system as being composed of earth-abundant environmentally benign elements also motivates this study.

Let us briefly discuss the general trends seen in the P2, O3 and P3 structures in the literature with a particular emphasis on the limited number of pure phase Na-Fe-Mn-O materials (NFMO). Generally, the P2 structure shows superior Na-ion conductivity and higher capacity than the O3.[11] However, the initial sodium content (typically x = 0.6~0.7) in P2 materials is lower than what is typically reported for O3 materials and this limits the first discharge capacity in full batteries[28]. To achieve full capacity, P2 materials need to first be discharged below their open-circuit voltage in order to introduce more Na into the structure.

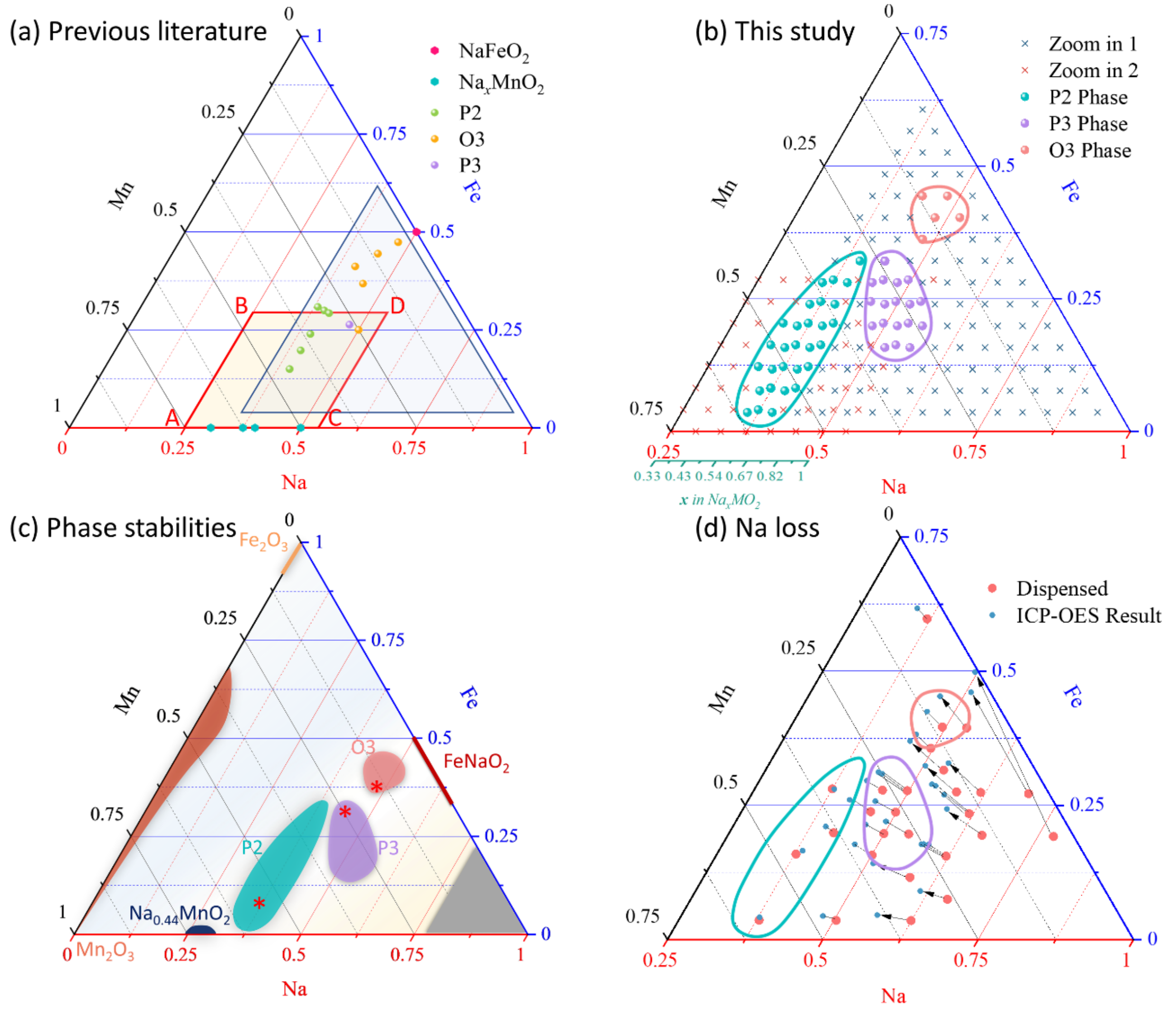

Figure 2.2 *(a) The entire Na-Fe-Mn-O phase diagram with compositions previously studied in the literature, along with outlines of the two zoom-in regions studied here. (b) Compositions studied here along with boundaries for the P2, P3 and O3 regions. For all materials, XRD and electrochemistry were performed in high-throughput. Not shown are compositions in the entire phase diagram that were used to determine the phase stabilities in (c). The three * symbols in (c) indicate the three compositions studied more in depth later in* ***Figure 2.11****. (d) A map of sodium loss during synthesis. All samples were heated at 850 ℃. For ease of comparison to the rest of the literature, a secondary axis in turquoise is provided to indicate the Na content as x in* Na_xMO_2.

In 2012, Yabuuchi *et al.* sparked great interest in the Na-Fe-Mn-O materials with a P2-$Na_{0.67}Fe_{0.5}Mn_{0.5}O_2$ and a phase impure O3-$NaFe_{0.5}Mn_{0.5}O_2$ material with capacities of 190 mAh/g and 110 mAh/g, respectively. In that study, the P2 material shows higher capacity and better retention over the O3 material[11]. However, the reported $NaFe_{0.5}Mn_{0.5}O_2$ composition was not phase pure at the chosen synthesis temperature of 700 °C.[11, 29] Recently, Tripathi *et al*. reported a P3-material at a very nearby composition of $Na_{0.9}Fe_{0.5}Mn_{0.5}O_2$ by a solution-based synthesis. The P3 material showed a capacity of 155 mAh/g[30], which provides a novel high-sodium phase in the Na-Fe-Mn-O system. However, the structure obtained from the XRD refinement assumes a Mn oxidation state of +3.2 while the XAS data clearly shows Mn is far closer to 4+ (>3.8+) and the resulting structure shows characteristics that we deem unphysical as shown in **Figure S2.1**. The structure shows a strong asymmetry in the z-direction with very short and very long Na-O distances even though the overall structure is symmetric in the z-direction. Although the material is undeniably P3, we find irregularities in the reported structure and so we revisit it herein with our own XRD data. It is also relevant to note that the P3 structure is often considered to be the sub-stable phase to P2 material only obtained at lower sintering temperatures[31]. It is therefore highly relevant that in the current study all materials are obtained by the same synthesis and temperatures such that whether or not P2 or P3 is stabilized is a result of composition only.

Previously, a few pure phase O3 materials have also been made in this pseudoternary system as shown in **Figure 2.2a**. They show a high Fe content, and also a high Na content (x = 0.8~1), where Na ions are stabilized at octahedra sites but with a higher energy barrier and phase transition at high voltage, resulting in a relatively low capacity and fast deterioration during cycling[32]. There are other materials of interest within the Na-Fe-Mn-O system that warrant some attention here. O3-type α-$NaFeO_2$ demonstrated electrochemical activity with a reversible capacity of 80 mAh/g with Fe^{3+}/Fe^{4+} redox couple at higher voltage, which has not been found in Li-ion batteries[3]. As-prepared P2 and O3 Na-Fe-Mn-O materials, however, have all contained Fe^{3+}only, demonstrated by Mössbauer spectroscopy[16, 33] and XAS analysis[11, 17, 34]. For Na-Mn-O materials, due to Jahn-Teller distortion of Mn^{3+}, various structures can be synthesized and lie on a binary in our system. These are: α-$NaMnO_2$ (700 °C)[35], β-$NaMnO_2$ (950 °C)[26], P2-$Na_{0.67}MnO_2$ (620 °C)[27], P'2-$Na_{0.67}MnO_2$(1100 °C)[36], and tunnel-structure $Na_{0.44}MnO_2$ (850 °C)[37]. Among them, P2 and P'2 are the most attractive materials that can deliver high reversible capacities. P2-$Na_{0.67}MnO_2$ will start to transform into P'2 over 620 °C. P'2 is a distorted P2 phase stabilized with co-operative Jahn-Teller distortion (CJTD). Here, we synthesize all materials at 850 °C which favours the tunnel structure, and results in some co-existence between P2 and P'2 along the binary. It should be noted that even though Kumakura *et al*. reported P'2 can deliver 216 mAh/g for the first discharge capacity[36], the challenge in synthesizing them (e.g. quenching from above 1000 °C) makes them impractical. We therefore do not put much emphasis on these materials here except to determine the Fe content needed to suppress these structures forming.

Chemical stability against air/moisture is a major challenge for the practical application of layered oxides as cathodes for Na-ion batteries. P2 materials, in particular, are known to be unstable in air, reacting both with moisture and carbon dioxide: TOF-SIMS[38] and TGA-MS[39] have been used previously to analyze the species formed during reactions with air/moisture. Duffort *et al*. reported that the uptake of CO_2 in P2-$Na_{0.67}Fe_{0.5}Mn_{0.5}O_2$ can form carbonate and oxidize Mn into 4+, which leads to a hysteresis on the first charge.[39] However, due to the lack of systematic analysis, there are few satisfying methodologies developed to evaluate the composition impact on air/moisture stability. Here, we utilize high-throughput XPS to evaluate the stability of our materials and find good agreement with the mechanism established by Duffort *et al.* and extend the analysis to quantify the reactivity across the phase diagram.

A final aspect of the literature that is highly applicable to the current study is the recent development of the cationic potential approach. This method is an attempt to develop a predictive parameter that can determine whether or not a certain composition will take the P2 or O3 structures[40]. This study plotted the cationic potential on the transition metal layers vs the cationic potential on the sodium layer. The result was a clear straight line dividing the P2 and O3 materials for a high number of materials mined in the literature. However, no attempt was made to include P3 structures, such that herein we will extend the cationic potential approach to consider P2, O3 and P3 structures for the first time.

Clearly, the rational design of sodium cathode materials requires unravelling the complex relationship between metal compositions, structures, and the resulting battery properties. Herein, we utilize a high throughput (HTP) system to investigate the relationship amongst chemical compositions, crystal structures, electrochemical properties, and air/moisture stability. We utilize HTP methods developed by our group previously to make quality Na-Fe-Mn-O materials on the 3-5 mg scale and demonstrated high-quality HTP electrochemistry obtained from these materials.[41] **Figure 2.2** shows that there are significant previously ignored portions of the phase diagram worthy of careful study as potential battery materials. We therefore show careful HTP characterization with XRD, CV and XPS across the entire system. In particular, we introduce high-throughput XPS as a means to quantify air/moisture instability in these materials and find a strong compositional dependence. This serves as the first systematic study of an entire pseudoternary system of importance to Na-ion battery cathodes.

2.3 Experimental methods

High-throughput approaches have been utilized for all synthesis and characterization herein, as shown schematically in **Figure 2.3**. First, a sol-gel method was adopted for the synthesis to achieve combinatorial NFMO materials, as described in detail in ref. [41]. Specifically, the samples were made by first dispensing varying volumes of 2M solutions of $NaNO_3$, $Fe(NO_3)_3$, and $Mn(NO_3)_2$ (all from Sigma-Aldrich) onto an 8×8 section of a standard 96-well plate with a total volume of 49 μL according to target stoichiometry (**Figure 2.3a**). Citric acid (2M) was then added as a chelating agent in a 1:1 molar ratio to the total metal cations. Next, the gelation process was performed at 65 °C for 2 days to form homogeneous precursor gels through strong bonding from carboxylic groups. The resulting 8×8 set of samples were crushed and transferred onto an alumina plate equipped with an 8×8 aluminum smokestack as a combustion chamber to avoid cross-contamination during the off-gassing of citrate bi-products during the initial stages of heating (**Figure 2.3b**). The samples were heated at 400 °C for 2 hr (heating rate: 2 °C/min) to decompose the nitrates and the citric acid in air. After lifting and removing the smokestack, the samples were further calcinated at 850 °C for 12 hr in ambient air (heating and cooling rates were 5 °C/min). The final products are illustrated in **Figure 2.3c**. In total, 448 samples, each weighing about 3-5 mg, were synthesized through the above high-throughput method for further characterization, the compositions are shown in **Figures 2.2b,c.**

All samples were first characterized using high-throughput XRD. The XRD measurements were performed in the transmission mode using a Panalytical Empyrean diffractometer with a Mo target (60 kV, 40 mA) and GalaPIX area detector (**Figure 2.3d**). For Mo Kα radiation ($\lambda = 0.70926$ Å for $K\alpha_1$), a scattering angle range of 4-30° was selected (this corresponds to approximately 10-70° for Cu radiation). For all samples, the main peak intensity was well over 1000 counts for the 10 min scans, demonstrating that the data is suitable for Rietveld refinements. Each scan took <10 min and an entire batch of 64 samples took <10 h. For ease of comparison to the rest of the literature, all patterns shown herein have had the Mo-$K\alpha_2$ peaks stripped, and scattering angles have been converted to those that would be obtained with Cu-Kα_1 (λ = 1.54051 Å) as described in detail in ref. [42]. All 448 samples were tested with XRD, and the resulting spectra were analyzed to map the phase stabilities. Home-written software was used to perform Pawley fits on all spectra in order to extract lattice parameters. To help answer some confusion in the literature regarding the structure of the P3 phase, we also performed Rietveld fits using the software Rietica on a single P3 material, $Na_{0.9}Mn_{0.5}Fe_{0.5}O_2$.

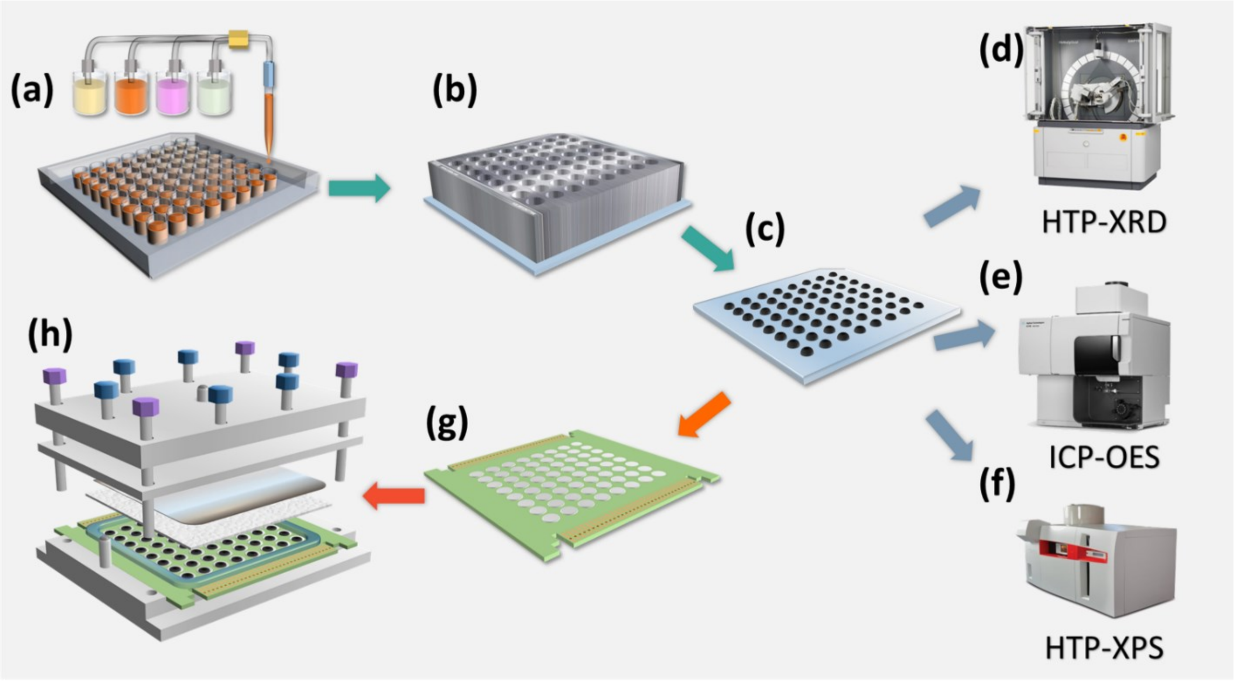

Figure 2.3 *A schematic of the experimental approach used in the current study. Precursor solutions are first added to a standard well plate (a), the samples are then dried and heated to 400 ℃ together with a smokestack to prevent mixing (b), then sintered at high temperature (c) before high-throughput characterization: (d) XRD, (e) ICP-OES , (f) HTP-XPS, and (g, h) electrochemistry. All high-throughput characterization is performed on the same 4 mg samples.*

After XRD, 2 mg from each sample was then utilized for electrochemical testing. Combinatorial cells with 8×8 samples as cathode materials were used to test electrochemical properties as described in detail in ref. [41] [42] [43]. Firstly, a custom-designed printed circuit board (PCB, Optima

Tech) with 64 aluminum covered pads was used as illustrated in **Figure 2.3g**. The composite cathode electrodes had 2 mg of active material and approximately 20 wt. % carbon black and 20 wt. % polyvinylidene fluoride (PVDF), both of which were added by drop-casting an N-methyl-2-pyrrolidone (NMP) solution. The PCB and electrodes were dried at 80 °C overnight to evaporate NMP. The assembly of the combinatorial cell was performed in an argon-filled glovebox. The electrolyte was 1M sodium perchlorate in propylene carbonate with 2 wt. % fluoroethylene carbonate (FEC). Na metal foil was used as the anode with a GF/D glass microfiber prefilter as a separator. The cell was then sealed using a 3M double-sided sealing tape as described in ref. [43]. Cyclic voltammetry (CV) was performed with the voltage range 1.5 to 4.3 V vs Na/Na^+ at a scan rate of 0.1 V/h on a lab-built high-throughput electrochemical system based on ref. [44], which utilizes a quad voltage source (Keithley 213) and a multimeter with a multiplexer (Keithley 2750). 64 CVs were performed simultaneously. Data were processed to extract average voltages, and specific capacities over the multiple cycles performed. After a few cycles, a few of the cells were also cycled in the range 1.5 – 4.6 V vs. Na/Na^+ (with 4.3-4.6 V being swept over 10 h) to determine if there is any activation at high potentials as obtained in Li-rich layered oxides at these potentials.

In order to quantify how much sodium was lost during synthesis throughout the phase diagram, certain samples were selected for inductively coupled plasma-optical emission spectrometry (ICP-OES). Samples were first dissolved by Aqua Regia in a 96-well plate overnight and diluted by deionized water. Blank control solutions were also prepared as a background to make sure there was no Na/Fe/Mn contamination source from the well plate. Agilent Technologies 5100 ICP-OES associated with the autosampler was used to analyze elemental compositions of combinatorial samples (**Figure 2.3e**). With the help of the autosampler, the ICP-OES can run automatically with a throughput of about 20 samples per hour making it ideal for this study.

In order to obtain a measure of the instability of the NFMO samples in air, high-throughput X-ray photoemission spectroscopy (XPS) was performed using a Kratos Axis Nova spectrometer using a monochromatic Al K(alpha) source (15mA, 15kV) illustrated in **Figure 2.3f**. The instrument work function was calibrated to give binding energy (BE) of 83.96 eV for the Au 4f7/2 line for metallic gold and the spectrometer dispersion was adjusted to give a BE of 932.62 eV for the Cu 2p3/2 line of metallic copper. The Kratos charge neutralizer system was used on all specimens. Survey scans were carried out with an analysis area of 300×700 microns and a pass energy of 160 eV. High-resolution scans were also performed for the Na 1s, Fe 2p, Mn 3s, and C 1s regions with a pass energy of 20/40 eV. Spectra have been charge-corrected to the mainline of the carbon 1s spectrum (adventitious carbon) set to 284.8 eV. Peak fitting was performed using the ESCApe software. Shirley backgrounds were applied to all *2p* spectral areas with components fitted with constrained (Gaussian 70%–Lorentzian 30%) peaks. Survey scans were acquired in 120 s, while high-resolution spectra were acquired in various times (30 - 720 s) depending on the count rate. Quantification used relative sensitivity factors developed by Cant *et al.*[45]. The instrument is suited for high-throughput analysis as it is equipped with three sample holders each capable of mounting >100 samples.

It is important to note that all of the characterizations were performed on the *same* samples. After XRD, 2 mg were removed for electrochemical testing, leaving enough left for ICP-OES and/or XPS for the samples selected for those measurements.

2.4 Results and Discussion

2.4.1 Structural phase diagram

To survey the phase distribution for Na-Fe-Mn-O pseudo ternary system, we synthesized 448 samples to both map out the entire Gibbs' triangle and to also focus in on the materials of highest interest for Na-ion batteries, as indicated in **Figure 2.2c**. The reproducibility of this high-throughput system is excellent as demonstrated on these materials in ref. [42]. Seven solid-solution regions were identified in the phase diagram: Mn_2O_3 (ICSD 159865), Fe_2O_3 (ICSD 154190), $Na_{0.44}MnO_2$ (ICSD 182617), β-$FeNaO_2$ (ICSD 158330), and three layered oxide phases of interest for Na-ion cathodes: P2, P3, and O3 phases. Due to the high volatility of sodium oxides, no sample was obtained for the gray region shown in **Figure 2.2c** near the sodium corner. The rest of the Gibbs' triangle is made up of multi-phase materials. The emphasis herein is on the layered oxides, such that a large number of samples were prepared in this region as shown in **Figure 2.2b** where 184 target compositions were made (120 for Zoom-in 1 and 64 for Zoom-in 2) with 256 total samples (72 samples were triplicates to check reproducibility, which was found to be excellent as shown in ref. [42]). In total, 256 XRD patterns were collected from samples in the zoom-in regions; all of which were visually compared to the reference patterns to identify phases present and subsequently fit using Pawley refinement. **Figures 2.4** and **S2.5** show representative XRD patterns along with their fits. **Figure 2.4b** shows the progression of the XRD patterns within the P2 single-phase region, illustrated by the red dashed line showing the shifting in peak position with composition. By contrast, **Figures 2.4c,d and S2.5** all demonstrate the progression of the XRD patterns through co-existence regions wherein secondary phases appear, and grow with composition. All XRD patterns are fully consistent with the phase stabilities shown in **Figure 2.2**.

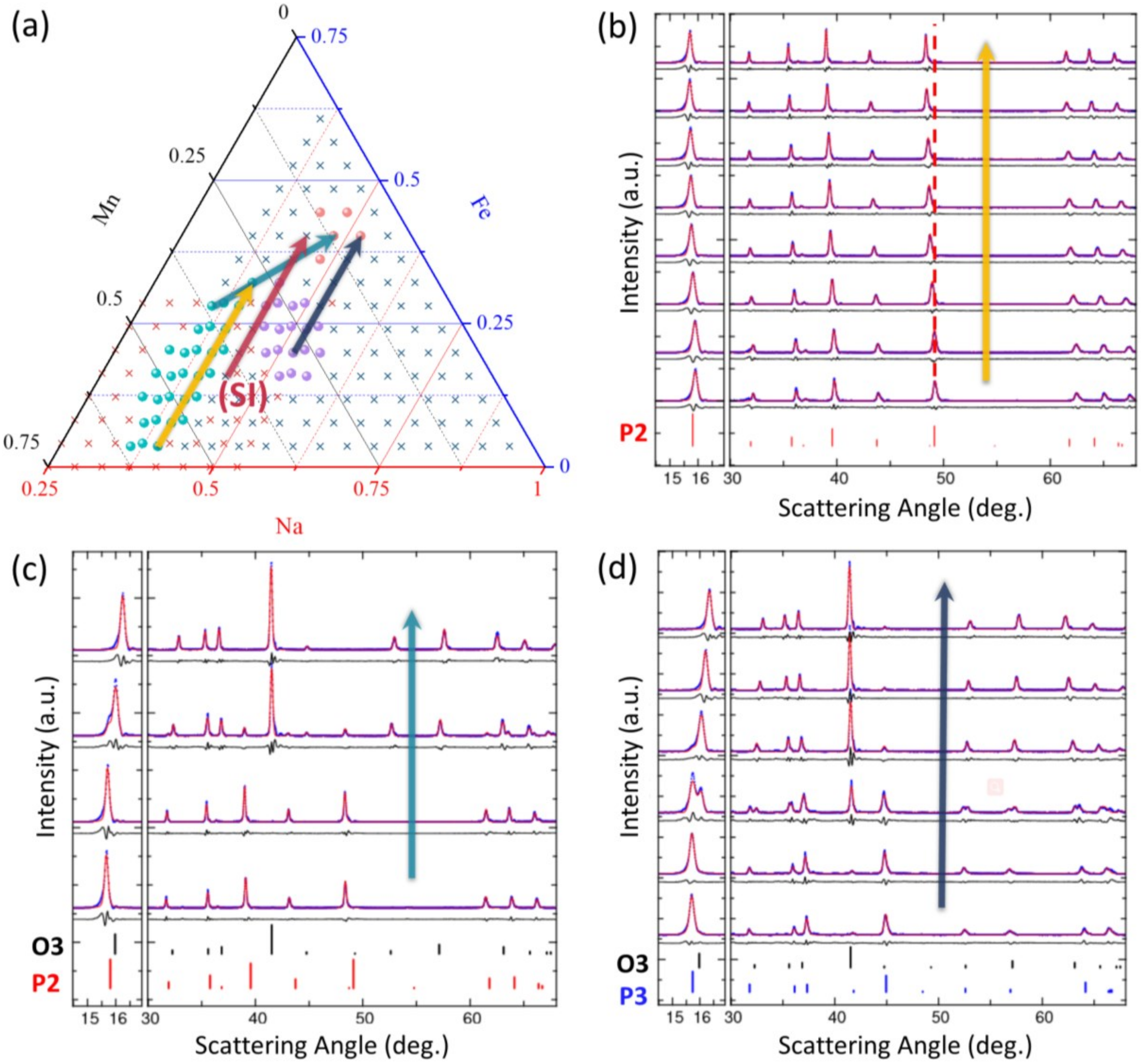

Figure 2.4 *XRD patterns for P2, P3 and O3 structures to understand the phase evolution with chemical compositions. The four arrows in (a) indicate the compositions shown in b-d and* ***Figure S2.5****. (b)-(d) XRD patterns (blue points) along with results of Pawley fits (red) and difference plots black. Relevant reference patterns are shown at the bottom of each XRD stack. In (b), the vertical red dashed line is a guide to the eye to illustrate shifting peak positions with composition within the solid solution.*

The dense sampling used here enabled the precise determination of the boundaries to each single-phase region of interest. In total, 29 P2, 18 P3, and 5 O3 single phases are identified based on the

XRD patterns. This study, therefore, represents the first investigation of the rich chemistry permitted in the Na-Fe-Mn-O system where only a few single-phase materials had been made previously as discussed in the introduction. The three solid-solution regions of greatest interest here (P2, P3, and O3) are shown in **Figure 2.2b** on the Gibbs' triangle and illustrate the thermodynamic-stable regions for each phase at 850 °C following by slow cooling. In detail, the P2 solid solution takes an ellipse shape over a large range in Fe:Mn ratio (0.05-0.55 for Fe/(Fe+Mn)). To help with comparison to other literature, we present this solid solution region as a series of sodium solubility windows in **Figure 2.6a** to illustrate the significant variations in Na solubility as a function of the Fe content (Fe/(Fe+Mn)) after taking Na-loss into account, and this applies to each of the 3 phases. The largest Na solubility window in the P2 structures is seen in the center of the ellipse where the sodium content varies from $x = 0.49$ to 0.71 for Na_xMO_2. Comparison to results from other literature[46-50] shows that larger ranges in Na content have been enabled with substitutions such as Mg, Ni and Li. Further study following this project will involve further substitutions into the best NFMO structures obtained here.

To further put these solid solutions into context, we first note that it is well established in the literature that iron will take the Fe^{3+} state under these conditions and that Mn can occupy either the 3+ or 4+ state in the P2 materials. We therefore seek to understand what is the maximum composition range of the form $\mathrm{Na}_x\mathrm{Fe}_y^{3+}\mathrm{Mn}_{(1-y)}^{3,4+}\mathrm{O}_2$ (i.e. we expect no vacancies on the transition metal layers). Charge balancing implies $\mathrm{Na}_x[\mathrm{Fe}_y^{3+}\mathrm{Mn}_{(x-y)}^{3+}]\mathrm{Mn}_{(1-x)}^{4+}\mathrm{O}_2$, which represents a triangular region in the Gibbs' triangle with vertices at Mn_2O_3, $NaMnO_2$ and $NaFeO_2$ as shown in **Figure S2.6**. Importantly, after accounting for Na loss during synthesis (**Figure 2.2d and S2.6**), all P2, P3 and O3 samples lie within the region defined by this formula. That is, all layered oxides made here are in principle consistent with fully occupied transition metal layers, and Fe^{3+} along with mixed $Mn^{3,4+}$ balancing the charge, although we find this does not strictly hold for the P3 structures as discussed further below.

Interestingly, although the structures are related, there is a miscibility gap between the P2 and P'2 $Na_{0.67}MnO_2$ phases. Below the bottom of the P2 ellipse, P2 with trace P'2 is observed instead of the pure P2. The reason for this is explained by the behaviour of the P2 material $Na_{0.67}MnO_2$ that starts to transform into P'2 at temperatures above 620 °C as discussed in the introduction. According to our phase diagram, as little as 5% of Fe (i.e. $Na_xFe_{0.05}Mn_{0.95}O_2$) is sufficient to suppress the Jahn-Teller distortion and stabilize the P2 structure at moderate temperatures without quenching.

It is also important to note that a great deal of variety is permitted in the structures within the triangular region defined by Fe^{3+} and $Mn^{3,4+}$. In particular, the P3 structure requires some attention as it has only recently been discovered in the Na-Fe-Mn-O system. Tripathi *et al*. reported P3-$Na_{0.9}Fe_{0.5}Mn_{0.5}O_2$ (implying an oxidation state of 3.2 for Mn)[30]. However, their XANES data clearly showed that Mn was far closer to the 4+ state, implying that the actual stoichiometry was closer to $Na_{0.82}Fe_{0.45}Mn_{0.45}O_2$. We have therefore performed Rietveld refinement on a P3 sample at this same composition, confirmed with ICP-OES. We consider 3 models: (1) $Na_{0.9}Fe_{0.5}Mn_{0.5}O_2$ as proposed by Tripathi *et al.,* (2) $Na_{0.82}(Fe_{0.45}Mn_{0.45}\square_{0.1})O_2$ (i.e. Mn^{4+} with vacancies on the TM layer), and (3) $Na_{0.72}[Na_{0.1}Fe_{0.45}Mn_{0.45}]O_2$ (*i.e.* Mn^{4+} with no vacancies on the TM layer). **Figure S2.4** shows the results of fitting with each of these models and clearly shows that model 3 yields the smallest residual in the XRD pattern and also gives the best quality parameters for the fits, however the differences between models 2 and 3 are small given that Na scatters X-rays weakly. We therefore conclude that Mn in the P3 phase is in a high oxidation state (near 4+) and that some Na may occupy the TM layer thereby lowering the Na content on the Na layer closer to the 2/3 seen in other P3 materials in the literature [51-54]. The occupation of Na on the transition metal layer will be explored in a follow-up study utilizing neutron powder diffraction. It is also significant to emphasize that the XRD patterns leave no doubt that the stable phase near the metal composition $NaFe_{1/2}Mn_{1/2}$ is in fact P3 and not O3 as originally reported in ref. [11] where Yabuuchi et al. reported a phase impure O3-$NaFe_{0.5}Mn_{0.5}O_2$ synthesized at 700 °C. The impurity implies that the mixing in traditional solid state synthesis was insufficient for the materials to reach equilibrium at the temperatures used and thus the result was an O3 material co-existing with another phase (probably a P3 material based on our phase diagram though it is difficult to extrapolate to lower temperatures). In this work, however, with the help of well mixed metal-ions via the sol-gel method, we obtained a pure phase at this composition and have confirmed the findings of Tripathi *et al*. that a pure P3 material is the phase stabilized at high temperatures at this composition.

Regarding the O3 single-phase materials, the thermodynamically stable region was found with Fe-rich content as shown in **Figure 2.2**. Delmas *et al.* [23] have previously obtained pure O3-$Na_{0.82}Fe_{2/3}Mn_{1/3}O_2$ with high Fe content but failed with Fe/Mn=1:1 ratio in complete agreement with our phase diagram. Nonetheless, the region where O3 materials can be stabilized is relatively small in the Na-Fe-Mn-O system. It should also be briefly mentioned that the fact we obtained β-$NaFeO_2$ (orthorhombic) instead of α-$NaFeO_2$ (O3, hexagonal) on the binary is expected given that α-$NaFeO_2$ is a low-temperature phase, whereas β-$NaFeO_2$ is stable above 750 °C [55]. Therefore, this again creates a small miscibility gap between the O3 and β-$NaFeO_2$ phase and also demonstrates that the addition of a small amount of Mn is needed to stabilize the α-$NaFeO_2$ (O3) phase over the β-$FeNaO_2$ phase at high temperatures.

Next, we examine the changes in structure with composition within the solid solutions by first looking at the lattice parameters plotted in **Figures 2.5 and S2.3**. Since all of the P2, P3, and O3 structures were fit with a hexagonal structure, the *a* parameter can all be compared easily, however the *c* parameter includes 3 slabs for P3 and O3 and only 2 for P2, so we plot the inter-slab distance (c/2 for P2 and c/3 for P3&O3) in **Figure 2.5a and S2.3a**.

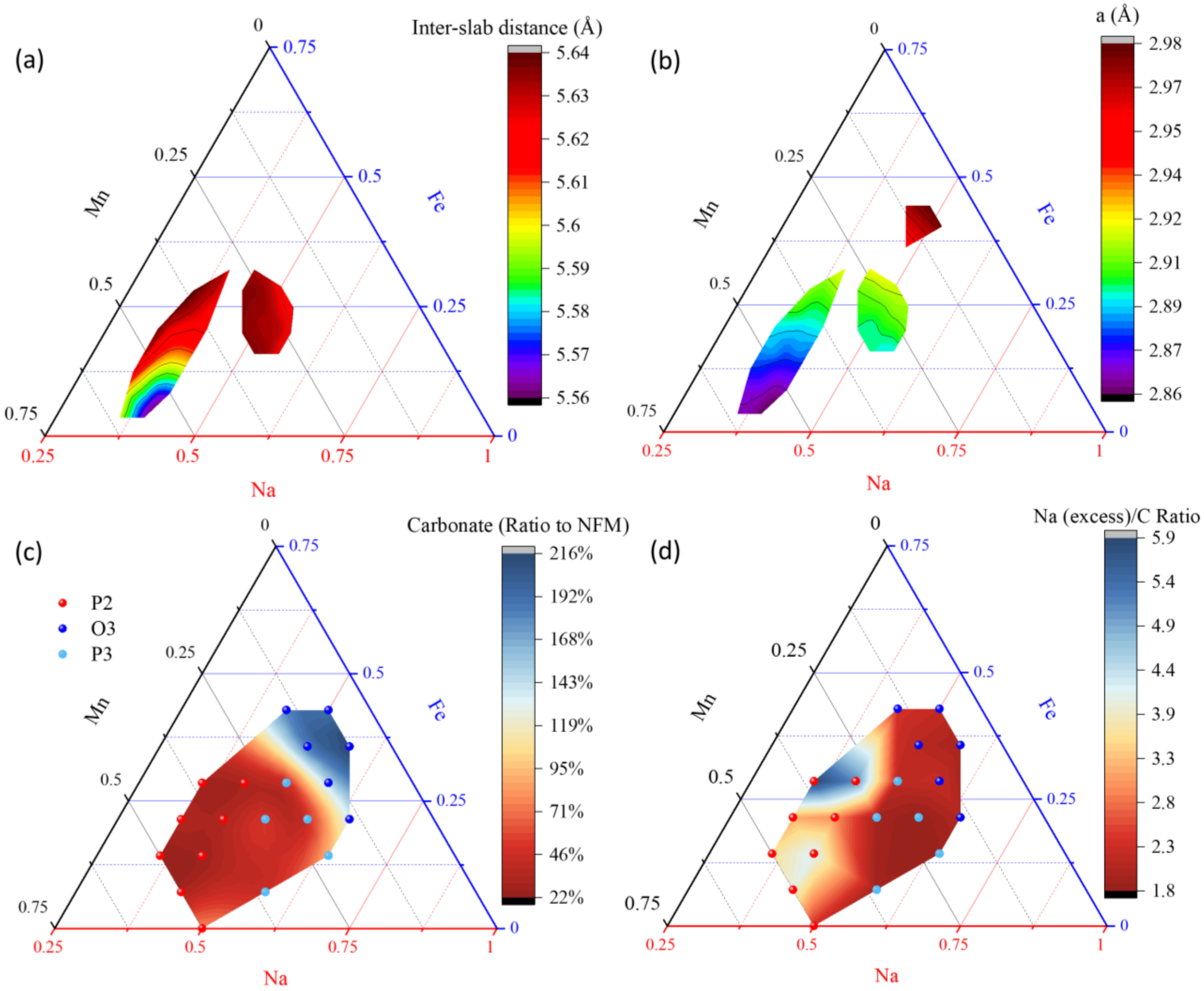

Figure 2.5 *(a,b) Lattice parameter maps for the P2, P3 and O3 (a only) phases. (c) Results of quantifying XPS results on samples aged for 6 months to determine both the carbonate to NFMO ratio, and (d) the excess Na seen at the surface to the carbonate ratio. P2, O3 and P3 labelled here are the phase-dominated samples. While (a,b) show the evolution of the structures, (c,d) shows the relative stabilities with air (low carbonate and low excess sodium indicate stability with* CO_2 *and moisture, respectively).*

Usefully, as was the case for Li layered oxides [56], the contours for the two lattice parameters do not run in the same direction such that a set of lattice parameters may be used to identify a single composition using the contours. The contours also show that the inter-slab distance is correlated strongly to the sodium content: a higher sodium content has more Na-O bonding and shrinks the lattice in the *c* direction. Moreover, **Figures 2.5a,b** also show that both *a* and *c* increase in the P2 materials as Fe content increases, which is not unexpected given that Fe^{3+} has a large ionic radius (0.645 Å), especially compared to the smaller Mn^{4+} (0.53Å).

As a final point of interest regarding the structures, we use our results to further refine the cationic potential approach recently used to predict whether given compositions will take the P2 or O3 structure [40]. Although that study did not consider P3 structures, we extend the calculations to these structures here. We therefore use the same approach as in ref. [40] here (see **Figure S2.7** for detailed calculation) and find that our results are dependent on what oxidation state we assign to Mn (Fe is maintained as 3+). **Figure 2.6b** shows the result when we assume that the P2 and O3 structures have Mn in either the 3 or 4+ state and no vacancies on the TM layer, while for P3 we assume that Mn is in the 4+ and some Na goes to the TM layer to yield full occupancy of these layers as discussed in regards to our XRD data above. Interestingly, the $Na_x[Fe^{3+}_y Mn^{3+}_{(x-y)}]Mn^{4+}_{(1-x)}O_2$triangle discussed previously collapses to a parabola in the cationic potential plot (shown as 'fitted line' in **Figure 2.6b**), such that the P2 and O3 materials lie on this line by definition. The P3 materials lie very close to both this line and the dividing line between P2 and O3 established in ref. [40], and interestingly they lie on the P2 side of the line. However, **Figure S2.7** shows that they lie on the O3 side of the line if we assume (incorrectly) that Mn can take predominantly the 3+ state in the P3 structure. This illustrates that although the cationic potential approach is useful to put the large body of work into context, it is not yet fully predictive as it takes the experimental determination of all oxidation states to correctly predict the structure based on cationic potential. It is also important to recognize that the space occupied here by P3 materials are occupied by other P2 materials in ref. [40] such that the cationic potential approach does not seem to distinguish P2 from P3 structures. By contrast, the calculated dividing sodium content x = 0.72 illustrated in **Figure 2.6b** can successfully separate the P2 and O3 materials, where the maximum sodium content obtained in this study is 0.71.

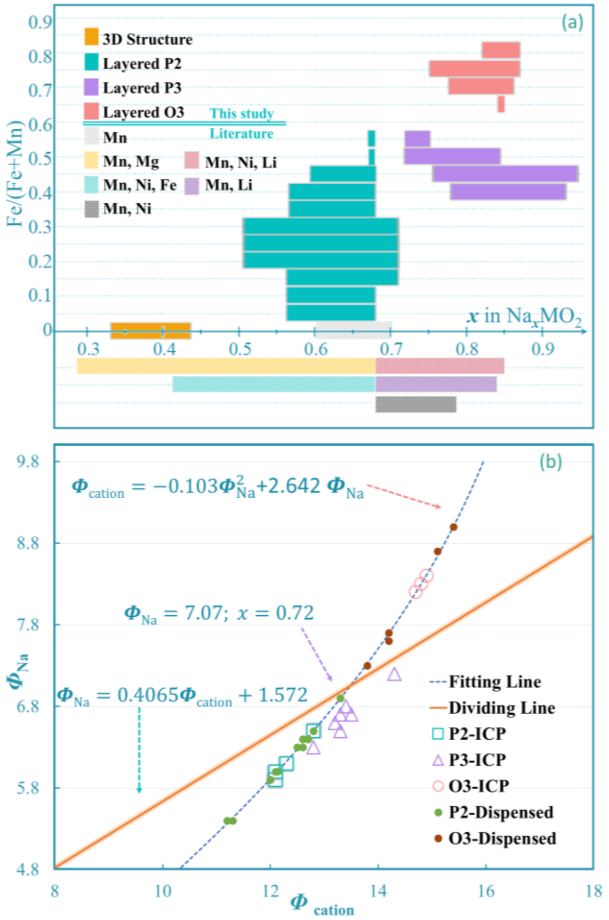

Figure 2.6 *(a) The solid solution regions are expressed as a series of sodium-solubility windows at various Fe:Mn ratios after taking Na-loss into account. Also shown are results from the literature[46-50]. (b) Results of cationic potential analysis as described in ref. [40]. The fitted line is described in the text, while the dividing line is defined in ref. [40] where it divides the P2 and O3 phases. For P3 materials that lie very near the boundary, only samples for which there was ICP data are shown so that exact compositions are used.*

2.4.2 Stability in air

As discussed in the introduction, the electrochemical performance of NFMO cathodes is significantly limited by the material stability in air, and the poor stability of the P2 materials in particular are currently preventing these materials from being commercialized. Figure S14 shows that samples obtained here for each of the three phases (P2, P3 and O3) show no significant changes in the XRD patterns after 6 months storage in dry air. We therefore utilize high-throughput XPS as shown in **Figures 2.7 and S2.8-S2.9** in order to systematically screen surface stability in air across the phase diagram and also determine oxidation states of Fe and Mn (though it is important to note that this is at the surface of particles only and after 6 months of exposure to air). We first performed survey scans to confirm the presence of Na, Fe, Mn, O and C; then high-resolution scans to quantify both the amounts of each of Na, Fe and Mn and also quantify the amounts of carbonate present. All peaks are fit for all samples, and labels identify them in **Figure S2.8**.

Systematically, we identify Fe in the 3+ state as determined by the Fe $2p_{3/2}$ peak position of ~710.5 eV with a satellite peak splitting of ~ 8.4 eV [57] consistent with NFMO materials from the literature. For Mn $2p_{3/2}$, all spectra are at similar locations at ~ 642.0 eV except for $FeMnO_3$ at 641.5 eV, where the Mn in $FeMnO_3$ should be 3+ given that Fe is in the 3+ state. Another way to analyze the Mn oxidation state is by using the splitting between the two Mn *3s* peaks. $FeMnO_3$ shows 5.6 eV corresponding to 3+ (as per ref. [58]). For all NFMO layered oxides studied here, the Mn *3s* splitting energies were in the range 4.6 ~ 4.7 eV, indicating we have Mn^{4+}. Again, as discussed in the introduction, this is consistent with Mn at the surface of particles being systematically oxidized to 4+ during reactions with moist air as discussed in ref. [39].

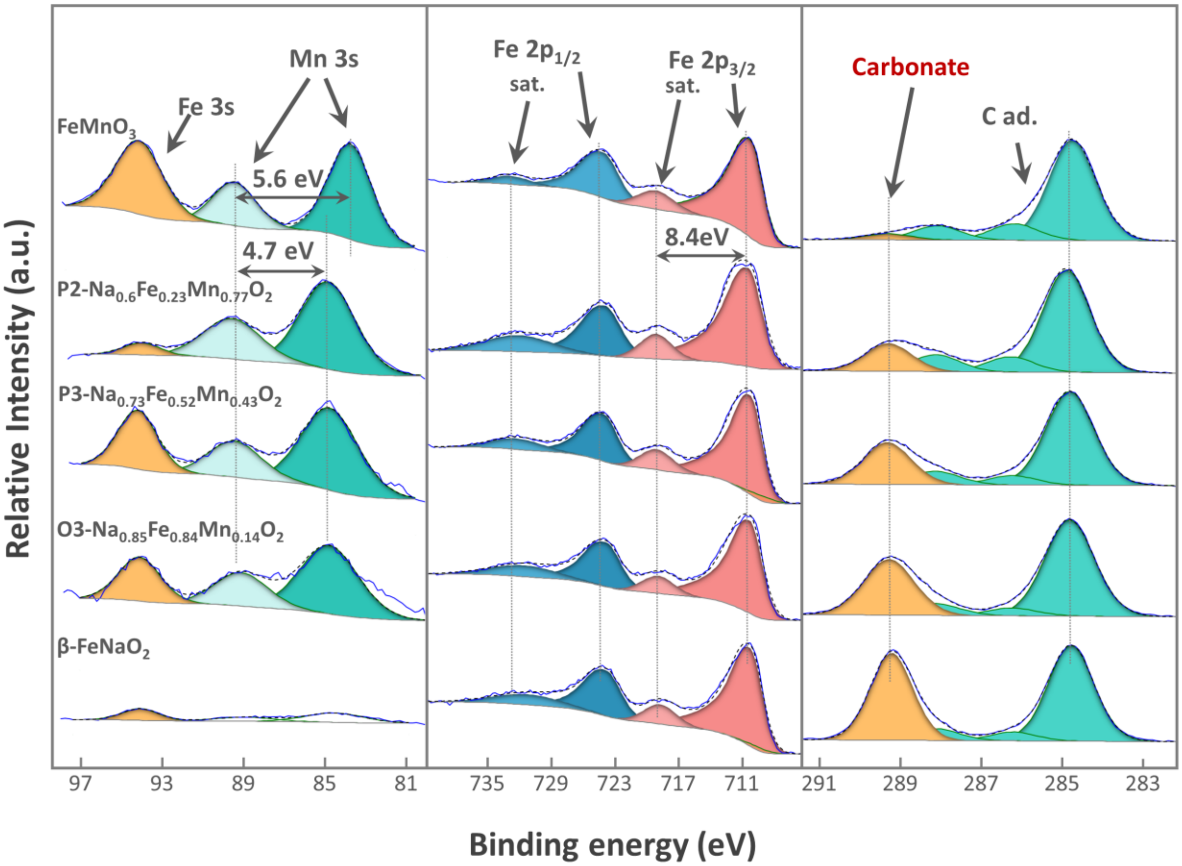

Figure 2.7 *A partial set of XPS results of Mn 3s, Fe 2p and C1s for key samples. Of highest note here the yellow peak in the C 1s spectra represents carbonates.*

Although surface oxidation states are of interest, the main purpose of using XPS here is to quantify surface reactivity in NFMO materials as a function of composition. We therefore use XPS to determine the relative atomic concentrations on material's surface. First, the Fe/Mn molar ratio is investigated and is found to systematically be close to the dispensed values (within 5% on average). Thus, the Fe/Mn ratio on the particle surface appears to match that of the bulk. By contrast, the Na *1s* peak at ~1071 eV, shown in **Figure S2.9**, was consistently far larger than expected. Interestingly, the sodium content from the XPS quantification is systematically well above that obtained in ICP analysis and even well above the dispensed values, as shown in **Figure S2.3** and this deviation is well above the precision of the instrument. Based on the literature discussed in the introduction, we consider two mechanisms that can lead to an excess of sodium at the surface of particles: **(1)** sodium is extracted from the bulk by moisture to form NaOH, **(2)** sodium reacts with carbon dioxide in air to form Na_2CO_3. In both cases the sodium phase formed at the surface will absorb electrons, shielding the NFMO cores such that the Na content seen in the XPS is disproportionally high.

The C *1s* peaks are therefore used to quantify the amount of carbonate formed on the surface. Two surface chemistries can be found for C *1s*: the lower BE peaks (285-288 eV) are from adventitious carbon and are typically found in this relative ratio on almost all air-exposed samples. The low binding energy peak (C-C/C-H) is used as a charge reference. The peak near 289 eV indicates carbonates are present. The ratio between carbonate and NFM (Na+Fe+Mn) is calculated and presented in **Figure 2.5c**. Importantly, the molar fraction of carbonate present varies from 22 to 216% clearly showing the dramatic impact that composition has on the surface reactivity. The carbonate content also shows a clear trend with composition across the 3 structures of interest here. For P2 and P3, less carbonate is found in comparison to O3 with an average of 35% and 55%, respectively. Thus, they appear more stable with air than the more Fe-rich O3 structures that have an average of 170% carbonate.

The ratio between the excess sodium and the carbonate is therefore expected to be 2.0 in mechanism **(2)** (reaction with carbon dioxide) above, and take a higher value when mechanism 1 (reaction with moisture) plays an important role. **Figure 2.5d** shows the excess Na to carbon ratio is closest to 2 in the O3 and P3 materials, while considerably higher for P2 materials, which indicates P2 is prone to reactivity with water. It is also important to note that P2 materials with higher Mn content (e.g. $Na_xMn_{3/4}Fe_{1/4}O_2$) show better stability against moisture than P2 materials with higher Fe content (e.g. the most heavily studied P2 material $Na_{2/3}Mn_{1/2}Fe_{1/2}O_2$). This will prove to be highly significant in discussing the electrochemical performances below.

Given that this approach to quantify stability in air is new, we use two well-known materials in the literature to demonstrate its effectiveness: β-$NaFeO_2$ and $FeMnO_3$ that show carbonate contents of 220% and 1.5%, respectively. According to the literature, β-$NaFeO_2$ is quite reactive with CO_2 and this material is even used for CO_2 capture[59], while $FeMnO_3$ is quite stable under air and moisture[60]. These two materials show dramatically different air stability from our quantified XPS results and illustrate that this method is accurate in quantifying stability in air. Furthermore, the excess Na to carbonate ratio for β-$NaFeO_2$ was 1.92 which is very close to the expected value of 2 for this material given that it is known to form Na_2CO_3 when reacting with air [38]. We therefore consider using the excess sodium content and the carbonate content together as a valid way to quantify both stability against moisture and carbon dioxide. Again, of greatest importance to this study, P2 materials do not all show the same instability against moisture as that seen in $Na_{2/3}Mn_{1/2}Fe_{1/2}O_2$, and P3 materials show improved stability both in air and moisture. Therefore, the air/moisture stability and the mechanism of degeneration are substantially determined by the structure and compositions of the layered oxides and not all NFMO materials are equally prone to air sensitivity.

2.4.3 Battery performance

To investigate the electrochemical properties across all NFMO compositions, high-throughput cyclic voltammetry (CV) was performed for all samples in both zoom-in 1 and 2 (as per **Figure 2.2b**). The reproducibility of the high throughput electrochemistry on these Na-ion cathodes is excellent with standard deviations <1% for average voltages and 7.6 % for discharge capacities as demonstrated in ref. [41]. For zoom-in 1, we first cycled between 1.5 and 4.3 V at 0.1 V/h for 3 cycles then cycled up to 4.6 V. We found no signs of extra capacity when cycled up to 4.6 V, so we focus here on the cutoff to 4.3 V only. For zoom-in 2, performed after zoom-in 1, we cycle solely between 1.5 and 4.3 V for 15 cycles. We show the first 1.5 cycles for zoom-in 2 in **Figures 2.8 and 2.9** (this is the same data, **Figure 2.9** shows the voltage curves calculated from the CVs). The shaded regions highlight the single-phase materials, and we will discuss these in sequence below.

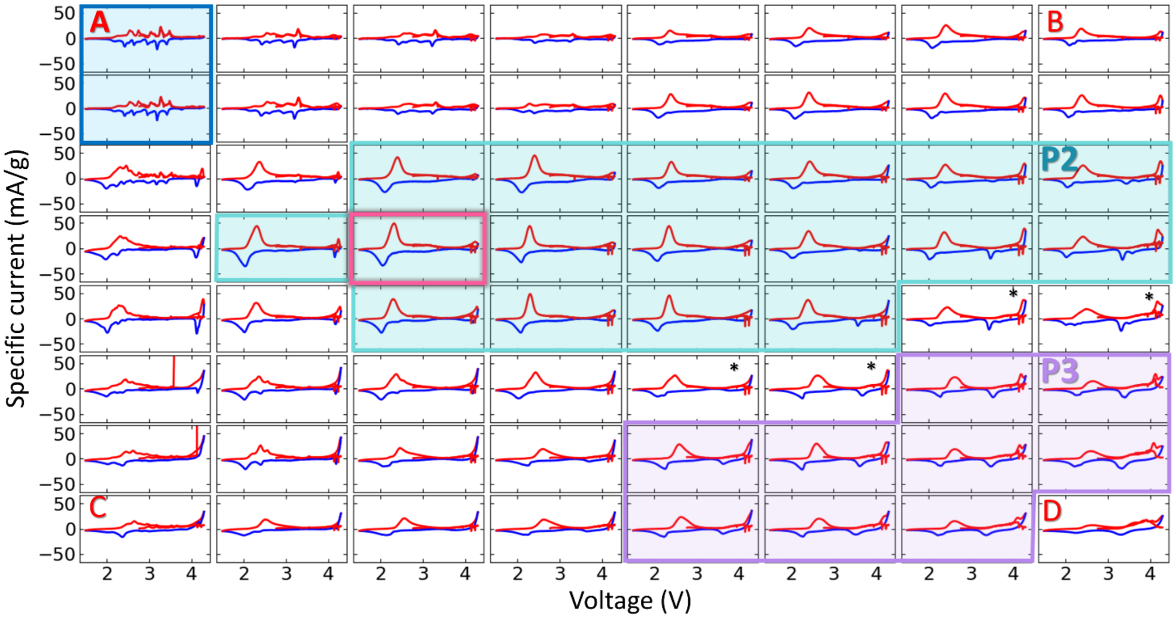

Figure 2.8 *The first 1.5 cycles of the combinatorial cell made in region zoom-in 2. The four corners ABCD are shown in the phase diagram in* ***Figure 2a****. Specifically, A has the most Mn, while A → B represents increasing Fe, and A→C represents increasing Na. Each of the single phase regions are highlighted : tunnel structure (blue), P2 (turquoise), and P3 (purple). The highest capacity material of all samples is in the pink rectangle and discussed extensively in the text.*

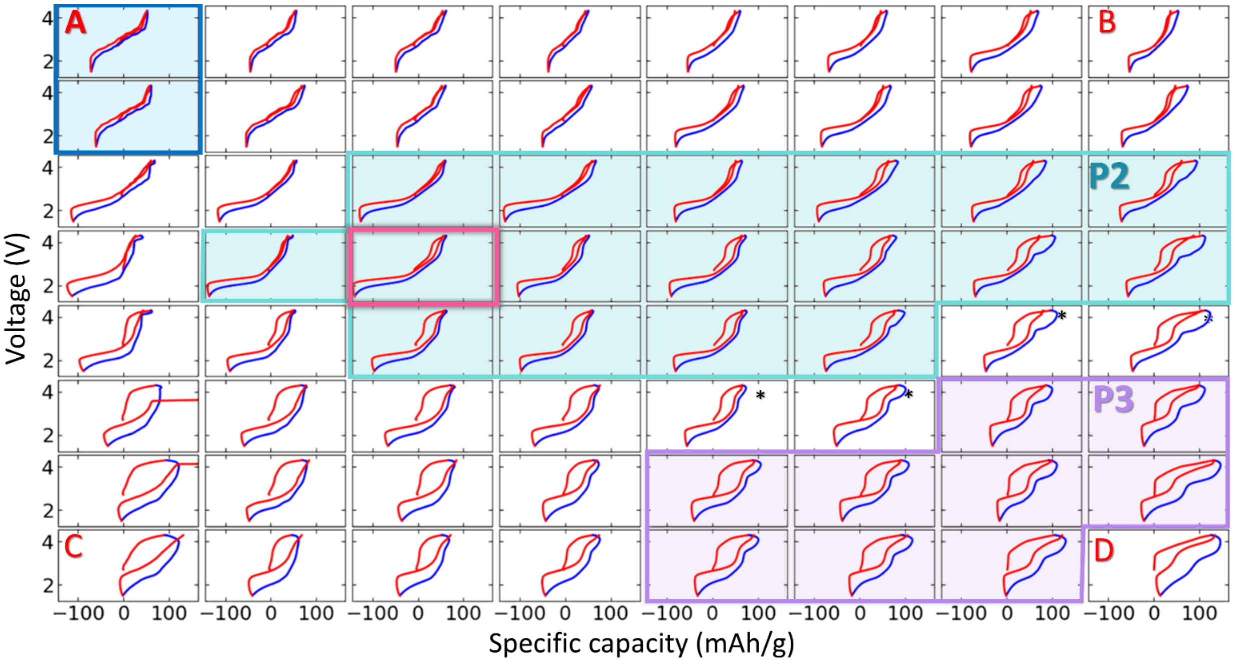

***Figure 2.9** The first 1.5 cycles in zoom-in 2 shown as voltage curves. The four corners ABCD are labelled in **Figure 2.2a** and the same colour coding is used as in **Figure 2.8** to highlight the various pure phases present.*

First, the two tunnel-structure Na_xMnO_2 materials (blue) show a high number of peaks in the CVs corresponding to the well-known high number of phase transitions during electrochemical cycling in $Na_{0.44}MnO_2$.[67] These transitions are all systematically suppressed in both the P2 and P3 structures; this suppression of transitions is typically associated with an increase in cycling stability. The first cycle discharge capacities of these two materials are 125 and 123 mAh/g, with capacity retentions of 88% and 89% after 15 cycles respectively, which shows an exceptional electrochemical performance with very close to the ref. [61] and the theoretical discharge capacity of 121 mAh/g calculated by Dai *et al* [62]. This result demonstrates HTP synthesis with sol-gel method provides quality materials and good electrochemical performance consistent with that obtained in the literature (as also demonstrated in ref. [41]).

In **Figures 2.8 and 2.9**, the single-phase P2 (turquoise) and P3 (purple) materials are highlighted, while the stars in the panels indicate P2/P3 biphasic materials. Two main redox peaks are seen in the CVs: **(1)** 2.1 V (discharge) and 2.4 V (charge) for Mn^{3+}/Mn^{4+} which is activated by discharge to below the open-circuit voltage of 2.7 V and **(2)** 3.2 V (discharge) and 4.0 V (charge) for Fe^{3+}/Fe^{4+} redox activity. These peak attributions are well established in the literature[63, 64]. For Mn-rich P2 samples, we indeed predominantly see the Mn^{3+}/Mn^{4+} peak, while the Fe^{3+}/Fe^{4+} redox peak grows with more Fe content. Interestingly, at the boundary between the P2 and P3 regions (marked by *), CVs are consistent with being linear combinations of the nearby P2 and P3 pure phase CVs. Therefore, **Figure 2.8** clearly demonstrates that the relative amounts of Mn^{3+}/Mn^{4+} and Fe^{3+}/Fe^{4+} redox activity in P2 and P3 materials are highly dependent on compositions and not particularly influenced by the structure being P2 or P3.

Figure 2.9 shows the voltage curves (voltage as a function of specific capacity) for the same zoom-in 2 samples. Although this is the same data as in Figure 8, the voltage curves reveal important trends not evident in CVs, the most important of which is overpotential which appears as a vertical offset between the first charge and the first discharge. While this overpotential is very small for P2 materials with high Mn content (including the highest capacity material shown in the brown rectangle), it becomes quite significant in the Fe-rich P2 and all P3 materials. Interestingly, this trend in increasing overpotential is consistent with the trend in Na_2CO_3 content on the surface of particles shown in **Figure 2.5c**. The high voltage on the first charge has been proposed to be due to the reactivity of surface Na_2CO_3 in refs.[39,65], and our findings are certainly consistent with this hypothesis. Furthermore, this higher overpotential in the P3 materials is not only seen in the first charge, but also can be found with a higher slope (voltage jump) at the capacity-voltage curve in **Figure 2.9**. Delmas *et al.* also reported this polarization effect by GITT [18]. At the stage with only

Mn^{4+} and Fe^{3+} species in the material during the cycling, the charge transfer process is much slower. The general trend that the Mn^{3+}/Mn^{4+} couple shows a lower overpotential (~0.3 V) than the Fe^{3+}/Fe^{4+} couple (0.8 V) is clearly maintained for both P2 and P3 materials across all compositions in **Figure 2.9**.

In **Figure S2.10**, the first 5 cycles for Zoom-in 2 are shown in order to illustrate that the charge endpoint slippage (which is caused by irreversible electrolyte consumption at the higher voltage [66]) varies greatly across the phase diagram. This test can demonstrate the cycling stability of the cathode material and even though we use the same electrolyte for the CV test, the different materials can show different effects on electrolyte oxidation. Of highest interest here, the slippage is very small in both Fe-rich P2 phases and the P3 phases. In fact, an Fe content of ~16% (Fe/(Na+Fe+Mn)) is found to separate the samples with high slippage from those with low slippage. This demonstrates that Fe can effectively suppress the electrolyte oxidation and thereby stabilize the interface between the cathode materials with the electrolyte.

Having discussed the main features in the electrochemical data, we next explore the impact of composition on the important metrics for battery operation, all extracted from the CVs. **Figure 2.10a** shows the first discharge capacities across both zoom-in plates, while **Figure 2.10b-d** shows the discharge capacity, average discharge voltage, and energy across 15 cycles. **Figures S2.11-S2.12** show the specific capacity and average voltage as a function of cycle number. Generally speaking, there is good capacity retention over the 15 cycles, and no signs of voltage fade. Overall, the P2 and P3 materials show higher capacities than the O3 and are therefore the main focus of this discussion. The energy contour plot in **Figure 2.10d** shows the same trends as seen in capacity (**Figure 2.10b**) implying that any change in average voltage is overshadowed by changes in capacity. Specifically, in the P2 materials, the average voltage decreases with increased manganese content as expected, but this decrease is more than compensated for by an increase in capacity, such that the highest energy P2 material is in fact quite rich in Mn ($Na_{0.59}Fe_{0.13}Mn_{0.87}O_2$) and this continues to be true through all 15 cycles.

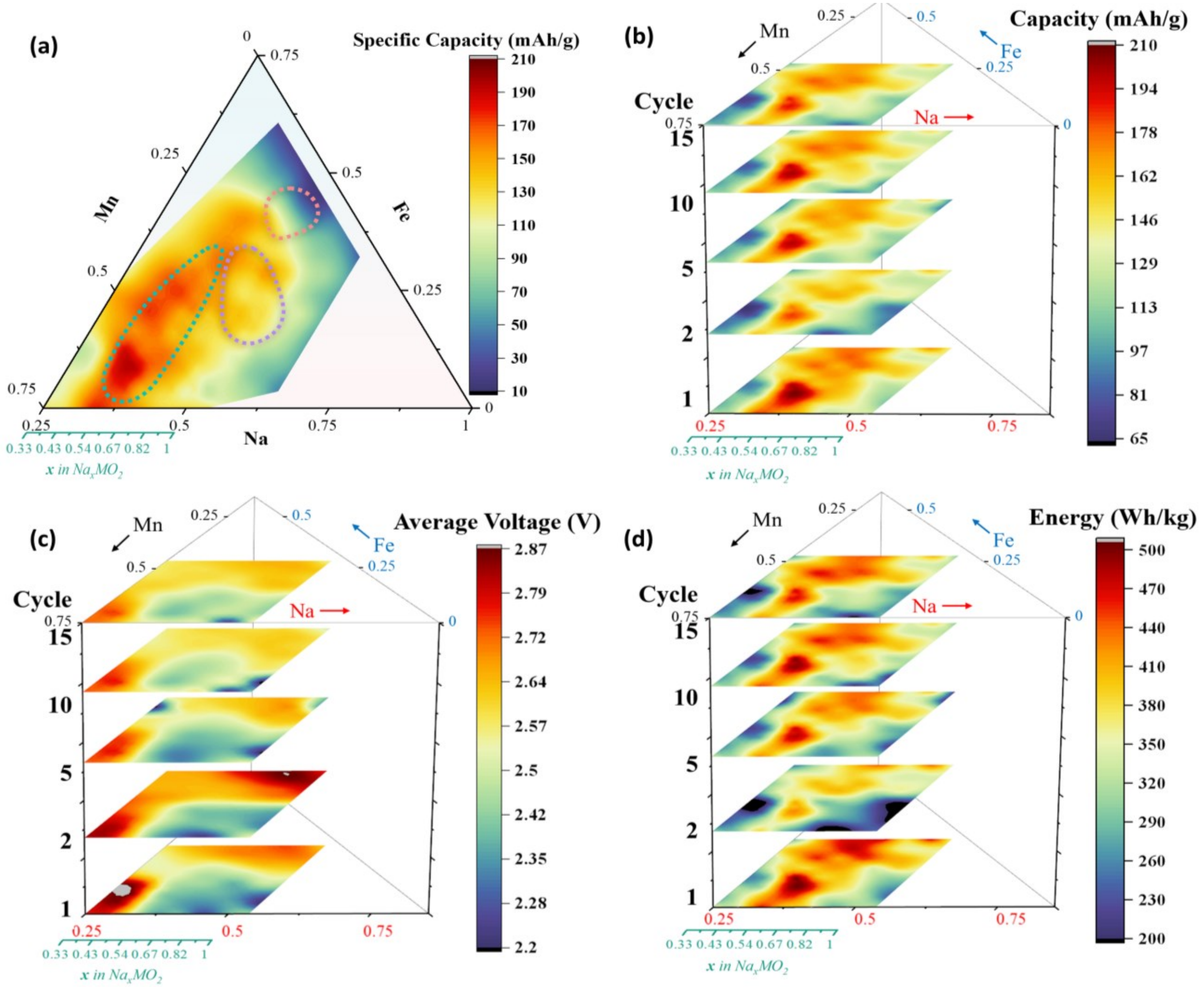

Figure 2.10 *Evolution of important battery metrics across the phase diagram: discharge capacity on first cycle (a), discharge capacity on extended cycling (b), average discharge voltage on extended cycling (c), and energy density (voltage times capacity) on extended cycling (d).*

2.4.4 Main consequences of this study on Na-ion cathode design

As a final point of focus regarding the battery performance, we summarize our findings by comparing the highest discharge capacity samples from each phase. These are:

$Na_{0.59}Fe_{0.13}Mn_{0.87}O_2$ (P2, 206 mAh/g), $Na_{0.74}Fe_{0.54}Mn_{0.41}O_2$ (P3, 180 mAh/g), and $Na_{0.85}Fe_{0.70}Mn_{0.30}O_2$ (O3, 131 mAh/g). **Figure 2.11** shows the cycling results for these 3 materials only. This figure certainly reinforces much of the above discussion: the Mn-rich P2 phase shows Mn-dominated redox activity and a great deal of activation below the open-circuit voltage as well as the smallest hysteresis. This material is both rich in Mn and slightly deficient in Na compared to the most heavily studied P2-$Na_{0.67}Fe_{0.5}Mn_{0.5}O_2$, such that this material is of particular interest for further study, especially given that it was found to be less reactive with air in the XPS results above. In particular, we consider studying the impact of further substitutions on the stability (both in air and in the electrolyte) to be of the highest priority. Given that its capacity retention in **Figure S2.11** was relatively noisy in the combinatorial cell, we made a Swagelok style cell with this material, and it showed high capacity retention of 87% over 50 cycles (**Figure S2.13**). By contrast to this P2 material, the O3 material is of little interest given the low capacities and large overpotentials. Finally, the P3 material (slightly more Fe rich than the single P3 material previously studied in this system) is also of further interest. Not only is the capacity quite high and cycling retention good, but the stability with moisture was found to be better than P2 materials based on XPS. The high iron content also results in a higher average voltage than in the P2 material. Given that stability in air/moisture is considered the strongest hindrance to commercialization for this class of cathodes, we consider this P3 material of high interest for further study.

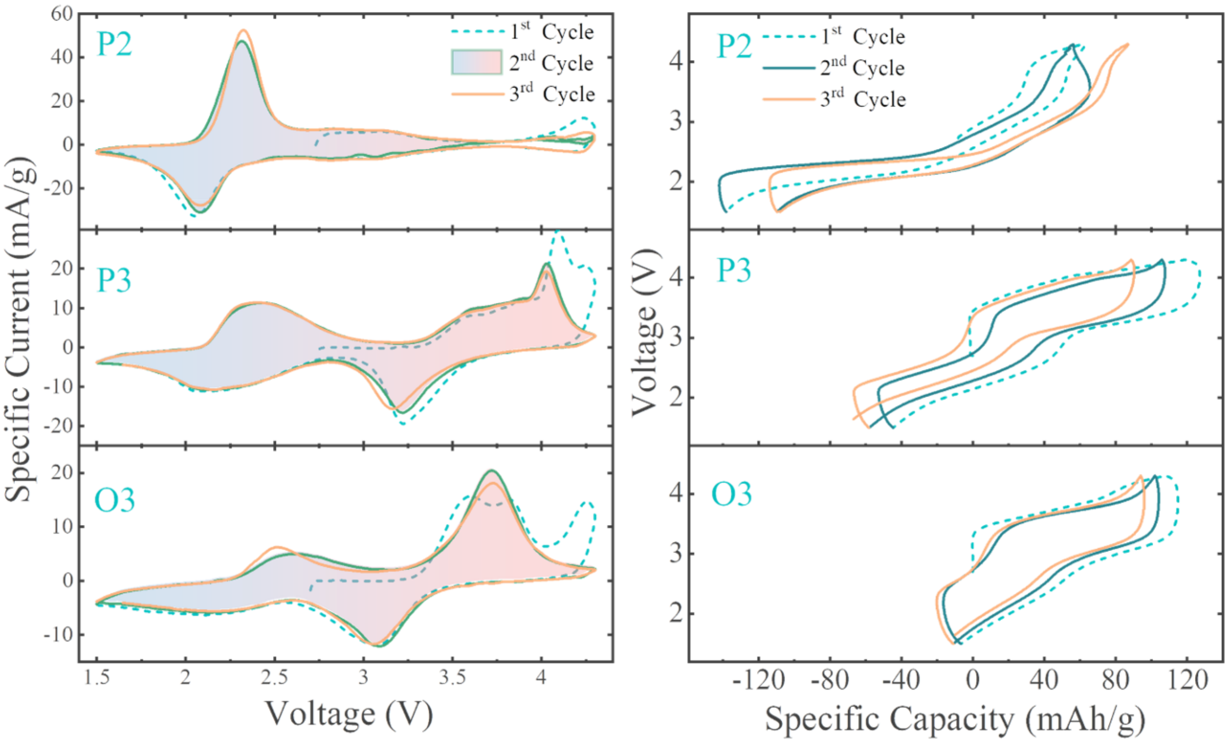

Figure 2.11 *The first 3 cycles shown as both CVs (left) and voltage curves (right) for the P2, P3 and O3 materials showing highest first discharge capacities within their respective phases. Specifically, the compositions are:* $Na_{0.59}Fe_{0.13}Mn_{0.87}O_2$ *(P2),* $Na_{0.74}Fe_{0.54}Mn_{0.41}O_2$ *(P3), and* $Na_{0.85}Fe_{0.70}Mn_{0.30}O_2$ *(O3). In the CVs, the blue region represents predominantly Mn redox, while the pink represents Fe dominated redox processes.*

To further understand the differences in performance of these 3 materials, SEM was performed on these 3 materials. **Figure S15** shows representative images for each of these phases. In all three samples the primary particles are in the range from 0.5 to 2 µm and form relatively porous secondary particles thereby giving easy access to electrolyte. We therefore see no correlation between electrochemical performance differences and morphology. Furthermore, to ensure that the selected voltage window did not bias the results in favor of the P2 and P3 phases, CVs were repeated on these 3 materials in the range 1.5 – 4.6 V as shown in Figure S16. The first discharge capacities did not change appreciably: 206 mAh/g for P2, 173 mAh/g for P3, and 136 mAh/g for

O3. All 3 phases showed an increase in irreversible capacity consistent with an increase in electrolyte oxidation at such high potentials. Overall, the Mn-rich P2 and P3 phases continue to show the best electrochemistry even when a larger potential window is utilized.

This work clearly identifies key compositions that warrant further exploration: the Mn-rich P2 phases. Despite their improved performance, they continue to show some instability in air and further improvement of their extended cycling is certainly required in order to commercialize these materials. Both coatings and further substitutions are promising approaches to further improve both these important properties. Follow-up to this study will include a systematic screening of substitutions (>50 substituents are currently possible with our sol-gel synthesis approach) into the Mn-rich P2 materials in order to further improve the materials' stability and extended cycling. Utilizing those substituents to make a coating (or shell) is also of high interest for further development of these promising materials.

2.5 Conclusions

Newly developed high-throughput synthesis methods for Na-ion cathodes were used to make 448 Na-Fe-Mn-O materials. They were characterized with high-throughput XRD, XPS, ICP-OES, and electrochemistry. The structural phase diagrams show that three phases are of interest as potential Na-ion battery cathodes: P2, P3 and O3, which all exist as 2D solid solutions within the phase diagrams. All 3 regions are larger than previously suspected in the literature, and the systematic study across compositions helped resolve some confusion in the literature such as whether O3 or P3 is made at the $NaFe_{1/2}Mn_{1/2}O_2$ compositions. The phase mappings were also interpreted within the context of the recently developed cationic potential approach, and we found that the P3 materials lie on the P2 side of the dividing line, but they are not distinguishable from the P2 materials based on cationic potentials alone. Also of significance, the highest energy density materials in each of the 3 solid solution regions were found at novel compositions. In particular, the highest energy density P2 material is relatively rich in Mn and has a slight deficiency in Na compared to the most heavily studied P2 material. The best performing material showed capacity retention of 87% after 50 slow CV cycles (56 h per cycle) showing very promising cycling behavior for a Na half cell. Importantly, we also quantify the stability in air/moisture using XPS on aged samples across the entire phase diagram and find that the high manganese P2 and the under-explored P3 materials are in fact the most stable. A P3 material also showed both high capacities and good cycling performance. Given that instability with air is currently preventing the commercialization of P2 materials, we expect the results for both P3 and Mn-rich P2 materials here to help guide further development of these materials.

2.6 Acknowledgements

This work was funded by the Natural Sciences and Engineering Research Council of Canada under the auspices of a Discovery grant. SJ also acknowledges a FRQNT graduate student scholarship.

2.7 Supporting Information

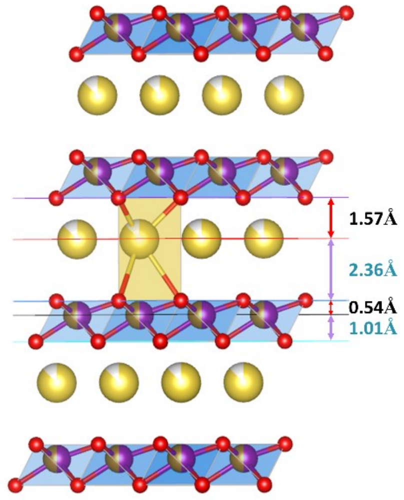

Figure S2.1 *The structure of P3 determined from ref. 30. Of particular note here, there is a strong asymmetry in the vertical direction for the* MO_6 *polyhedra that is inconsistent with the symmetry in the stacking of the other layers. The z-direction as discussed in the main text is vertical in this image.*

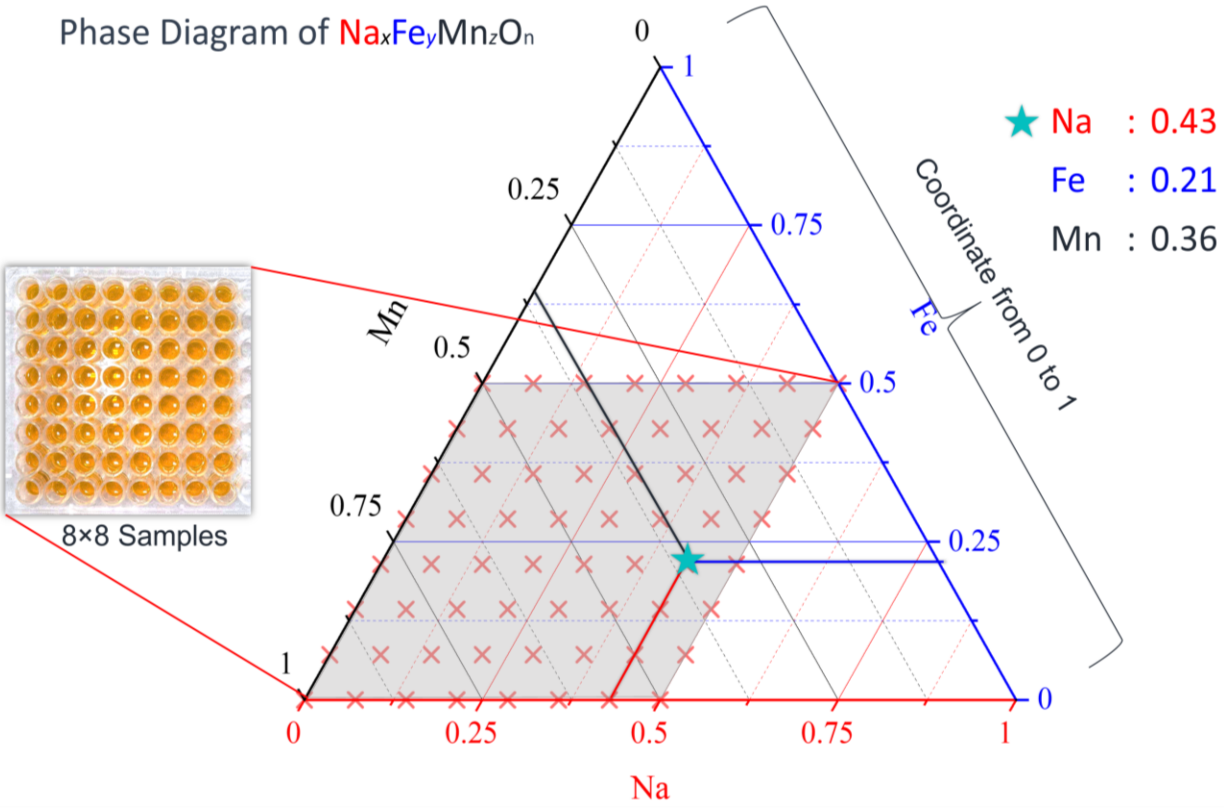

Figure S2.2 *Illustration of how volume ratios are utilized to map out a ternary phase diagram using mixtures of equimolar solutions of the three corners.*

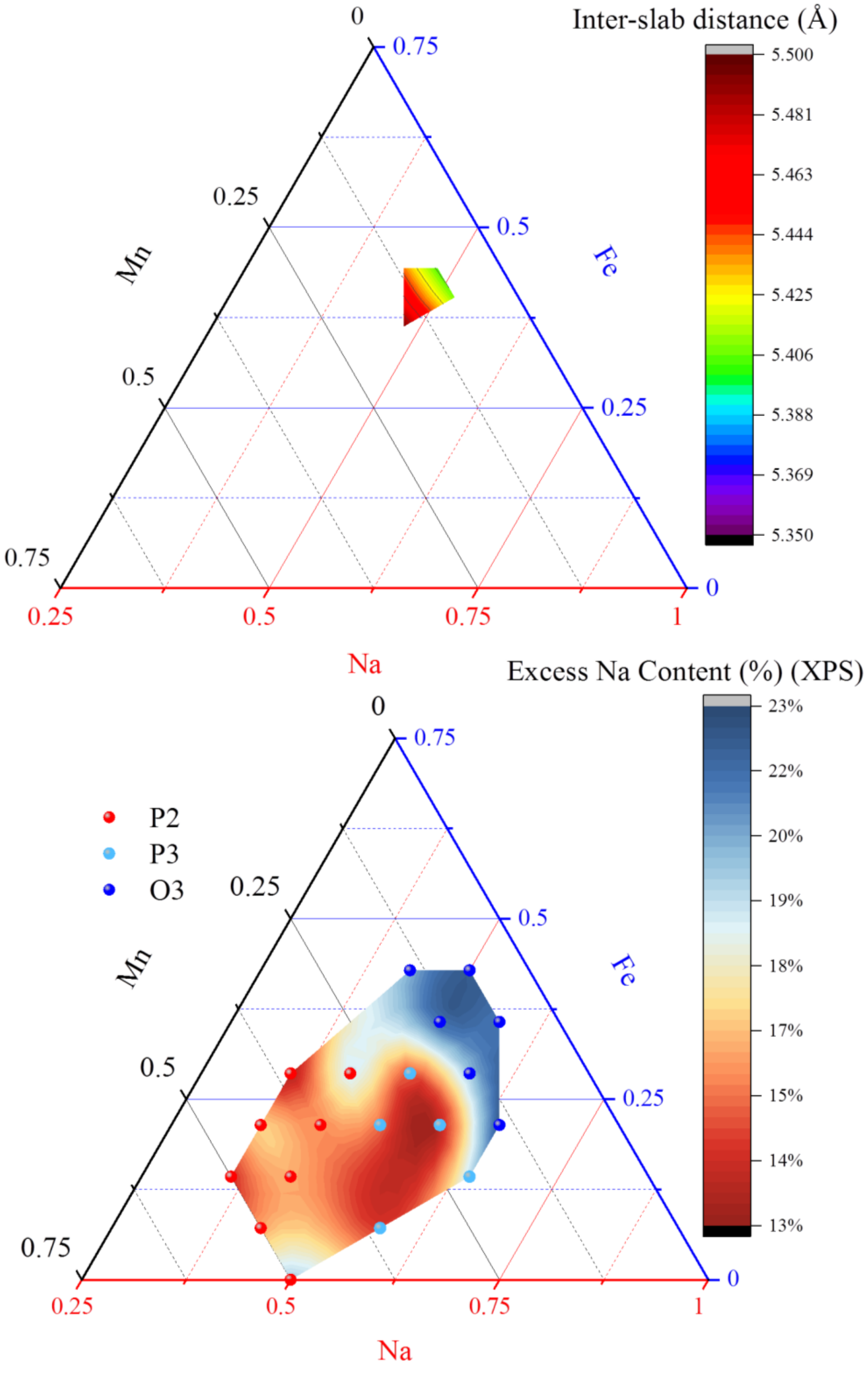

Figure S2.3 *Top: inter-slab distance for the O3 phase only. Bottom: the excess Na content calculated from the XPS quantitative analysis.*

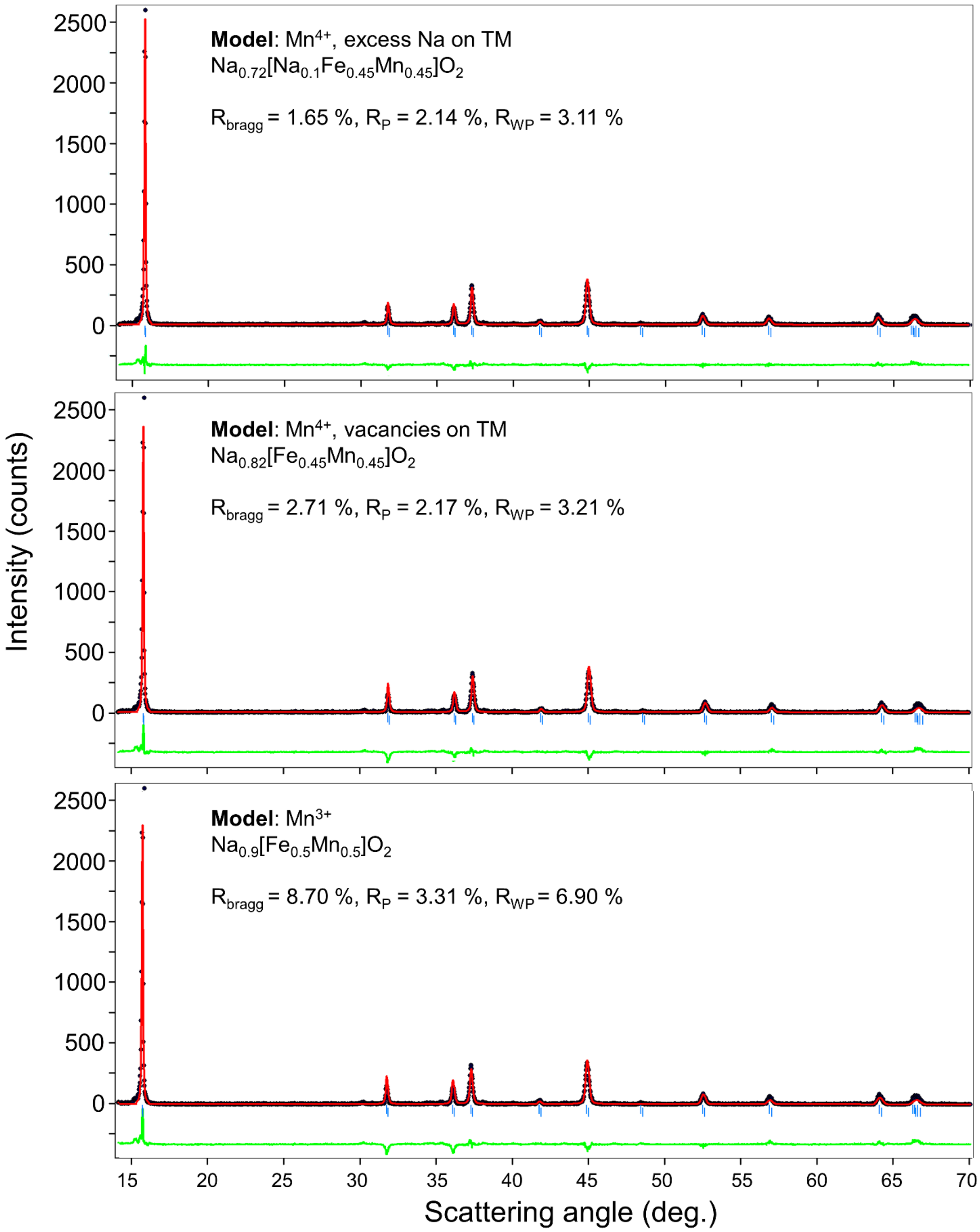

Figure S2.4 *Three Rietveld fits for a P3 sample. The background has been subtracted for clarity. Black: data, red: fit result, green: difference plot. The values of the fit quality parameters are shown form all 3 models discussed in the main text. The fits are undeniably improved when one considers Mn in the 4+ state, consistent with XAS results from ref. 30.*

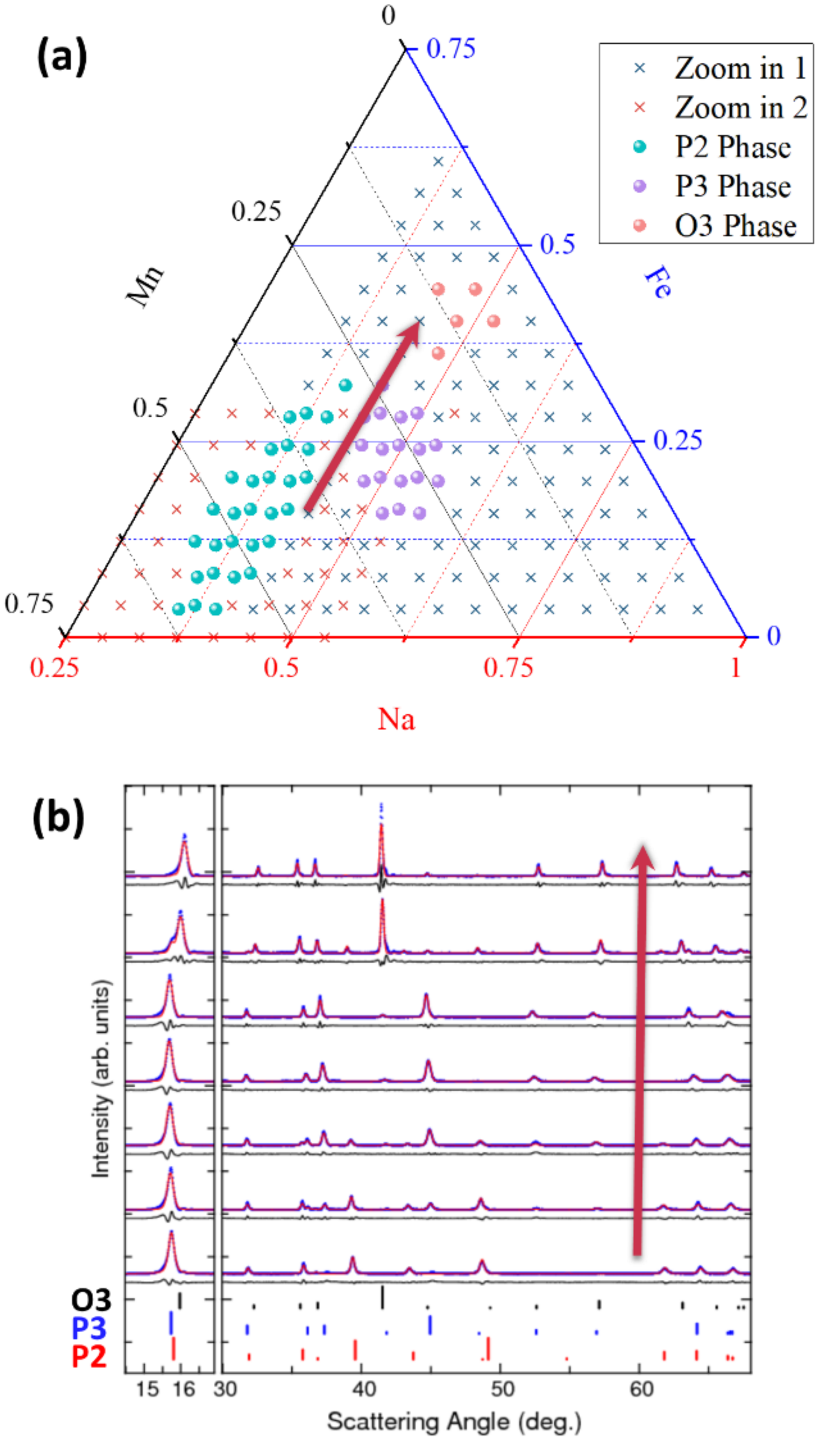

Figure S2.5 *(a) Composition line through the phase diagram that shows a transition from P2 to P3 and then very near to the O3 region. (b) The corresponding XRD patterns, with fits in red, and difference plots below each pattern.*

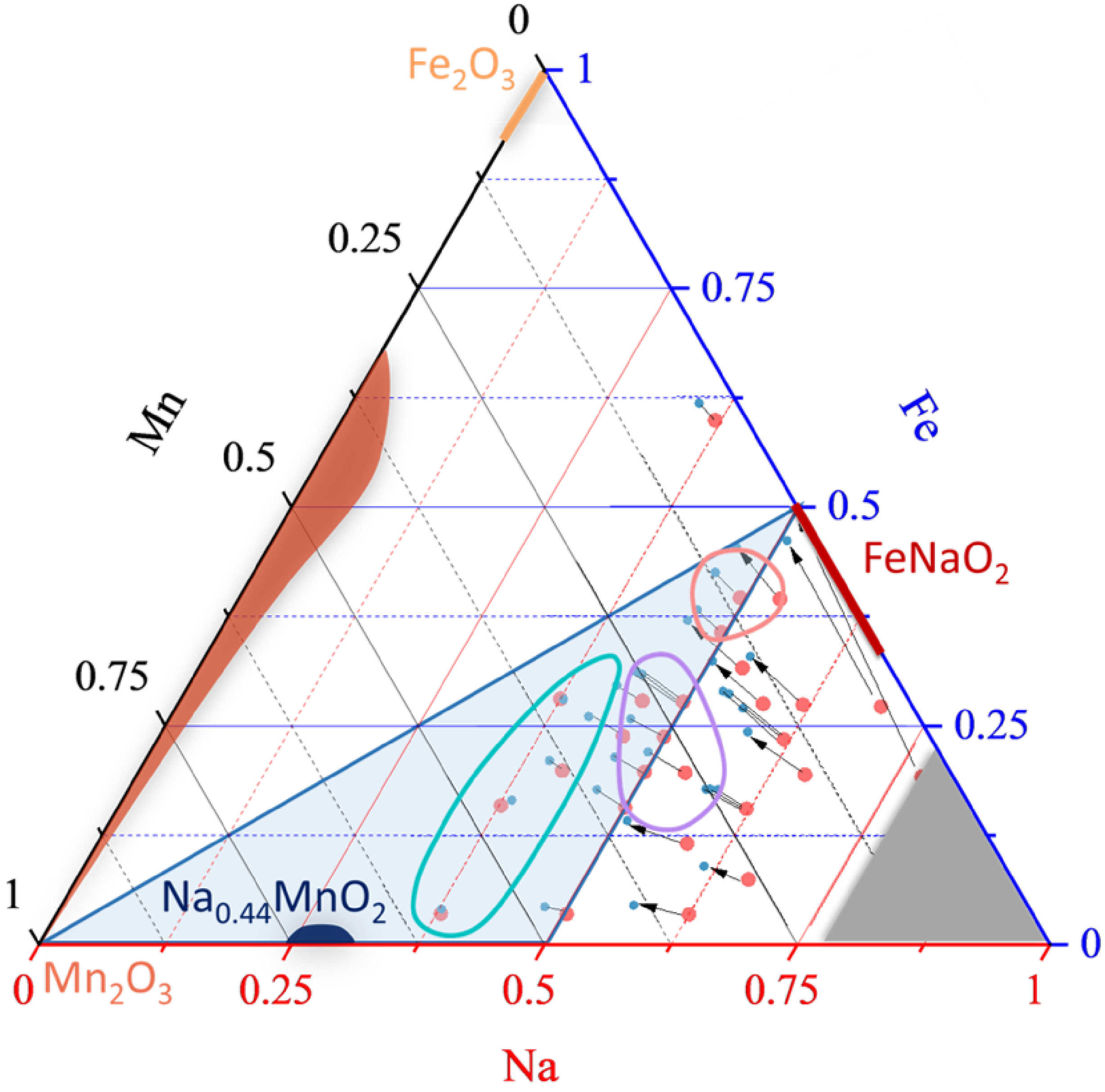

Figure S2.6 *The phase stabilities determined herein along with the map of Na loss and the blue triangular region where layered oxides can form with Fe in the 3+ state, Mn taking a mixed 3,4+ state and no vacancies on the TM layers.*

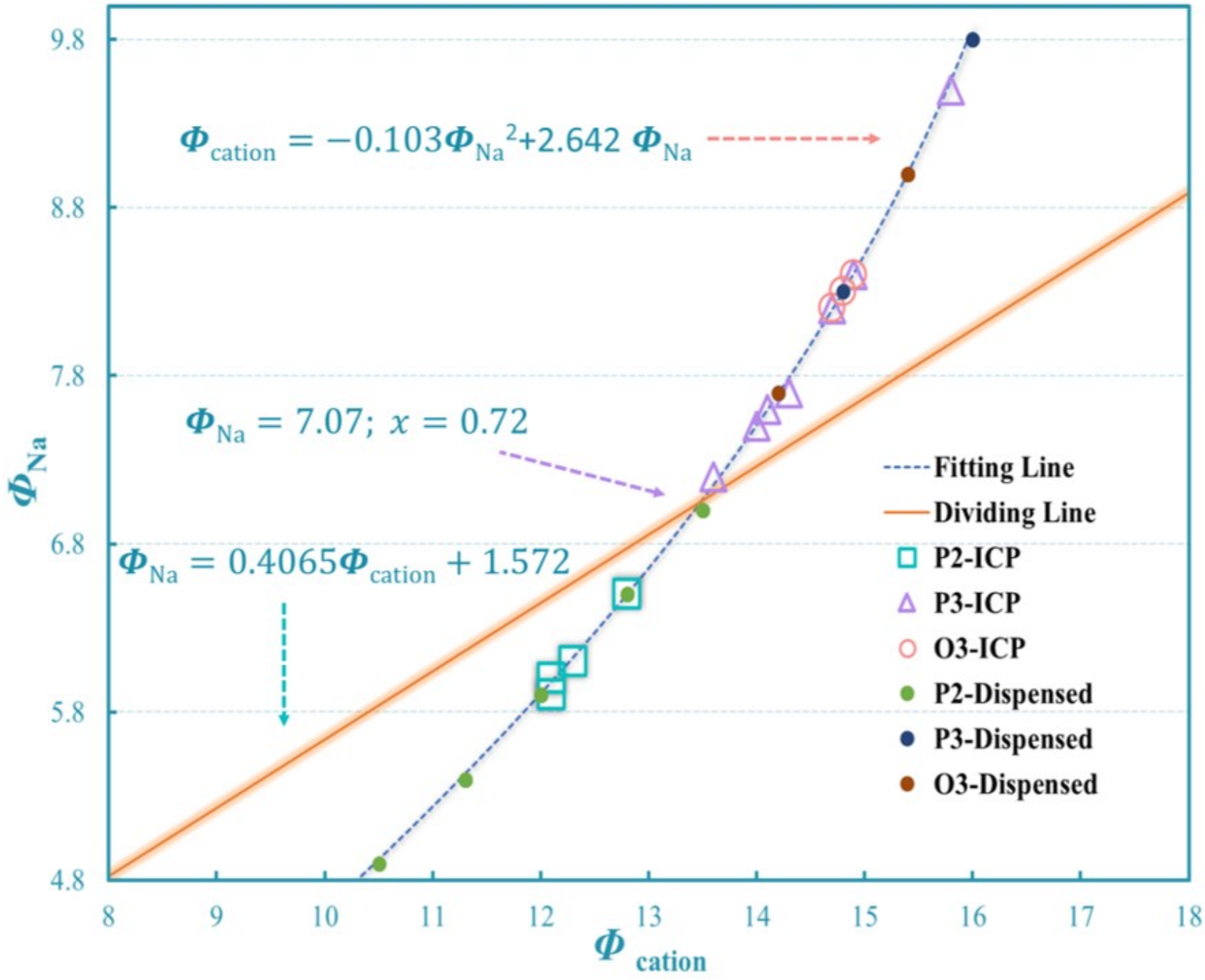

Figure S2.7 *Result of the cationic potential analysis if Mn is assumed to be in a state such that Mn and Fe fully occupy the TM layers. As discussed throughout, this condition does not hold for the P3 structures based on our Rietveld refinement and XAS measurements from ref. 30.*

Note: The calculation of Cationic Potential is reproduced from ref. 30 by the equation shown below:

$$\Phi_{cation} = \frac{\overline{\Phi_{TM}\Phi_{Na}}}{\overline{\Phi_O}}$$

where $\overline{\Phi_{TM}}$ *is calculated from the weighted average ionic potential of TMs:* $\overline{\Phi_{TM}} = \sum \frac{w_i n_i}{R_i}$*;* w_i *is the weighted content of* TM_i *with a charge of* n_i *and radius* R_i*;* $\overline{\Phi_{Na}}$ *is calculated from the weighted average ionic potential of* Na^+ *ion.* $\overline{\Phi_O}$ *represent the ionic potential of* O^{2-}*.*

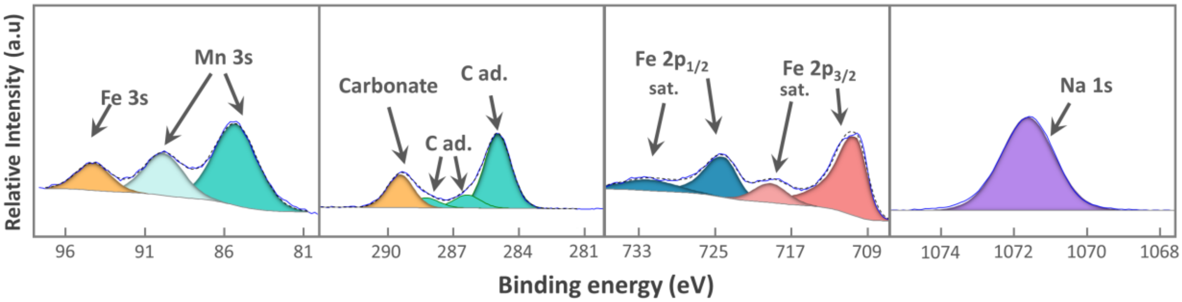

Figure S2.8 *XPS of a single P2 sample. Peaks of Mn 3s, C 1s, Fe 2p, and Na 1s are labelled.*

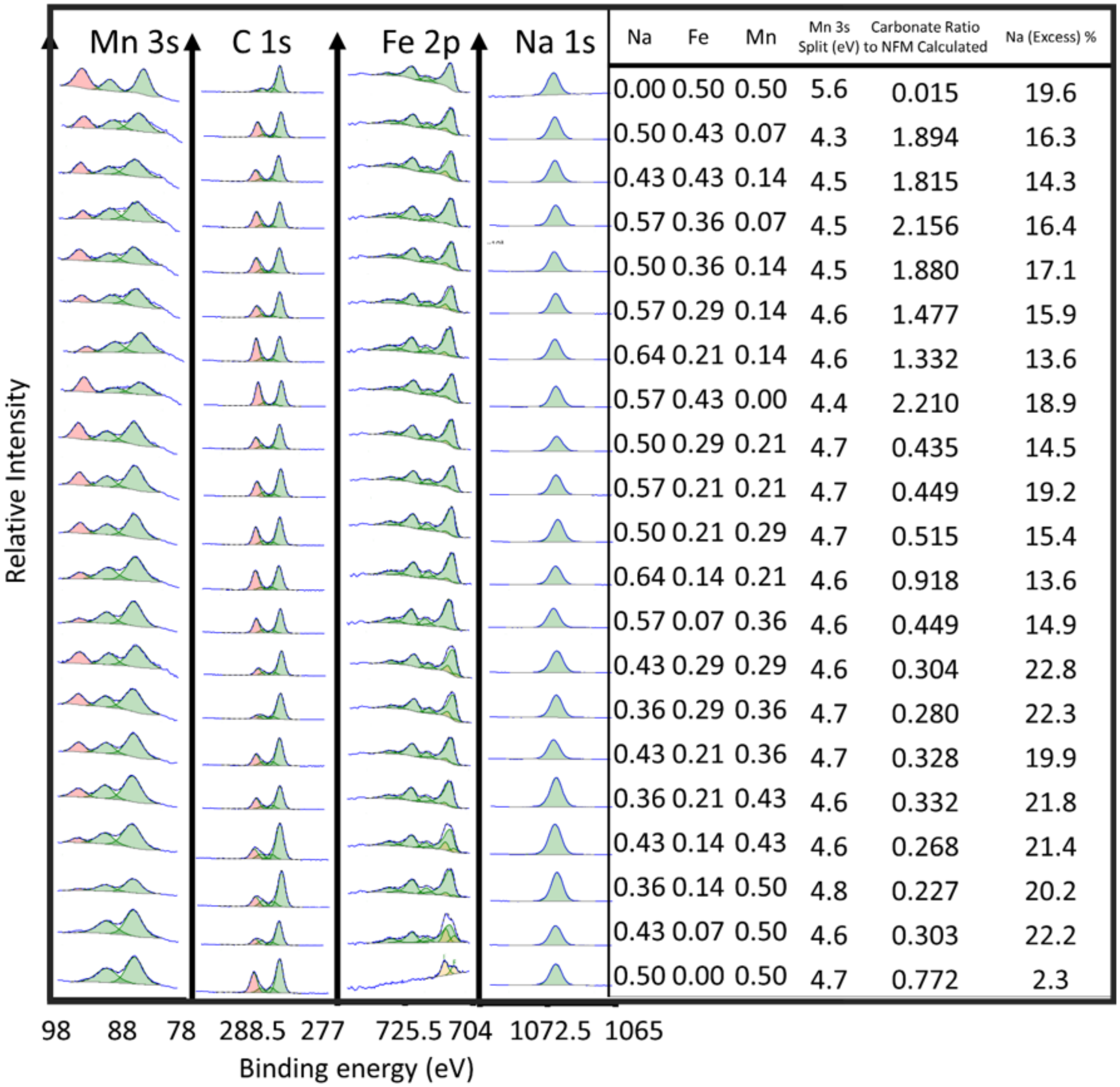

Na	Fe	Mn	Mn 3s Split (eV)	Carbonate Ratio to NFM Calculated	Na (Excess) %
0.00	0.50	0.50	5.6	0.015	19.6
0.50	0.43	0.07	4.3	1.894	16.3
0.43	0.43	0.14	4.5	1.815	14.3
0.57	0.36	0.07	4.5	2.156	16.4
0.50	0.36	0.14	4.5	1.880	17.1
0.57	0.29	0.14	4.6	1.477	15.9
0.64	0.21	0.14	4.6	1.332	13.6
0.57	0.43	0.00	4.4	2.210	18.9
0.50	0.29	0.21	4.7	0.435	14.5
0.57	0.21	0.21	4.7	0.449	19.2
0.50	0.21	0.29	4.7	0.515	15.4
0.64	0.14	0.21	4.6	0.918	13.6
0.57	0.07	0.36	4.6	0.449	14.9
0.43	0.29	0.29	4.6	0.304	22.8
0.36	0.29	0.36	4.7	0.280	22.3
0.43	0.21	0.36	4.7	0.328	19.9
0.36	0.21	0.43	4.6	0.332	21.8
0.43	0.14	0.43	4.6	0.268	21.4
0.36	0.14	0.50	4.8	0.227	20.2
0.43	0.07	0.50	4.6	0.303	22.2
0.50	0.00	0.50	4.7	0.772	2.3

Figure S2.9 *The complete set of XPS patterns, along with Na, Fe, Mn content, Mn 3s splitting and carbonate ratio.*

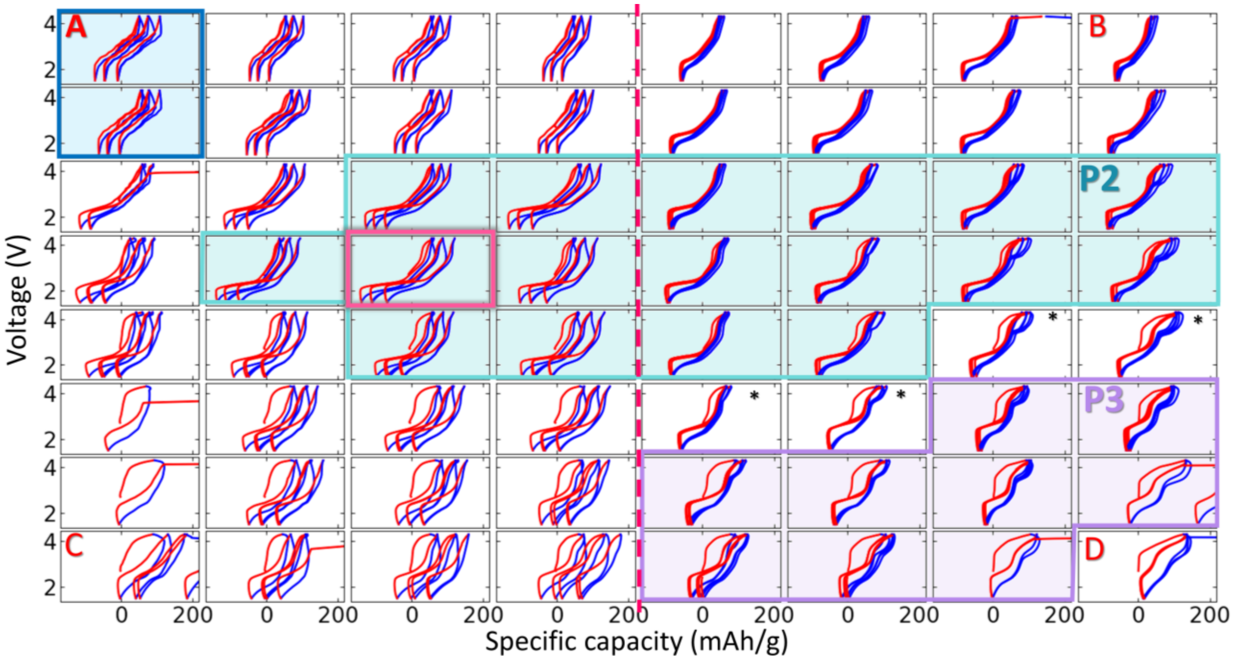

Figure S2.10 *5 cycles of zoom-in 2. The focus here is on charge endpoint slippage (the voltage curves drift to the right with extended cycling): the entire left half shows high slippage, while the right half shows greatly reduced slippage. The line between the two halves is an iron content of 16% as discussed in the main text.*

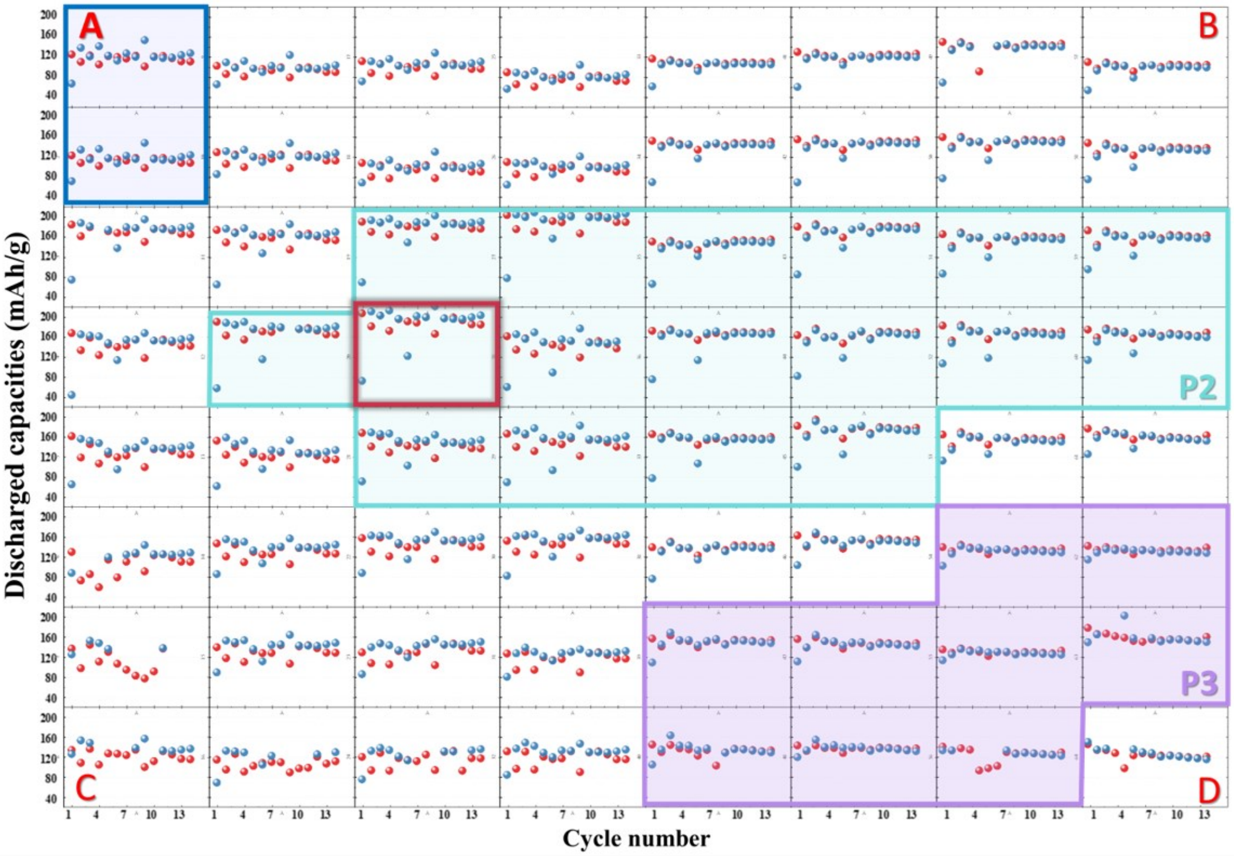

Figure S2.11 *Specific capacity during charge (blue) and discharge (red) for 15 cycles for the materials made in zoom-in 2. The compositions at the four corners are indicated and match the labels on* ***Figure 2.2a****.*

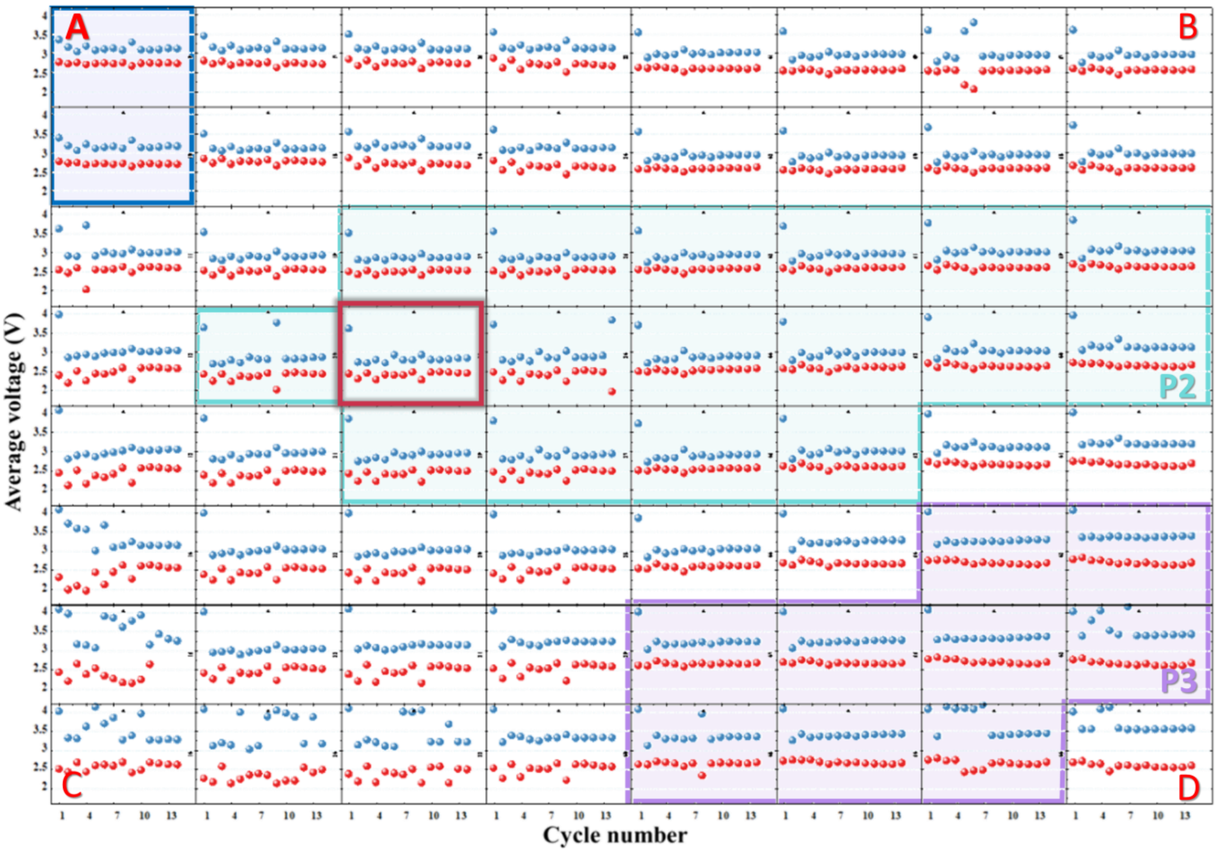

Figure S2.12 *Average voltage during charge (blue) and discharge (red) for 15 cycles for the materials made in zoom-in 2.*

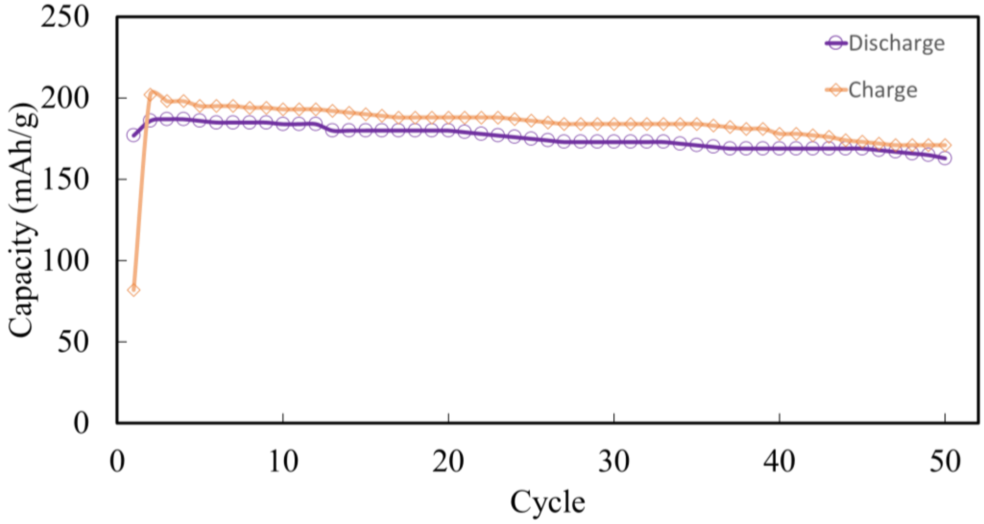

Figure S2.13: *Specific capacity (orange is for charge, blue is for discharge) vs. cycle number for the highest capacity P2 material cycled in a Swagelok cell.*

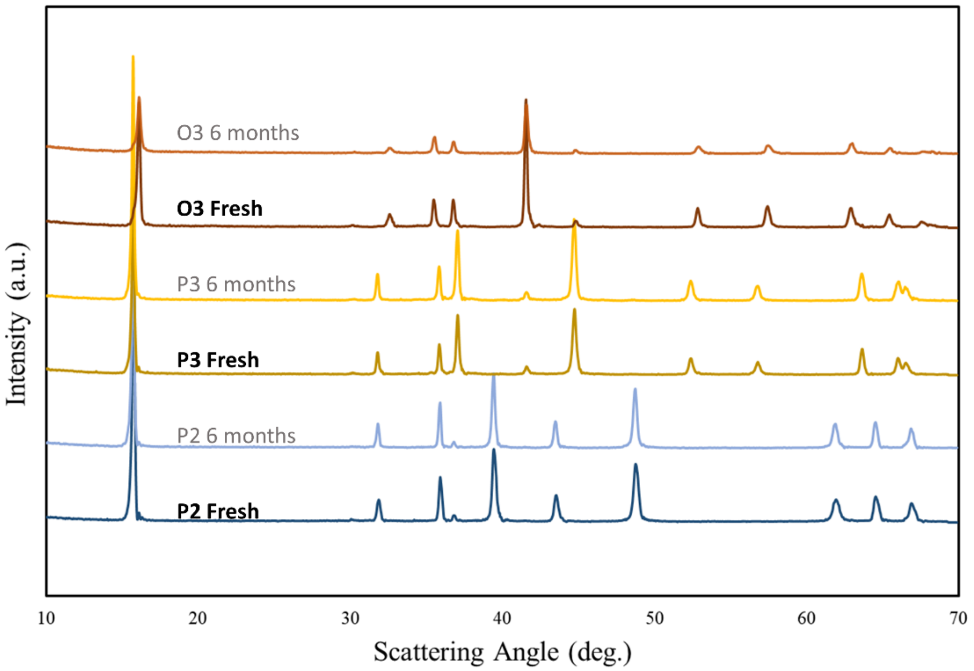

Figure S2.14 *XRD results for dry air stability with as-prepared and after-6-month P2, P3, and O3 materials with the same compositions as used in* ***Figure 2.10****.*

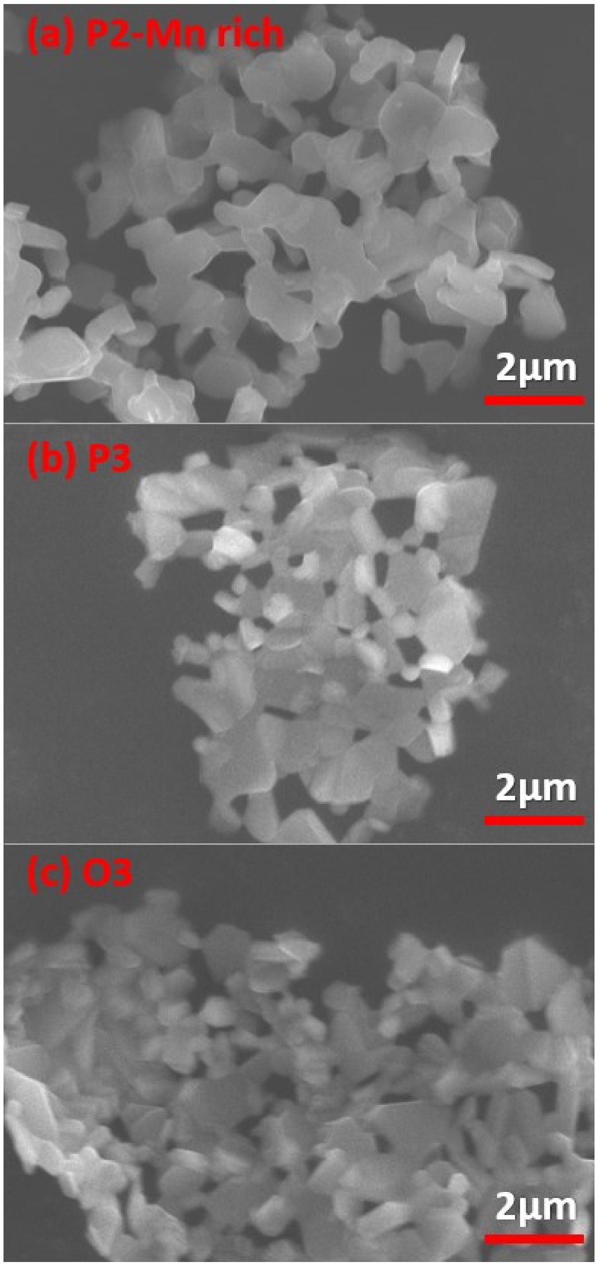

Figure S2.15 *Representative SEM image for sol-gel combinatorial samples (a) P2-*$Na_{0.59}Fe_{0.13}Mn_{0.87}O_2$*, (b) P3-*$Na_{0.74}Fe_{0.54}Mn_{0.41}O_2$*, and (c) O3-*$Na_{0.85}Fe_{0.70}Mn_{0.30}O_2$*.*

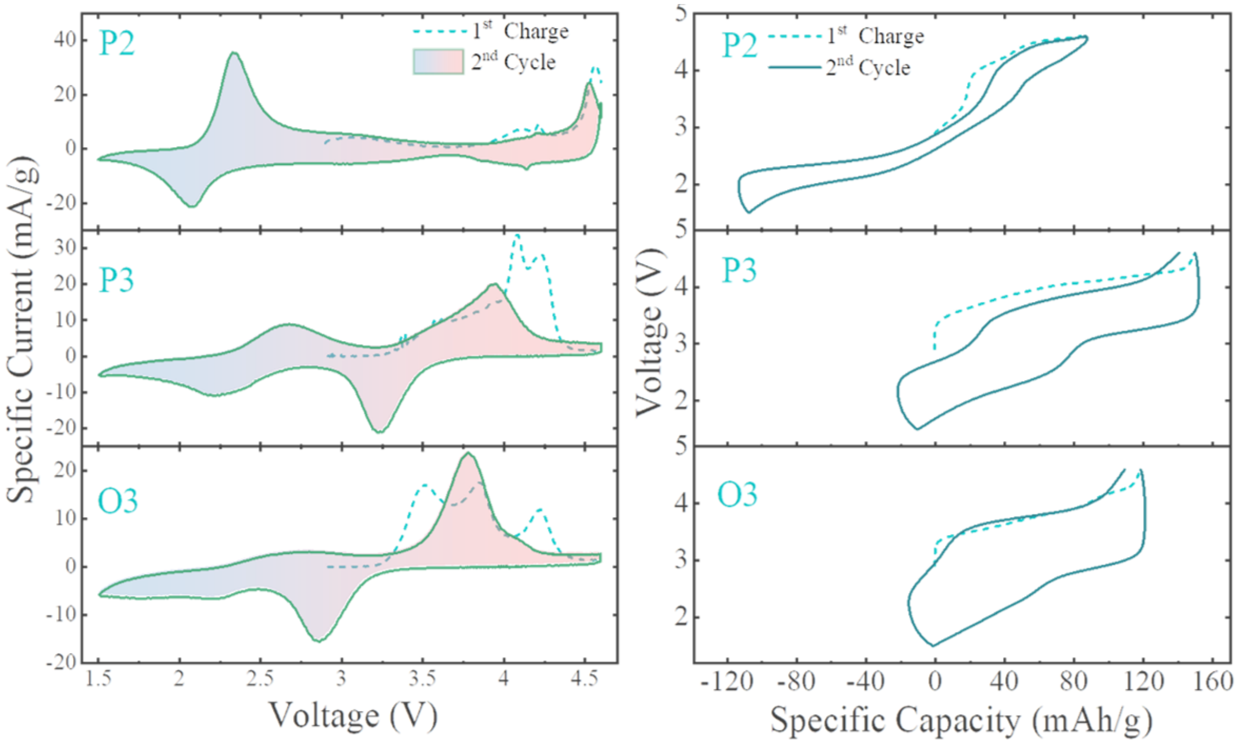

Figure S2.16 *The first 1.5 cycles shown as both CVs (left) and voltage curves (right) from 1.5 V to 4.6 V at the scan rate 0.1 V/h for the P2, P3 and O3 materials showing highest first discharge capacities within their respective phases. Specifically, the compositions are:* $Na_{0.59}Fe_{0.13}Mn_{0.87}O_2$ *(P2),* $Na_{0.74}Fe_{0.54}Mn_{0.41}O_2$ *(P3), and* $Na_{0.85}Fe_{0.70}Mn_{0.30}O_2$ *(O3).*

2.8 References

(1) Liu, Q.; Hu, Z.; Chen, M.; Zou, C.; Jin, H.; Wang, S.; Chou, S. L.; Dou, S. X., Recent progress of layered transition metal oxide cathodes for sodium ‐ ion batteries. *Small* **2019,** *15* (32), 1805381.

(2) Yabuuchi, N.; Kubota, K.; Dahbi, M.; Komaba, S., Research development on sodium-ion batteries. *Chemical Reviews* **2014,** *114* (23), 11636-11682.

(3) Yabuuchi, N.; Yoshida, H.; Komaba, S., Crystal structures and electrode performance of alpha-NaFeO2 for rechargeable sodium batteries. *Electrochemistry* **2012,** *80* (10), 716-719.

(4) Bordet-Le Guenne, L.; Deniard, P.; Biensan, P.; Siret, C.; Brec, R., Structural study of two layered phases in the NaxMnyO2 system. Electrochemical behavior of their lithium substituted derivatives. *Journal of Materials Chemistry* **2000,** *10* (9), 2201-2206.

(5) Berthelot, R.; Carlier, D.; Delmas, C., Electrochemical investigation of the P2–Na x CoO 2 phase diagram. *Nature Materials* **2011,** *10* (1), 74-80.

(6) Delmas, C.; Braconnier, J.-J.; Fouassier, C.; Hagenmuller, P., Electrochemical intercalation of sodium in NaxCoO2 bronzes. *Solid State Ionics* **1981,** *3*, 165-169.

(7) Yu, C.-Y.; Park, J.-S.; Jung, H.-G.; Chung, K.-Y.; Aurbach, D.; Sun, Y.-K.; Myung, S.-T., NaCrO 2 cathode for high-rate sodium-ion batteries. *Energy & Environmental Science* **2015,** *8* (7), 2019-2026.

(8) Maazaz, A.; Delmas, C.; Hagenmuller, P., A study of the Na x TiO 2 system by electrochemical deintercalation. *Journal of Inclusion Phenomena* **1983,** *1* (1), 45-51.

(9) Guignard, M.; Didier, C.; Darriet, J.; Bordet, P.; Elkaïm, E.; Delmas, C., P2-Na x VO 2 system as electrodes for batteries and electron-correlated materials. *Nature Materials* **2013,** *12* (1), 74-80.

(10) Lee, D. H.; Xu, J.; Meng, Y. S., An advanced cathode for Na-ion batteries with high rate and excellent structural stability. *Physical Chemistry Chemical Physics* **2013,** *15* (9), 3304-3312.

(11) Yabuuchi, N.; Kajiyama, M.; Iwatate, J.; Nishikawa, H.; Hitomi, S.; Okuyama, R.; Usui, R.; Yamada, Y.; Komaba, S., P2-type Na x [Fe 1/2 Mn 1/2] O 2 made from earth-abundant elements for rechargeable Na batteries. *Nature Materials* **2012,** *11* (6), 512-517.

(12) Tournadre, F.; Croguennec, L.; Saadoune, I.; Carlier, D.; Shao-Horn, Y.; Willmann, P.; Delmas, C., On the mechanism of the P2 ‐ Na0.70CoO2 → O2 ‐ LiCoO2 exchange reaction—Part I: proposition of a model to describe the P2–O2 transition. *Journal of Solid State Chemistry* **2004,** *177* (8), 2790-2802.

(13) Li, Z.-Y.; Gao, R.; Sun, L.; Hu, Z.; Liu, X., Designing an advanced P2-Na 0.67 Mn 0.65 Ni 0.2 Co 0.15 O 2 layered cathode material for Na-ion batteries. *Journal of Materials Chemistry A* **2015,** *3* (31), 16272-16278.

(14) Han, M. H.; Gonzalo, E.; Singh, G.; Rojo, T., A comprehensive review of sodium layered oxides: powerful cathodes for Na-ion batteries. *Energy & Environmental Science* **2015,** *8* (1), 81-102.

(15) Delmas, C.; Fouassier, C.; Hagenmuller, P., Structural classification and properties of the layered oxides. *Physica B+C* **1980,** *99* (1-4), 81-85.

(16) Thorne, J.; Dunlap, R.; Obrovac, M. d., Structure and electrochemistry of NaxFexMn1-xO2 (1.0≤ x≤0.5) for Na-ion battery positive electrodes. *Journal of the Electrochemical Society* **2012,** *160* (2), A361.

(17) Pang, W. K.; Kalluri, S.; Peterson, V. K.; Sharma, N.; Kimpton, J.; Johannessen, B.; Liu, H. K.; Dou, S. X.; Guo, Z., Interplay between electrochemistry and phase evolution of the P2-type Nax(Fe1/2Mn1/2)O2 cathode for use in sodium-ion batteries. *Chemistry of Materials* **2015,** *27* (8), 3150-3158.

(18) Mortemard de Boisse, B.; Carlier, D.; Guignard, M.; Bourgeois, L.; Delmas, C., P2-Na x Mn1/2Fe1/2O2 Phase Used as Positive Electrode in Na Batteries: Structural Changes Induced by the Electrochemical (De) intercalation Process. *Inorganic Chemistry* **2014,** *53* (20), 11197-11205.

(19) Mortemard de Boisse, B.; Carlier, D.; Guignard, M.; Guerin, E.; Duttine, M.; Wattiaux, A.; Delmas, C., Influence of Mn/Fe Ratio on Electrochemical and Structural Properties of P2-Na x Mn1–y Fe y O2 Phases as Positive Electrode Material for Na-Ion Batteries. *Chemistry of Materials* **2018,** *30* (21), 7672-7681.

(20) Kodera, T.; Ogihara, T., Synthesis and electrochemical properties of Na2/3Fe1/3Mn2/3O2 cathode materials for sodium ion battery by spray pyrolysis. *Journal of the Ceramic Society of Japan* **2014,** *122* (1426), 483-487.

(21) Hirsh, H.; Olguin, M.; Chung, H.; Li, Y.; Bai, S.; Feng, D.; Wang, D.; Zhang, M.; Meng, Y. S., Meso-Structure Controlled Synthesis of Sodium Iron-Manganese Oxides Cathode for Low-Cost Na-Ion Batteries. *Journal of the Electrochemical Society* **2019,** *166* (12), A2528.

(22) Xu, H.; Zong, J.; Liu, X.-j., P2-type Na0.67Mn0.6Fe0.4-xyZnxNiyO2 cathode material with high-capacity for sodium-ion battery. *Ionics* **2018,** *24* (7), 1939-1946.

(23) De Boisse, B. M.; Carlier, D.; Guignard, M.; Delmas, C., Structural and electrochemical characterizations of P2 and New O3-NaxMn1-yFeyO2 Phases prepared by auto-combustion synthesis for Na-ion batteries. *Journal of the Electrochemical Society* **2013,** *160* (4), A569.

(24) Okada, S.; Takahashi, Y.; Kiyabu, T.; Doi, T.; Yamaki, J.-I.; Nishida, T. In *Layered transition metal oxides as cathodes for sodium secondary battery*, ECS Meeting Abstracts, IOP Publishing: 2006; p 201.

(25) Caballero, A.; Hernan, L.; Morales, J.; Sanchez, L.; Pena, J. S.; Aranda, M., Synthesis and characterization of high-temperature hexagonal P2-Na 0.6 MnO 2 and its electrochemical behaviour as cathode in sodium cells. *Journal of Materials Chemistry* **2002,** *12* (4), 1142-1147.

(26) Billaud, J.; Clément, R. J.; Armstrong, A. R.; Canales-Vázquez, J.; Rozier, P.; Grey, C. P.; Bruce, P. G., β-NaMnO2: a high-performance cathode for sodium-ion batteries. *Journal of the American Chemical Society* **2014,** *136* (49), 17243-17248.

(27) Parant, J.-P.; Olazcuaga, R.; Devalette, M.; Fouassier, C.; Hagenmuller, P., Sur quelques nouvelles phases de formule NaxMnO2 (x⩽1). *Journal of Solid State Chemistry* **1971,** *3* (1), 1-11.

(28) Clément, R. J.; Bruce, P. G.; Grey, C. P., manganese-based P2-type transition metal oxides as sodium-ion battery cathode materials. *Journal of the Electrochemical Society* **2015,** *162* (14), A2589.

(29) Lu, X.; Wang, Y.; Liu, P.; Gu, L.; Hu, Y.-S.; Li, H.; Demopoulos, G. P.; Chen, L., Direct imaging of layered O3-and P2-NaxFe1/2Mn1/2O2 structures at the atomic scale. *Physical Chemistry Chemical Physics* **2014,** *16* (40), 21946-21952.

(30) Tripathi, A.; Xi, S.; Gajjela, S. R.; Balaya, P., Introducing Na-sufficient P3-Na0.9Fe0.5Mn0.5O2 as a cathode material for Na-ion batteries. *Chemical Communications* **2020,** *56* (73), 10686-10689.

(31) Nguyen, N.-A.; Kim, K.; Choi, K. H.; Jeon, H.; Lee, K.; Ryou, M.-H.; Lee, Y. M., Effect of calcination temperature on a P-type Na0.6Mn0.65Ni0.25Co0.10O2 cathode material for sodium-ion batteries. *Journal of the Electrochemical Society* **2016,** *164* (1), A6308.

(32) Komaba, S.; Yabuuchi, N.; Nakayama, T.; Ogata, A.; Ishikawa, T.; Nakai, I., Study on the reversible electrode reaction of Na1–xNi0.5Mn0.5O2 for a rechargeable sodium-ion battery. *Inorganic Chemistry* **2012,** *51* (11), 6211-6220.

(33) Lee, E.; Brown, D. E.; Alp, E. E.; Ren, Y.; Lu, J.; Woo, J.-J.; Johnson, C. S., New insights into the performance degradation of Fe-based layered oxides in sodium-ion batteries: instability of Fe3+/Fe4+ redox in α-NaFeO2. *Chemistry of Materials* **2015,** *27* (19), 6755-6764.

(34) Zhao, J.; Xu, J.; Lee, D. H.; Dimov, N.; Meng, Y. S.; Okada, S., Electrochemical and thermal properties of P2-type Na2/3Fe1/3Mn2/3O2 for Na-ion batteries. *Journal of Power Sources* **2014,** *264*, 235-239.

(35) Ma, X.; Chen, H.; Ceder, G., Electrochemical properties of monoclinic NaMnO2. *Journal of the Electrochemical Society* **2011,** *158* (12), A1307.

(36) Kumakura, S.; Tahara, Y.; Kubota, K.; Chihara, K.; Komaba, S., Sodium and Manganese Stoichiometry of P2 - Type Na2/3MnO2. *Angewandte Chemie* **2016,** *128* (41), 12952-12955.

(37) Zhou, X.; Zhao, A.; Chen, Z.; Cao, Y., Research progress of tunnel-structural Na0. 44MnO2 cathode for sodium-ion batteries: a mini review. *Electrochemistry Communications* **2020**, 106897.

(38) You, Y.; Dolocan, A.; Li, W.; Manthiram, A., Understanding the air-exposure degradation chemistry at a nanoscale of layered oxide cathodes for sodium-ion batteries. *Nano Letters* **2018,** *19* (1), 182-188.

(39) Duffort, V.; Talaie, E.; Black, R.; Nazar, L. F., Uptake of CO2 in layered P2-Na0. 67Mn0. 5Fe0. 5O2: insertion of carbonate anions. *Chemistry of Materials* **2015,** *27* (7), 2515-2524.

(40) Zhao, C.; Wang, Q.; Yao, Z.; Wang, J.; Sánchez-Lengeling, B.; Ding, F.; Qi, X.; Lu, Y.; Bai, X.; Li, B., Rational design of layered oxide materials for sodium-ion batteries. *Science* **2020,** *370* (6517), 708-711.

(41) Adhikari, T.; Hebert, A.; Adamic, M.; Yao, J.; Potts, K.; McCalla, E., Development of High-Throughput Methods for Sodium-Ion Battery Cathodes. *ACS Combinatorial Science* **2020,** *22* (6), 311-318.

(42) McCalla, E.; Parmaklis, M.; Rehman, S.; Anderson, E.; Jia, S.; Hebert, A.; Potts, K.; Jonderian, A.; Adhikari, T.; Adamič, M., Combinatorial methods in advanced battery materials design. *Canadian Journal of Chemistry* **2021,** *100*(2), 132-143.

(43) Potts, K. P.; Grignon, E.; McCalla, E., Accelerated Screening of High-Energy Lithium-Ion Battery Cathodes. *ACS Applied Energy Materials* **2019,** *2* (12), 8388-8393.

(44) Fleischauer, M.; Hatchard, T.; Rockwell, G.; Topple, J.; Trussler, S.; Jericho, S.; Jericho, M.; Dahn, J., Design and testing of a 64-channel combinatorial electrochemical cell. *Journal of the Electrochemical Society* **2003,** *150* (11), A1465.

(45) Shard, A. G.; Counsell, J. D.; Cant, D. J.; Smith, E. F.; Navabpour, P.; Zhang, X.; Blomfield, C. J., Intensity calibration and sensitivity factors for XPS instruments with monochromatic Ag Lα and Al Kα sources. *Surface and Interface Analysis* **2019,** *51* (7), 763-773.

(46) Yabuuchi, N.; Hara, R.; Kajiyama, M.; Kubota, K.; Ishigaki, T.; Hoshikawa, A.; Komaba, S., New O2/P2 - type Li - Excess Layered Manganese Oxides as Promising Multi -

Functional Electrode Materials for Rechargeable Li/Na Batteries. *Advanced Energy Materials* **2014,** *4* (13), 1301453.

(47) Cabana, J.; Chernova, N. A.; Xiao, J.; Roppolo, M.; Aldi, K. A.; Whittingham, M. S.; Grey, C. P., Study of the Transition Metal Ordering in Layered Na x Ni x/2Mn1 ‐ x/2O2 (2/3⩽ x⩽ 1) and Consequences of Na/Li Exchange. *Inorganic Chemistry* **2013,** *52* (15), 8540-8550.

(48) Hasa, I.; Buchholz, D.; Passerini, S.; Hassoun, J., A comparative study of layered transition metal oxide cathodes for application in sodium-ion battery. *ACS Applied Materials & Interfaces* **2015,** *7* (9), 5206-5212.

(49) Buchholz, D.; Vaalma, C.; Chagas, L. G.; Passerini, S., Mg-doping for improved long-term cyclability of layered Na-ion cathode materials–The example of P2-type NaxMg0.11Mn0.89O2. *Journal of Power Sources* **2015,** *282*, 581-585.

(50) Kim, D.; Kang, S. H.; Slater, M.; Rood, S.; Vaughey, J. T.; Karan, N.; Balasubramanian, M.; Johnson, C. S., Enabling sodium batteries using lithium ‐ substituted sodium layered transition metal oxide cathodes. *Advanced Energy Materials* **2011,** *1* (3), 333-336.

(51) Kim, E. J.; Ma, L. A.; Duda, L. C.; Pickup, D. M.; Chadwick, A. V.; Younesi, R.; Irvine, J. T.; Armstrong, A. R., Oxygen redox activity through a reductive coupling mechanism in the P3-type nickel-doped sodium manganese oxide. *ACS Applied Energy Materials* **2019,** *3* (1), 184-191.

(52) Maddukuri, S.; Valerie, P.; Upadhyayula, V. V., Synthesis and Electrochemical Study of New P3 Type Layered Na0.6Ni0.25Mn0.5Co0.25O2 for Sodium ‐ Ion Batteries. *ChemistrySelect* **2017,** *2* (20), 5660-5666.

(53) Song, B.; Hu, E.; Liu, J.; Zhang, Y.; Yang, X.-Q.; Nanda, J.; Huq, A.; Page, K., A novel P3-type Na2/3Mg1/3Mn2/3O2 as high capacity sodium-ion cathode using reversible oxygen redox. *Journal of Materials Chemistry A* **2019,** *7* (4), 1491-1498.

(54) Zhou, Y.-N.; Wang, P.-F.; Zhang, X.-D.; Huang, L.-B.; Wang, W.-P.; Yin, Y.-X.; Xu, S.; Guo, Y.-G., Air-stable and high-voltage layered P3-type cathode for sodium-ion full battery. *ACS Applied Materials & Interfaces* **2019,** *11* (27), 24184-24191.

(55) Grey, I.; Li, C., New silica-containing ferrite phases in the system NaFeO2 SiO2. *Journal of Solid State Chemistry* **1987,** *69* (1), 116-125.

(56) McCalla, E.; Rowe, A.; Shunmugasundaram, R.; Dahn, J., Structural study of the Li–Mn–Ni oxide pseudoternary system of interest for positive electrodes of Li-ion batteries. *Chemistry of Materials* **2013,** *25* (6), 989-999.

(57) Grosvenor, A.; Kobe, B.; Biesinger, M.; McIntyre, N., Investigation of multiplet splitting of Fe 2p XPS spectra and bonding in iron compounds. *Surface and Interface Analysis: An International Journal devoted to the development and application of techniques for the analysis of surfaces, interfaces and thin films* **2004,** *36* (12), 1564-1574.

(58) Galakhov, V.; Demeter, M.; Bartkowski, S.; Neumann, M.; Ovechkina, N.; Kurmaev, E.; Lobachevskaya, N.; Mukovskii, Y. M.; Mitchell, J.; Ederer, D., Mn 3s exchange splitting in mixed-valence manganites. *Physical Review B* **2002,** *65* (11), 113102.

(59) Gómez-García, J. F.; Pfeiffer, H., Effect of chemical composition and crystal phase of (Li, Na) FeO2 ferrites on CO2 capture properties at high temperatures. *The Journal of Physical Chemistry C* **2018,** *122* (37), 21162-21171.

(60) Vasiljevic, Z. Z.; Dojcinovic, M. P.; Krstic, J. B.; Ribic, V.; Tadic, N. B.; Ognjanovic, M.; Auger, S.; Vidic, J.; Nikolic, M. V., Synthesis and antibacterial activity of iron

manganite (FeMnO 3) particles against the environmental bacterium Bacillus subtilis. *RSC Advances* **2020,** *10* (23), 13879-13888.

(61) Zhou, X.; Guduru, R. K.; Mohanty, P., Synthesis and characterization of Na0.44MnO2 from solution precursors. *Journal of Materials Chemistry A* **2013,** *1* (8), 2757-2761.

(62) Dai, K.; Mao, J.; Song, X.; Battaglia, V.; Liu, G., Na0. 44MnO2 with very fast sodium diffusion and stable cycling synthesized via polyvinylpyrrolidone-combustion method. *Journal of Power Sources* **2015,** *285*, 161-168.

(63) Han, M. H.; Acebedo, B.; Gonzalo, E.; Fontecoba, P. S.; Clarke, S.; Saurel, D.; Rojo, T., Synthesis and Electrochemistry Study of P2-and O3-phase Na2/3Fe1/2Mn1/2O2. *Electrochimica Acta* **2015,** *182*, 1029-1036.

(64) Viswanatha, R.; Kishore, B.; Bharath, U.; Munichandraiah, N., Communication—electrochemical investigation of plate-like Na2/3Fe1/2Mn1/2O2 for sodium ion cathode. *Journal of the Electrochemical Society* **2018,** *165* (2), A263.

(65) Sathiya, M.; Thomas, J.; Batuk, D.; Pimenta, V.; Gopalan, R.; Tarascon, J.-M., Dual Stabilization and Sacrificial Effect of Na2CO3 for Increasing Capacities of Na-Ion Cells Based on P2-NaxMO2 Electrodes. *Chemistry of Materials* **2017,** *29* (14), 5948-5956.

(66) Rowe, A.; Camardese, J.; McCalla, E.; Dahn, J., High precision coulometry studies of single-phase layered compositions in the Li-Mn-Ni-O system. *Journal of the Electrochemical Society* **2014,** *161* (9), A1189.

Chapter 3 Chemical Speed Dating: the Impact of 52 Dopants in Na-Mn-O Cathodes

In **Chapter 2**, I highlighted the successful application of high-throughput methodologies to the Na-Mn-Fe-O pseudoternary system. The investigation revealed that high-Mn P2 materials, which have garnered significant attention, exhibit superior electrochemical performance. Notably, only 5% substitution of iron was found to stabilize the Jahn-Teller distortion, while a further 10% substitution improved cycling stability. However, these high-Mn materials still face challenges such as moisture instability in air and low voltages. Additionally, the exploration within the pseudoternary system is limited to certain combinations of elements. Recognizing the significant impact that even small amounts of Fe substitution have on various properties, we expanded our high-throughput system to explore novel materials and include a broader range of chemical options. We introduce a "chemical speed dating" approach to showcase the diverse effects of different dopants in **Chapter 3**. Notably, the complexity of the study increased significantly, incorporating 52 different chemical elements to facilitate high-throughput screening and optimization, supported by exploratory data analysis. Furthermore, we evaluated additional properties, such as rate performance and Na^+ diffusion constants. This chapter not only provides insights into the effects of various dopants but also serves as a comprehensive guide for rational material design, offering a broad perspective on the potential modifications achievable through doping.

Chapter 3 is adapted with permission from “Jia, S.; Yao, E.; Peng, R.; Jonderian, A.; Abdolhosseini, M.; McCalla, E. Chemical Speed Dating: The Impact of 52 Dopants in Na–Mn–O Cathodes. *Chemistry of Materials* **2022**, *34* (24), 11047–11061.”

3.1 Abstract

Na-Mn-O cathodes are very promising for sodium-ion batteries but suffer major setbacks related to long-term cycling and stability in air. With our high-throughput approach, a systematic investigation of 52 different dopants from across the periodic table into $Na_{0.66}MnO_2$ is performed. The chemical composition of $Na_{0.66}Mn_{0.9}M_{0.1}O_{2+\delta}$ (M: dopant) is utilized to unravel the impact of dopants on the layered structure and investigate how different dopants influence the battery performance and air/moisture stability. A broad range of doping was possible with 20 different dopants fully integrating into the Na-Mn-O structures, including several previously unstudied dopants (Si, Sc, Ga, Rb, Rh, Cs, Re, and Tl). This yields high interest novel cathodes including the Rb-doped sample with a high specific capacity of 200 mAh g^{-1}, as well as Mo and Nb-doped samples with excellent capacity retentions of 98 % and 100 % respectively after 10 cycles compared to 92 % in the undoped $Na_{0.66}MnO_2$. Air/moisture stability of the cathode material is systematically studied, and a number of compositions show ultra-high stability in air. This systematic approach provides a rapid overview of the benefits of individual dopants, and also provides an excellent opportunity to elucidate trends across the periodic table. Significantly, we find that the presence of reversible anionic redox (absent in the undoped samples) correlates remarkably well to the bond valence sum of the dopants, implying that dopants can serve to tune the polarity of M-O bonds and encourage anionic redox behavior. Such “speed dating” reveals fundamental chemical insights and guides further design.

3.2 Introduction

The secondary battery is one of the most important energy storage technologies due to its high energy density, fast response rate, and versatile application scenarios.[1–3] Particularly, the lithium-ion battery is in high demand with outstanding electrochemical performance. However, long-term reliance on this technology is far from assured with limited mineral resources of lithium, the environmental/geopolitical problems from the usage of cobalt and nickel, and the sustainability challenge with recycling spent batteries.[4–7] Such anxieties about the future of the lithium-ion battery leads researchers toward the potentially more sustainable and cost-effective sodium-ion battery, which has a similar operating mechanism and comparable electrochemical properties.

There have been a number of attempts to develop cathode materials appropriate for sodium-ion batteries. These include layered oxides[2,8] compared to lithium-ion cathodes like $LiCoO_2$, tunnel-structure materials[9], and polyanionic compounds.[10,11] Among different materials, layered oxides are one of the most prominent candidates due to their facile manufacture, high energy density, large specific capacity, and excellent Na^+ conductivity. Delmas et al. demonstrated two principal types of layered oxides: P (Na in prismatic sites) and O (Na in octahedral sites). In the Delmas notation, a number is used to indicate the minimum number of sodium layers that must be considered before the structure repeats itself.[12] The commonly reported structures are P2, P3, and O3. In particular, the P2-type structure shown in **Figure 3.1** often demonstrates the best electrochemical properties with fast Na^+ diffusion and good capacity retention. However, there are only three well-reported elements Mn[13], Co[14], and V[15] that can form P2 materials without dopants being added. Owing to disadvantages from the toxicity and limited resources of Co and low working voltage of V, Mn is the most promising candidate for P2 material. Meanwhile, Mn-based materials have several merits, such as cheap cost, low toxicity, high reversible capacity, and tunable properties by doping.[16,17]

For $Na_{0.66}MnO_2$ (NMO) materials, the sintering temperature is crucial.[18] At temperatures below 620 °C, the P2 phase is formed. While at temperatures above 620 °C, the P2 structure will transform into distorted orthorhombic structure, noted as the P'2 structure. Kumakura et al. reported P2-$Na_{0.6}Mn_{0.9}\square_{0.1}O_2$ material (P2-NMO) and found 0.1 vacancies (□) in the MnO_6 layer were introduced during cooling.[19] However, cyclability was compromised by the local distortion caused by the Mn vacancies. Pure P'2-$Na_{0.64}MnO_2$ was reported by quenching from 1050 °C with co-operative Jahn-Tell distortion (CJTD) triggered by Mn^{III} (t_{2g}^{3}-e_{g}^{1}) ions. However, since the P'2 material shows multiple sub-phase transformations and Na^+/vacancy distortions, it has been believed that the Jahn-Teller distortion (JTD) leads to irreversible transition and degradation of the layered structure.[19,20] Even though Na_xMnO_2 materials have been investigated for decades, Recently, Kulka et al. demonstrates the synergic effect in P2 and P'2 structure, where the appropriate composite of both P2 and P'2 can achieve long-term cycling.[21] Moreover, there are a number of studies showing that the P2-NMO material can be stabilized at 850 °C or above by doping. Previously tested dopants included Li[22,23], Mg [24–26], Fe[27–29], Co[30,31], Ni[32–34], Zn[35,36], Al[37], Cu[38], and their combinations[39–42]. Doping has been proven as an effective approach to modify the structure, enhance the electrochemical property and cyclability, and increase air/moisture stability. For example, Kwon studied $Na_{0.7}[Mn_{1-x}Li_x]O_{2+y}$, and found that when $x = 0.07$, the charge/discharge curve was smoothed, and negligible capacity decay was observed with 150 mAh g^{-1} after 120 cycles when cycled from 3.0 to 3.8 V vs Na/Na^+.[43] Mg-doped material $Na_{0.66}Mg_{0.28}Mn_{0.72}O_2$ is reported with large reversible capacity of 220 mAh g^{-1} with a smooth CV curve.[26] However, only this very limited list of dopants has been studied and there is no clear trend or fundamental understanding as to why one dopant outperforms the others, or even a clear picture as to which dopant is best. Furthermore, new high-entropy materials such as $NaNi_{0.12}Cu_{0.12}Mg_{0.12}Fe_{0.15}Co_{0.15}Mn_{0.1}Ti_{0.1}Sn_{0.1}Sb_{0.04}O_2$ are now being studied[44], though without a clear understanding of the role of each dopant in these outstandingly complex compositions it is very difficult to glean any benefit from the high-entropy aspect. The recent work from Zhao et al. revealed the pattern between the chemical compositions and structures by means of extensive data mining. This work allows the prediction of whether P2 or O3 layered oxide crystal structures will form using the concept of cationic potential.[45] Therefore, such data-driven research is most effective when it leads to a simple parameter as a predictor for future design. The current research has as objective to establish such relationships for the battery performance of the materials, not only the structure taken.

Another important aspect of research into layered oxides for Na cathodes is the extent to which anionic redox (oxygen redox in the layered oxide case) can be accessed reversibly in order to enhance capacity. The extent of anionic redox is highly affected by doping. According to Zheng et al., the Cu-doped material $Na_{0.67}Mn_{0.72}Cu_{0.28}O_2$ displays oxygen redox activity with low voltage hysteresis, which is encouraged by Cu-O bonding directed to the O-*2p* orbital.[46] Furthermore, Mg/Cu-codoping into P2-$Na_{0.67}Mn_{0.75}Ni_{0.25}O_2$ demonstrates that the oxygen redox reversibility is enhanced through modifying the metal-oxygen bond energy with the presence of peroxo-like O_2^{2-} species at 4.2 V charged stage.[47] Two dominant theories have been used to explain the activity of anionic redox.[48–50] One is through transition metal-driven reduction coupling mechanism, where the oxygen symmetry rearrangement of the MO_6 octahedra can stabilize the peroxo-like O_2^{2-} species, allowing for electron transfer. The other theory assumes that anionic redox is triggered by the presence of alkali metal ions, as a result of the reduced overlap between the O *2p* orbitals and alkaline *s* orbital. In both theories, the degree of ionic-covalent nature of the M-O bond evidently plays an important role of anionic redox activity by altering the electron density available for redox reactions in the vicinity of the oxygen ions. Thus, this leads to the reasonable assumption that doping, or a substitution of the metal of that M-O bond would alter the anionic redox activity as the nature of the bond is changed.

Moreover, the structural stability of the layered oxides when exposed to air/moisture is a crucial practical consideration. This issue is particularly important considering that cathode materials may be manufactured from one country and shipped overseas for assembly. Some Mn-based oxides are extremely unstable in humid air, posing a great challenge in maintaining the structural integrity during the manufacturing process. Zuo et al. reported that the change of the XRD patterns can be observed only under air condition (RH 18 %) after exposure to air for $Na_{0.67}MnO_2$ material.[51] For Mn-based materials, Nazar et al.[52] found that Mn^{3+} can be oxidized into Mn^{4+} in the presence of the oxidizer O_2 in humid air to maintain charge neutrality while structural deformation happens. This process can increase the first charge hysteresis and degrade the battery performance.[52] Therefore, an approach to transforming Mn^{3+} into Mn^{4+} by substituting low-valence dopant in the pristine material can increase air stability. However, owing to the lack of rational design for air-stable materials, there are only a few air-stable compositions reported such as $Na_{0.66}Ni_{0.33}Mn_{0.67}O_2$[51] and $Na(Fe_{0.32}Ni_{1/3}Mn_{1/3}Al_{0.01})O_2$[53].

In **Chapter 2**, we used high-throughput methods to systematically screen the Na-Fe-Mn-O pseudo-ternary system. This system showed a large P2 solid-solution region with a rich variety of both performance and air-stability as the Fe and Na content varies. For example, we found that 10% doping of Fe into the Na-Mn-O materials was sufficient to dramatically change the cyclic voltammograms such that the numerous phase transformations rampant in the Na-Mn-O materials were suppressed. The material with low Fe content also showed the best air stability as determined by X-ray photoelectron spectroscopy (XPS). Herein, we applied the high throughput screening illustrated in **Figure 3.1** to make $Na_{0.66}Mn_{0.9}M_{0.1}O_{2+\delta}$ (M: dopant) materials with 52 different dopants in order to further understand what dopants can play a similar (or even improved) role to Fe. The target phases in this study are therefore any layered oxides that are electrochemically active, including P2, P'2, and P3. We aim to both discover the impact of dopants on the phase compositions and also on the battery performance. Through this systematic approach we establish the relationships between the dopants and resulting structure, electrochemical properties, and air stability. We further correlate trends to common chemical properties such as electronegativity and bond valence. New insights provided herein will serve as effective guidelines toward rational design of novel materials.

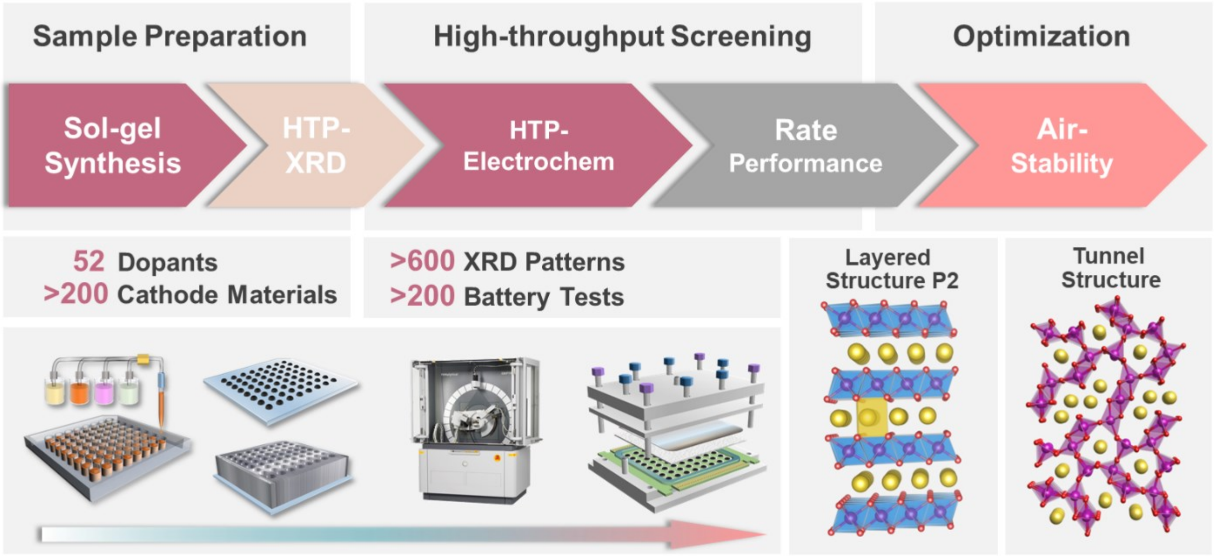

Figure 3.1 *The scheme of the workflow to realize fast chemical "speed dating" and the two main active materials investigated in this study, the layered structure, and the tunnel structure. It should be noted that the P'2 structure appears identical to the P2 structure on the scale shown here, however, the* MO_6 *octahedra are slightly distorted.*

3.3 Experimental Section

3.3.1 Material preparation

A sol-gel method was applied for the high-throughput synthesis to achieve combinatorial $Na_{0.66}Mn_{0.9}M_{0.1}O_2$ materials, as described in detail in refs.[54–56]. $NaNO_3$ and $Mn(NO_3)_2$ (Sigma-Aldrich) solutions (2.4 M) were prepared as precursors and dispensed into an 8×8 well plate with the molar ratio of 0.66:0.90 according to the stoichiometry. Aqueous solutions (1M) of various dopants listed in **Table S3.1** were prepared into 1M solution and added to the above precursor solutions at a rate of 1:9 to manganese. Since the choice of precursor might influence the final products, the nitrate salts were preferably selected as the dopant solution for sol-gel synthesis and the full list of precursors is given in **Table S3.2**. Citric acid (3 M), as a chelating agent with an equal molar fraction to the metal cations, was pipetted subsequently to stabilize the oxidation states of transition metal ions, where the carboxyl group can coordinate with transition metal ions by forming chelates. The gelation process was then carried out at 65 °C for 2 days to create homogeneous precursor gels via strong carboxylic group bonding. To prevent cross-contamination, the obtained 8×8 set of gels were pulverized and transferred onto an alumina plate mounted with an 8×8 aluminum smokestack by separating samples into independent combustion chambers. The samples were preheated at 400 °C for 2 hr to combust the citric acid and nitrates (heating rate: 2 °C min^{-1}). After removing the smokestack, the samples were then calcined at 850 °C for 12 hr in ambient air (heating rate: 5 °C min^{-1}), followed by 5 °C min^{-1} cooling rate. The lowest temperature at the position of a sample in the Muffle furnace was measured to be 843 °C, which assures even heat distribution across all samples considering the good thermal conductivity of the alumina substrate. The P'2 and P2 $Na_{0.66}MnO_{2+\delta}$ samples were synthesized by the above method but followed by quenching at 650 °C and 500 °C, respectively. The samples were transferred directly from the furnace onto a copper foil placed on a steel slab within 10 sec of opening the furnace door. Through the above high-throughput method, 52 different doped samples (5 mg each) and undoped P2 and P'2 NMO layered oxides were synthesized. 4 batches of samples (a total of 256 samples) were synthesized to demonstrate the reproducibility and feasibility.

3.3.2 X-ray diffraction

The obtained samples were characterized all via high-throughput powder X-ray diffraction (XRD) measurement[56]. Equipped with a Panalytical Empyrean diffractometer with a Mo target, the high-throughput XRD was carried out in transmission mode (60 kV, 40 mA). To develop fast but high-quality XRD patterns for Mo Kα radiation ($\lambda = 0.70926$ Å for $K\alpha_1$), a scatting angle range of 4–30° was investigated, which corresponds to 10-70° for Cu radiation. The major peak intensity with over 3000 counts was obtained for each sample within 10-min scan, which can be adopted for further Rietveld refinements. A 3D-printed sample holder was designed to keep samples on a clear mylar foil without cross-contamination in order to realize a high-throughput and automated detection. The resulting XRD patterns have had Mo $K\alpha_2$ stripped and converted to Cu-$K\alpha_1$ angles for ease of comparison to the literature that typically uses Cu-radiation XRD. The identification and refinement of all XRD patterns were conducted using Panalytical's HighScore Plus software. Multiple phase Rietveld refinement was performed on all XRD patterns using the CIF files selected by the automated phase identification performed in batch mode, shown in **Table S3.1**.

3.3.3 Electrochemistry

To investigate the electrochemical performance, combinatorial cells were utilized using 8×8 sample materials as the cathode, as described in refs.[54,55,57]. 64 parallel channels were devised into a printed circuit board (PCB, Optima Tech) with 64 gold pads coated in aluminum foil. The cathodes were composed of 2 mg of active materials combined with 20 wt. % carbon black, followed by drop-casted onto the contact pads via N-methyl-2-pyrrolidone (NMP) with 20 wt. % polyvinylidene fluoride (PVDF). NMP was then vaporized overnight at 80 °C, to yield an active material loading of 20 mg/cm^2. In an Ar-filled glove box, the assembly of the combinatorial cell was performed with 1M sodium perchlorate in propylene carbonate (PC) with 2 wt. % fluoroethylene carbonate (FEC) as the electrolyte. Sodium metal foil was used as the anode, along with a GF/D glass microfibre prefilter as a separator. On a lab-built high-throughput electrochemical system[56], cyclic voltammetry (CV) was carried out with the voltage between 1.5 and 4.3 V versus Na/Na$^+$ at different scan rates (2750 Keithley). The electrochemical properties such as specific capacities and average voltages were extracted from the processed data for multiple cycles and scan rates. The CVs were also converted to voltage profiles by integrating *Idt* to obtain the capacity as a function of voltage. The excellent reproducibility was investigated and reported with RSD of 7% on specific capacities.[55] Two protocols were used, one to investigate capacity retention and the other to determine the rate performance. The capacity retention was tested at a constant scan rate of 0.1 V/h CV for 10 cycles. The rate performance was carried out at different rates sequentially: 0.1, 0.2, 0.4, 1.0, and 2.0 V/h with 2 cycles at each rate.

3.3.4 Accelerated aging

Following the above work on single-dopant samples, several dopants that effectively stabilize the P2 phase and/or improved electrochemical performance were then selected for a co-doping study aimed at determining stability in air. The compositions were $Na_{0.66}Mn_{0.9}M_{0.05}M'_{0.05}O_2$ where M and M’ were limited to: Li, Mg, Al, Si, Fe, Co, Ni, Cu, Ga, and Rb. The resulting array of co-doped samples was synthesized with the above-described method and stored for various periods of time in different atmospheres to test stability. First, they were stored for 2 weeks in dry air (RH

< 10 %), then ambient air for 1 week (RH = 45 %), finally, humid air for 1 week (RH > 90 %). The different humidity level environments were obtained using a vapor source and a desiccant (Drerite™) in an enclosed system and monitored by a humidity meter. The temperature was maintained within 23 ± 1 °C. X-ray diffraction was performed after each storage step. The XRD patterns were fit and analyzed as described above.

3.4 Results and Discussion

3.4.1 Structure analysis

A few representative XRD patterns are shown in **Figure 3.2** along with the fits obtained after automated phase identification and Rietveld refinement of the XRD results. Four distinct electrochemically active phases (P2, P’2, P3, and the tunnel structure) are observed, revealing that dopants have a significant influence on the phase stability. Three different undoped NMO materials are obtained, with the obtained phase depending on both composition and temperature profile as described in the introduction. Based on the literature, we expect to form P’2 - NMO above 620 °C and P2-NMO below 620 °C by intaking oxygen to form vacancies on the transition metal layers. Herein, pure P’2 and P2 are achieved by quenching from 650 °C and 500 °C, respectively, as shown in **Figure 3.2b** at the same starting stoichiometry of $Na_{0.66}MnO_2$. However, a binary sample with P2 and P’2 phases was obtained for the sample slowly cooled down from 850 °C (i.e., the synthesis conditions used for all doped samples herein). The XRD patterns with some dopants are simple to analyze, Li and Si, for instance, stabilize the pure P2 and pure P’2 phases, respectively. Rb-doped sample, however, resulted in a similar XRD pattern as slow-cooling NMO (mixture of P2 and P’2), which makes it difficult to confirm that Rb integrated into both (**Table S3.1** shows changes in lattice parameters in both phases with Rb substitution suggesting it at least partially dopes both phases). In other cases, such as Mo, the fraction of P2 present drops dramatically with the P’2 phase becoming dominant. This demonstrates that the introduction of dopants can modify structural compositions dramatically, as changing formation energies of the two phases allows for the preferences of one phase conversion over the other.

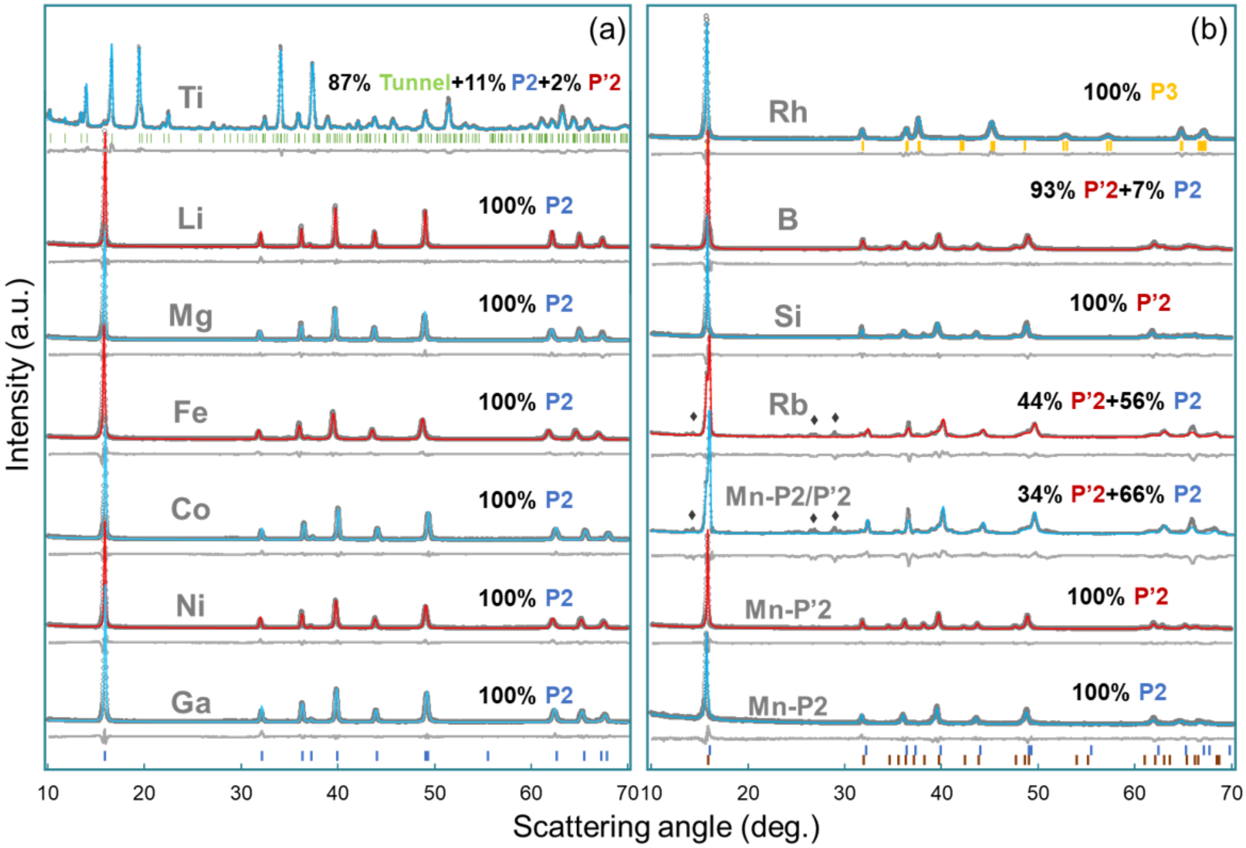

***Figure 3.2** Representative XRD patterns for different doped and undoped samples fit in 4 active material phases: P2, P’2, P3, and tunnel structure. 3 different undoped samples, Mn-P2/P’2, Mn-P’2, and Mn-P2 are obtained by slow cooling from 850 °C, quenching from 650 °C, and quenching from 500 °C, respectively.*

Quantitative analysis of the phase compositions is based on the Rietveld refinement results and are summarized in **Figure 3.3** and shown in detail in **Table S3.1**. In **Table S3.1**, we report the percent doped as being the fraction of dopant that is estimated to be in the NMO phases (either P2, P’2, tunnel, or P3) by accounting for the amount of dopant in the other phases identified in HighScore

Software. Ultimately, **Figure 3.3** and **Table S3.1** show that 20 different dopants fully dope into the NMO structures. Interestingly, of these 20 effective dopants Si, Sc, Ga, Rb, Rh, Cs, Re, and Tl have not been reported previously. Accessing such breadth of available chemistry illustrates the power of a systematic high-throughput approach. It should also be recognized when considering dopants with large ionic radii such as K, Rb, Cs that the dopants may in fact substitute into the Na sites which has 33% vacancies in the target compositions. For example, P2-$Na_{0.612}K_{0.056}MnO_2$ was successfully synthesized and reported by Wang et al.[58] with 240 mAh/g, implying that such 1s dopants doping into the sodium layer can be an attractive design strategy, and this will be discussed further below in regard to the electrochemical results. It is also important to recognize that among the inactive phases shown in **Table S3.1**, a number of these phases may form solid solution, making it impossible to determine the fraction of dopant introduced into the layered structures. For example, Mn_2O_3 is the most common phase, and many dopants can form binary oxides with manganese as illustrated in **Table S3.1**, such as Ca, V, Sr, Y, Pd, Te, Ba, W, Ir and La. This makes the level of dopant impossible to identify in such samples given that the dopant concentration in the Mn_2O_3 phase cannot be identified. Similarly, Mn solubility into a dopant-containing 'other' phase may result in an overestimation of dopant in this phase and thus leading to calculated dopant levels being underestimated or even negative in **Table S3.1**. Even considering an underestimation of doping, the XRD analysis clearly demonstrate a high degree of doping into the NMO phases of interest for Na-ion batteries as discussed above and the impact of the dopants will be further discussed in the electrochemistry section.

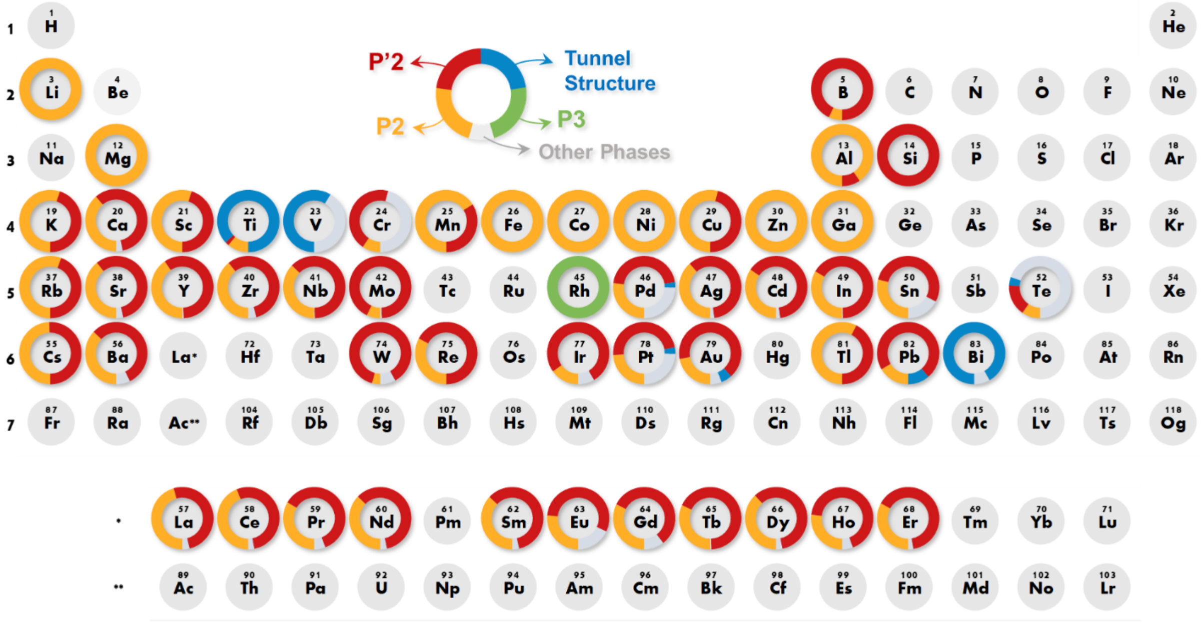

Figure 3.3 *Relative phase compositions of the 4 electrochemically active phases (P2, P'2, P3, and tunnel structure) and other phases, distributed over the periodic table for M in* $Na_{0.66}Mn_{0.9}M_{0.1}O_{2+\delta}$ *materials.*

In **Figure 3.3**, the fractions of the layered P2 and P'2 phases are illustrated in red and yellow, respectively, and are the dominant phases throughout much of the periodic table in this study. These two dominant phases are the focus of this study and generally grouped in hexagonal (P2) and orthorhombic (P'2) crystal structures respectively. The shape of the first high-intensity peak at around 16° can indicate the relative ratio of these two phases as the P'2 peak appears at a slightly lower angle than the P2 peak as shown in **Figure S3.1** shows at a slightly higher angle. Specifically, P'2 shows a slightly larger lattice parameter c than that of P2. Specific to the goodness-of-fit (*GoF*) values, excellent fits are obtained for *GoF* values less than 3 when XRD patterns have low backgrounds as is the case here.[59] The range of *GoF* values for scans with P'2 and P2 phases only are from 1.15 to 2.68 and by visual inspection these all correspond to high quality fits where the residuals at every peak are within 10% of the peak height. There are some meaningful trends over the periodic table related to the presence of these two phases. First, the slow-cooled NMO material in **Figure 3.3** was obtained with 66% P2 and 34% P’2, while the nominal composition of $Na_{0.66}MnO_2$ implies 66% Mn^{3+} and 33% Mn^{4+}. The XRD results here show that a number of dopants (Li, Mg, Fe, Co, Ni, Zn, and Ga) produce pure P2 materials, again with only 10 % substitution of Mn. All of these substituents are subvalent to Mn^{4+} such that their integration is expected to result in some Mn^{3+} being oxidized to Mn^{4+} thereby reducing the Jahn Teller distortion effect. Moreover, the ionic sizes of these dopants are all close enough to form solid solutions in the MnO_2 slab. However, Al doping resulted in 91 % P2 structure, indicating that it is not as effective in suppressing the transformation to P’2 as say Ga (100 % P2) which takes the same oxidation state (3+), and its ionic size is very close to that of Mn^{4+} (0.535 vs. 0.53 Å in 6-fold coordination). Thus, the nature of the dopants plays a critical role in stabilizing the P2 structure concerning providing Jahn-Teller active Mn ions and also being the right size to fit the space.

On the other hand, a single P’2 structure is only obtained with Si doping. This is certainly in part due to the fact that Si^{4+} doping results in reduction of Mn^{4+} back to Mn^{3+}, thereby increasing the J-T effect, but there are other supervalent dopants that do not purely stabilize the P’2 phase. Boron in this study also shows a dominant P’2 structure at 93%, shown in Figure 2b, despite taking the 3+ state. Boron doping into NMO material was recently reported by Vaalma et al. who demonstrated that at 900 °C B-doped NMO could be achieved but this resulted in 4 different phases being present [60]. We also found that Mo, W can lead to more P’2 structure. Again, there is more to the role of the dopants in stabilizing phases other than can be simply understand from their oxidation states.

Besides P2 and P’2 phases, P3 and tunnel structure $Na_{0.44}MnO_2$ were also found by doping as shown by **Figure 3.3**. The Rh-doped material results in a pure P3 structure as shown in **Figure 3.2**.

This P3 structure shows a larger *c* lattice parameter compared to the P2 structure, after converting *c* to the same scale as P2 (i.e. to a unit cell with the same number of layers), obtaining 11.26(4) Å compared 11.05(3) Å for slowly-cooled NMO, indicating larger interstitial distance allowing for Na^+ diffusion. P3 structures can also be potential cathode materials with reported excellent capacity retention: 78 % after 500 cycles[61]. From our previous report[54], we found that the P3 material can accommodate more Na content than that of P2, which can potentially solve the Na deficiency issue for P-type cathode materials. Further work examining Rh-doped materials with higher Na content may therefore be warranted. The tunnel structure (shown in **Figure 3.1**) was mainly found in Ti, V and Bi-doped samples. Compared to undoped $Na_{0.44}MnO_2$, the Ti-doped sample shows a larger lattice volume, where the lattice parameters show an increase as follows: : *a* from 9.064(9) (undoped) to 9.127(1) Å, for *b* from 26.22(3) to 26.32(4) Å, for *c* from 2.814(4) to 2.838(4) Å. A similar trend was also reported by Doeff et al.[62]. Such volume enlargement can potentially increase the Na^+ diffusion channel, this will be revisited below.

3.4.2 Electrochemical analysis

High-throughput electrochemical cyclic voltammetry (CV) was performed on all 10 % doped samples, as shown in **Figures 3.4** (as CVs) and **3.5** (as voltage curves calculated from the CVs). The electrochemical properties are extracted and summarized in **Figures 3.6** and **S3.2-S3.4**. In the CV curves, the difference dopants demonstrate dramatic differences in the charge/discharge curves. Effectively, the CV curves can be well-correlated to the structure as discussed above. Li, Mg, Al, Fe, Co, Ni, Zn, Cu, and Ga-doped samples show very smooth CV curves for the P2 structure, where the main redox Mn^{3+}/Mn^{4+} peaks located at 2.3 V and 2.1 V. In contrast, the Rh-doped P3 sample shows smooth and broad redox Mn^{3+}/Mn^{4+} peaks at 3.0 V and 2.1 V, a characteristic shape of a P3 structure consistent with our previous study.[54] However, P3 materials typically undergo

P3-O3/O3’ structural change, which can result in sluggish Na^+ transport at higher voltages.[63–66] This is consistent with the fact that the P3 structure has a considerably larger voltage difference (polarization) than the P2 structure as shown in **Figure 3.6b**.

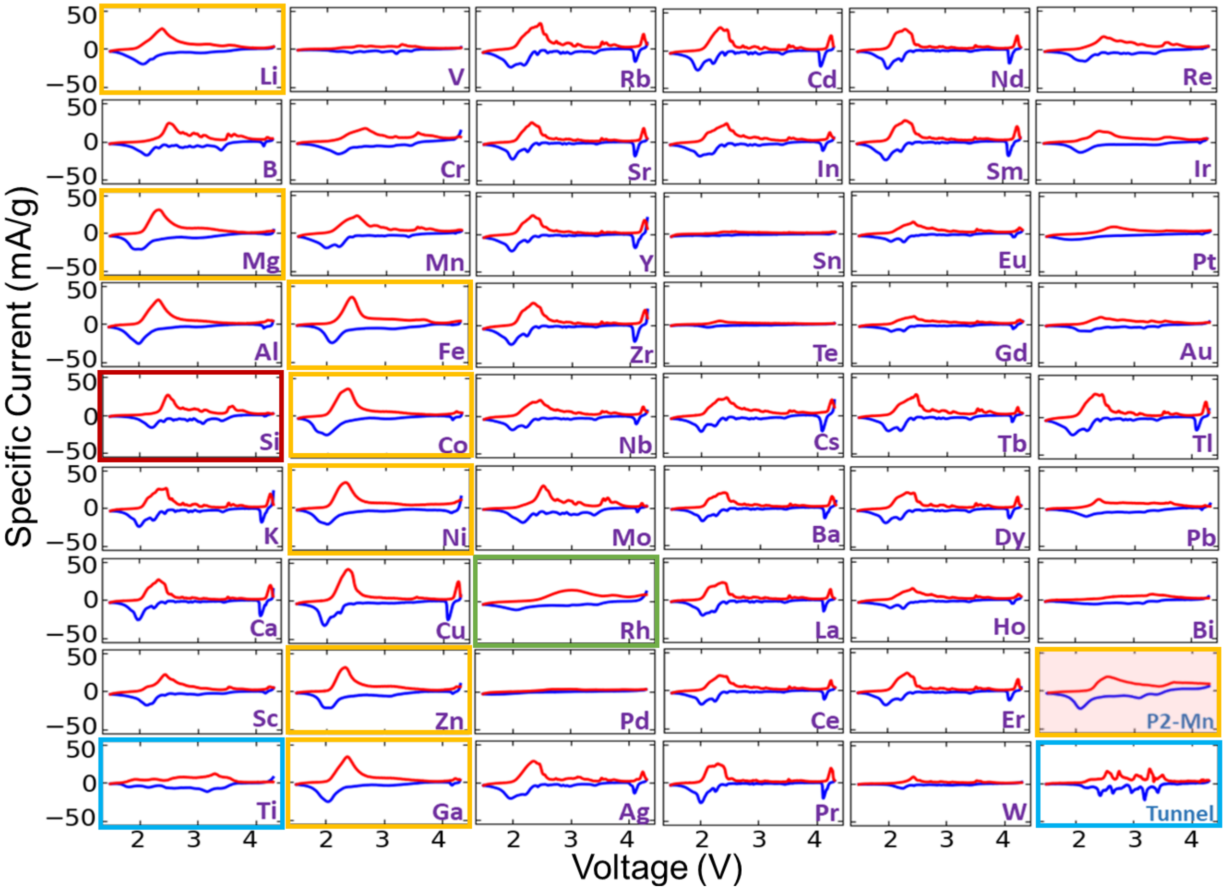

Figure 3.4 *The first cycle of the combinatorial cell with 52 different doped* $Na_{0.66}Mn_{0.9}M_{0.1}O_{2+\delta}$ *samples and the tunnel-structure* $Na_{0.44}MnO_2$ *samples. The P2-NMO sample is highlighted in light pink. The outline indicates the pure phase: yellow-P2, red-P’2, green-P3, and blue-tunnel structure. The cyclic voltammetry is performed between 1.5 V to 4.3 V vs* Na/Na^+ *at the scan rate of 0.1* $V\ h^{-1}$.

In contrast to the P2 structure, the P’2 structure can produce multiple peaks in the CVs as shown in **Figure 3.4**, which has been consistently associated with multiple phase transitions taking place during electrochemical cycling.[19,21] During the Na^+ insertion and extraction, Na^+/vacancy ordering forms, leading to different diffusion energy paths on the different sites and resulting in multiple peaks. Si and Al-doped samples shown in **Figure 3.4** demonstrate that the main oxidation peaks of the P’2 material shift up to a higher voltage as compared to P2 materials. Simultaneously, the difference between charge/discharge peak voltage is increased, indicating higher polarization for the P’2 phase, also confirmed in **Figure 3.6b**.

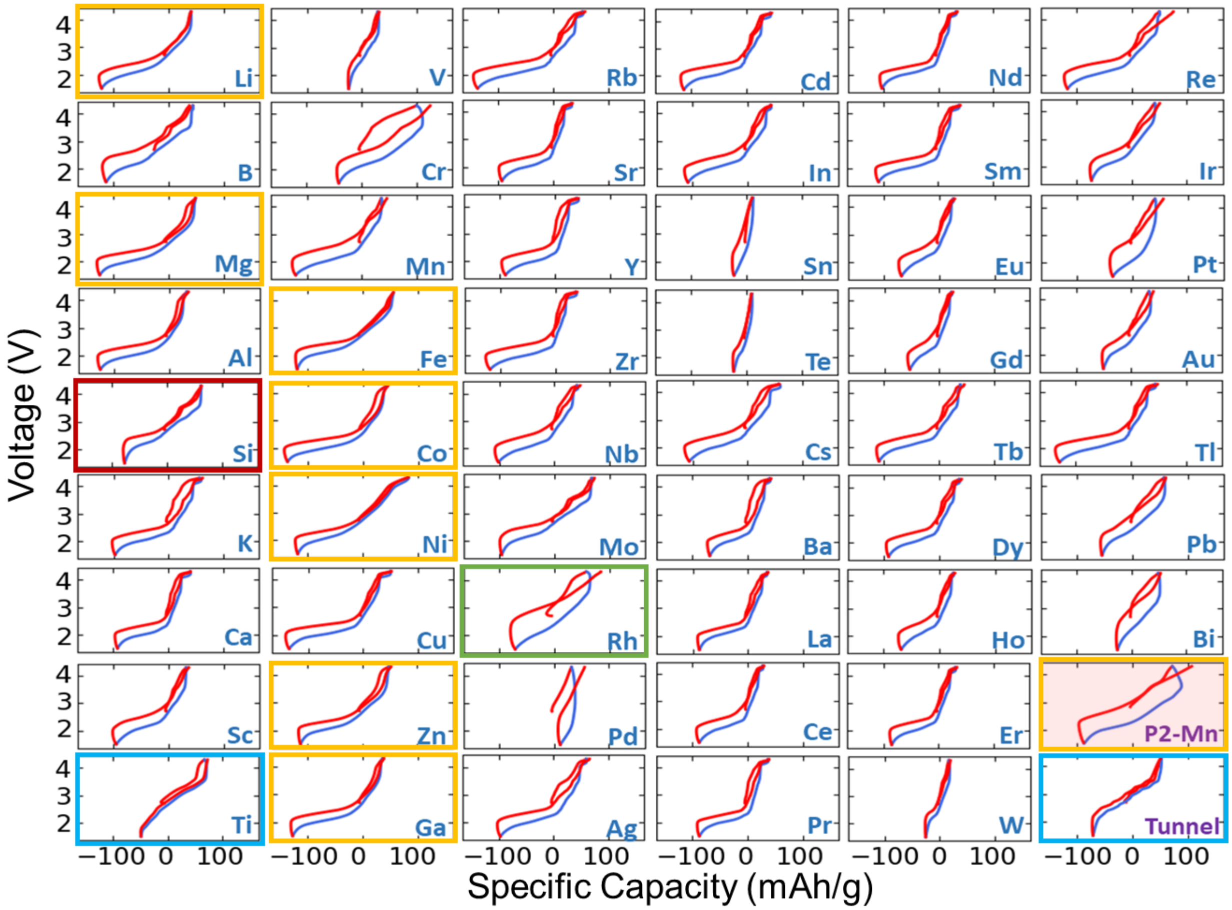

Figure 3.5 *The first charge, discharge and second charge of the combinatorial cell with 52 different doped* $Na_{0.66}Mn_{0.9}M_{0.1}O_{2+\delta}$ *samples and the tunnel-structure* $Na_{0.44}MnO_2$ *sample. The voltage curves here were obtained by processing the CVs shown in Figure 4. The outline indicates the pure phase materials: yellow-P2, red-P’2, green-P3, and blue-tunnel structure. Due to sodium-deficiency in the pristine materials, it is possible to reinsert more sodium into the cathode than was removed during the charge; this appears as negative capacities in the voltage curves here.*

Kumakura et al. demonstrated that 7 sub-phases of P’2-NMO can be identified by operando XRD.[19] Even though several sub-phases were found, the P’2 material still showed comparable cyclability to P2, which indicates such phase transitions can still be highly reversible. Similarly, we also found that P'2 materials (Si and Mo-doped) in this study exhibit decent capacity retentions after 10 cycles of about 91 and 98 %, as compared to 89 % for pure P2 phases (Co, Ni, and Zn-doped). For the average discharge voltage, B, Si, and Mo-doped samples (P'2 domain) show higher voltages than undoped NMO. Due to the distortion of the MnO_6 octahedra, the cooperative Jahn-Teller effect caused by doping alters the crystal structure, which in turn adjusts the local chemical environment of Mn and the electrochemical potential of the cathode materials.

Regarding the tunnel structure, the Ti-doped sample shows the highest discharge voltage and the lowest voltage difference (shown in **Figure 3.6b**), which adds a new strategy to modify the average voltage by introducing the tunnel structure. **Figure 3.5** shows the Ti-doped sample has the lowest hysteresis compared to the layered structure. Enhancements to the electrochemical performance of this material is assumed to be due to the increased lattice parameters allowing for higher degree of Na^+ diffusion, to be discussed below with regards to diffusion constants. The practical capacity of the tunnel structure $Na_{0.44}MnO_2$ was reported as 121 mAh g^{-1},[67,68] while the Ti-doped material herein shows an initial discharge capacity of 120 mAh/g and 99 % retention after 10 cycles. Compared to the CV for the tunnel-structure $Na_{0.44}MnO_2$ shown in **Figure 3.4**, the Ti-doped sample exhibits fewer phase transition peaks, which means the Ti-doped composite material can be a promising cathode material featuring smooth charge/discharge curves, high voltage, and low hysteresis.

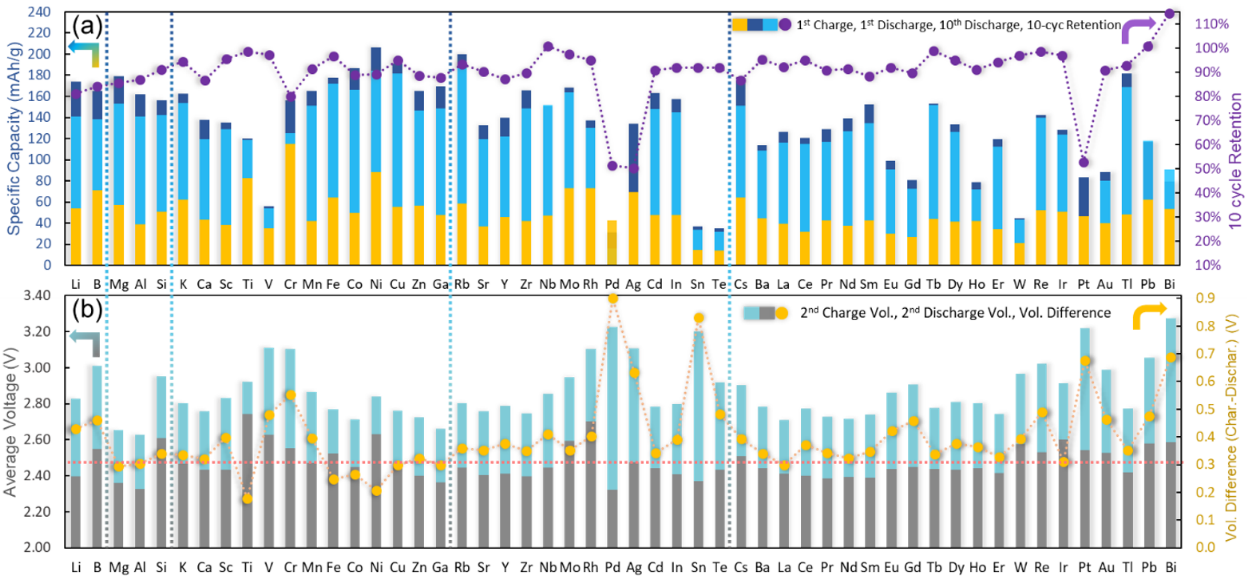

Figure 3.6 *Electrochemical properties for the 52 different doped* $Na_{0.66}Mn_{0.9}M_{0.1}O_{2+\delta}$ *samples extracted from the combinatorial cell. (a) Specific capacities on the first charge in yellow, the first discharge in deep blue, and the tenth discharge in cyan. 10-cycle retention is calculated and plotted in purple as the secondary y-axis. (b) Average voltage of the second change in turquoise, the second discharge in gray. The voltage difference is calculated by the subtraction of the charge and discharge average voltages, as shown in yellow as the secondary y-axis.*

Despite the successes outlined above, some doping elements show negative effects on the cathode performance. Often, as is the case for Te, Pt, and Sn, this correlates to a lower fraction of the layered phases (**Figure 3.3**). This demonstrates that the inactive phases can potentially restrain the battery performance, shown in **Figure 3.6**, where the poorly performing samples with extra inactive phases show depressed capacities and larger voltage differences as a result of higher electrode polarization. To reduce these inactive phases, strategies including changing the precursor material and modifying the synthesis temperature are required.

Figure 3.5 shows the voltage profiles of the first charge and discharge, and the second charge. Several electrochemical properties can be investigated by this plot. Firstly, the overlapping of the first and second charge curve could imply the air stability and irreversible phase transformation on the first charge.[52] Ni, Fe, Li, Cu, and Ga-doped samples show better overlapping, which indicates that the as-prepared samples at open-circuit voltage (OCV) show a very similar Na^+ diffusion profile. From our previous study and Duffort et al.,[52] the first charge curve can show less overlapping due to the intake of CO_2 and moisture or Na_2CO_3 deposit on the particle surface, which could hinder the Na^+ and electron conductivity. Moreover, such an air-stable feature has practical significance, inspiring us to conduct the air-stability test, discussed in the section below.

Secondly, hysteresis of the charge/discharge curve can indicate the polarization of the charge/discharge processes. In **Figure 3.5**, the materials with primarily the P'2 phase (such as Si, B-doped samples) show a larger hysteresis at the high voltage plateau, compared to P2 materials (e.g. Ni-doped). This is because fewer phase transition processes are found in P2. However, the undoped P2-NMO and Rh-doped P3 show a large hysteresis, which can imply lower conductivity of the material.

Moreover, the voltage profile can also be an indicator of the electrolyte-cathode interphase stability as shown in previous studies.[54,69] The charge endpoint slippage effect can demonstrate the irreversible electrolyte consumption by oxidation at high voltage operation. Mg, Al, Co, Ni-doped samples exhibit minor slippage effects. Particularly, the Mg-doped sample shows the least electrolyte oxidation, which implies Mg doping can sustain interphase stability at high voltage.

Given the benefits seen for a number of dopants, it is important to determine the role of morphology on improving battery performance. **Figure S3.9** shows SEM images obtained for 9 highly performing materials including the undoped. There is no systematic change in morphology with all samples showing porous agglomerates of platelets that are on the order of 1 μm in size. The Rb-doped sample however shows larger platelets such that a longer diffusion path may be needed in this sample. Otherwise, there is no clear change in morphology with the dopants studied here.

3.4.3 Rate Performance

After analysis of initial CV, the rate performance is investigated by performing cycles at different scan rates, with representative CVs shown in **Figure 3.7**. As the scan rate increases, not only do peak currents increase but the redox peaks are also separated by increasing overpotentials, as shown in **Figures 3.7a-f**. The capacities at different scan rates are calculated and summarized in **Figures 3.7g and 3.8a**. The peak current under the different scan rates is subsequently obtained and plotted in **Figure 3.7h**.

In a CV, the faradaic current is influenced by the gradient concentration of the Na^+, which may be limited by diffusion. By changing the scan rate, such diffusion control will behave differently. In **Figures 3.7a-c**, P2 materials maintain the smooth CV curve. Notably, the Fe-doped sample shows the lowest increased specific current at the endpoint of charge, indicating better rate performance with lower overpotential. While the Fe-doped sample has a lower specific capacity than the Ni-doped, it surpasses the Ni-doped in performance at 2.0 V h^{-1} as seen in **Figure 3.7g**. When more P’2 is present than in the undoped sample (34 %), the multiple peaks are still visible but they are less sinuous at higher scan rates as shown in **Figures 3.7d-f**. Although it seems counterintuitive, the multiple peaks do not interfere with the rate performance. There is a long-held belief that the multiple subphase transition and Na^+/vacancy ordering will have a negative impact the rate performance. Our systematic study, however, shows that rate performance is comparable with or without these transitions. For example, P’2 Si-doped sample with multiple phase transitions has a rate performance of 80 % (1 V h^{-1} capacity/0.1 V h^{-1} capacity), compared to 81 % for P2 Fe-doped sample.

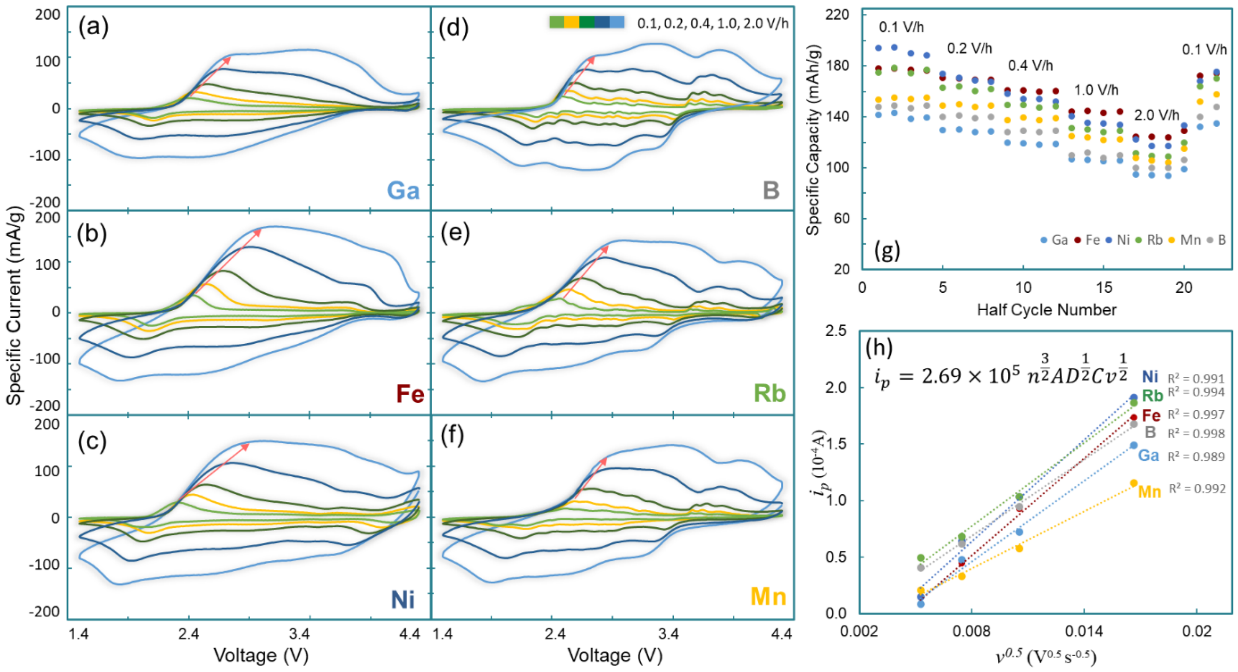

***Figure 3.7** (a-f) The CV rate test results for the Ga, Fe, Ni, B, and Rb-doped and undoped samples at the sequential scan rates of 0.1, 0.2, 0.4, 1.0, and 2.0 V h^{-1} with half cycle number started with discharge and followed by charge capacities. (g) Specific capacities extracted from the CV rate test. (h) The linear regression of the peak current and square root of scan rate. The Randles-Sevcik equation shown in (h) demonstrates the linear relationship between the peak current (i_p) and square root of scan rate (v), which is used to calculate the Na$^+$ diffusion coefficient (D).*

The Randles–Ševčík (R-S) diffusion coefficient is calculated using the R-S equation shown in **Figure 3.7h**. The correlation factors demonstrate that these layered structures obey the R-S eq., where the redox peak current is proportional to the square root of the scan rate. In the R-S eq., n is the number of electron transferred in the redox Mn^{3+}/Mn^{4+}, A is the electrode area (cm^2), C is the concentration of the electrolyte (mol cm^{-3}), and v is the scan rate (V s^{-1}). It is worth noting that the calculated diffusion coefficient D is the overall Na$^+$ diffusion within the battery. The R-S diffusion coefficient can therefore be utilized here to compare the Na$^+$ conductivities of different cathode materials tested in our high-throughput study. It should be noted that diffusion constant extracted in this manner become an estimate in cases where multiple phases are present as the diffusion constant of each phase will contribute differently depending on a number of factors such as particle size, and spatial distribution of phases. Nonetheless, samples that show a high diffusion constant despite having multiple phases present must have excellent diffusion through at least one of the phases.

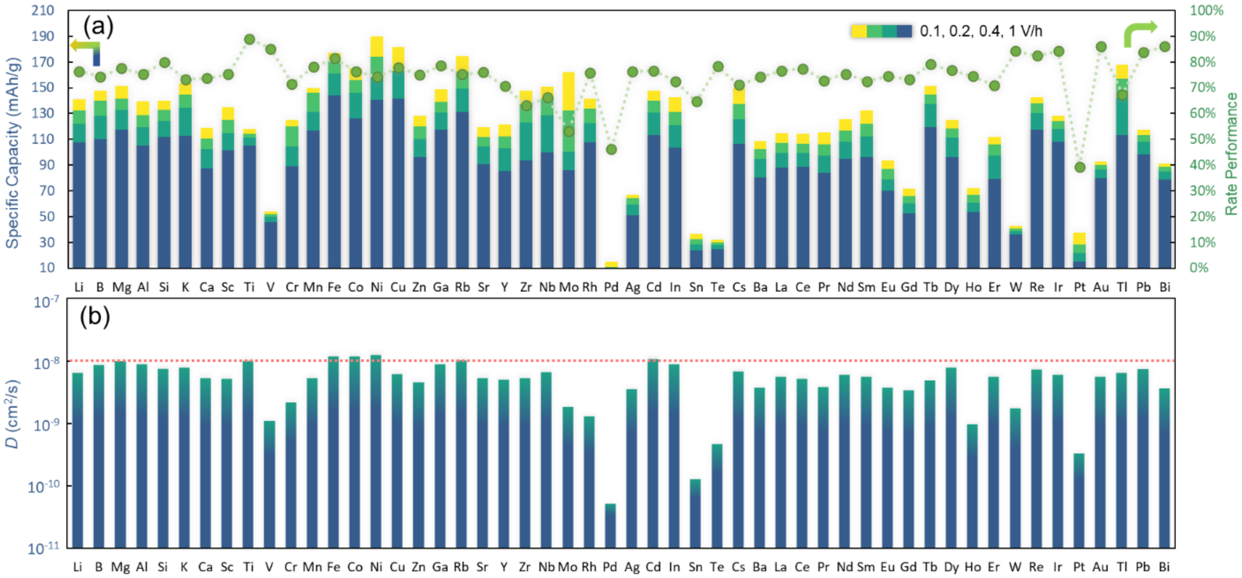

Figure 3.8 *The rate performance properties extracted from the CV rate test. (a) Specific discharge capacities extracted at different scan rate of 0.1, 0.2, 0.4, 1.0 V h^{-1}. The rate performance is calculated from the ratio of the discharge capacities (extracted from CVs) between the rate of 1.0 V h^{-1} and 0.1 V h^{-1}. (b) Randles-Sevcik diffusion coefficients are extracted from the rate test. The red dashed line shows 10^{-8} cm^2 s^{-1} as the threshold obtained here for the diffusion coefficient.*

In **Figure 3.8b**, it seems there is a diffusion constant threshold of about 10^{-8} cm^2 s^{-1}, which is probably due to an innate Na^+ diffusion mechanism. This is in good agreement with results from ref.[70] who obtained values in the range of 4.4 - 8.6×10^{-8} cm^2 s^{-1} for P2-$Na_{0.67}Mn_xCo_{1-x}O_2$ materials. The threshold shows that there may be an intrinsic limitation to how far we can design high-rate-performance NMO-based materials. This limiting effect can also be seen in **Figure 3.8a**, where the capacity ratio of about 80 % between 1 V h^{-1} and 0.1 V h^{-1} is systematically obtained for the majority of layered structures. From the Pearson correlation chart in **Figure S3.6**, we also found there is a correlation between certain parameters as shown in scatter plots in **Figures S3.6** and **3.9d**. Of highest interest specific capacities correlate well to diffusion coefficients (**Figure 3.9d**). It can be concluded that diffusion of Na^+ is a bottleneck in the layered structures, and that the inactive phases found in **Tables S3.1** not only decrease the capacity of the battery, but also hinder Na^+ diffusion through the composite electrodes.

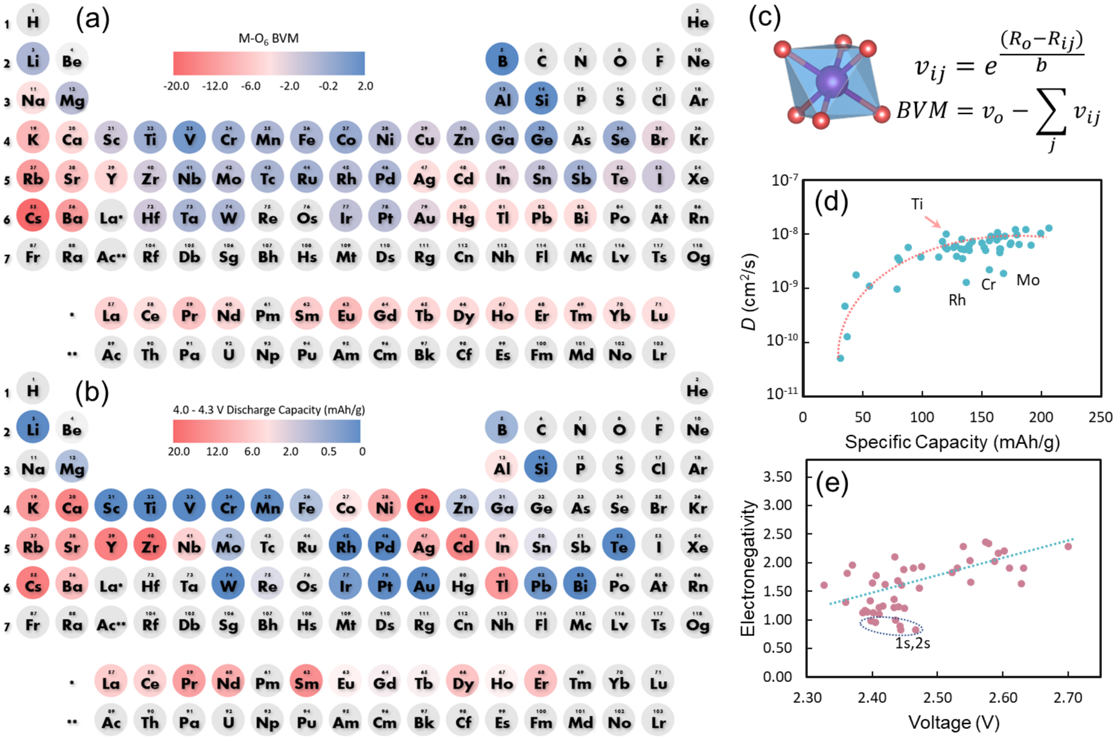

Figure 3.9 Chemical property trends over the periodic table in $Na_{0.66}Mn_{0.9}M_{0.1}O_{2+\delta}$*. (a) The heat map of the calculated bond valence mismatch of* MO_6 *octahedra. (b) The heat map of the extracted discharge capacities from 4.0 – 4.3 V. (c) The scheme of* MO_6 *octahedra and the calculation of the bond valence theory, where* v_{ij} *is the individual bond valence contribution for the i-j bond,* R_{ij} *is the bond length between the* i^{th} *and* j^{th} *ions,* R_o *is a tabulated parameter of ideal bond lengths, and b is an empirical constant. (d) The plot of diffusion coefficients vs. first specific discharge capacities. (e) The trend between the electronegativities of the dopants and the first average discharge voltage.*

It is also worth noting that the Rh-doped P3 material shows a lower rate performance and diffusion coefficient compared to the P2 structure (e.g. Ni-doped). As we discussed above, **Figures 3.4** and **3.6b** show that the P3 material has a larger voltage difference and broader redox peak, which is consistent with the lower diffusion coefficient. The tunnel structure, however, shows better rate performance with 90 % capacity retained at 1 V h^{-1} compared to 0.1 V h^{-1} for Ti-doped NMO. Even though multiple peaks and Na^+ diffusion steps are shown in **Figure 3.4**, such an excellent rate performance can be a fascinating foundation to design novel materials.

3.4.4 Accelerated aging

As mentioned above, air stability is an important metric of the cathode material for practical Na-ion battery applications. Hence, we utilize an accelerated aging protocol to investigate air stability. XRD patterns were collected from materials at four stages: fresh prepared; 2 weeks in dry air (RH < 10 %); 1 week in ambient air (RH = 45 %); and 1 week in humid air (RH > 90 %). The results are summarized in **Figure 3.10**. All pristine co-doped samples shown in **Figure 3.10d** are made up of the P2 and P'2 phases only. The representative XRD patterns in **Figures 3.10a,b** show dramatically different behavior when exposed to various air and moisture environments. The undoped-P2 phase degrades rapidly by intaking water even under dry air with less than 10 % RH, showing the instability of undoped P2 as it can easily transform into the birnessite phase ($Na_{0.23}MnO_2 \cdot 0.7H_2O$), shown in **Figure 3.10c**. During the transformation, water molecules are incorporated into the layered structure. Interestingly, hydrated birnessite phase shows a very sharp (002) peak. The interslab distance (proportional to the c axis) rises from 5.6 Å in the P2/P'2 structures to 7.1 Å in birnessite, which explains why the (002) peak appears at a much lower angle. The sharp birnessite peaks indicate that this hydrate phase has excellent crystallinity implying high conversion rates from the original layered structures within particles. Such finding is consistent with the report from Zhang et al.[71]

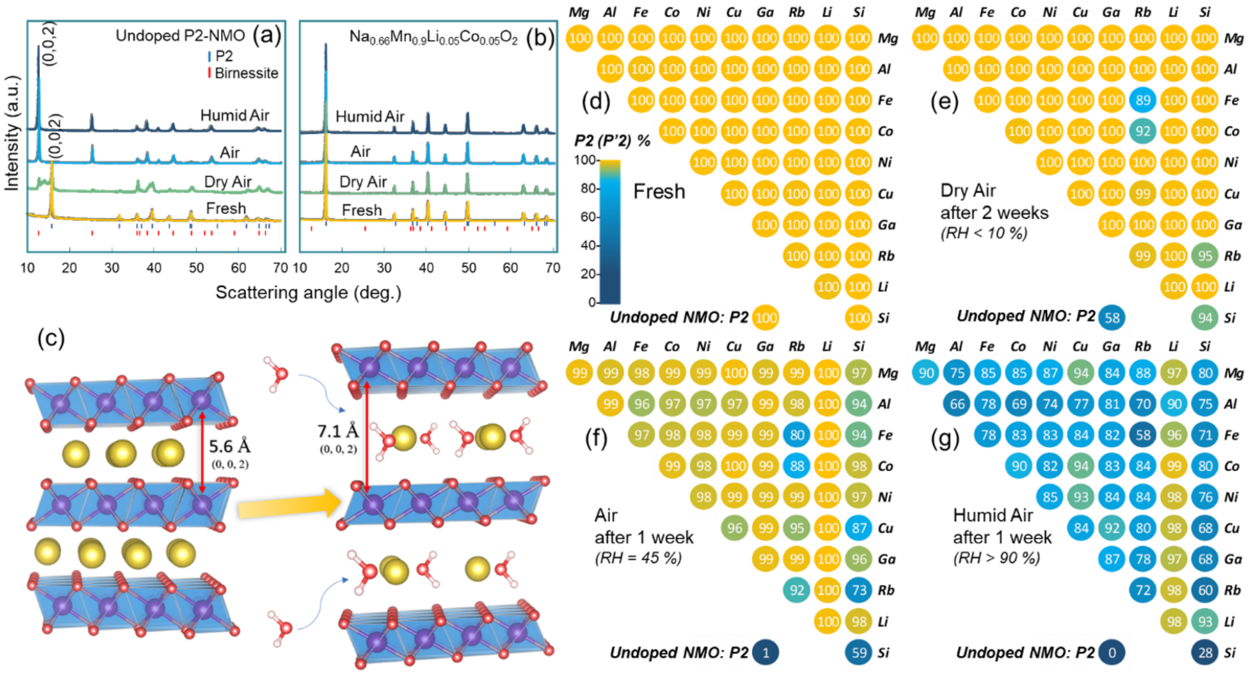

Fresh

	Mg	Al	Fe	Co	Ni	Cu	Ga	Rb	Li	Si
Mg	100	100	100	100	100	100	100	100	100	100
Al		100	100	100	100	100	100	100	100	100
Fe			100	100	100	100	100	100	100	100
Co				100	100	100	100	100	100	100
Ni					100	100	100	100	100	100
Cu						100	100	100	100	100
Ga							100	100	100	100
Rb								100	100	100
Li									100	100
Si										100

Undoped NMO: P2 100

Dry Air
after 2 weeks
(RH < 10 %)

	Mg	Al	Fe	Co	Ni	Cu	Ga	Rb	Li	Si
Mg	100	100	100	100	100	100	100	100	100	100
Al		100	100	100	100	100	100	100	100	100
Fe			100	100	100	100	100	89	100	100
Co				100	100	100	100	92	100	100
Ni					100	100	100	100	100	100
Cu						100	100	99	100	100
Ga							100	100	100	100
Rb								99	100	95
Li									100	100
Si										94

Undoped NMO: P2 58

Air
after 1 week
(RH = 45 %)

	Mg	Al	Fe	Co	Ni	Cu	Ga	Rb	Li	Si
Mg	99	99	98	99	99	100	99	99	100	97
Al		99	96	97	97	97	99	98	100	94
Fe			97	98	98	99	99	80	100	94
Co				99	98	100	99	88	100	98
Ni					98	99	99	99	100	97
Cu						96	99	95	100	87
Ga							99	99	100	96
Rb								92	100	73
Li									100	98
Si										59

Undoped NMO: P2 1

Humid Air
after 1 week
(RH > 90 %)

	Mg	Al	Fe	Co	Ni	Cu	Ga	Rb	Li	Si
Mg	90	75	85	85	87	94	84	88	97	80
Al		66	78	69	74	77	81	70	90	75
Fe			78	83	83	84	82	58	96	71
Co				90	82	94	83	84	99	80
Ni					85	93	84	84	98	76
Cu						84	92	80	98	68
Ga							87	78	97	68
Rb								72	98	60
Li									98	93
Si										28

Undoped NMO: P2 0

Figure 3.10 *The accelerated aging investigation. (a, b) XRD patterns and fitting for the undoped P2-NMO and $Na_{0.66}Mn_{0.9}Li_{0.05}Co_{0.05}O_2$ at different storage conditions, and shown on a larger scale in* ***Figure S3.8****. (c) The schematic diagram based on ref.* [51] *of the mechanism of water insertion into the layered structure resulting in an increase in the interslab distance and thereby shifting the (002) peak to lower angles in the XRD patterns. Layered structures P2 and P'2 composition ratios under different storage scenarios (i.e. 100 % represents any combination of P2 and P'2 phases only): fresh (d), after 2 weeks in dry air (e), after 1 week in regular air (f) and after 1 more week in humid air (g). Note: d-g are measurements on a single set of samples, the storage is performed sequentially.*

The Li/Co-codoped sample, however, shows a very high resistance against air and moisture (**Figure 3.10b**), indicating that such doping can greatly hinder the kinetics of the transformation. Zuo et al. reported that this transformation may accompany the oxidation of the transition metal.[51] Therefore, low oxidation-state dopants can prevent the transformation process by increasing the Mn^{4+} content over Mn^{3+} by charge balancing. This explanation agrees well with the trend we found in **Figure 3.10d-e**, where monovalent Li shows the best stability; the bivalent Mg and Cu show mild stability; and the tetravalent Si shows the worse stability. Besides the chemical valence, there are also synergistic effects from the co-doping, especially for trivalent dopants. The single-doped Al and Fe samples show only 66 % and 78 % of the P2 phase remaining after exposure to humid air, but the air stability improved after co-doping, such as with Ni, Co, and Ga. Therefore, the combinatorial map offered in **Figure 3.10** can be a very useful guideline for the designing of air-stable materials, overcoming the major roadblock to commercialization of these materials.

3.4.5 Trends across all dopants

Exploratory data analysis was conducted with visual statistic approaches such as Pearson correlation and the heat-map periodic table to investigate the trend for material designing, illustrated in **Figures 3.9, S3.2**. Therefore, we can understand if any strong or mild correlation exists amongst various variables including the chemical nature of the dopants, structures, and electrochemical properties. As mentioned above, **Figure 3.9d** demonstrates that Na^+ diffusion acts as a bottleneck limiting the amount of Na that can be cycled. Only when the diffusion constant reaches the threshold of 10^{-8} cm^2 s^{-1} is it possible to obtain specific capacities above 160 mAh g^{-1}. This is a noticeable finding that further modifications meant to improve other properties in the layered oxides must not be at the expense of the diffusion constant. Moreover, with the help of the Pearson chart, we found there is a mild positive correlation between the electronegativity of the dopants and the average voltage. When a more electronegative dopant is incorporated into the material, the voltage is subsequentially raised, as a result of the inductive effect to lift the electrochemical potential higher than the Na/Na^+ (0 V). Such trend can also be observed from the literatures, where the voltage increases with the electronegativity, such as for 3d metals from Ti to Cu: Ti (0.7-1.2 V)[72,73], V (1.5-1.8 V)[74,75], Mn (2.2-2.7 V)[17], Fe (3.2-3.4 V)[76], Co (2.7-3.7 V)[77], Ni

(3.5-4.0 V)[78], and Cu (3.7-4.1 V)[38]. Additionally, the voltage decay is one of the significant issues to maintain the energy of the battery. In this study, we observed the voltage retention is inverse proportional to the discharge voltage, where the low-voltage materials however gain voltage after 10 cycles, as demonstrated in **Figure S3.7a**. Such aspect of voltage retention is also an interesting strategy to design the material to sustain the energy density during extended cycling.

Finally, **Figure 3.4** shows some dopants have a distinct pair of reversible redox peaks at 4.1 V (discharge) and 4.2 V (charge). The undoped materials do not show any peak here indicating that this is not manganese redox. In the doped materials, we observed these peaks in both samples where the dopant is electrochemically active (e.g., Cu and Ni), and also in a high number of dopants that are electrochemically inactive (e.g., K, Rb, Cs, Zr, Cd, and Tl). In the case of inactive dopants, the extra peak at 4.1/4.2 V can only be attributed to reversible oxygen redox as electrolyte oxidation can be ruled out since it is primarily irreversible and continues to oxidize during the down sweep of voltage which does not occur here.

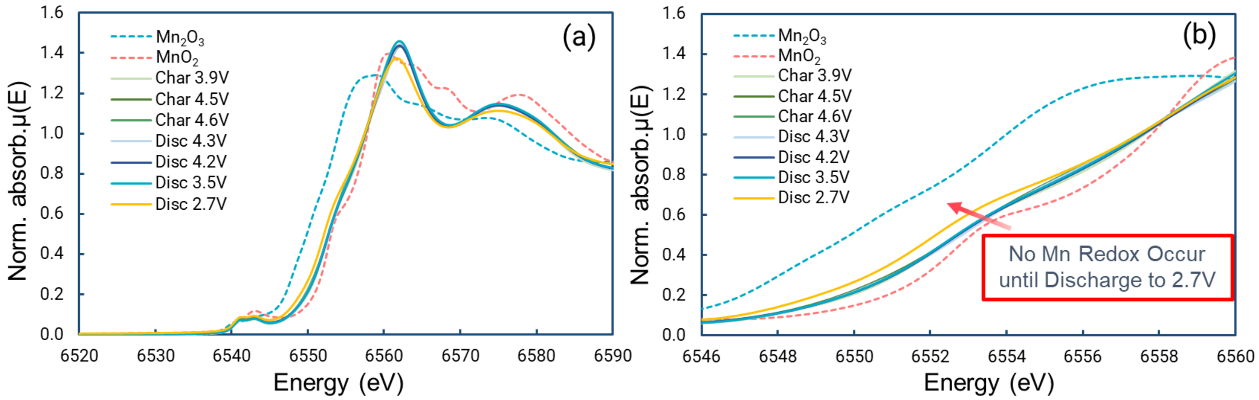

Figure 3.11 *X-ray absorption spectroscopy of ex situ cathode sample* $Na_{0.6}Mn_{0.9}Cu_{0.1}O_2$ *obtained at different charge and discharge voltages. (a) XANES spectra at Mn K-edge with zoomed in region shown in (b).*

To confirm the presence of high-voltage redox peaks resulting from anionic redox, we performed X-ray absorption spectroscopy (XAS) on *ex situ* samples of $Na_{0.6}Mn_{0.9}Cu_{0.1}O_2$, taken at various voltages during the charge and discharge cycles, as depicted in **Figure 3.11**. The results clearly show that the Mn K-edge remains unchanged during the charge process from 3.9 to 4.6 V and during discharge down to 3.5 V. It is only when the discharge reaches 2.7 V that the Mn K-edge begins to shift towards lower energy, indicating a change to lower oxidation states (similar results also observed for K-doped sample, see **Figure S3.10**). Additionally, Cu K-edge does not manifest obvious shift during cycling, as shown **Figure S3.11**. These data clearly indicate that manganese does not contribute to the high-voltage capacities observed. Thus, it is likely that these high-voltage redox peaks are associated with oxygen redox processes instead.

Interestingly, in ref. [19] undoped $Na_{0.6}Mn_{0.9}\square_{0.1}O_2$ materials (both P2 and P'2 phases) show an oxidation peak near 4.1 V but no corresponding discharge peak until below 3.5 V. Although this is likely oxygen redox, it is poorly reversible; clearly the dopants discussed here result in highly reversible oxygen redox, as opposed to what has been seen in $Na_{0.6}Mn_{0.9}\square_{0.1}O_2$ materials that rely on the transition metal vacancies only to induce oxygen redox. The anionic redox process is deemed to be a capacity booster to the cathode material and a way to dramatically increase the energy density.[48] The high number of inactive dopants that induce anionic redox here provides us with a unique opportunity to determine what property in these dopants enables the anionic redox. Therefore, we quantify the high voltage capacity in **Figure 3.9b** by calculating the discharge capacity from 4.0 to 4.3 V. The capacity ranges from 0 to 20 mAh/g, a seemingly small amount, but it should be noted that this is for 10 % substitution only, such that materials with a greater percentage of these dopants will result in considerably higher anionic capacity. **Figure 3.9b** shows a remarkable pattern across the periodic table with a number of inactive dopants in the left section of the table showing activity, but also another set of elements near the end of the transition metals (e.g., Tl, In, Cd, Ga).

The trend of anionic redox across the periodic table is so systematic that it warrants deeper understanding. The first parameter we consider that could be related to induction of anionic redox is the electronegativity of the elements, shown in **Figure S3.5**. It could be expected that a low electronegativity would allow oxygens to pull more electrons to themselves and thereby have them not lying so deep in the band structure (this can be viewed as increasing the ionic character of the Mn-O bonds via the inductive effect[79]). There are certainly similarities between **Figures 3.9b** and **S3.4**, particularly with the left side of the table showing high activities (red in both cases). However, the electronegativity does not show the trend near the end of the transition metals (e.g. In, Tl have relatively high electronegativities). We speculate that the limitation of the electronegativity here is that it does not take into account the oxidation states and the ionic-covalent nature of the M-O bond, and as such it only explains part of the trend. We therefore explore the bond valence sum approach. **Figure 3.9c** shows the bond valance mismatch (BVM)[80] for each dopant when introduced at a Mn site into the P2 structure (though the trend is unaffected if the P'2 structure is used instead as the local structure is very similar). The trend in BVM in **Figure 3.9c** is incredibly well related to that of the anionic activity in **Figure 3.9b** with ions with extremely high valence values (high negative mismatch values) with values below approximately -1.4 (value for Sn which shows the smallest anionic peak) correlating with induced anionic activity. In fact, the only elements that break the pattern are: (i) Pb, Bi and Te, (that all show low anionic activity, but they also show either the tunnel or 'other' phases in **Figure 3.4**), (ii) the Zr sample with ZrO_2 as a secondary phase (as reported by Yu et al., this exhibits anionic redox activity by Zr^{4+} forming a coating and doping by regulation of electronic state of O *2p* energy level[81]), and (iii) Ni, Cu that show more anionic activity than expected but are both known to show cationic redox.

We therefore propose that bond valence mismatch may be an excellent predictor of whether or not a dopant may induce oxygen redox in its vicinity in the NMO layered structures. It should be noted that elements like K, Rb and Cs may in fact have such a large mismatch that they occupy Na sites, but nonetheless their mismatch on the Na site is also very large (-2.3 to -6.2). A highly negative value in **Figure 3.9a** implies that the dopant is too big for the site in the lattice, which again implies the electron(s) occupy the space near the neighbouring oxygens more so than when smaller dopants are utilized. The fact that the bond valence approach is a calculation for given ions (rather than atoms as is the case for electronegativity) clearly gives a better predictor of anionic redox activity.

3.5 Conclusions

Further to previous research, this high-throughput doping study on $Na_{0.66}Mn_{0.9}M_{0.1}O_{2+\delta}$ was performed with 52 different M elements, followed by comprehensive and informative exploratory data analysis. The structure information and electrochemical properties of 4 active phases, P2, P’2, P3, and tunnel structure, have been identified and investigated, with the help with high-throughput XRD and electrochemical tests. The results confirm a strong correlation between the structure and battery performance. This broad-view doping study of Na-Mn-O materials provides the framework for rational design guidelines for this family of materials, highlighting how combinatorial studies are imperative. The dopants, Li, Mg, Fe, Co, Ni, Zn, and Ga, show beneficial impact on stabilizing the P2 structure and suppress phase transformations during electrochemical cycling as indicated by the smoothed CV curve. The dopants, Si, B, Mo, and W, however, preserve the co-operative Jahn-Teller distortion for Mn^{III} (t_{2g}^{3}-e_{g}^{1}), which leads to the P’2 phase, and multiple peaks observed on CV.

Even though the conventional view concerning P’2 materials is that multiple sub-phase transitions lead to degradation of the battery, we still found the promising dopants such as Si, B, and Mo can stabilize the distorted structure with comparable electrochemical properties. Mo-doped sample delivers 168 mAh g^{-1} first discharge capacity with 98 % retention after 10 cycles. Moreover, the serendipity in this work demonstrated a number of previously unstudied (or understudied) dopants such as Ga, B, Si, Rb, Mo, In, Re, Cs, Tl, and Tb lead to promising novel battery materials.

Beyond simply uncovering promising new materials, exploratory data analysis was utilized to explore correlations over the periodic table. For the capacity booster, the anionic redox triggered by various dopants were identified and investigated, which exhibits the similar trend with calculated bond-valence mismatch for the octahedral MO_6. Considering that the air/moisture instability of Mn-containing Na cathodes is a crucial roadblock to commercialization, accelerated aging tests provide an invaluable guideline for designing stable materials. The co-doping study demonstrates that as little as 5 % Li-codoped samples, $Na_{0.66}Mn_{0.9}Li_{0.05}Co_{0.05}O_2$, for example, substantially improve the air stability to over 99 % structure retention, compared to 0 % in the undoped P2 NMO in a one-month aging regimen. We have demonstrated that a small content of subvalent dopants such as Li, Mg, and Cu are sufficient to dramatically enhance the air stability.

In sum, through the high-throughput method and data-driven exploration, this study successfully provided many novel insights towards higher energy density, fast charging, and more-air-stable cathode materials in sodium-ion batteries. These new understandings among the chemical compositions, crystal structures, air/moisture stability, and electrochemical properties can lead to new methodologies of rational material design and development.

3.6 Acknowledgments

This work was funded by NSERC under the auspices of a discovery grant and the Canadian Foundation for Innovation. SJ acknowledges an FRQNT graduate student scholarship.

3.7 Supporting Information

Table S3.1 *The results of XRD refinement with different dopants.*

Dopant	Phase	Molar %	Dope %	Unidentified Peak %	GoF (χ2)	Space group	*a* [Å]	*b* [Å]	*c* [Å]
Li	P2-Na0.66 Mn0.9 O2	100%	10%		1.68	P 63/m m c	2.873(3)	2.873(3)	11.22(1)
B	P2-Na0.66 Mn0.9 O2	7%	10%		1.85	P 63/m m c	2.863(1)	2.863(1)	11.27(5)
	P'2-Na0.66 Mn O2	93%				C m c m	2.83(1)	5.19(2)	11.27(5)
Mg	Na0.66 Mn0.90 Mg0.10 O2	100%	10%		1.38	P 63/m m c	2.872(1)	2.872(1)	11.241(3)
Al	P2-Na0.66 Mn0.9 O2	91%	10%	2%	1.82	P 63/m m c	2.841(5)	2.841(5)	11.15(2)
	P'2-Na0.66 Mn O2	9%				C m c m	2.84(3)	4.81(5)	11.30(3)
Si	P'2-Na0.66 Mn O2	100%	10%		1.99	C m c m	2.88(2)	4.95(5)	11.26(5)
K	P2-Na0.66 Mn0.9 O2	55%	10%	3%	1.77	P 63/m m c	2.836(1)	2.836(1)	11.04(5)
	P'2-Na0.66 Mn O2	45%				C m c m	2.91(1)	4.76(2)	11.21(5)
Ca	P2-Na0.66 Mn0.9 O2	39%	-1%		1.73	P 63/m m c	2.846(9)	2.846(9)	11.08(3)
	P'2-Na0.66 Mn O2	58%				C m c m	2.92(2)	4.78(2)	11.24(3)
	Ca4 Mn4 O12	3%				P n m a	5.281(2)	7.441(2)	5.261(1)
Sc	P2-Na0.66 Mn0.9 O2	55%	10%	3%	1.15	P 63/m m c	2.84(6)	2.84(6)	11.11(2)
	P'2-Na0.66 Mn O2	45%				C m c m	2.9(6)	4.89(1)	11.27(2)
Ti	P2-Na0.66 Mn0.9 O2	11%	10%		1.71	P 63/m m c	2.86(1)	2.86(2)	11.03(2)
	P'2-Na0.66 Mn O2	2%				C m c m	2.88(5)	4.96(2)	11.26(3)
	Na7.04 Mn18 O36	87%				P b a m	9.127(1)	26.32(4)	2.838(4)
V	V32 O48	26%			1.71	I a -3	9.37(3)	9.37(3)	9.37(3)
	Na8.64 Mn18 O36	59%				P b a m	9.06(2)	26.27(5)	2.813(4)
	Mn32 O48	15%				I a -3	9.37(2)	9.37(2)	9.37(2)
Cr	Na0.80 Cr2 O4	41%			1.59	C 1 2/m 1	5.05(3)	2.86(1)	5.83(2)
	Mn32 O48	1%				I a -3	9.37(2)	9.37(2)	9.37(2)
	Na8 Cr4 O16	4%				P 1	5.83(8)	7.1(2)	9.22(2)
	P2-Na0.66 Mn0.9 O2	9%				P 63/m m c	2.843(1)	2.843(1)	11.06(3)
	P'2-Na0.66 Mn O2	45%				C m c m	2.94(3)	4.818(2)	11.27(3)
Mn	P2-Na0.66 Mn0.9 O2	66%	10%	3%	2.68	P 63/m m c	2.834(7)	2.834(7)	11.05(3)
	P'2-Na0.66 Mn O2	34%				C m c m	2.91(1)	4.83(2)	11.23(3)
Fe	Na0.66 Mn0.9 Fe0.1 O2	100%	10%		2.21	P 63/m m c	2.885(2)	2.885(2)	11.28(3)
Co	Na0.66 Mn0.9 Co0.1 O2	100%	10%		2.13	P 63/m m c	2.847(4)	2.847(4)	11.17(1)
Ni	Na0.66 Mn0.9 Ni0.1 O2	100%	10%		1.98	P 63/m m c	2.865(4)	2.865(4)	11.21(2)
Cu	P2-Na0.66 Mn0.9 O2	54%	10%	3%	2.50	P 63/m m c	2.83(1)	2.83(1)	11.03(4)
	P'2-Na0.66 Mn O2	46%				C m c m	2.91(1)	4.78(1)	11.23(4)
Zn	P2-Na0.66 Mn0.9 O2	100%	10%	2%	1.92	P 63/m m c	2.872(4)	2.872(4)	11.22(2)
Ga	Na0.66 Mn0.9 Ga0.1 O2	100%	10%		2.08	P 63/m m c	2.862(8)	2.862(8)	11.19(3)
Rb	P2-Na0.66 Mn0.9 O2	56%	10%	3%	2.01	P 63/m m c	2.83(1)	2.83(1)	11.03(4)
	P'2-Na0.66 Mn O2	44%				C m c m	2.91(1)	4.87(2)	11.23(4)

Dopant	Phase	Molar %	Dope %	Unidentified Peak %	GoF (χ2)	Space group	*a* [Å]	*b* [Å]	*c* [Å]
Sr	P2-Na0.66 Mn0.9 O2	39%	-2%		1.26	P 63/m m c	2.84(1)	2.84(1)	11.06(3)
	P'2-Na0.66 Mn O2	57%				C m c m	2.92(2)	4.79(3)	11.24(4)
	Sr4 Mn4 O12	4%				P 63/m m c	5.43(2)	5.43(2)	9.06(3)
Y	P2-Na0.66 Mn0.9 O2	40%	7%	10%	1.58	P 63/m m c	2.84(2)	2.84(2)	11.08(8)
	P'2-Na0.66 Mn O2	59%				C m c m	2.92(3)	4.77(5)	11.23(9)
	Y4 Mn4 O12	1%				P n m a	5.97(5)	7.27(6)	5.22(4)
Zr	P2-Na0.66 Mn0.9 O2	39%	-2%		1.97	P 63/m m c	2.85(9)	2.85(9)	11.1(3)
	P'2-Na0.66 Mn O2	57%				C m c m	2.93(1)	4.82(1)	11.25(4)
	Zr4 O8	2%				P 1 21/c 1	5.03(6)	5.23(9)	5.29(8)
	Zr2 O4	2%				P 42/n m c	3.6(1)	3.6(1)	5.17(2)
Nb	P2-Na0.66 Mn0.9 O2	37%	4%		2.02	P 63/m m c	2.852(9)	2.852(9)	11.12(3)
	P'2-Na0.66 Mn O2	63%				C m c m	2.93(1)	4.89(2)	11.32(3)
	Na24 Nb24 O72	0.2%				P n m a	5.5(4)	47.1(2)	5.5(5)
Mo	P2-Na0.66 Mn0.9 O2	7%	3%		2.26	P 63/m m c	2.833(7)	2.833(7)	11.09(3)
	P'2-Na0.66 Mn O2	92%				C m c m	2.86(1)	4.97(2)	11.26(2)
	Na16 Mo8 O32	1%				F d -3 m	9.08(2)	9.08(2)	9.08(2)
Rh	P3-Na0.66 Mn0.9 Rh0.1 O2	100%	10%		1.85	C 1 2/m 1	4.98(2)	2.88(1)	5.88(2)
Pd	P2-Na0.66 Mn0.9 O2	27%			1.48	P 63/m m c	2.835(7)	2.835(7)	11.12(1)
	P'2-Na0.66 Mn O2	45%				C m c m	2.89(4)	4.71(7)	11.28(4)
	Pd2 O2	14%				P 42/m m c	3.039(2)	3.039(2)	5.33(6)
	Mn32 O48	9%				P b c a	9.38(1)	9.41(3)	9.41(3)
	Na8.64 Mn18 O36	3%				P b a m	9.09(1)	26.21(4)	2.82(3)
	Pd2.94 Mn0.94	2%				P m -3 m	3.9(1)	3.9(1)	3.9(1)
Ag	P2-Na0.66 Mn0.9 O2	39%	2%		2.26	P 63/m m c	2.855(6)	2.855(6)	11.11(2)
	P'2-Na0.66 Mn O2	59%				C m c m	2.946(1)	4.822(1)	11.29(3)
	Ag4	2%				F m -3 m	4.089(7)	4.089(7)	4.089(7)
Cd	P2-Na0.66 Mn0.9 O2	35%	2%		2.07	P 63/m m c	2.852(5)	2.852(5)	11.09(2)
	P'2-Na0.66 Mn O2	63%				C m c m	2.94(1)	4.82(2)	11.27(2)
	Cd4 O4	2%				F m -3 m	4.69(6)	4.69(6)	4.69(6)
In	P2-Na0.66 Mn0.9 O2	33%	1%		1.92	P 63/m m c	2.856(7)	2.856(7)	11.14(3)
	P'2-Na0.66 Mn O2	66%				C m c m	2.91(1)	4.92(2)	11.31(3)
	In32 O48	0.3%				I a -3	10.12(2)	10.12(2)	10.12(2)
Sn	P2-Na0.66 Mn0.9 O2	29%	0%		1.61	P 63/m m c	2.843(8)	2.843(8)	11.13(2)
	P'2-Na0.66 Mn O2	54%				C m c m	3.01(3)	4.72(5)	11.26(5)
	Sn2 O4	13%				P 42/m n m	4.733(5)	4.733(5)	3.18(4)
	Mn32 O48	4%				I a -3	9.42(1)	9.42(1)	9.42(1)
Te	Na7.04 Mn18 O36	4%	0%		1.21	P b a m	9.1(2)	26.3(2)	2.823(4)
	Mn32 O48	21%				I a -3	9.3(3)	9.3(3)	9.3(3)
	P'2-Na0.66 Mn O2	16%				C m c m	2.7(1)	5.1(2)	11.3(5)
	P2-Na0.66 Mn0.9 O2	10%				P 63/m m c	2.83(1)	2.83(1)	11.052(1)
Cs	P2-Na0.66 Mn0.9 O2	49%	10%	3%	2.14	P 63/m m c	2.84(2)	2.84(2)	11.02(5)
	P'2-Na0.66 Mn O2	51%				C m c m	2.91(2)	4.81(2)	11.21(6)
Ba	P2-Na0.66 Mn0.9 O2	37%	-2%		1.83	P 63/m m c	2.842(6)	2.842(6)	11.07(2)
	P'2-Na0.66 Mn O2	56%				C m c m	2.92(1)	4.76(2)	11.23(3)
	Ba2 Mn2 O6	7%				P 63/m m c	5.68(1)	5.68(1)	4.81(8)
La	P2-Na0.66 Mn0.9 O2	46%	-5%		1.61	P 63/m m c	2.848(4)	2.848(4)	11.12(2)
	P'2-Na0.66 Mn O2	51%				C m c m	2.91(2)	4.83(3)	11.28(2)
	La5.32 Mn6 O18	4%				R -3 c	5.47(8)	5.47(8)	13.29(2)

Dopant	Phase	Molar %	Dope %	Unidentified Peak %	GoF (χ2)	Space group	*a* [Å]	*b* [Å]	*c* [Å]
Ce	P2-Na0.66 Mn0.9 O2	44%	-2%		1.55	P 63/m m c	2.847(6)	2.847(6)	11.11(2)
	P'2-Na0.66 Mn O2	53%				C m c m	2.93(1)	4.83(2)	11.29(3)
	Ce4 O8	3%				F m -3 m	5.41(8)	5.41(8)	5.41(8)
Pr	P2-Na0.66 Mn0.9 O2	33%	-5%		1.62	P 63/m m c	2.847(6)	2.847(6)	11.09(2)
	P'2-Na0.66 Mn O2	61%				C m c m	2.93(2)	4.78(2)	11.23(3)
	Pr3.40 Na0.660 Mn4 O12	6%				P n m a	5.43(1)	7.66(1)	5.44(1)
Nd	P2-Na0.66 Mn0.9 O2	37%	-1%		2.18	P 63/m m c	2.853(6)	2.853(6)	11.11(2)
	P'2-Na0.66 Mn O2	59%				C m c m	2.93(2)	4.8(3)	11.28(3)
	Nd3.80 Mn4 O12	3%				P n m a	5.43(1)	7.68(2)	5.43(1)
Sm	P2-Na0.66 Mn0.9 O2	37%	-2%		2.34	P 63/m m c	2.85(1)	2.85(1)	11.11(3)
	P'2-Na0.66 Mn O2	60%				C m c m	2.93(2)	4.8(3)	11.26(4)
	Sm4 Mn4 O12	4%				P n m a	5.47(1)	7.61(2)	5.39(2)
Eu	P2-Na0.66 Mn0.9 O2	26%	-9%		1.50	P 63/m m c	2.84(1)	2.84(1)	11.13(2)
	P'2-Na0.66 Mn O2	56%				C m c m	2.97(4)	4.72(8)	11.34(4)
	Eu4 Mn8 O20	16%				P b a m	7.38(1)	8.51(1)	5.67(8)
	Mn32 O48	2%				I a -3	9.41(1)	9.41(1)	9.41(1)
Gd	P2-Na0.66 Mn0.9 O2	32%	-11%		1.41	P 63/m m c	2.85(6)	2.85(6)	11.12(2)
	P'2-Na0.66 Mn O2	57%				C m c m	2.94(2)	4.85(4)	11.34(4)
	Gd4 Mn4 O12	3%				P n m a	5.59(9)	7.49(1)	5.32(1)
	Gd4 Mn8 O20	7%				P b a m	7.34(8)	8.54(9)	5.68(6)
Tb	P2-Na0.66 Mn0.9 O2	32%	8%	9%	1.90	P 63/m m c	2.836(4)	2.836(4)	11.079(1)
	P'2-Na0.66 Mn O2	68%				C m c m	2.86(3)	4.92(5)	11.26(2)
	Na2.68 Tb1.32 O4	1%				F m -3 m	4.73(1)	4.73(1)	4.73(1)
	Tb32 O53.92	0.02%				I a -3	10.69(1)	10.69(1)	10.69(1)
Dy	P2-Na0.66 Mn0.9 O2	38%	-1%		2.23	P 63/m m c	2.85(1)	2.85(1)	11.12(3)
	P'2-Na0.66 Mn O2	59%				C m c m	2.92(2)	4.93(3)	11.33(4)
	Dy4 Mn4 O12	3%				P n m a	5.67(1)	7.44(2)	5.29(1)
Ho	P2-Na0.66 Mn0.9 O2	27%	-3%		1.84	P 63/m m c	2.845(6)	2.845(6)	11.11(2)
	P'2-Na0.66 Mn O2	68%				C m c m	2.89(2)	4.93(4)	11.31(2)
	Ho4 Mn8 O20	4%				P b a m	7.25(1)	8.47(1)	5.666(7)
	Mo8 Na16 O32	1%				F d -3 m	9.11(1)	9.11(1)	9.11(1)
Er	P2-Na0.66 Mn0.9 O2	33%	-1%		2.60	P 63/m m c	2.848(4)	2.848(4)	11.08(1)
	P'2-Na0.66 Mn O2	64%				C m c m	2.94(2)	4.801(3)	11.26(2)
	Er4 Mn8	0.3%				P 63/m m c	5.345(1)	5.345(1)	8.706(1)
	Er32 O48	0.1%				I 21 3	10.45(1)	10.45(1)	10.45(1)
	Er4 Mn8 O20	2%				P b a m	7.22(1)	8.45(1)	5.66(7)
W	P2-Na0.66 Mn0.9 O2	4%	2%		1.65	P 63/m m c	2.83(2)	2.83(2)	11.09(3)
	P'2-Na0.66 Mn O2	88%				C m c m	2.87(6)	4.98(9)	11.27(4)
	W8 Na16 O32	3%				F d -3 m	9.118(8)	9.118(8)	9.118(8)
	Mn32 O48	5%				I a -3	9.401(7)	9.401(7)	9.401(7)
Re	P2-Na0.66 Mn0.9 O2	33%	10%	8%	1.97	P 63/m m c	2.837(1)	2.837(1)	11.081(3)
	P'2-Na0.66 Mn O2	67%				C m c m	2.91(1)	4.89(2)	11.27(3)
Ir	P2-Na0.66 Mn0.9 O2	15%	1%		1.48	P 63/m m c	2.83(1)	2.83(1)	11.14(4)
	P'2-Na0.66 Mn O2	77%				C m c m	2.87(2)	4.99(3)	11.29(2)
	Ir2 O4	3%				P 42/m n m	4.478(7)	4.478(7)	3.132(5)
	O6 Mn1.84 Ir1.16 Na1.85	2%				R -3 m	2.88(1)	2.88(1)	16.88(7)
	Mn32 O48	3%				I a -3	9.38(1)	9.38(1)	9.38(1)

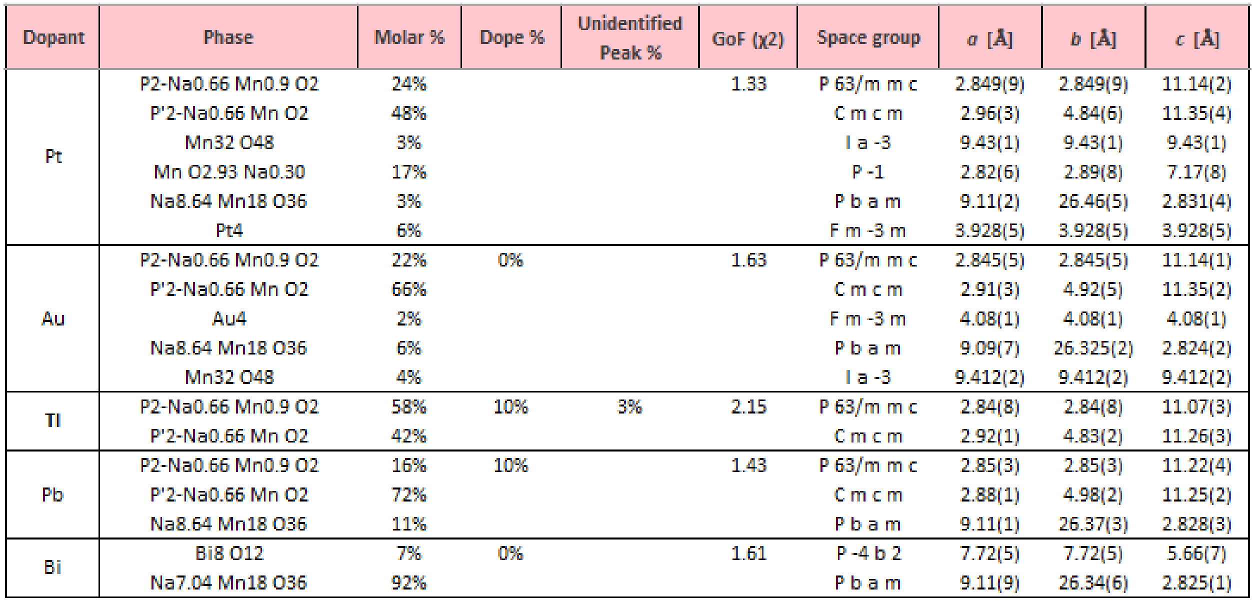

Dopant	Phase	Molar %	Dope %	Unidentified Peak %	GoF (χ2)	Space group	*a* [Å]	*b* [Å]	*c* [Å]
Pt	P2-Na0.66 Mn0.9 O2	24%			1.33	P 63/m m c	2.849(9)	2.849(9)	11.14(2)
	P'2-Na0.66 Mn O2	48%				C m c m	2.96(3)	4.84(6)	11.35(4)
	Mn32 O48	3%				I a -3	9.43(1)	9.43(1)	9.43(1)
	Mn O2.93 Na0.30	17%				P -1	2.82(6)	2.89(8)	7.17(8)
	Na8.64 Mn18 O36	3%				P b a m	9.11(2)	26.46(5)	2.831(4)
	Pt4	6%				F m -3 m	3.928(5)	3.928(5)	3.928(5)
Au	P2-Na0.66 Mn0.9 O2	22%	0%		1.63	P 63/m m c	2.845(5)	2.845(5)	11.14(1)
	P'2-Na0.66 Mn O2	66%				C m c m	2.91(3)	4.92(5)	11.35(2)
	Au4	2%				F m -3 m	4.08(1)	4.08(1)	4.08(1)
	Na8.64 Mn18 O36	6%				P b a m	9.09(7)	26.325(2)	2.824(2)
	Mn32 O48	4%				I a -3	9.412(2)	9.412(2)	9.412(2)
Tl	P2-Na0.66 Mn0.9 O2	58%	10%	3%	2.15	P 63/m m c	2.84(8)	2.84(8)	11.07(3)
	P'2-Na0.66 Mn O2	42%				C m c m	2.92(1)	4.83(2)	11.26(3)
Pb	P2-Na0.66 Mn0.9 O2	16%	10%		1.43	P 63/m m c	2.85(3)	2.85(3)	11.22(4)
	P'2-Na0.66 Mn O2	72%				C m c m	2.88(1)	4.98(2)	11.25(2)
	Na8.64 Mn18 O36	11%				P b a m	9.11(1)	26.37(3)	2.828(3)
Bi	Bi8 O12	7%	0%		1.61	P -4 b 2	7.72(5)	7.72(5)	5.66(7)
	Na7.04 Mn18 O36	92%				P b a m	9.11(9)	26.34(6)	2.825(1)

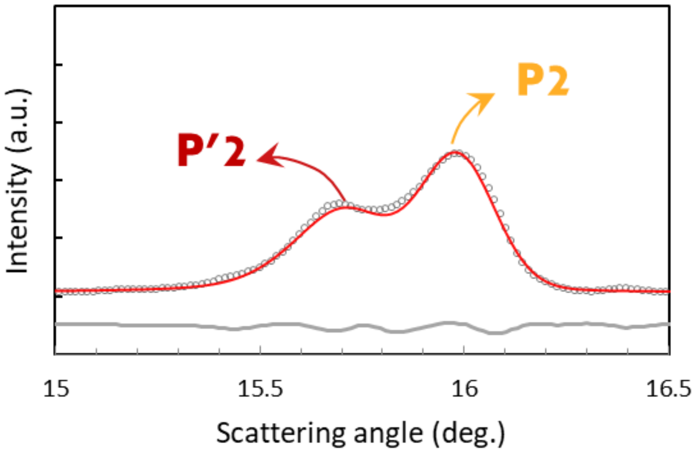

Figure S3.1 *Zoom in on the XRD pattern for Rb-doped sample to demonstrate the resolved P'2 and P2 peaks.*

Table S3.2 *List of solutions prepared for the various dopant reagents.*

Element	Dopant reagent	Solvent
Li	Lithium nitrate	H_2O
B	Boric acid	H_2O
Na	Sodium nitrate	H_2O
Mg	Magnesium nitrate hexahydrate	H_2O
Al	Aluminum nitrate monohydrate	H_2O
Si	Tetraethyl orthosilicate	EtOH
K	Potassium nitrate	H_2O
Ca	Calcium nitrate tetrahydrate	H_2O
Sc	Scandium (III) nitrate hydrate	H_2O
Ti	Titanium (IV) butoxide	EtOH
V	Ammonium metavanadate	HCl/H_2O
Cr	Chromium (III) nitrate monohydrate	H_2O
Mn	Manganese (II) nitrate	H_2O
Fe	Iron (III) nitrate monohydrate	H_2O
Co	Cobalt (II) nitrate	H_2O
Ni	Nickel (II) nitrate hexahydrate	H_2O
Cu	Copper (II) nitrate hemi(pentahydrate)	H_2O
Zn	Zinc nitrate hexahydrate	H_2O
Ga	Gallium (III) nitrate hydrate	H_2O
Rb	Rubidium nitrate	H_2O
Sr	Strontium nitrate	H_2O
Y	Yttrium (III) nitrate hexahydrate	H_2O
Zr	Zirconium dinitrate oxide hydrate	H_2O
Nb	Ammonium niobate(V) oxalate hydrate	H_2O
Mo	Ammonium molybdate (para)tetrahydrate	NH_4OH/H_2O
Rh	Rhodium (III) nitrate hydrate	H_2O
Rh	Rhodium (III) nitrate hydrate	H_2O
Pd	Palladium (II) nitrate hydrate	HCl
Ag	Silver nitrate	H_2O
Cd	Cadmium nitrate tetrahydrate	H_2O
In	Indium (III) nitrate hydrate	H_2O
Sn	Tin (II) chloride	H_2O
Cs	Cesium nitrate	H_2O
Ba	Barium nitrate	H_2O
La	Lanthanum (III) nitrate hexahydrate	H_2O
Pr	Praseodymium (III) nitrate hydrate	H_2O
Nd	Neodymium (III) nitrate hexahydrate	H_2O
Sm	Samarium (III) nitrate hexahydrate	H_2O
Eu	Europium nitrate pentahydrate	H_2O
Gd	Gadolinium nitrate hexahydrate	H_2O
Tb	Terbium nitrate hexahydrate	H_2O
Dy	Dysprosium nitrate pentahydrate	H_2O
Ho	Holmium nitrate pentahydrate	H_2O
Er	Erbium nitrate pentahydrate	H_2O
W	Tungsten (VI) oxide	NH_4OH/H_2O
Re	Ammonium perrhenate	H_2O
Ir	Iridium chloride hydrate	H_2O
Pt	Platinum (IV) chloride	H_2O
Au	Gold (III) chloride trihydrate	H_2O
Tl	Thallium nitrate pentahydrate	H_2O
Pb	Lead (II) nitrate	H_2O
Bi	Ammonium bismuth citrate	H_2O

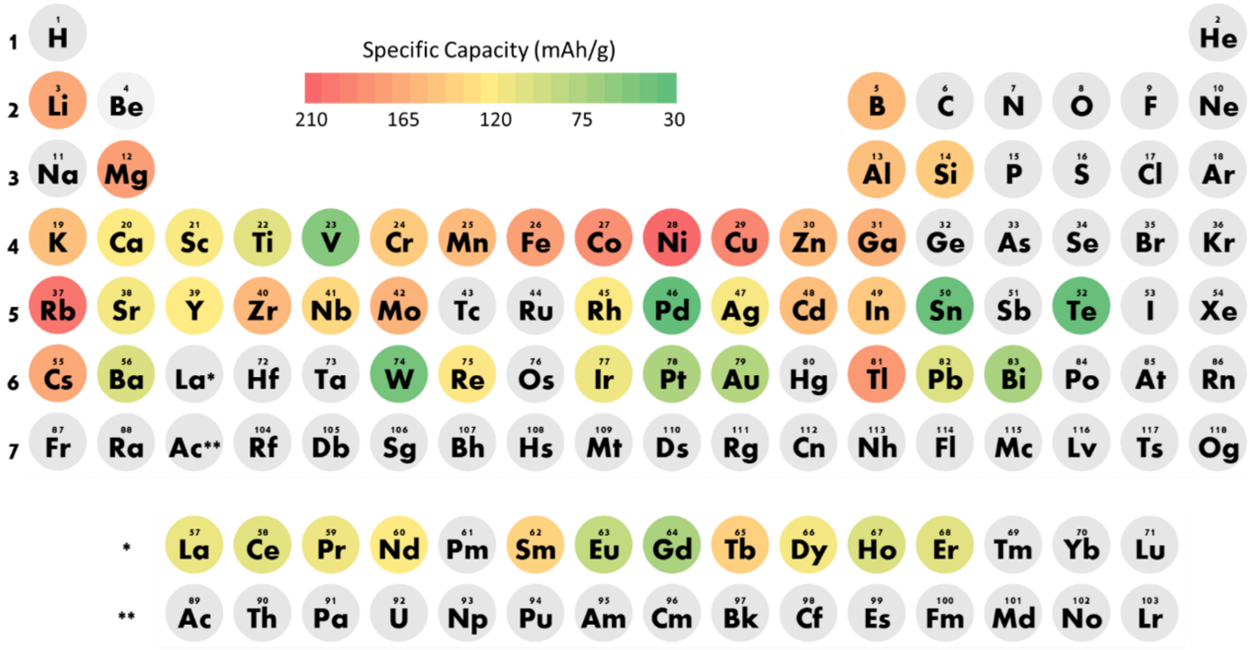

Figure S3.2 *First cycle specific discharge capacity expressed on the periodic table indicating M in* $Na_{0.66}Mn_{0.9}M_{0.1}O_{2+\delta}$.

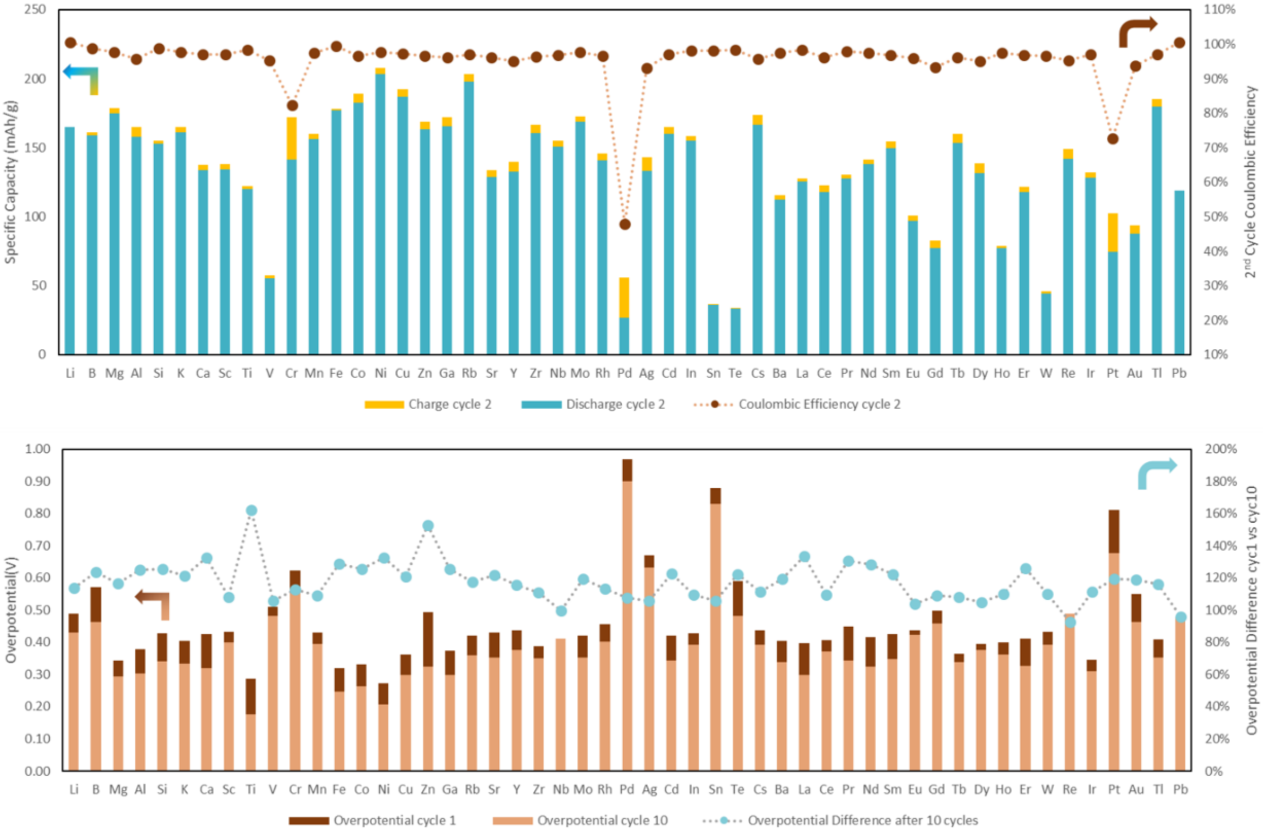

Figure S3.3 *Electrochemical properties for the* $Na_{0.66}Mn_{0.9}M_{0.1}O_{2+\delta}$ *samples extracted from the high-throughput electrochemistry.*

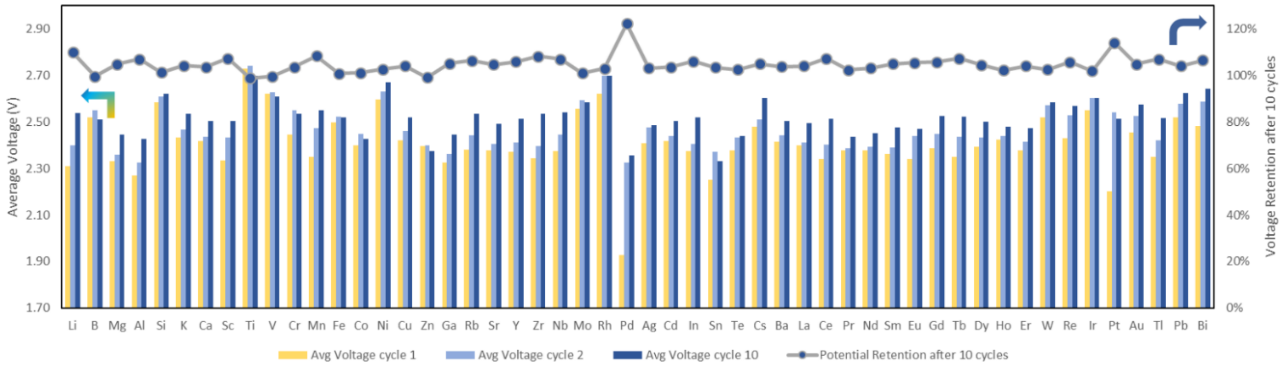

Figure S3.4 *Various voltage values for the* $Na_{0.66}Mn_{0.9}M_{0.1}O_{2+\delta}$ *samples extracted from the high-throughput electrochemistry.*

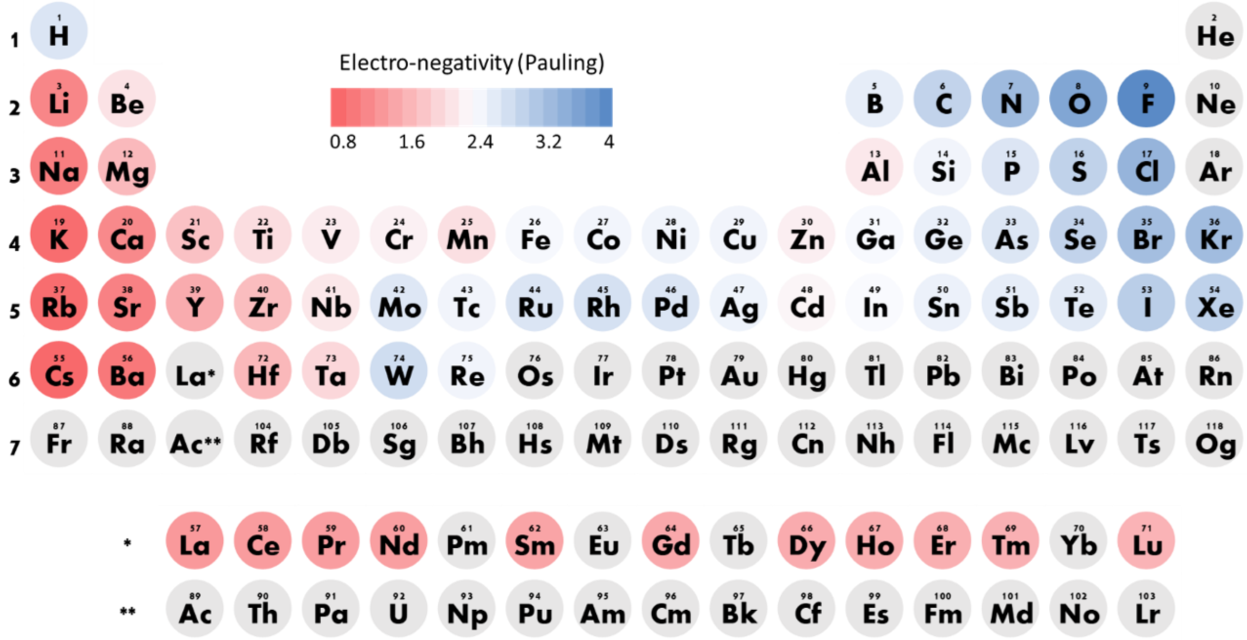

***Figure S3.5** Periodic table of electronegativity of the elements.*

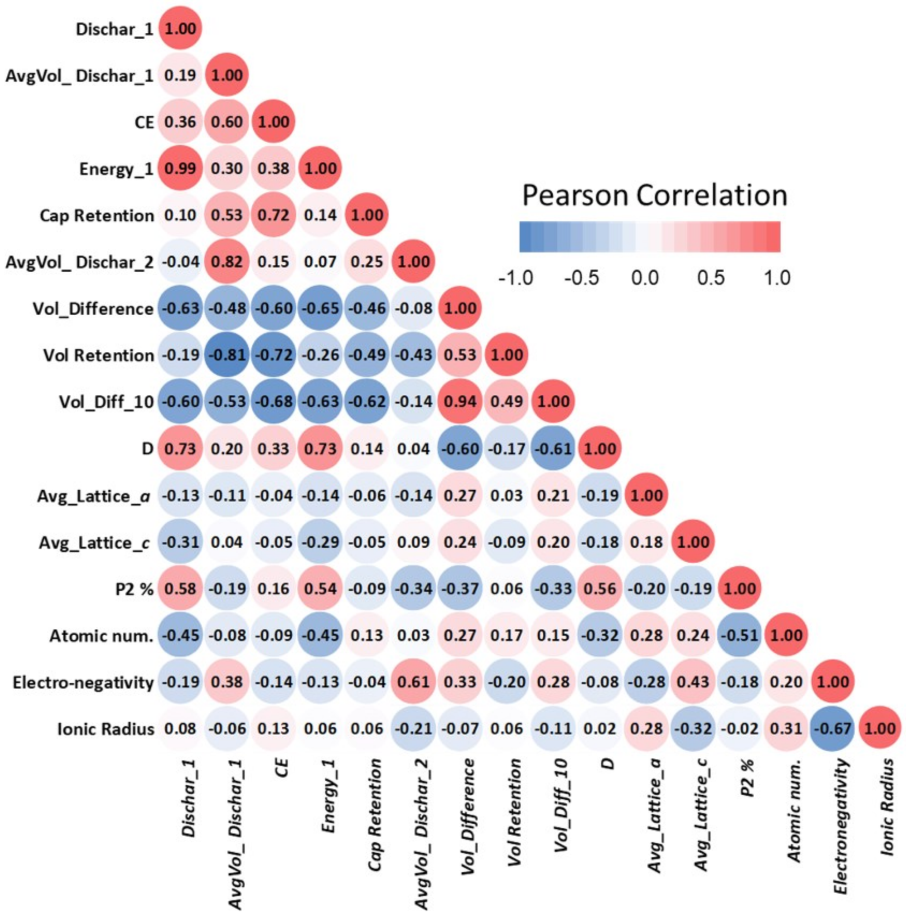

	Dischar_1	AvgVol_ Dischar_1	CE	Energy_1	Cap Retention	AvgVol_ Dischar_2	Vol_Difference	Vol Retention	Vol_Diff_10	D	Avg_Lattice_*a*	Avg_Lattice_*c*	P2 %	Atomic num.	Electronegativity	Ionic Radius
Dischar_1	1.00															
AvgVol_ Dischar_1	0.19	1.00														
CE	0.36	0.60	1.00													
Energy_1	0.99	0.30	0.38	1.00												
Cap Retention	0.10	0.53	0.72	0.14	1.00											
AvgVol_ Dischar_2	-0.04	0.82	0.15	0.07	0.25	1.00										
Vol_Difference	-0.63	-0.48	-0.60	-0.65	-0.46	-0.08	1.00									
Vol Retention	-0.19	-0.81	-0.72	-0.26	-0.49	-0.43	0.53	1.00								
Vol_Diff_10	-0.60	-0.53	-0.68	-0.63	-0.62	-0.14	0.94	0.49	1.00							
D	0.73	0.20	0.33	0.73	0.14	0.04	-0.60	-0.17	-0.61	1.00						
Avg_Lattice_*a*	-0.13	-0.11	-0.04	-0.14	-0.06	-0.14	0.27	0.03	0.21	-0.19	1.00					
Avg_Lattice_*c*	-0.31	0.04	-0.05	-0.29	-0.05	0.09	0.24	-0.09	0.20	-0.18	0.18	1.00				
P2 %	0.58	-0.19	0.16	0.54	-0.09	-0.34	-0.37	0.06	-0.33	0.56	-0.20	-0.19	1.00			
Atomic num.	-0.45	-0.08	-0.09	-0.45	0.13	0.03	0.27	0.17	0.15	-0.32	0.28	0.24	-0.51	1.00		
Electro-negativity	-0.19	0.38	-0.14	-0.13	-0.04	0.61	0.33	-0.20	0.28	-0.08	-0.28	0.43	-0.18	0.20	1.00	
Ionic Radius	0.08	-0.06	0.13	0.06	0.06	-0.21	-0.07	0.06	-0.11	0.02	0.28	-0.32	-0.02	0.31	-0.67	1.00

Figure S3.6 *Pearson correlation parameters obtained for various parameters for the dataset presented in this study. Legend:*

Abbreviation	***Parameters***
Dischar_1	Discharge capacity cycle 1
AvgVol_ Dischar_1	Average voltage discharge cycle 1
CE	Coulombic efficiency cycle 2
Energy_1	Discharge energy cycle 1
Cap Retention	Capacity retention after 10 cycles
AvgVol_ Dischar_2	Average voltage discharge cycle 2
Vol_Difference	Voltage difference between charge and discharge cycle 2
Vol Retention	Voltage retention after 10 cycles
Vol_Diff_10	Voltage difference between charge and discharge after 10 cycles
D	Diffusion coefficient
Avg_Lattice_*a*	Weighted averaged *a* lattice parameter (P2&P'2)
Avg_Lattice_*c*	Weighted averaged *c* lattice parameter (P2&P'2)
P2 %	Molar ratio of P2 phase
Atomic num.	Atomic number of the dopants
Electro-negativity	Electro-negativity of the dopants
Ionic Radius	Ionic radius of the dopants

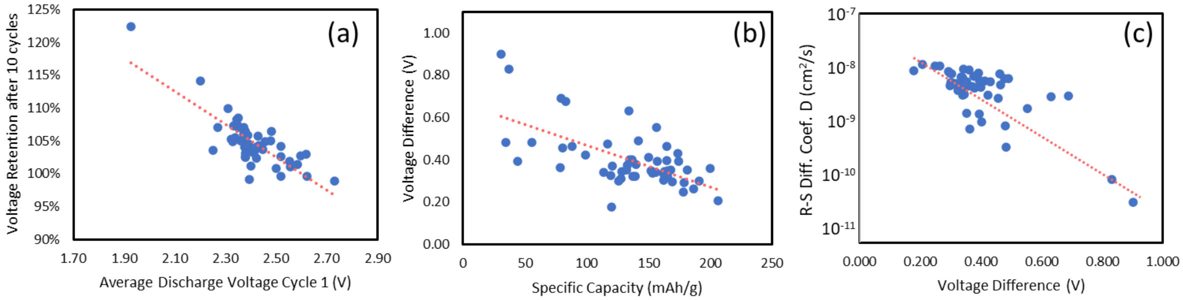

Figure S3.7 *Scatter plots to demonstrate extent of correlation for various parameters with high Pearson correlation parameter values.*

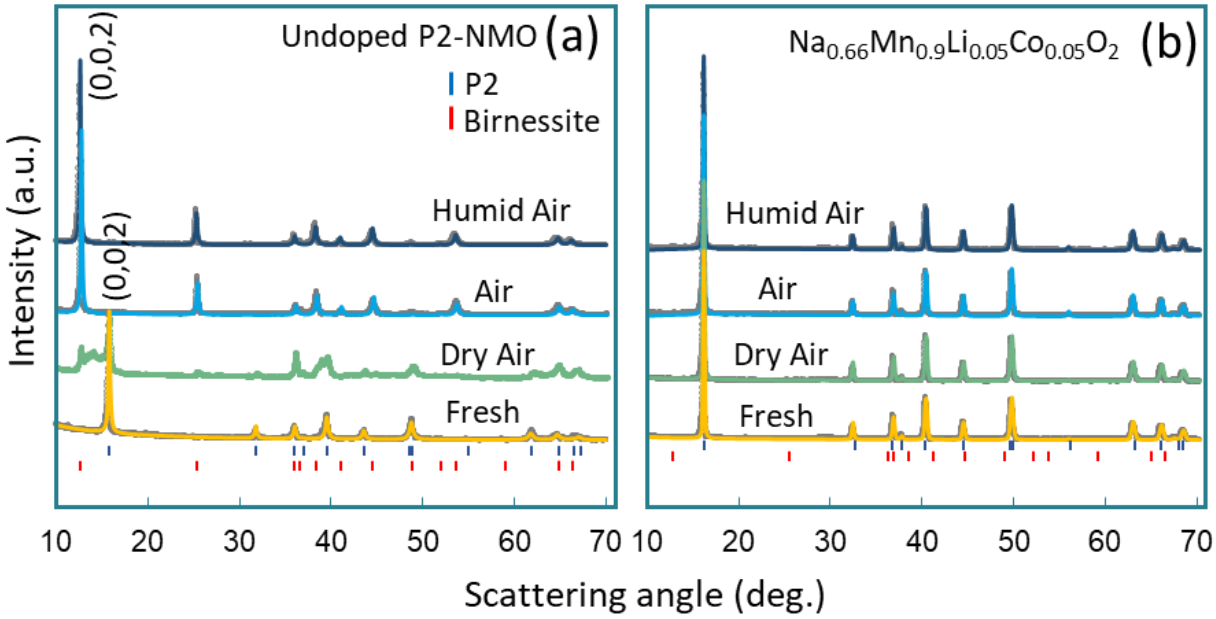

Figure S3.8 *XRD patterns and fitting for the undoped P2-NMO and* $Na_{0.66}Mn_{0.9}Li_{0.05}Co_{0.05}O_2$ *at different storage conditions.*

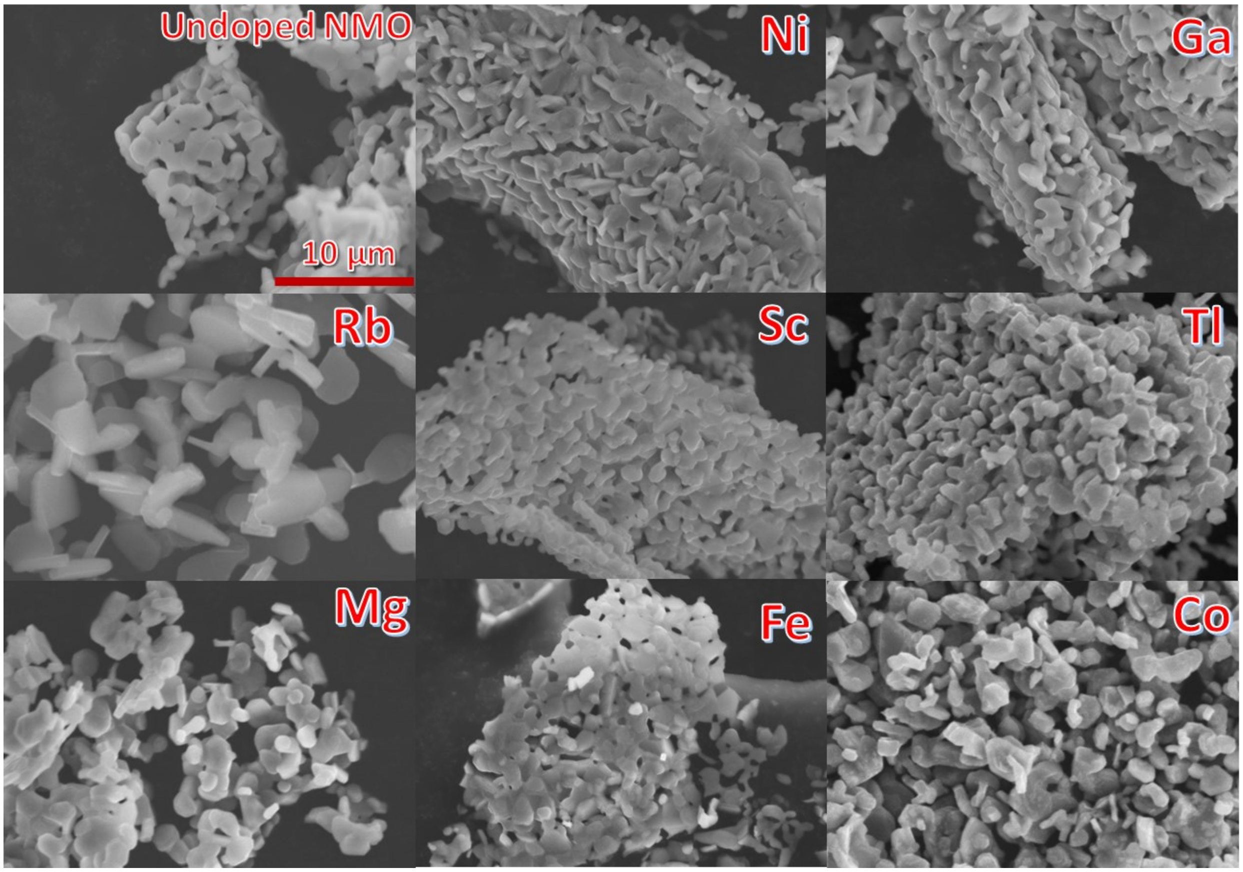

Figure S3.9 *SEM images of the undoped NMO sample and various doped samples. The scale is the same for all images*

.

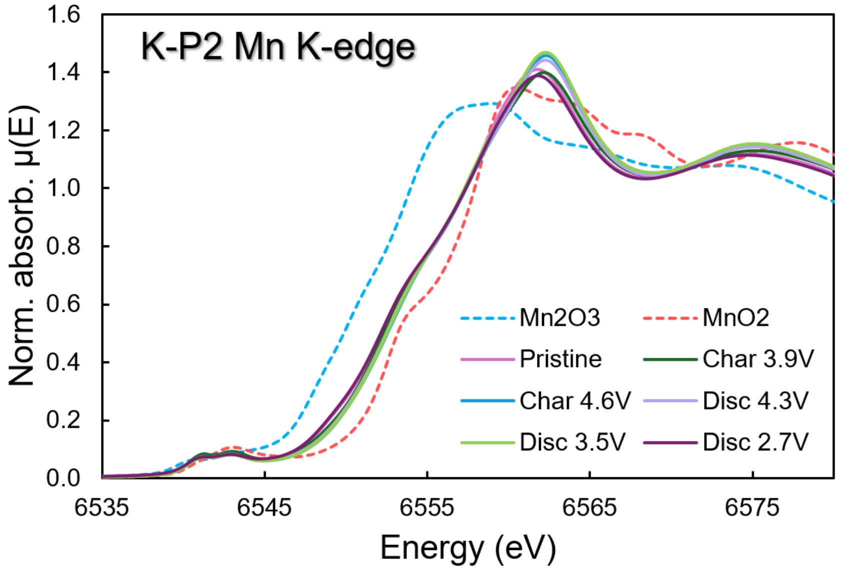

Figure S3.10 *X-ray absorption spectroscopy of ex situ cathode sample* $Na_{0.6}Mn_{0.9}K_{0.1}O_2$ *obtained at different charge and discharge voltages. XANES spectra at Mn K-edge.*

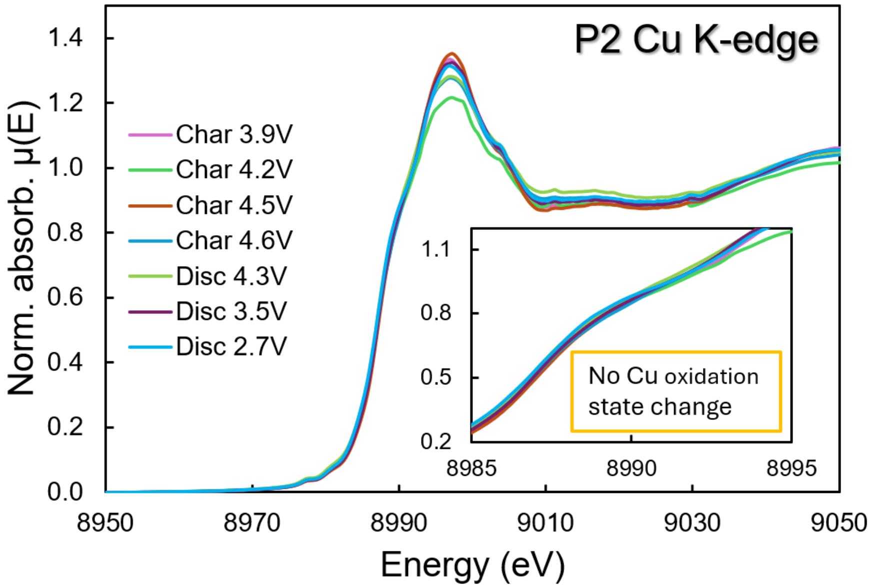

Figure S3.11 *X-ray absorption spectroscopy of ex situ cathode sample* $Na_{0.6}Mn_{0.9}Cu_{0.1}O_2$ *obtained at different charge and discharge voltages. XANES spectra at Cu K-edge.*

3.8 References

(1) Han, M. H.; Gonzalo, E.; Singh, G.; Rojo, T. A Comprehensive Review of Sodium Layered Oxides: Powerful Cathodes for Na-Ion Batteries. *Energy & Environmental Science* **2014**, *8* (1), 81–102.

(2) Kubota, K.; Yabuuchi, N.; Yoshida, H.; Dahbi, M.; Komaba, S. Layered Oxides as Positive Electrode Materials for Na-Ion Batteries. *MRS Bulletin* **2014**, *39* (5), 416–422.

(3) Gonzalo, E.; Zarrabeitia, M.; Drewett, N. E.; López del Amo, J. M.; Rojo, T. Sodium Manganese-Rich Layered Oxides: Potential Candidates as Positive Electrode for Sodium-Ion Batteries. *Energy Storage Materials* **2021**, *34*, 682–707.

(4) Hwang, J.-Y.; Myung, S.-T.; Sun, Y.-K. Sodium-Ion Batteries: Present and Future. *Chemical Society Reviews* **2017**, *46* (12), 3529–3614.

(5) Chayambuka, K.; Mulder, G.; Danilov, D. L.; Notten, P. H. L. Sodium-Ion Battery Materials and Electrochemical Properties Reviewed. *Advanced Energy Materials* **2018**, *8* (16), 1800079.

(6) Yabuuchi, N.; Kubota, K.; Dahbi, M.; Komaba, S. Research Development on Sodium-Ion Batteries. *Chemical Reviews* **2014**, *114* (23), 11636–11682.

(7) Vaalma, C.; Buchholz, D.; Weil, M.; Passerini, S. A Cost and Resource Analysis of Sodium-Ion Batteries. *Nature Reviews Materials* **2018**, *3* (4), 1–11.

(8) Wang, P.-F.; You, Y.; Yin, Y.-X.; Guo, Y.-G. Layered Oxide Cathodes for Sodium-Ion Batteries: Phase Transition, Air Stability, and Performance. *Advanced Energy Materials* **2018**, *8* (8), 1701912.

(9) Feng, J.; Luo, S.; Cai, K.; Yan, S.; Wang, Q.; Zhang, Y.; Liu, X. Research Progress of Tunnel-Type Sodium Manganese Oxide Cathodes for SIBs. *Chinese Chemical Letters* **2022**, *33* (5), 2316–2326.

(10) Ni, Q.; Bai, Y.; Wu, F.; Wu, C. Energy Storage: Polyanion-Type Electrode Materials for Sodium-Ion Batteries (Adv. Sci. 3/2017). *Advanced Science* **2017**, *4* (3).

(11) Barpanda, P.; Lander, L.; Nishimura, S.; Yamada, A. Polyanionic Insertion Materials for Sodium-Ion Batteries. *Advanced Energy Materials* **2018**, *8* (17), 1703055.

(12) Delmas, C.; Fouassier, C.; Hagenmuller, P. Structural Classification and Properties of the Layered Oxides. *Physica B+C* **1980**, *99* (1), 81–85.

(13) Caballero, A.; Hernán, L.; Morales, J.; Sánchez, L.; Peña, J. S.; Aranda, M. a. G. Synthesis and Characterization of High-Temperature Hexagonal P2-Na0.6 MnO2 and Its Electrochemical Behaviour as Cathode in Sodium Cells. *Journal of Materials Chemistry* **2002**, *12* (4), 1142–1147.

(14) Berthelot, R.; Carlier, D.; Delmas, C. Electrochemical Investigation of the P2–NaxCoO2 Phase Diagram. *Nature Materials* **2011**, *10* (1), 74–80.

(15) Guignard, M.; Didier, C.; Darriet, J.; Bordet, P.; Elkaïm, E.; Delmas, C. P2-NaxVO2 System as Electrodes for Batteries and Electron-Correlated Materials. *Nature Materials* **2013**, *12* (1), 74–80.

(16) Ortiz-Vitoriano, N.; E. Drewett, N.; Gonzalo, E.; Rojo, T. High Performance Manganese-Based Layered Oxide Cathodes: Overcoming the Challenges of Sodium Ion Batteries. *Energy & Environmental Science* **2017**, *10* (5), 1051–1074.

(17) Liu, H.; Deng, W.; Gao, X.; Chen, J.; Yin, S.; Yang, L.; Zou, G.; Hou, H.; Ji, X. Manganese-Based Layered Oxide Cathodes for Sodium Ion Batteries. *Nano Select* **2020**, *1* (2), 200–225.

(18) Parant, J.-P.; Olazcuaga, R.; Devalette, M.; Fouassier, C.; Hagenmuller, P. Sur quelques nouvelles phases de formule NaxMnO2 (x ⩽ 1). *Journal of Solid State Chemistry* **1971**, *3* (1), 1–11.

(19) Kumakura, S.; Tahara, Y.; Kubota, K.; Chihara, K.; Komaba, S. Sodium and Manganese Stoichiometry of P2-Type Na2/3MnO2. *Angewandte Chemie* **2016**, *128* (41), 12952–12955.

(20) Chen, X.; Wang, Y.; Wiaderek, K.; Sang, X.; Borkiewicz, O.; Chapman, K.; LeBeau, J.; Lynn, J.; Li, X. Super Charge Separation and High Voltage Phase in NaxMnO2. *Advanced Functional Materials* **2018**, *28* (50), 1805105.

(21) Kulka, A.; Marino, C.; Walczak, K.; Borca, C.; Bolli, C.; Novák, P.; Villevieille, C. Influence of Na/Mn Arrangements and P2/P′2 Phase Ratio on the Electrochemical Performance of Na x MnO 2 Cathodes for Sodium-Ion Batteries. *Journal of Materials Chemistry A* **2020**, *8* (12), 6022–6033.

(22) Yabuuchi, N.; Hara, R.; Kajiyama, M.; Kubota, K.; Ishigaki, T.; Hoshikawa, A.; Komaba, S. New O2/P2-Type Li-Excess Layered Manganese Oxides as Promising Multi-Functional Electrode Materials for Rechargeable Li/Na Batteries. *Advanced Energy Materials* **2014**, *4* (13), 1301453.

(23) de la Llave, E.; Talaie, E.; Levi, E.; Nayak, P. K.; Dixit, M.; Rao, P. T.; Hartmann, P.; Chesneau, F.; Major, D. T.; Greenstein, M.; Aurbach, D.; Nazar, L. F. Improving Energy Density and Structural Stability of Manganese Oxide Cathodes for Na-Ion Batteries by Structural Lithium Substitution. *Chemistry of Materials* **2016**, *28* (24), 9064–9076.

(24) Billaud, J.; Singh, G.; Armstrong, A. R.; Gonzalo, E.; Roddatis, V.; Armand, M.; Rojo, T.; Bruce, P. G. Na0.67Mn1−xMgxO2 (0 ≤ x ≤ 0.2): A High Capacity Cathode for Sodium-Ion Batteries. *Energy & Environmental Science* **2014**, *7* (4), 1387–1391.

(25) Buchholz, D.; Vaalma, C.; Chagas, L. G.; Passerini, S. Mg-Doping for Improved Long-Term Cyclability of Layered Na-Ion Cathode Materials – The Example of P2-Type NaxMg0.11Mn0.89O2. *Journal of Power Sources* **2015**, *282*, 581–585.

(26) Yabuuchi, N.; Hara, R.; Kubota, K.; Paulsen, J.; Kumakura, S.; Komaba, S. A New Electrode Material for Rechargeable Sodium Batteries: P2-Type Na2/3[Mg0.28Mn0.72]O2 with Anomalously High Reversible Capacity. *Journal of Materials Chemistry A* **2014**, *2* (40), 16851–16855.

(27) Dose, W. M.; Sharma, N.; Pramudita, J. C.; Brand, H. E. A.; Gonzalo, E.; Rojo, T. Structure–Electrochemical Evolution of a Mn-Rich P2 Na2/3Fe0.2Mn0.8O2 Na-Ion Battery Cathode. *Chemistry of Materials* **2017**, *29* (17), 7416–7423.

(28) Yabuuchi, N.; Komaba, S. Recent Research Progress on Iron- and Manganese-Based Positive Electrode Materials for Rechargeable Sodium Batteries. *Science and Technology of Advanced Materials* **2014**, *15* (4), 043501.

(29) Hasa, I.; Buchholz, D.; Passerini, S.; Hassoun, J. A Comparative Study of Layered Transition Metal Oxide Cathodes for Application in Sodium-Ion Battery. *ACS Applied Materials & Interfaces* **2015**, *7* (9), 5206–5212.

(30) Wang, X.; Tamaru, M.; Okubo, M.; Yamada, A. Electrode Properties of P2–Na2/3MnyCo1–yO2 as Cathode Materials for Sodium-Ion Batteries. *Journal of Physical Chemistry C* **2013**, *117* (30), 15545–15551.

(31) Bucher, N.; Hartung, S.; Gocheva, I.; Cheah, Y. L.; Srinivasan, M.; Hoster, H. E. Combustion-Synthesized Sodium Manganese (Cobalt) Oxides as Cathodes for Sodium Ion Batteries. *Journal of Solid State Electrochemistry* **2013**, *17* (7), 1923–1929.

(32) Manikandan, P.; Ramasubramonian, D.; Shaijumon, M. M. Layered P2-Type Na0.5Ni0.25Mn0.75O2 as a High Performance Cathode Material for Sodium-Ion Batteries. *Electrochimica Acta* **2016**, *206*, 199–206.

(33) Wang, H.; Yang, B.; Liao, X.-Z.; Xu, J.; Yang, D.; He, Y.-S.; Ma, Z.-F. Electrochemical Properties of P2-Na2/3[Ni1/3Mn2/3]O2 Cathode Material for Sodium Ion Batteries When Cycled in Different Voltage Ranges. *Electrochimica Acta* **2013**, *113*, 200–204.

(34) Lee, S. Y.; Kim, J. H.; Kang, Y. C. Electrochemical Properties of P2-Type Na2/3Ni1/3Mn2/3O2 Plates Synthesized by Spray Pyrolysis Process for Sodium-Ion Batteries. *Electrochimica Acta* **2017**, *225*, 86–92.

(35) Wu, X.; Xu, G.-L.; Zhong, G.; Gong, Z.; McDonald, M. J.; Zheng, S.; Fu, R.; Chen, Z.; Amine, K.; Yang, Y. Insights into the Effects of Zinc Doping on Structural Phase Transition of P2-Type Sodium Nickel Manganese Oxide Cathodes for High-Energy Sodium Ion Batteries. *ACS Applied Materials & Interfaces* **2016**, *8* (34), 22227–22237.

(36) Wu, X.; Guo, J.; Wang, D.; Zhong, G.; McDonald, M. J.; Yang, Y. P2-Type Na0.66Ni0.33–xZnxMn0.67O2 as New High-Voltage Cathode Materials for Sodium-Ion Batteries. *Journal of Power Sources* **2015**, *281*, 18–26.

(37) Hasa, I.; Passerini, S.; Hassoun, J. Toward High Energy Density Cathode Materials for Sodium-Ion Batteries: Investigating the Beneficial Effect of Aluminum Doping on the P2-Type Structure. *Journal of Materials Chemistry A* **2017**, *5* (9), 4467–4477.

(38) Kang, W.; Zhang, Z.; Lee, P.-K.; Ng, T.-W.; Li, W.; Tang, Y.; Zhang, W.; Lee, C.-S.; Yu, D. Y. W. Copper Substituted P2-Type Na0.67CuxMn1−xO2: A Stable High-Power Sodium-Ion Battery Cathode. *Journal of Materials Chemistry A* **2015**, *3* (45), 22846–22852.

(39) Gonzalo, E.; Ortiz-Vitoriano, N.; Drewett, N. E.; Acebedo, B.; López del Amo, J. M.; Bonilla, F. J.; Rojo, T. P2 Manganese Rich Sodium Layered Oxides: Rational Stoichiometries for Enhanced Performance. *Journal of Power Sources* **2018**, *401*, 117–125.

(40) Li, Y.; Yang, Z.; Xu, S.; Mu, L.; Gu, L.; Hu, Y.-S.; Li, H.; Chen, L. Air-Stable Copper-Based P2-Na7/9Cu2/9Fe1/9Mn2/3O2 as a New Positive Electrode Material for Sodium-Ion Batteries. *Advanced Science* **2015**, *2* (6), 1500031.

(41) Guo, S.; Liu, P.; Yu, H.; Zhu, Y.; Chen, M.; Ishida, M.; Zhou, H. A Layered P2- and O3-Type Composite as a High-Energy Cathode for Rechargeable Sodium-Ion Batteries. *Angewandte Chemie International Edition* **2015**, *54* (20), 5894–5899.

(42) Yoshida, J.; Guerin, E.; Arnault, M.; Constantin, C.; Boisse, B. M. de; Carlier, D.; Guignard, M.; Delmas, C. New P2 - Na0.70Mn0.60Ni0.30Co0.10O2 Layered Oxide as Electrode Material for Na-Ion Batteries. *Journal of the Electrochemical Society* **2014**, *161* (14), A1987.

(43) Kwon, M.-S.; Lim, S. G.; Park, Y.; Lee, S.-M.; Chung, K. Y.; Shin, T. J.; Lee, K. T. P2 Orthorhombic Na0.7[Mn1–xLix]O2+y as Cathode Materials for Na-Ion Batteries. *ACS Applied Materials & Interfaces* **2017**, *9* (17), 14758–14768.

(44) Zhao, C.; Ding, F.; Lu, Y.; Chen, L.; Hu, Y.-S. High-Entropy Layered Oxide Cathodes for Sodium-Ion Batteries. *Angewandte Chemie International Edition* **2020**, *59* (1), 264–269.

(45) Zhao, C.; Wang, Q.; Yao, Z.; Wang, J.; Sánchez-Lengeling, B.; Ding, F.; Qi, X.; Lu, Y.; Bai, X.; Li, B., Rational design of layered oxide materials for sodium-ion batteries. *Science* **2020,** *370* (6517), 708-711.

(46) Zheng, W.; Liu, Q.; Wang, Z.; Wu, Z.; Gu, S.; Cao, L.; Zhang, K.; Fransaer, J.; Lu, Z. Oxygen Redox Activity with Small Voltage Hysteresis in Na0.67Cu0.28Mn0.72O2 for Sodium-Ion Batteries. *Energy Storage Materials* **2020**, *28*, 300–306.

(47) Kong, W.; Gao, R.; Li, Q.; Yang, W.; Yang, J.; Sun, L.; Liu, X. Simultaneously Tuning Cationic and Anionic Redox in a P2-Na0.67Mn0.75Ni0.25O2 Cathode Material through Synergic Cu/Mg Co-Doping. *Journal of Materials Chemistry A* **2019**, *7* (15), 9099–9109.

(48) Ren, H.; Li, Y.; Ni, Q.; Bai, Y.; Zhao, H.; Wu, C. Unraveling Anionic Redox for Sodium Layered Oxide Cathodes: Breakthroughs and Perspectives. *Advanced Materials* **2022**, *34* (8), 2106171.

(49) Ben Yahia, M.; Vergnet, J.; Saubanère, M.; Doublet, M.-L. Unified Picture of Anionic Redox in Li/Na-Ion Batteries. *Nature Material.* **2019**, *18* (5), 496–502.

(50) Xu, H.; Guo, S.; Zhou, H. Review on Anionic Redox in Sodium-Ion Batteries. *Journal of Materials Chemistry A* **2019**, *7* (41), 23662–23678.

(51) Zuo, W.; Qiu, J.; Liu, X.; Ren, F.; Liu, H.; He, H.; Luo, C.; Li, J.; Ortiz, G. F.; Duan, H.; Liu, J.; Wang, M.-S.; Li, Y.; Fu, R.; Yang, Y. The Stability of P2-Layered Sodium Transition Metal Oxides in Ambient Atmospheres. *Nature communications* **2020**, *11* (1), 3544.

(52) Duffort, V.; Talaie, E.; Black, R.; Nazar, L. F. Uptake of CO2 in Layered P2-Na0.67Mn0.5Fe0.5O2: Insertion of Carbonate Anions. *Chemistry of Materials* **2015**, *27* (7), 2515–2524.

(53) Li, X.; Shen, X.; Zhao, J.; Yang, Y.; Zhang, Q.; Ding, F.; Han, M.; Xu, C.; Yang, C.; Liu, H.; Hu, Y.-S. O3-NaFe(1/3–x)Ni1/3Mn1/3AlxO2 Cathodes with Improved Air Stability for Na-Ion Batteries. *ACS Applied Materials & Interfaces* **2021**, *13* (28), 33015–33023.

(54) Jia, S.; Counsell, J.; Adamič, M.; Jonderian, A.; McCalla, E. High-Throughput Design of Na–Fe–Mn–O Cathodes for Na-Ion Batteries. *Journal of Materials Chemistry A* **2022**, *10* (1), 251–265.

(55) Adhikari, T.; Hebert, A.; Adamič, M.; Yao, J.; Potts, K.; McCalla, E. Development of High-Throughput Methods for Sodium-Ion Battery Cathodes. *ACS Combinatorial Science* **2020**, *22* (6), 311–318.

(56) McCalla, E.; Parmaklis, M.; Rehman, S.; Anderson, E.; Jia, S.; Hebert, A.; Potts, K.; Antranik Jonderian; Adhikari, T.; Adamič, M. Combinatorial Methods in Advanced Battery Materials Design. *Canadian Journal of Chemistry* **2022**, *100* (2), 132–143.

(57) Potts, K. P.; Grignon, E.; McCalla, E. Accelerated Screening of High-Energy Lithium-Ion Battery Cathodes. *ACS Applied Energy Materials* **2019**, *2* (12), 8388–8393.

(58) Wang, C.; Liu, L.; Zhao, S.; Liu, Y.; Yang, Y.; Yu, H.; Lee, S.; Lee, G.-H.; Kang, Y.-M.; Liu, R.; Li, F.; Chen, J. Tuning Local Chemistry of P2 Layered-Oxide Cathode for High Energy and Long Cycles of Sodium-Ion Battery. *Nature communications* **2021**, *12* (1), 2256.

(59) Toby, B. H. R Factors in Rietveld Analysis: How Good Is Good Enough? *Powder Diffraction* **2006**, *21* (1), 67–70.

(60) Vaalma, C.; Buchholz, D.; Passerini, S. Beneficial Effect of Boron in Layered Sodium-Ion Cathode Materials – The Example of Na2/3B0.11Mn0.89O2. *Journal of Power Sources* **2017**, *364*, 33–40.

(61) Risthaus, T.; Chen, L.; Wang, J.; Li, J.; Zhou, D.; Zhang, L.; Ning, D.; Cao, X.; Zhang, X.; Schumacher, G.; Winter, M.; Paillard, E.; Li, J. P3 Na0.9Ni0.5Mn0.5O2 Cathode Material for Sodium Ion Batteries. *Chemistry of Materials* **2019**, *31* (15), 5376–5383.

(62) Doeff, M. M.; Richardson, T. J.; Hwang, K.-T. Electrochemical and Structural Characterization of Titanium-Substituted Manganese Oxides Based on Na0.44MnO2. *Journal of Power Sources* **2004**, *135* (1), 240–248.

(63) Song, B.; Hu, E.; Liu, J.; Zhang, Y.; Yang, X.-Q.; Nanda, J.; Huq, A.; Page, K. A Novel P3-Type Na2/3Mg1/3Mn2/3O2 as High Capacity Sodium-Ion Cathode Using Reversible Oxygen Redox. *Journal of Materials Chemistry A* **2019**, *7* (4), 1491–1498.

(64) Matsui, M.; Mizukoshi, F.; Hasegawa, H.; Imanishi, N. Ca-Substituted P3-Type NaxNi1/3Mn1/3Co1/3O2 as a Potential High Voltage Cathode Active Material for Sodium-Ion Batteries. *Journal of Power Sources* **2021**, *485*, 229346.

(65) Maddukuri, S.; Valerie, P.; Upadhyayula, V. V. Synthesis and Electrochemical Study of New P3 Type Layered Na0.6Ni0.25Mn0.5Co0.25O2 for Sodium-Ion Batteries. *ChemistrySelect* **2017**, *2* (20), 5660–5666.

(66) Kalapsazova, M.; Ortiz, G. F.; Tirado, J. L.; Dolotko, O.; Zhecheva, E.; Nihtianova, D.; Mihaylov, L.; Stoyanova, R. P3-Type Layered Sodium-Deficient Nickel–Manganese Oxides: A Flexible Structural Matrix for Reversible Sodium and Lithium Intercalation. *ChemPlusChem* **2015**, *80* (11), 1642–1656.

(67) Zhou, X.; Zhao, A.; Chen, Z.; Cao, Y. Research Progress of Tunnel-Structural Na0.44MnO2 Cathode for Sodium-Ion Batteries: A Mini Review. *Electrochemistry Communications* **2021**, *122*, 106897.

(68) Dai, K.; Mao, J.; Song, X.; Battaglia, V.; Liu, G. Na0.44MnO2 with Very Fast Sodium Diffusion and Stable Cycling Synthesized via Polyvinylpyrrolidone-Combustion Method. *Journal of Power Sources* **2015**, *285*, 161–168.

(69) Rowe, A. W.; Camardese, J.; McCalla, E.; Dahn, J. R. High Precision Coulometry Studies of Single-Phase Layered Compositions in the Li-Mn-Ni-O System. *Journal of the Electrochemical Society.* **2014**, *161* (9), A1189.

(70) Hemalatha, K.; Jayakumar, M.; S. Prakash, A. Influence of the Manganese and Cobalt Content on the Electrochemical Performance of P2-Na 0.67 MnxCo1−xO2 Cathodes for Sodium-Ion Batteries. *Dalton Transactions* **2018**, *47* (4), 1223–1232.

(71) Zhang, X.; Hou, Z.; Li, X.; Liang, J.; Zhu, Y.; Qian, Y. Na-Birnessite with High Capacity and Long Cycle Life for Rechargeable Aqueous Sodium-Ion Battery Cathode Electrodes. *Journal of Materials Chemistry A* **2016**, *4* (3), 856–860.

(72) Lou, S.; Zhao, Y.; Wang, J.; Yin, G.; Du, C.; Sun, X. Ti-Based Oxide Anode Materials for Advanced Electrochemical Energy Storage: Lithium/Sodium Ion Batteries and Hybrid Pseudocapacitors. *Small* **2019**, *15* (52), 1904740.

(73) Nowak, M.; Zając, W.; Hanc, E.; Molenda, J. Enhanced Electrochemical Behavior of Na0.66Li0.22Ti0.78O2/C Layered P2-Type Composite Anode Material for Na-Ion Batteries. *Composites Part B: Engineering* **2021**, *213*, 108729.

(74) Wang, Q.; Xu, J.; Zhang, W.; Mao, M.; Wei, Z.; Wang, L.; Cui, C.; Zhu, Y.; Ma, J. Research Progress on Vanadium-Based Cathode Materials for Sodium Ion Batteries. *Journal of Materials Chemistry A* **2018**, *6* (19), 8815–8838.

(75) Chen, G.; Huang, Q.; Wu, T.; Lu, L. Polyanion Sodium Vanadium Phosphate for Next Generation of Sodium-Ion Batteries—A Review. *Advanced Functional Materials* **2020**, *30* (34), 2001289.

(76) Fang, Y.; Chen, Z.; Xiao, L.; Ai, X.; Cao, Y.; Yang, H. Recent Progress in Iron-Based Electrode Materials for Grid-Scale Sodium-Ion Batteries. *Small* **2018**, *14* (9), 1703116.

(77) Qi, S.; Wu, D.; Dong, Y.; Liao, J.; Foster, C. W.; O'Dwyer, C.; Feng, Y.; Liu, C.; Ma, J. Cobalt-Based Electrode Materials for Sodium-Ion Batteries. *Chemical Engineering Journal* **2019**, *370*, 185–207.

(78) Zuo, W.; Qiu, J.; Hong, C.; Liu, X.; Li, J.; Ortiz, G. F.; Li, Q.; Zheng, S.; Zheng, G. R.; Yang, Y. Structure-Performance Relationship of Zn2+ Substitution in P2–Na0.66Ni0.33Mn0.67O2 with Different Ni/Mn Ratios for High-Energy Sodium-Ion Batteries. *ACS applied energy materials* **2019**, *2* (7), 4914–4924.

(79) Melot, B. C.; Tarascon, J.-M. Design and Preparation of Materials for Advanced Electrochemical Storage. *Accounts of Chemical Research Journal* **2013**, *46* (5), 1226–1238.

(80) Brown, I. D. Recent Developments in the Methods and Applications of the Bond Valence Model. *Chemical Reviews* **2009**, *109* (12), 6858–6919.

(81) Yu, Y.; Ning, D.; Li, Q.; Franz, A.; Zheng, L.; Zhang, N.; Ren, G.; Schumacher, G.; Liu, X. Revealing the Anionic Redox Chemistry in O3-Type Layered Oxide Cathode for Sodium-Ion Batteries. *Energy Storage Materials* **2021**, *38*, 130–140.

Chapter 4 Stabilization of Na-ion Cathode Surfaces: Combinatorial Experiments with Insights from Machine Learning Models

Building on the success outlined in **Chapter 2**, where optimal high-Mn materials were identified, and **Chapter 3**, which explored 52 chemical doping into Na-Mn-O, we further extend the high-throughput methodology to more complex material design to the doped Na-Mn-Fe-O systems. **Chapter 4** expands upon another combinatorial doping study, focusing not only on the bulk properties of the cathodes but also on critical surface properties such as transition metal dissolution. We also explore the potential to investigate various mechanisms affecting these properties using high-throughput approaches. In particular, we screen for cathode stability in the electrolyte by assessing transition metal dissolution, a key factor for long-term cycling performance and safety. Additionally, we examine fundamental chemical principles and employ advanced characterization techniques to assess air stability. Techniques like thermogravimetric analysis are employed to monitor water insertion behavior, while X-ray absorption spectroscopy helps identify local structural transformation. Leveraging the extensive data obtained from our high-throughput investigations, we integrate machine learning for advanced data mining and cheminformatics analysis. This integration of wet-lab work with machine learning represents a pioneering effort, paving the way for the future of ML/AI-driven advancements in scientific research.

Chapter 4 is adapted with permission from “Jia, S.; Abdolhosseini, M.; Liu, C.; Jonderian, A.; Li, Y.; Kwak, H.; Kumakura, S.; Sieffert, J. M.; Eisnor, M.; McCalla, E. Stabilization of Na-Ion Cathode Surfaces: Combinatorial Experiments with Insights from Machine Learning Models. *Advanced Energy and Sustainability Research* **2024** 2400051.”

4.1 Abstract

Na-Fe-Mn-O cathodes hold promise for environmentally benign high-energy sodium-ion batteries, addressing material scarcity concerns in Li-ion batteries. To date, these materials show poor stability in air and suffer significant Fe/Mn dissolution during use. These two detrimental surface effects have so far prevented commercialization of these materials. Herein, we utilize high-throughput experiments to make hundreds of substitutions into a previously optimized Na-Fe-Mn-O material. Numerous single-phase materials are made with good electrochemical performance that show moderate improvements over the unsubstituted. By contrast, dramatic improvements are made in suppressing decomposition in air and Fe/Mn dissolution. Machine-learning algorithms are utilized to further understand the changes in air stability and to decouple the effects of various structural parameters such as lattice parameters and crystallite size. The comprehensive dataset and methodology established here lay the groundwork for future exploration and optimization of cathode materials, driving the advancement of next-generation sodium-ion batteries.

4.2 Introduction

The growing global energy demand has propelled the widespread adoption of lithium batteries in electronic devices and transportation. However, concerns about the increasing demanding and raw material crisis arising from overreliance on lithium batteries have intensified. As a result, sodium batteries have emerged as a viable alternative for a technological revolution in energy storage, particularly when considering the need for large-scale energy storage solutions[1,2]. Among components of sodium batteries, cathode materials play a crucial role with layered oxides, in particular, exhibiting promise due to their exceptional electrochemical performance, feasibility of synthesis, and versatility in elemental choices[3–6].

Optimization of the chemical composition is a pivotal factor in controlling the structure stability, battery performance, air stability, manufacturing costs, and environmental impact of cathode materials[7,8]. Over a decade ago, Yabuuchi *et al.* reported P2-type $Na_xMn_{1/2}Fe_{1/2}O_2$, which employs earth-abundant elements, garnering significant attention for high energy environmentally benign cathodes[9]. Nonetheless, this material encounters several challenges such as poor cycling performance[10], phase transitions (Z-phase) at high voltages[11,12], inadequate air stability[13], and transition metal dissolution[14]. Previously, we investigated 448 materials in the Na-Fe-Mn-O system and discovered wide solid-solution regions within which properties such as air stability were highly tunable.[15] The material P2-$Na_{0.66}Fe_{0.13}Mn_{0.87}O_2$ had optimal capacity and improved air stability within the Na-Fe-Mn-O system. In another recent study, we observed dramatic changes in the properties of doped $Na_{0.66}MnO_2$ materials with 52 different dopants, and most notably certain dopants (e.g. Li) contributed strongly to improved air stability.[16] However, the capacities and the cyclability were not as high as for P2-$Na_{0.66}Fe_{0.13}Mn_{0.87}O_2$. Consequently, optimal doping into the best P2 material, especially considering multiple metrics, becomes critical. Moreover, the compositional complexity of materials poses a significant hurdle in material composition analysis. Understanding the individual effects of different elements and conducting rational design in such complex compositions remains challenging.

To advance above research, herein we utilize high-throughput doping with 52 elements into the optimal P2-$Na_{0.66}Fe_{0.13}Mn_{0.87}O_2$. Our primary focus lies in elucidating the influence of different dopants on material properties, specifically addressing the air stability of layered materials and the suppressing transition metal dissolution during battery operation. Both of these major hurdles to commercialization are surface effects that are known to be influenced by the addition of dopants.[18–20] Through the integration of experimental and theoretical approaches, we develop a machine learning model to predict air stability based on pristine XRD patterns only and learn from the trained model what features in the pristine XRD lead to improve stability. Through these concerted efforts, we contribute to the advancement of sodium battery technology and the realization of sustainable energy.

4.3 Experimental Section

4.3.1 Material preparation

For the high throughput synthesis, a sol-gel auto-combustion method was employed to achieve combinatorial doping into different compositions[23]. Sodium nitrate ($NaNO_3$), manganese nitrate ($Mn(NO_3)_2$), and iron nitrate ($Fe(NO_3)_3$) from Sigma-Aldrich were prepared as 2.4 M solutions and dispensed into an 8×8 well plate according to the desired ratios listed below. Nitrate salts were chosen for the sol-gel synthesis, considering their potential influence on the final products. Aqueous solutions (1M) of various dopants listed in **Table S4.3** were added to the precursor solutions at 5% or 10% doping levels on the transition metal sites. To stabilize the metal ions, citric acid (3M) was added in an equal molar ratio to the metal cations as a chelating agent. The gelation process was carried out at 65 °C for 2 days to form homogeneous gels via strong carboxylic-metal bonding. To prevent cross-contamination, the resulting gels were pulverized and transferred onto an alumina plate covered with an 8×8 aluminum smokestack, with the gels separated into different combustion chambers. Combustion was performed at 400 °C for 2 hours to remove the citric acid and nitrates (heating rate: 2 °C min^{-1}). After removing the smokestack, the preheated samples were further heated at 850 °C for 12 hours in ambient air (heating rate: 5 °C min^{-1}), followed by a cooling rate of 5 °C min^{-1} to room temperature. Three sets of samples were chosen for systematic doping in the Na-Mn-Fe-O system with 52 elements, **Set 1**: $Na_{0.66}Fe_{0.13}Mn_{0.77}X_{0.1}O_2$, **Set 2**:

$Na_{0.66}Fe_{0.13}Mn_{0.82}X_{0.05}O_2$, and **Set 3**: $Na_{0.66}Fe_{0.08}Mn_{0.87}X_{0.05}O_2$. Additionally, $Na_{0.66}Mn_{0.5}Fe_{0.4}X_{0.1}O_2$ with series dopants listed in Figure 7 was synthesized to study the transition metal dissolution.

4.3.2 X-ray diffraction

The X-ray diffraction (XRD) measurements were conducted using a Panalytical Empyrean diffractometer equipped with a Mo target (60 kV, 40 mA) and PIXcel3D detector in high throughput measurement mode. The samples were mounted onto a transparent mylar film with 3D-printed 96 sample slots without cross-contamination. A scattering angle range (λ = 0.70926 Å for Mo $K\alpha_1$) of 4–30° was initially investigated and then converted into 10-70° for Cu radiation. The major peak intensity with over 3000 counts was achieved in under 10 min per sample assuring the high-quality XRD for further Pawley fitting and Rietveld refinement. The phase identification and refinement of XRD patterns were performed on Panalytical's HighScore Plus software combined with manual and batch modes. The results of multiple phase identification and quantification can be found in **Table S4.1**.

4.3.3 Electrochemistry

The electrochemical performance assessment was evaluated using lab-developed combinatorial cells consisting of 64 parallel channels. A printed circuit board (PCB, Optima Tech) with 64 parallel gold pads served as cathode current collectors and was coated with aluminum foil. The cathodes were prepared by combining 2 mg of active materials with 20 wt% carbon black, followed by drop-casted onto the contact pads via 20 wt% polyvinylidene fluoride (PVDF) as a binder in N-methyl-2-pyrrolidone (NMP). NMP was then removed and dried for 12 hours at 80 °C, resulting in a cathode loading of 20 mg cm^{-2}. In an argon-filled glove box, the assembly of the combinatorial cell was carried out using the electrolyte composed of 1M sodium perchlorate in propylene carbonate (PC) with 2 wt% fluoroethylene carbonate (FEC). Sodium metal foil served as the anode, and a GF/D glass microfiber prefilter was used as a separator, as shown in Figure S11. Cyclic voltammetry (CV) measurements were conducted using a lab-built high-throughput electrochemical system, equipped with a quad voltage source (Keithley 213) and a multimeter with a multiplexer (Keithley 2750). The voltage range was set between 1.5 and 4.3 V versus Na/Na^+ at a scan rate of 0.1 V h^{-1}. The CV curves were further processed by integrating the current-time product (*Idt*) to obtain capacity as a function of voltage. The high throughput measurements exhibited excellent reproducibility for the same cathode materials, with a relative standard deviation (RSD) of 7% for specific capacities[23].

4.3.4 Accelerated aging

To investigate the air stability of the doped samples, we conducted experiments using three sets of freshly synthesized samples with the compositions mentioned earlier. These samples were carefully stored under identical conditions using a 3D-printed XRD holder to ensure consistency. High throughput XRD measurements were conducted at different time intervals and under varying relative humidity (RH) conditions. Initially, the samples were stored in dry air (RH < 10%) for two months, followed by exposure to ambient air (RH = 45%) for one week, and finally subjected to humid air (RH > 90%) for another week. An enclosed system was assured to provide stable relative humidity levels without interference, where the temperature was maintained within 23 ± 1 °C. The XRD scans obtained from these storage conditions were first analyzed by identifying the different phases present and subsequently subjected to quantitative refinement using the method described above.

4.3.5 X-ray absorption spectroscopy (XAS)

The XAS spectra of the Mn K-edge, featuring both XANES and EXAFS, were acquired at Hard X-ray Micro-Analysis (HXMA), Canadian Light Source, a 2.9 GeV third-generation synchrotron source. The pristine samples were meticulously handled, promptly stored in an Argon-filled glove box following synthesis with minimum exposure of air and moisture. Aged samples underwent a rigorous treatment in an extremely humid environment (RH > 90%) for a duration of 7 days. Post-aging, X-ray Diffraction (XRD) analyses were conducted, revealing that the Li-doped sample retained its pristine P2 crystalline structure, while the Sc-doped sample degraded into the Birnessite phase. All the samples were prepared and hermetically sealed onto Kapton tapes, ensuring minimal contact with the surrounding environment prior to testing.

4.3.6 Machine learning model

We have devised a novel methodology that combines wet chemistry with model training to process raw XRD data, consisting of five key processes: **(1)** data collection and labelling, **(2)** dimensionality reduction, **(3)** machine learning model set-up, **(4)** model training and validation, and **(5)** interpretation and prediction. The XRD processing and machine model set-up were conducted based on HighScore Plus software and Scikit-learn package. Firstly, the XRD data were collected and labelled based on their air stability derived from the Rietveld refinement. Since XRD data typically exhibits multicollinearity between different peaks due to their similar physical origins, we performed dimensionality reduction to simplify the regression analysis. Principal Component Analysis (PCA) and t-Distributed Stochastic Neighbor Embedding (t-SNE) were utilized as widely adopted unsupervised learning techniques to reduce the dimensionality of the XRD data, facilitating exploratory data analysis and pattern recognition. Compared to PCA, t-SNE exhibited superior ability in explaining and classifying XRD data, revealing well-defined boundaries for each cluster corresponding to different aging levels. Additionally, the heat map of structural correlation exhibited excellent performance in rapidly classifying samples, presenting a substantial contrast to manual identification. By projecting the XRD data onto a lower-dimensional space, we can visualize the relationship between different clusters of materials. Partial Least Squares Regression (PLSR) was used as machine learning algorithm to predict the air stability of the layered materials. PLSR is utilized for high-dimensional predictor variables (raw XRD data) and performing dimensionality reduction by feature extracting and matrix transformations, which involves extracting salient features from XRD patterns and obtaining the correlation to response variables (air stability) as quantified metrics. The performance of the model was evaluated using Root Mean Squared Error of Cross-Validation (RMSECV) to quantify the average magnitude of prediction errors of the model during cross-validation. RMSECV aids in the validation and optimization of the model to assure its suitability for prediction based on XRD patterns. Consequently, the regression model captures the underlying relationship between the XRD patterns and the air stability of cathode materials, thereby providing invaluable insights for the advancement and design of cathode materials with enhanced air stability.

4.3.7 Transition metal dissolution

To access the dissolution behavior of transition metals, we conducted systematic investigations on various doped $Na_{0.66}Mn_{0.5}Fe_{0.4}X_{0.1}O_2$ samples. These doped samples were assembled into Swagelok-type cells following the above-described method in a batch process. The cells were subjected to cycling from 1.5 V to 4.6 V under galvanostatic conditions at a rate of 10 mA g^{-1}. After 10 full cycles, the cells were disassembled in an argon-filled glovebox. The separators and Na anodes were collected for further analysis using inductively coupled plasma-optical emission spectrometry (ICP-OES) analysis, performed by Agilent Technologies 5100 ICP-OES with the autosampler. The reliability of the elemental analysis was confirmed by inspecting the RSD% of all results, which were within 2% from 9 tests per sample. X-ray photoelectron spectroscopy (XPS) from Thermo Fisher-Scientific Nexsa G2 was utilized to analyze the surface elemental compositions of the cycled cathode materials. MAGCIS ion gun with an ion energy of 500 eV and medium current intensity was utilized to perform depth profiling through Ar gun etching, as shown in **Figures S4.10** and **S4.11**. The splutter rate on oxide material was estimated at 0.09 nm/sec. This profiling technique enabled us to determine the relative compositions from the surface to the bulk of the samples.

4.4 Results and Discussion

4.4.1 Structure analysis

We achieved systematic doping of 52 different elements (X) in three sets of samples denoted as **set 1**: $Na_{0.66}Fe_{0.13}Mn_{0.77}X_{0.1}O_2$ (10% on Mn site) in Figs. 2, S1, **set 2**: $Na_{0.66}Fe_{0.13}Mn_{0.82}X_{0.05}O_2$ (5% on Mn site) in Fig. S2, and **set 3**: $Na_{0.66}Fe_{0.08}Mn_{0.87}X_{0.05}O_2$ (5% on Fe site) in Fig. S3. The three sets of doped samples are based on a stoichiometric design derived from $Na_{0.66}Fe_{0.13}Mn_{0.87}O_2$. The target of the synthesis is the P2 structure, shown in **Figure 4.1a** for both the undoped (consistent with our previous results in ref.[15]) and for a number of dopants from **set** 1. The multiphase identification and refinement first used in ref.[16] are completed and summarized in **Figure 4.1b** and **Table S4.1** for **set 1**. At a 10% doping level, we obtained 16 elements (shown in **Figure 4.1b**) that can be fully incorporated into the P2 structure as compared to only 7 in ref.[16]. This indicates the success of the high-throughput (HTP) doping study, relying on the fact that the undoped material here lies within a solid solution such that making single-phase materials is more easily achieved. As depicted in **Figure 4.1a** for P2 materials, there is no discernible sign of a superstructural peak after peak identification and refinement. This suggests a well-mixed transition metal layer (consisting of Mn and Fe) and solid-solution formation within the transition metal layer. Our primary objective is to fast screen the phase compositions following various doping treatments. By calculating the presence of impurity phases, we can estimate the doping amount, facilitating rapid material screening. Furthermore, the lattice parameters summarized in **Table S1** may also indicate the doping effect on the alteration of layered structures.

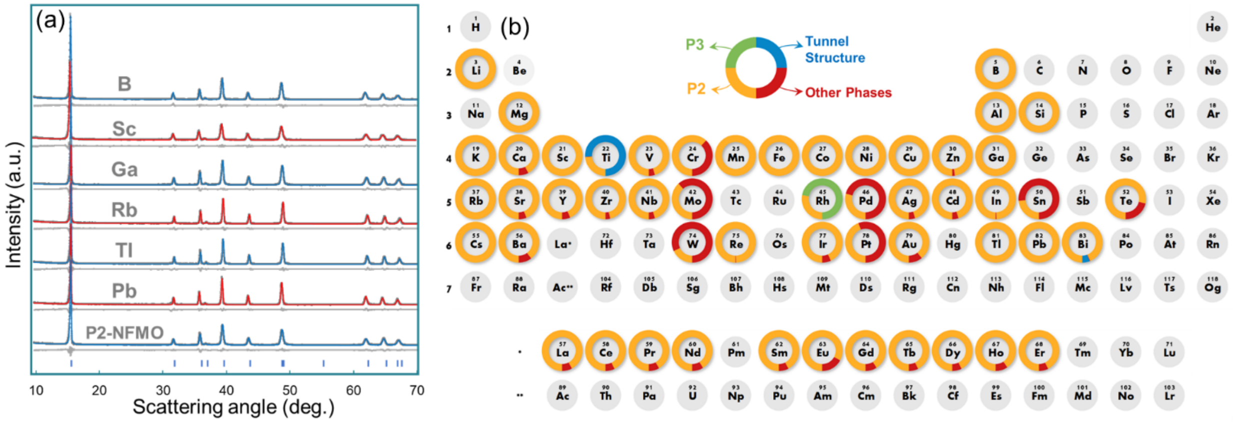

Figure 4.1 *(a) Representative XRD patterns for different doped samples in **set 1**:* $Na_{0.66}Fe_{0.13}Mn_{0.77}X_{0.1}O_2$ *(X: dopant), all exhibiting the pure P2 phase. (b) The periodic table illustrating the relative phase compositions of the doped samples in **set 1**. The phase ratios are determined using quantitative Rietveld refinement and represented by different colors: P2 (yellow), P3 (green), tunnel structure (blue), and other phases (red).*

Notably, we discovered new compositions facilitated by dopants such as Rb, Cs, Sc, Ga, B, Re, Tl, and Pb, significantly diversifying the dopant list and enriching the selection of metals for layered oxide through combinatorial study. This expansion of dopants, along with the incorporation of Fe, allows for a wider range of elements to be considered for achieving the P2 phase. For instance, Si^{4+} doping to make $Na_{0.66}Mn_{0.9}Si_{0.1}O_2$ was found in ref.[16] to make pure P'2 phase. Here, in the presence of Fe, the $Na_{0.66}Fe_{0.13}Mn_{0.77}Si_{0.1}O_2$ demonstrates a pure P2 phase instead, highlighting the significant influence of combinations of dopants and again justifying the need for experimental combinatorial techniques. Besides the P2 phase, we also identified dopants that promote the P3 phase (Rh) and tunnel structure (Ti) in Fig. 1b. These findings demonstrate that dopants, even at only 10%, can have a dominant impact on the phases stabilized during synthesis.

4.4.2 Electrochemical analysis

To evaluate the battery performance, we applied the high throughput electrochemical analysis developed in refs.[21–24] to the different doped samples as cathode materials in half cells. The voltage range was set between 1.5 and 4.3 V versus Na/Na$^+$ at a scan rate of 0.1 V h^{-1}. The high throughput measurements exhibited excellent reproducibility for the same cathode materials, with a relative standard deviation (RSD) of 7% for specific capacities, and outstanding agreement with previously published results (2 % or less on both specific capacities and average voltage)[21–23]. The cyclic voltammetry (CV) curves of all 3 sample sets are shown in **Figure S4.1-S4.3**. Moreover, the CV curves for **set 1** were transformed into voltage profile plots by integrating the current over time, as shown in **Figure 4.2**. As previously demonstrated, such calculated voltage curves show excellent agreement with results from galvanostatic cycling at slow rates (C/10 and below).[21–23] The primary redox plateaus observed at 2.1 V and 2.3 V indicate that most of the capacity arises from the redox pair of Mn^{3+}/Mn^{4+}.[9,10,25] It can also be easily seen in **Figure 4.2** that the pure P2 phases show suppressed phase transitions (plateaus) compared to the Na-Mn-O sample (NMO). Furthermore, we conducted *in-situ* XRD analysis on the Ga-doped sample $Na_{0.66}Fe_{0.13}Mn_{0.77}Ga_{0.1}O_2$ as illustrated in **Figure 4.7**. Notably, only the P2 phase was observed in the XRD pattern during the cycling within the voltage range of 1.5 V to 4.3 V. This observation once again highlights the suppressing effects of doping on phase transition, especially in comparison to previous work on undoped materials[26]. Interestingly, they also show no reversible peaks above 4.0 V where oxygen redox would occur, in contrast to our previous results[16] in doped $Na_{0.66}MnO_2$. Overall, the voltage curves of the P2 materials show low overpotentials (quite a bit lower than in the original $Na_{0.66}Fe_{0.5}Mn_{0.5}O_2$ proposed by Yabuuchi et al.[9]) and excellent reversibility. **Figures 4.3, S4.3-S4.4** show the extracted battery metrics which gives a broad view of the effects of dopants. Firstly, considering the undoped was already optimized for specific capacities and capacity retention in the Na-Fe-Mn-O system, the improvements in specific capacities and retention of doped samples are expected to be marginal. Undoped $Na_{0.66}Fe_{0.13}Mn_{0.87}O_2$ has 184 mAh/g while the highest capacities in **set 3** are 198 mAh/g for Li, 197 mAh/g for Co, and 212 mAh/g for Tl, showing extra improvement. These values certainly outperform currently commercialized cathodes, especially if pre-sodiated hard carbon can be used as the anode. However, as discussed extensively below, a high energy density is not sufficient as this material is currently prevented from being used primarily due to poor air stability[27]. Similarly, capacity retentions after 10 cycles for the undoped NFMO exhibited 97% retention, while several doped samples from **set 1** displayed enhanced retention, such as Zn (99%), Ga (100%), and Ni (102%). Hence, our systematic examination of doping effects on three sets of samples revealed several benefits in the cycling performance, including the smoothing of CV curves, reduction in phase transition, mitigation of voltage hysteresis, and overall improvement in battery performance. However, the roadblocks to commercialization are not primarily associated with these metrics. Instead, the main challenges lie in the poor stability in air and the excessive dissolution of transition metals during cycling such that we focus on these for the rest of this article.

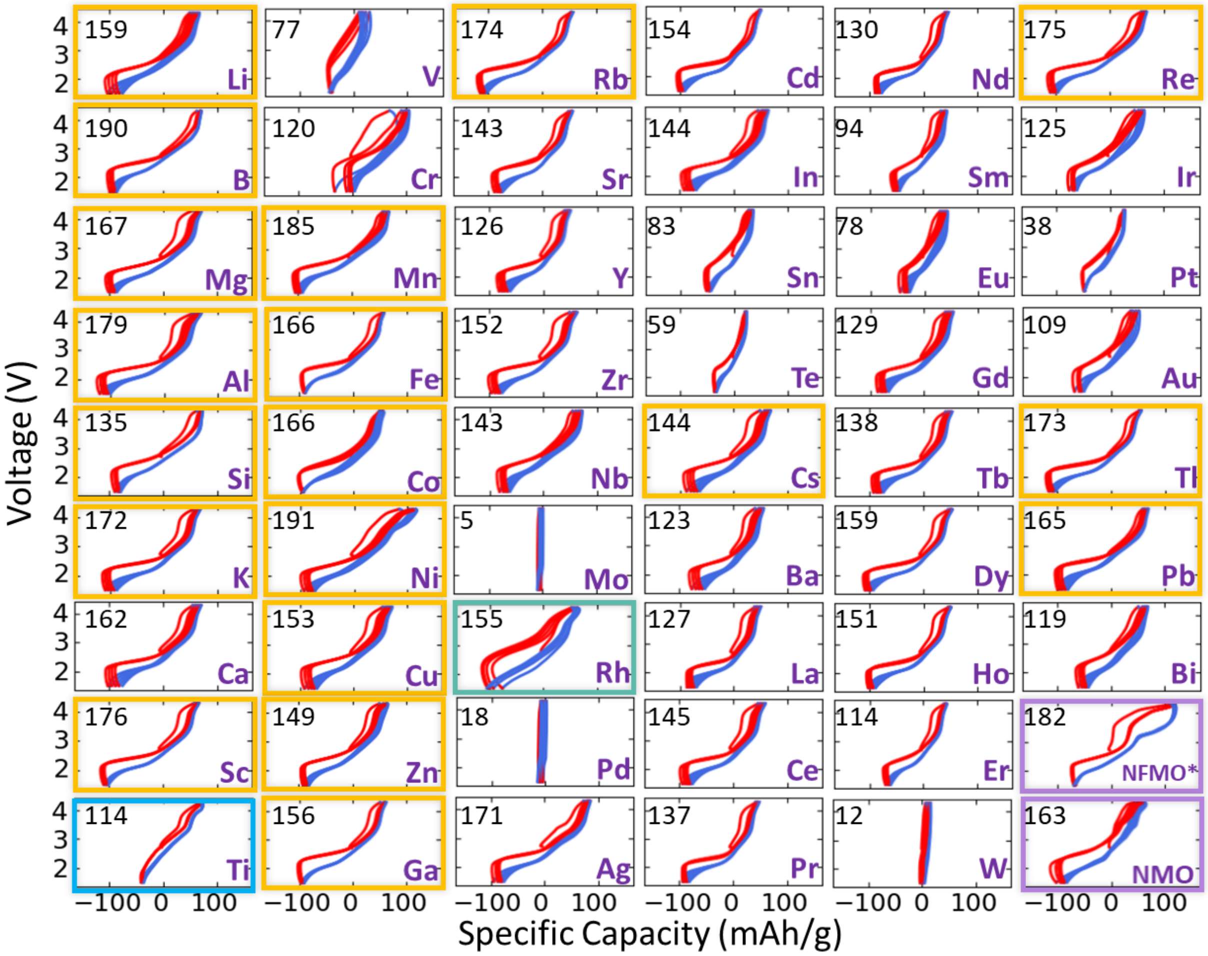

Figure 4.2 *Voltage profile plots derived from processing the CVs presented in* ***Figure S4.1****, cycled within the voltage range of 1.5 V to 4.3 V vs Na/Na*$^+$ *at the scan rate of 0.1 V h*$^{-1}$. *On each panel is indicated the first cycle discharge capacity in mAh g*$^{-1}$. *The plots depict the first charge and subsequent 5 cycles for* ***set 1*** *samples. The colored outlines indicate the distinct phases: pure P2 structure (yellow), P3 structure (green), tunnel structure (blue), and P2-*$Na_{0.66}Fe_{0.5}Mn_{0.5}O_2$ *(NFMO*) and P2/P'2-*$Na_{0.66}MnO_2$ *(NMO).*

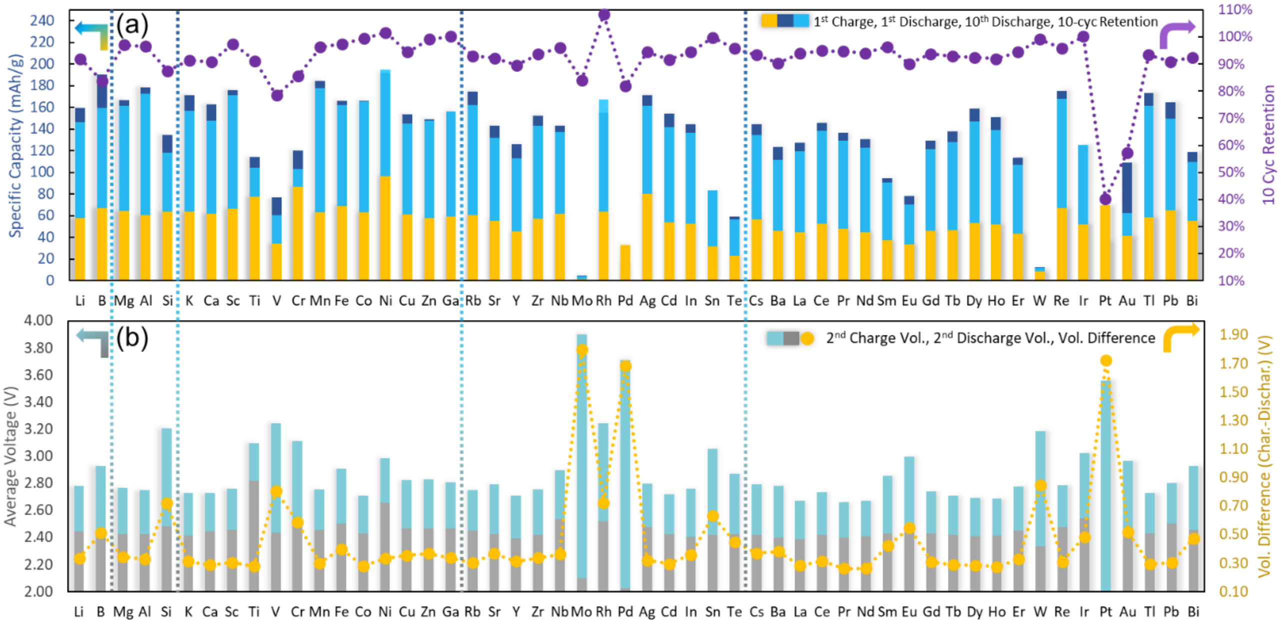

Figure 4.3 *Electrochemical properties extracted from the combinatorial cells for* ***set 1*** *samples. (a) Specific capacities for 1st charge (yellow), 1st discharge (deep blue), and 10th cycle discharge (cyan) are plotted on the primary y-axis. The 10-cycle capacity retention is represented by the purple scatter plot and plotted on the secondary y-axis. (b) Average voltages for 2nd charge (turquoise) and 2nd discharge (gray). The voltage difference is obtained by the subtraction of the average voltages of charge and discharge and plotted on secondary y-axis as the yellow scatter plot.*

4.4.3 Accelerated aging

To assess the air stability, we subjected sample **sets 1-3** to accelerated aging, as detailed in the methods section. The XRD was performed after different time intervals and storage environments to obtain the structural degradation over time (**Figure 4.4**). Utilizing Rietveld refinement, we quantified the fraction of pristine phase remaining in order to determine air stability (**Figure 4.4b**). Clearly, dopants play a critical role in determining the air stability of the materials with the Li-doped sample retaining 96% of the P2 phase while the Sc-doped sample was completely degraded with 0% retention. Consequently, we established an air stability ranking based on the different mother compositions of the three sets of samples to minimize bias, shown as a heat map in **Figure 4.4c**, where the colors depict the stability of the different doped samples. Specifically, dopants at both ends of the ranking such as Li and Sc, demonstrate decisive effects on air stability regardless of which sample set they were in, while the dopants in the middle indicate moderate effects, which are also influenced by the specific composition of the sample sets. Interestingly, **set 2** samples exhibited air stability comparable to that of **set 1** even though doping level was lower (5% vs. 10%), suggesting that a high doping level is not required for improved air stability. Hence, the reasonable amount of dopants will vary dopant to dopant. For example, Li content can and should be reduced to 5% in order to improve surface stability without detriment to the specific capacity (198 mAh/g was obtained for Li in **set 3** at 5% doping); such limits will also need to account for the changing cost and emerging sustainability concerns related to Li. Conversely, dopants such as Ni, Cu, or Ga may necessitate a higher doping level (10%) to achieve satisfactory air stability, and this may be troublesome from a cost point of view. Overall, the obtained air stability ranking strongly suggests that dopant identity is crucial, and further concerns related to critical minerals may need to be considered as these materials are considered for commercialization. This discussion certainly highlights the need to consider additional cost and sustainability factors when determining the optimal doping level.

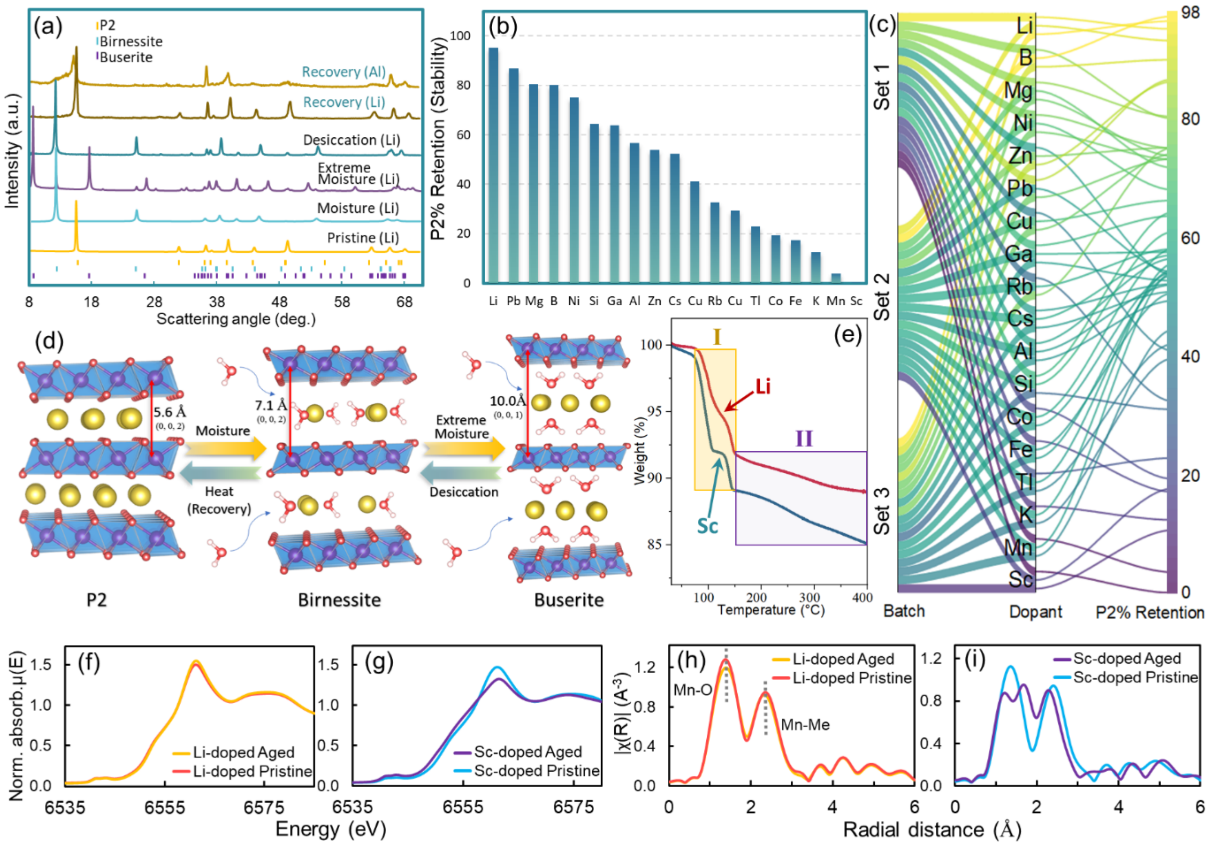

Figure 4.4 *Investigation of air stability. (a) Representative XRD patterns for the Li-doped sample (**set 1**) under different aged conditions: pristine, moisture (RH = 45%), extreme moisture (RH > 90%), desiccation (RH < 10%). Recovery was performed at 160 °C for 12 hours for Li and Al-doped samples. (b) P2% retention obtained from quantitative Rietveld refinement for aged **set 1** samples. (c) Heat map representing the P2% retention for three sets of aged samples with different dopants. The dopant order is determined based on the average P2% retention across the three sets of aged samples. (d) Schematic diagram illustrating the process of water insertion and structural transformations involving the P2, birnessite, and buserite phases. (e) Thermogravimetric analysis (TGA) plot showing weight loss and temperature for Li and Sc-doped samples. (f) and (g) XANES spectra at Mn K-edge of Li and Sc-doped **set 1** samples and their aged samples at RH>90% after 7 days. (h) and (i) corresponding Fourier-transformed EXAFS spectra.*

To investigate the correlation between dopant identity and air stability, we have reviewed several mechanisms. Duffort et al. studied the aging mechanism of P2-$Na_{0.67}Mn_{0.5}Fe_{0.5}O_2$ and proposed that during air-induced aging, Mn^{3+} may oxidize to compensate for Na deintercalation, forming sodium carbonate[13]. Consequently, the presence of Mn^{3+} renders the material more air sensitive. They found that doping with Ni improved air stability. In **Figure 4.4c**, we also observed that the presence of Ni indeed enhances air stability compared to Fe- and Mn-based materials. Based on these assumptions, lower valence dopants may be favored as they can increase the Mn average oxidation state through charge balancing, such as Li, Mg, Ni, Zn, and Cu. However, these assumptions may not always hold true. Alkali metals such as K and Cs in doped samples may suffer from worse air stability, as the large ions may destabilize the material. Moreover, Zuo et al. proposed a correlation between redox potentials and air stability[28], which holds true only for active dopants such as $Cu^{2+/3+}$ and $Ni^{2+/4+}$. However, considering that most dopants are inactive, this method is difficult to apply universally. Although a few theories have shown partial predictability, some inactive dopants pose challenges for predicting air stability, especially considering that some dopants can exhibit multiple valences. This again highlights the importance of wide testing as performed in the current study.

It is also essential to investigate the potential impact of morphological changes due to doping on the air stability. Larger particles will have a lower surface area per unit volume (this is inversely proportional to the radius) so they could be expected to show improved air stability. **Figure S4.13** shows SEM images for in **Figure S4.13**. As depicted in the SEM images, most of the doped samples exhibit similar particle sizes (approximately 1-3 μm) to the undoped sample. There is certainly no order of magnitude or more change in particle size as we have previously seen in doped Li-ion cathodes[24]. It is also worth noting that large porous secondary particles are seen for all samples such that primary particle size is the key to air stability (i.e. the materials are porous enough for air/electrolyte to reach all primary particles). Some dopants that show good air stability, like B and Si, also show larger primary particles than the undoped. However, others, like Li, show quite comparable particle sizes. On the other hand, Sc showing poor air stability also shows smaller particle sizes than the undoped. We therefore conclude that doping certainly plays a role in particle size control and this impacts air stability, but other factors are important as well and this will be explored further below using Machine-Learning algorithms to decouple size effects (via XRD peak widths) from structural effects like latticed size.

To unravel the air degradation mechanism, we analyzed the large sets of XRD data from the accelerated aging, allowing us to identify the primary mechanisms illustrated in **Figure 4.4d**. Initially, the P2 structure undergoes conversion to the birnessite structure in the presence of moisture[29]. As water molecules insert into the Na^+ layers, the P2-$Na_{0.66}Fe_{0.13}Mn_{0.87}O_2$ crystal structure will expand along the *c*-axis, where the distance between the neighbor transition metal slabs increased from 5.6 Å to 7.1 Å. Under higher moisture (RH > 90%), the water molecules will continue to insert into the Na^+ layers to form the buserite phase and expand the interslab distance to 10 Å, as shown in **Figure 4.4a,d**. The polarity and intermolecular forces of water molecules facilitate hydrogen interaction to oxygen from transition metal slab to form M-O···H, while oxygen from water molecules is attracted to Na^+ ions. Notably, the intensity of the (0,0,4) peak in the birnessite structure increases. Consequently, the increased interslab distance enhances the ionic nature of Na^+, promoting its migration onto the surface where it reacts with atmospheric CO_2 to form carbonates[13,30]. To validate the formation of hydrogen bond[31], the distance between hydrogen and oxygen from the metal slab in P2-$Na_{0.66}Fe_{0.13}Mn_{0.87}O_2$ was calculated based on the given configuration and interslab distance, resulting in a calculated distance of 2.75 Å, indicative of weak hydrogen bonding.

X-ray absorption spectroscopy (XAS) was conducted on both Li and Sc-doped pristine samples and aged samples for 7 days in high humidity (RH > 90%), as shown in **Figure 4.4f-i**. The near edge spectroscopy demonstrates a discernible shift towards lower energy and reduced absorption magnitude in the Sc-doped sample after aging. This suggests a potential reduction of Mn to a lower oxidation state[32,33]. The pair distribution function (PDF) obtained from the EXAFS region for the aged Sc-doped sample reveals a significant alteration in the local structure, particularly evident in the Mn-O bond. This transformation could potentially be attributed to the heightened presence of Mn^{3+} ions, possibly inducing Jahn-Teller distortion[26]. Additionally, the interaction between M-O···H_2O can also alter the chemical environment around the Mn, we attribute the new peak in the aged Sc-doped sample in **Figure 4.4i** to intercalated water in the aged structure. In contrast, the Li-doped sample exhibits excellent stability both in near-edge and the PDF after aging. This shows that the Li-doped structure is remarkably robust, with the local structure showing no change throughout the aging process. Thermogravimetric analysis (TGA) was also carried out to investigate aged Li and Sc-doped samples (**Figure 4.4e**). Despite both samples starting with a single phase birnessite, the Sc-doped sample exhibited higher weight loss. Notably, the Sc-doped sample showed a distinct step after 100 °C, suggesting stronger bonding of crystalline water. Even after the main weight-loss region I at 160 °C, weight-loss persisted in the Sc-doped sample, indicating the potential presence of even stronger bonding crystalline water and carbonate decomposition in region II. Therefore, the TGA reveals that both samples can de-intercalate water, indicating the possibility of material recovery. Subsequent XRD analysis was performed on both samples post-TGA, as shown in **Figure S4.6**. The Li-doped sample exhibited excellent recovery back to the original P2 structure, while the Sc-doped sample only partially recovered, possibly due to irreversible Na^+ loss during aging. Recovery was also systematically studied at 160 °C for 12 hours, corresponding to the completion temperature of region I from TGA. While the Li-doped sample successfully reverted to the P2 structure, other samples such as Al-doped displayed partial reversion, indicating a higher energy requirement, as shown in **Figure 4.4a**. Interestingly, the (1,0,0) peaks for both samples still stay sharp, indicating that degradation primarily occurred along the c-axis, with the transition metal slabs largely preserved after aging. The effects of the dopants were evident not only in the air stability of the materials but also in their ability to recover to the P2 structure. Hence, we demonstrate recovery can serve as another viable strategy to overcome the hygroscopicity bottleneck of layered oxides, but the ability to recover is also clearly dopant dependent.

4.4.4 Machine learning analysis

Despite uncovering the processes and mechanisms of material degradation, predicting air stability remains a significant challenge that requires time during aging and large amounts of data as illustrated in **Figure 4.5**. Over 1000 XRD patterns were obtained in the air stability study, and this presents an opportunity to leverage machine learning (ML) techniques[34–38] as detailed in the methods section. Specifically, we aim to predict air stability using pristine XRD only; this would accelerate our testing significantly. First, the XRD scans from materials at different aging levels were represented as single points and projected onto three-dimensional coordinates, as illustrated in **Figure S4.8**. Each coordinate represents the latent structural information (matrix), maximizing the amount of explanatory predictor variables (input XRD data). We successfully implemented dimensionality reduction, by transforming the high-dimensional XRD data (>4000 predictor variables) into a low-dimensional space, enabling visualization of the structural relationships between materials at different aging levels. To predict air stability based on XRD patterns, we applied Partial Least Squares Regression (PLSR) as algorithm[39,40]. PLSR is a supervised learning algorithm that can be used to predict a continuous output variable (in this case, air stability) from a set of input variables (in this case, the XRD data). As shown in **Figures 4.5 and S4.8**, we trained the PLSR model based on a subset of the XRD data with known air stability properties. The remaining XRD data was used to validate the model using cross-validation technique (**Figure S4.8**). **Figure 4.5a** shows the prediction trained from both pristine and aged samples with an excellent R^2 value of 0.981. Furthermore, the ML model tested exclusively on XRD patterns from pristine samples after training on the full set yielded a very good prediction with an R^2 value of 0.912 (**Figure 4.5b**). Therefore, we have successfully trained and cross-validated an ML model capable of directly predicting air stability from pristine XRD patterns. This accomplishment has the potential to expedite the exploration of novel materials, particularly in the context of more complex composition studies.

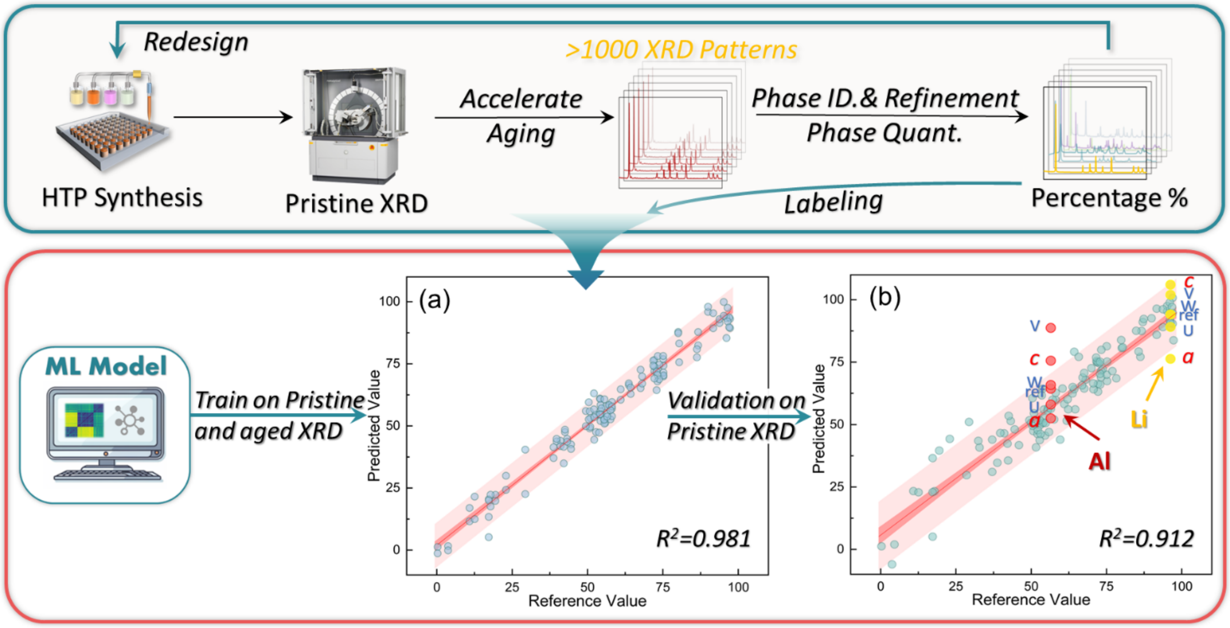

***Figure 4.5** Workflow scheme of lab-based analysis and data-driven machine learning model. (a) PLSR prediction plot trained using pristine and aged samples. (b) PLSR prediction plot trained using pristine samples and validated against lattice parameters and peak profiles. XRD data from Li and Al-doped samples are utilized to fine-tune the peak profiles and enable a comprehensive assessment of the variations in different parameters.*

It also provides a unique opportunity to gain a deeper understanding of what features the ML model has recognized in the pristine XRD in order to predict air stability in further research. We first use the fully trained model to predict the air stability of the Rietveld fits to two samples (Li and Al doped). As shown in **Table S4.2**, these both show results close to the experimental, though clearly the noise in the original data affected the predictions slightly. Next, we repeat the predictions but after changing a single parameter in the Rietveld calculation[41]. We explore 5 parameters: the U, V, W parameters that govern peak widths in Caglioti formula, as well as the lattice parameters *a* and *c*. **Figure S4.9** show that air stability vs. either peak widths or lattice parameters show very scattered behavior with no clear correlation; any information is hidden in the noise and interdependence between various parameters. **Table S4.2** and **Figure 4.5b** show the results of using the ML model to study the impact of these parameters. We first discover that W had minimal impact, while increasing U (peak broadening) resulted in an air stability decrease. Similarly, increasing V by 100% (with V being negative) resulted in sharper peaks and an increase in the predicted stability. For both U and V, the broadening of peak profiles may stem from smaller crystallite sizes and larger microstrain. This leads to the expected conclusion that smaller particles and more strained crystals lead to materials that are less stable in air. We speculate that smaller crystallite sizes may facilitate expansion along the *c*-axis and also present a higher surface area for contact with air, while larger microstrains may undergo structural expansion to alleviate the strain. Therefore, we can interpret and conclude from the ML model that broadening of peak profiles is associated with lower air stability. Surprisingly, we found that the ML model expects significant changes in air stability due to lattice parameters, but they are in opposite directions: increasing the lattice parameters *a* led to a decrease in air stability, while increasing *c* led to a decrease in predicted stability. We speculate that the poor correlations seen in **Figure S4.9a,b,c** are due to coupling between the effects of both lattice parameters (*i.e. c* vs *a* also shows a scattered plot with a weak correlation, **Figure S4.9d**) such that the ML model can decouple these effects (and any others at play) for the first time. The result that a larger *c* value may be beneficial is counterintuitive, as a larger *c* value was expected to indicate worse stability suggesting greater space for the Na layer. We propose two possible reasons where a larger *c* could be beneficial: **(1)** if large dopants are on the transition metal layers then the MO_2 slabs will be larger and interfere with intercalation in the layers in between, **(2)** if dopants occupy Na sites, they may interfere directly with the intercalation of water. This first application of ML to our large air stability data sets clearly shows promise for both predictability and also for a deeper understanding of why certain materials show dramatically improved air stability.

4.4.5 Transition metal dissolution

To address the challenge of transition metal dissolution in layered cathode materials, we investigated the impact of dopants on this phenomenon using ICP-OES analysis, as detailed in the methods section. 20 different dopants in $Na_{0.66}Mn_{0.5}Fe_{0.4}X_{0.1}O_2$ were tested as shown in **Figure 4.6a,b**. This composition is chosen because it can show better contrast on both Mn and Fe dissolution[14]. The ICP results revealed the presence of both Fe and Mn with high contrast between samples, with some dopants like Li and B being effective in suppressing the dissolution of both metals. To account for potential contamination of Fe from steel cell parts in our Swagelok cells, $Na_{0.66}MnO_2$ (notes as NMO) was also analyzed, revealing significantly lower Fe content than for doped $Na_{0.66}Mn_{0.5}Fe_{0.4}X_{0.1}O_2$ samples (as high as 2000 ppm), confirming that only a relatively small amount of Fe comes from the cell components, which is used as the baseline for iron. For $Na_{0.66}Mn_{0.5}Fe_{0.5}O_2$, the Fe dissolution is about 5 times more severe than Mn, emphasizing the greater concern regarding Fe dissolution. Analysis of Fe dissolution in **Figure 4.6a** revealed that

11 dopants such as Li, B, Cu, Pb demonstrated improvements in Fe dissolution. On the other hand, the improvement of the dopants is more effective for Mn dissolution, with 16 dopants demonstrating suppression.

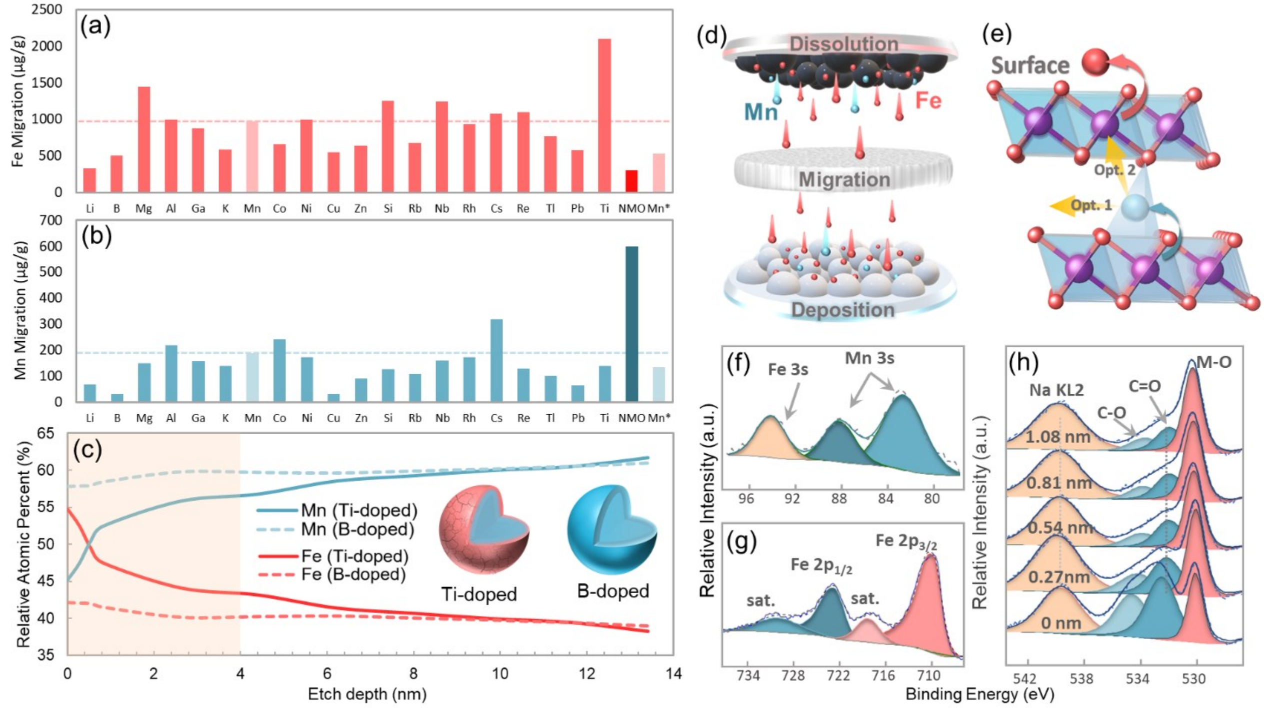

Figure 4.6 *Investigation of transition metal dissolution. Dissolution concentration of (a) Fe and (b) Mn determined by ICP-OES of the Na anode in cycled* $Na_{0.66}Fe_{0.4}Mn_{0.5}X_{0.1}O_2$*, the undoped* $Na_{0.66}Fe_{0.5}Mn_{0.5}O_2$ *(noted as Mn for cycled, Mn* for uncycled cell), and* $Na_{0.66}MnO_2$ *(noted as NMO). The ICP results were normalized by the mass of the cathode with μg metal per g of cathode. (c) Relative atomic profile of Ti and B-doped samples obtained from XPS with Ar etching (rate: 0.09 nm/sec). The inset plot illustrates the simulated reordering of transition metals from the surface to the bulk. (d) Schematic representation of transition metal dissolution pathways from the cathode to the electrolyte and deposition on the anode. (e) Illustration of metal dissolution at the surface and in the bulk, depicting two options for neighbor transition ions to hop into the surface vacancy or into the Na ion layer. (f, g) XPS analysis of Fe and Mn for quantifying the relative ratios. (h) XPS analysis of O 1s and Na KL2 profiles at different etching levels.*

Surprisingly, the B-doped sample shows a significant suppression effect on Mn dissolution with over 10 times more than the Cs-doped sample and 20 times greater than $Na_{0.66}MnO_2$, highlighting doping as a highly effective strategy for suppressing transition metal dissolution. The intriguing discovery revealed that the elements Li, B, Cu, and Pb exhibited the highest efficacy in suppressing both Fe and Mn dissolution.

Moreover, we also investigated the mechanism underlying transition metal dissolution. Firstly, we measured the metal dissolution of uncycled $Na_{0.66}Mn_{0.5}Fe_{0.5}O_2$, in which the cell was assembled but only rested for the same days of 10 cycles, as shown in **Figure 4.6a,b** (noted as Mn*). Strikingly, even without cycling, Fe and Mn dissolution from the cathode was observed, indicating instability in the cathode-electrolyte interphase or electrolyte corrosion. This also indicates that cycling contributes to increased metal dissolution, as evidenced by the cycled $Na_{0.66}Mn_{0.5}Fe_{0.5}O_2$ (noted as Mn).

To gain further insights into the surface characteristics affected by different doping effects, XPS was used to analyze the surface of the particles. Firstly, **Figure 4.6h** depicts the detection of the cathode-electrolyte interface, where the organic C-O/C=O signals exhibit a decay from the surface, while the M-O peak increases within 1 nm showing that the SEI is limiting to a very small depth[42]. Also, pristine B-doped and Ti-doped samples showed consistent ratios of Fe and Mn as dispensed as a function of depth during Ar^+ sputtering (**Figure 4.6c**), with Fe/(Fe+Mn) = 40% (dispensed: 44%). However, after cycling, the two cathodes displayed different composition profiles from Ar^+ etching at about 4 nm from the surface. The B-doped sample (low metal dissolution) maintained its composition ratio after cycling (about 40%), while the Ti-doped sample (high Fe dissolution) exhibits a heterogeneous distribution of Fe and Mn, indicating that the surface has been reconstructed after cycling, possibly attributed to Fe dissolution from deeper regions and cracks[43,44]. Moreover, the integrated intensity of Fe in **Figure S4.10** indicated that Fe dissolution is more severe on the surface, even up to a depth of 14 nm from the surface. Therefore, the mechanisms discussed above clearly propagate deeply into the particles, unless the correct dopant like B is utilized.

Notably, our findings suggest that the doping effect may also induce surface reconstruction by altering the surface and strain energy. This phenomenon is exemplified by the work of Guo et al., where Ti dopants, even without an additional coating process, can trigger surface reconstruction[45]. Li et al. identified the overexploitation of Mn in NFM materials, resulting in the instability of layered materials and initiating significant metal dissolution[46]. Although Ti and Mg dopants are often associated with various benefits such as improved air stability and modified electrochemistry, as mentioned in the aforementioned studies and literature[47–53], they are not found to effectively suppress Fe dissolution, but rather exhibit minor suppression on Mn dissolution, with compromised surface stability as demonstrated by XPS profile studies. In addition, previously reported Mg-doped samples often exhibit higher Mg content (>20%), which can induce a superstructure that enhances structural stability and anionic activity[54,55]. In our study, with a doping level of 10%, we did not observe either a superstructure via XRD or enhanced anionic activity. This may contribute to the inconsistency observed in the literature. Additionally, Suyeon Lee et al. observed the Mg-doped NFMO materials undergo heterostructure alteration from layered to disordered phases, including spinel-like and rock salt-like nanostructures, after Na^+ deintercalation during moisture storage[56]. This suggests that the unstable surface may undergo structural evolution.

It is important to emphasize that the primary objective of our study is to compare various properties altered by doping. It is logical to infer that doping may not consistently enhance all material properties. Instead, our findings suggest that while some dopants may improve certain properties, others may not. To our knowledge, there remains a dearth of comparative studies on the impact of different dopants on transition metal dissolution, despite this being a well-recognized and detrimental phenomenon. Our investigations have unveiled that the doping effect on surface and bulk chemistry may exhibit inconsistency. The mitigation of transition metal dissolution could potentially enhance surface stability via doping strategy.

4.5 Conclusion

In this study, we conducted a systematic comparison of the effects of over 50 dopants in cathode materials, with the aim of facilitating material rational design. Our research addresses a significant gap in the literature, as most studies have focused on the effects of single dopants, thereby limiting the understanding of the broader range of options available for layered oxide materials.

By employing high-throughput and data-driven analysis, we identified new compositions that incorporate novel dopants such as Rb, Cs, Sc, Ga, B, Re, Tl, and Pb. These findings greatly enhance the selection of compositions for layered oxide materials, opening up new possibilities for material design. Additionally, we systematically reported on the electrochemical properties of the doped materials and achieved notable improvements in capacities and retentions. For instance, $Na_{0.66}Fe_{0.08}Mn_{0.87}Tl_{0.05}O_2$ exhibited a capacity of 212 mAh/g, while $Na_{0.66}Fe_{0.13}Mn_{0.77}Ga_{0.1}O_2$ demonstrated no capacity decay over 10 cycles with well-maintained P2 structure during charge and discharge. These findings warrant further investigation and hold promise for the development of advanced cathode materials.

Furthermore, we explored the influence of dopants on the surface properties of the materials, particularly their resistance to air and moisture corrosion. Our study revealed a ranking list of different dopants, providing valuable insights for material design. Notably, the Li-doped sample exhibited remarkable air stability even after accelerated aging. We leveraged machine learning techniques and analyzed over 1000 XRD data, which allowed us to identify that improved air stability correlated with reduced microstrain and larger particle size. Additionally, we found that the lattice parameter of the materials also played a role in air stability. Moreover, doping was found to effectively suppress metal dissolution from the particle surface. Notably, Li, B, Cu, and Pb dopants demonstrated enhanced metal dissolution issue, as evidenced by the profile investigation. This comprehensive study sheds light on the intricate effects of doping on the electrode-electrolyte interface, providing meaningful insights into the design and optimization of cathode materials. Furthermore, this study serves as a valuable guide for future co-doping investigations, allowing for the combination of multiple improved properties in finely tuned compositions. The wealth of knowledge gained from this research lays a solid foundation for further exploration and advances in the field of material science and energy storage systems.

4.6 Acknowledgments

This work was funded by a research contract with Umicore, as well as by NSERC under the auspices of a discovery grant and the Canadian Foundation for Innovation. We thank Dr. Thomas Degen from Malvern Panalytical for useful conversations regarding machine learning algorithms. Part of the research described in this paper was performed using the HXMA beamline at the Canadian Light Source, a national research facility of the University of Saskatchewan, which is supported by the Canada Foundation for Innovation (CFI), the Natural Sciences and Engineering Research Council (NSERC), the National Research Council (NRC), the Canadian Institutes of Health Research (CIHR), the Government of Saskatchewan, and the University of Saskatchewan.

4.7 Supporting Information

Table S4.1 *The results of automated XRD refinement for samples with different dopants. Site occupancies are not relaxed.*

Dopant	ICSD Code	Phase	Molar %	Dope %	Unidentified Peak %	GoF (χ2)	Spacegroup	*a* [Å]	*b* [Å]	*c* [Å]
Li	196276	P2-Na0.66Mn0.77Fe0.13M0.1O2	100%	10%		1.89	P63/mmc	2.85(3)	2.85(3)	11.17(9)
B	196276	P2-Na0.66Mn0.77Fe0.13M0.1O2	100%	10%		1.24	P63/mmc	2.86(9)	2.86(9)	11.19(9)
Mg	196276	P2-Na0.66Mn0.77Fe0.13M0.1O2	100%	10%		1.95	P63/mmc	2.87(9)	2.87(9)	11.26(6)
Al	196276	P2-Na0.66Mn0.77Fe0.13M0.1O2	100%	10%		1.88	P63/mmc	2.85(8)	2.85(8)	11.22(2)
Si	196276	P2-Na0.66Mn0.77Fe0.13M0.1O2	100%	10%		1.55	P63/mmc	2.88(7)	2.88(7)	11.25(6)
K	196276	P2-Na0.66Mn0.77Fe0.13M0.1O2	100%	10%		2.08	P63/mmc	2.87(2)	2.87(2)	11.16(8)
Ca	196276	P2-Na0.66Mn0.77Fe0.13M0.1O2	92%	0%		2.22	P63/mmc	2.87(1)	2.87(1)	11.16(6)
	258991	Ca4Mn4O12	8%			2.22	Pnma	5.26(9)	7.40(6)	5.25(5)
Sc	196276	P2-Na0.66Mn0.77Fe0.13M0.1O2	100%	10%		1.80	P63/mmc	2.87(9)	2.87(9)	11.20(6)
Ti	196276	P2-Na0.66Mn0.77Fe0.13M0.1O2	24%	10%		2.06	P63/mmc	2.87(1)	2.87(1)	11.22(4)
	182617	Na7.04Mn18O36	76%			2.06	Pbam	9.12(9)	26.2(2)	2.852(2)
V	196276	P2-Na0.66Mn0.77Fe0.13M0.1O2	95%	0%		1.92	P63/mmc	2.87(5)	2.87(5)	11.26(9)
	33561	Fe16Mn16O48	5%			1.92	Ia-3	9.34(3)	9.34(3)	9.343(3)
Cr	196276	P2-Na0.66Mn0.77Fe0.13M0.1O2	62%	0%		3.14	P63/mmc	2.87(4)	2.87(4)	11.24(2)
	257184	Na2Cr4O8	37%			3.14	P121/m1	4.99(1)	5.75(2)	5.869(9)
	61271	Mn32O48	1%			3.14	Ia-3	9.43(3)	9.43(3)	9.43(3)
Mn	196276	P2-Na0.66Mn0.77Fe0.13M0.1O2	100%	10%		2.03	P63/mmc	2.87(4)	2.87(4)	11.22(5)
Fe	196276	P2-Na0.66Mn0.77Fe0.13M0.1O2	100%	10%		1.65	P63/mmc	2.89(3)	2.89(3)	11.28(8)
Co	196276	P2-Na0.66Mn0.77Fe0.13M0.1O2	100%	10%		1.86	P63/mmc	2.86(1)	2.86(1)	11.22(2)
Ni	196276	P2-Na0.66Mn0.77Fe0.13M0.1O2	100%	10%		1.80	P63/mmc	2.87(7)	2.87(7)	11.24(9)
Cu	196276	P2-Na0.66Mn0.77Fe0.13M0.1O2	100%	10%	2%	2.80	P63/mmc	2.87(6)	2.87(6)	11.21(1)
Zn	196276	P2-Na0.66Mn0.77Fe0.13M0.1O2	98%	4%		1.90	P63/mmc	2.87(5)	2.87(5)	11.20(8)
	28512	Zn7.20Mn0.80Fe16O32	2%			1.90	Fd-3m	8.37(5)	8.37(5)	8.375(5)
Ga	196276	P2-Na0.66Mn0.77Fe0.13M0.1O2	100%	10%		2.19	P63/mmc	2.87(8)	2.87(8)	11.22(1)
Rb	196276	P2-Na0.66Mn0.77Fe0.13M0.1O2	100%	10%		1.99	P63/mmc	2.87(7)	2.87(7)	11.19(6)
Sr	196276	P2-Na0.66Mn0.77Fe0.13M0.1O2	94%	0%		1.34	P63/mmc	2.86(9)	2.86(9)	11.16(7)
	202615	Sr4Mn4O12	6%			1.34	P63/mmc	5.41(7)	5.41(7)	9.03(3)
Y	196276	P2-Na0.66Mn0.77Fe0.13M0.1O2	94%	0%		1.34	P63/mmc	2.85(8)	2.85(8)	11.13(8)
	166217	Y4Mn4O12	6%			1.34	Pnma	5.62(2)	7.41(4)	5.232(2)
Zr	196276	P2-Na0.66Mn0.77Fe0.13M0.1O2	96%	4%		2.29	P63/mmc	2.86(1)	2.86(1)	11.14(8)
	33561	Fe16Mn16O48	1%			2.29	Ia-3	8.35(5)	8.35(5)	8.35(5)
	237006	Zr4O8	3%			2.29	Fm-3m	5.08(4)	5.08(4)	5.084(4)
Nb	196276	P2-Na0.66Mn0.77Fe0.13M0.1O2	95%	4%		1.79	P63/mmc	2.89(2)	2.89(2)	11.28(2)
	74642	Nb4Na4O12	3%			1.79	Pmc21	7.77(6)	5.49(9)	5.568(8)
Mo	196276	P2-Na0.66Mn0.77Fe0.13M0.1O2	38%	0%		2.11	P63/mmc	2.51(9)	2.51(9)	12.21(4)
	159865	Mn32O48	62%			2.11	Ia-3	9.41(7)	9.41(7)	9.417(7)
Rh	196276	P2-Na0.66Mn0.77Fe0.13M0.1O2	28%	10%		2.63	P63/mmc	2.86(8)	2.86(8)	11.45(6)
	291601	P3-Na0.66Mn0.77Fe0.13M0.1O2	72%			2.63	C12/m1	5.02(2)	2.88(8)	5.869(9)

Dopant	ICSD Code	Phase	Molar %	Dope %	Unidentified Peak %	GoF (χ2)	Spacegroup	*a* [Å]	*b* [Å]	*c* [Å]
Pd	30237	Fe16Mn16O48	23%			2.11	Ia-3	9.36(9)	9.36(9)	9.369(9)
	29281	Pd2O2	32%			2.11	P42/mmc	3.02(8)	3.02(8)	5.305(5)
	76612	Mn6.80Fe5.20O16	17%			2.11	I41/amd	5.97(2)	5.97(2)	8.456(6)
Ag	196276	P2-Na0.66Mn0.77Fe0.13M0.1O2	95%	2%		2.27	P63/mmc	2.86(9)	2.86(9)	11.19(9)
	33561	Fe16Mn16O48	0.4%			2.27	Ia-3	9.04(5)	9.04(5)	9.045(5)
	670299	Ag4	5%			2.27	Fm-3m	4.06(4)	4.06(4)	4.064(4)
Cd	196276	P2-Na0.66Mn0.77Fe0.13M0.1O2	95%	0%		2.26	P63/mmc	2.86(6)	2.86(6)	11.15(3)
	87222	Cd3.60Mn0.40O4	5%			2.26	Fm-3m	4.65(7)	4.65(7)	4.657(7)
In	196276	P2-Na0.66Mn0.77Fe0.13M0.1O2	99%	0%		2.02	P63/mmc	2.87(7)	2.87(7)	11.21(3)
	252369	In32O48	1%			2.02	Ia-3	10.0(3)	10.0(3)	10.07(3)
Sn	196276	P2-Na0.66Mn0.77Fe0.13M0.1O2	23%	0%		1.40	P63/mmc	2.86(9)	2.86(9)	11.26(3)
	262768	Sn2O4	15%			1.40	P42/mnm	4.71(5)	4.71(5)	3.169(9)
	290640	Mn32O48	4%			1.40	Pbca	9.38(1)	9.39(9)	9.41(1)
	291601	Na0.80Cr2O4	58%			1.40	C12/m1	4.97(5)	2.87(5)	5.858(8)
Te	196276	P2-Na0.66Mn0.77Fe0.13M0.1O2	79%	0%		1.75	P63/mmc	2.86(6)	2.86(6)	11.22(9)
	0	Fe16Mn16O48	21%			1.75	Ia-3	9.34(4)	9.34(4)	9.344(4)
Cs	196276	P2-Na0.66Mn0.77Fe0.13M0.1O2	100%	10%	2%	3.00	P63/mmc	2.87(3)	2.87(3)	11.18(3)
Ba	196276	P2-Na0.66Mn0.77Fe0.13M0.1O2	90%	0%		2.76	P63/mmc	2.86(7)	2.86(7)	11.15(3)
	89994	Ba2Mn2O6	9%			2.76	P63/mmc	5.66(8)	5.66(8)	4.788(8)
	672059	Ba4O4	2%			2.76	Fm-3m	5.40(6)	5.40(6)	5.406(6)
La	196276	P2-Na0.66Mn0.77Fe0.13M0.1O2	92%	0%		1.75	P63/mmc	2.86(1)	2.86(1)	11.15(7)
	82191	La4.92Na0.96Mn6O18	8%			1.75	R-3c	5.43(7)	5.43(7)	13.33(4)
Ce	196276	P2-Na0.66Mn0.77Fe0.13M0.1O2	93%	0%		1.96	P63/mmc	2.86(8)	2.86(8)	11.18(6)
	670742	Ce4O8	7%			1.96	Fm-3m	5.39(1)	5.39(1)	5.391(1)
Pr	196276	P2-Na0.66Mn0.77Fe0.13M0.1O2	92%	0%		4.83	P63/mmc	2.85(7)	2.85(7)	11.39(1)
	173546	Pr3.16Na0.84Mn4O12	0.2%			4.83	Pnma	5.40(2)	7.64(5)	5.493(3)
	93615	Pr3.40Na0.60Mn4O12	8%			4.83	Pnma	5.35(5)	7.61(4)	5.549(9)
Nd	196276	P2-Na0.66Mn0.77Fe0.13M0.1O2	91%	0%		2.70	P63/mmc	2.86(6)	2.86(6)	11.18(8)
	163729	Nd3.60Mn4O12	9%			2.70	Pnma	5.40(6)	7.63(8)	5.401(1)
Sm	196276	P2-Na0.66Mn0.77Fe0.13M0.1O2	92%	0%		1.82	P63/mmc	2.86(9)	2.86(9)	11.19(8)
	258440	Sm4Fe2.40Co1.60O11.20	8%			1.82	Pnma	5.44(6)	7.6(6)	5.369(9)
Eu	196276	P2-Na0.66Mn0.77Fe0.13M0.1O2	83%	0%		1.78	P63/mmc	2.87(6)	2.87(6)	11.28(3)
	84672	Eu4Mn8O20	17%			1.78	Pbam	7.37(8)	8.52(5)	5.67(7)
Gd	196276	P2-Na0.66Mn0.77Fe0.13M0.1O2	91%	0%		1.69	P63/mmc	2.86(9)	2.86(9)	11.20(1)
	150362	Gd4Fe4O12	9%			1.69	Pnma	5.53(3)	7.54(8)	5.318(8)

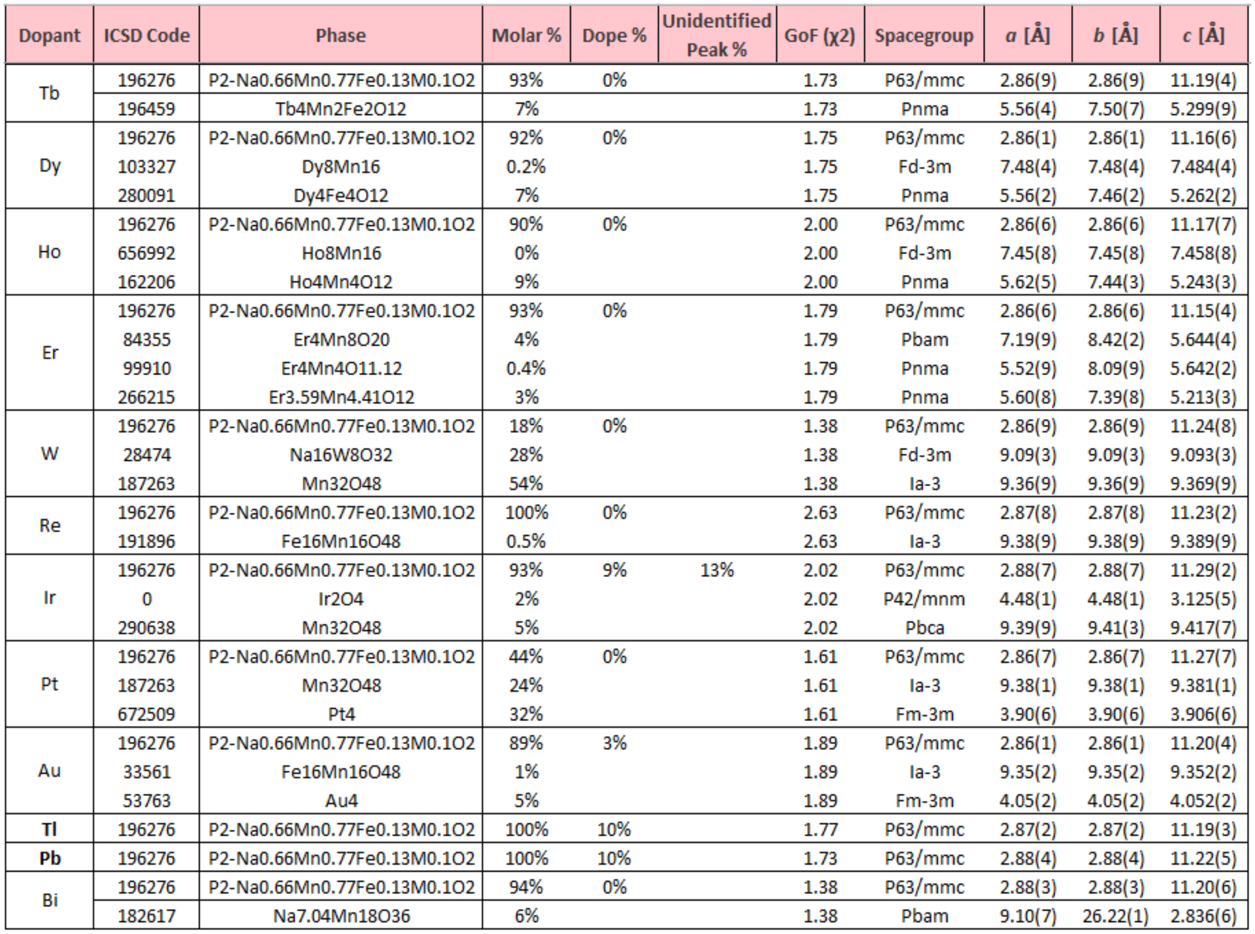

Dopant	ICSD Code	Phase	Molar %	Dope %	Unidentified Peak %	GoF (χ2)	Spacegroup	*a* [Å]	*b* [Å]	*c* [Å]
Tb	196276	P2-Na0.66Mn0.77Fe0.13M0.1O2	93%	0%		1.73	P63/mmc	2.86(9)	2.86(9)	11.19(4)
	196459	Tb4Mn2Fe2O12	7%			1.73	Pnma	5.56(4)	7.50(7)	5.299(9)
Dy	196276	P2-Na0.66Mn0.77Fe0.13M0.1O2	92%	0%		1.75	P63/mmc	2.86(1)	2.86(1)	11.16(6)
	103327	Dy8Mn16	0.2%			1.75	Fd-3m	7.48(4)	7.48(4)	7.484(4)
	280091	Dy4Fe4O12	7%			1.75	Pnma	5.56(2)	7.46(2)	5.262(2)
Ho	196276	P2-Na0.66Mn0.77Fe0.13M0.1O2	90%	0%		2.00	P63/mmc	2.86(6)	2.86(6)	11.17(7)
	656992	Ho8Mn16	0%			2.00	Fd-3m	7.45(8)	7.45(8)	7.458(8)
	162206	Ho4Mn4O12	9%			2.00	Pnma	5.62(5)	7.44(3)	5.243(3)
Er	196276	P2-Na0.66Mn0.77Fe0.13M0.1O2	93%	0%		1.79	P63/mmc	2.86(6)	2.86(6)	11.15(4)
	84355	Er4Mn8O20	4%			1.79	Pbam	7.19(9)	8.42(2)	5.644(4)
	99910	Er4Mn4O11.12	0.4%			1.79	Pnma	5.52(9)	8.09(9)	5.642(2)
	266215	Er3.59Mn4.41O12	3%			1.79	Pnma	5.60(8)	7.39(8)	5.213(3)
W	196276	P2-Na0.66Mn0.77Fe0.13M0.1O2	18%	0%		1.38	P63/mmc	2.86(9)	2.86(9)	11.24(8)
	28474	Na16W8O32	28%			1.38	Fd-3m	9.09(3)	9.09(3)	9.093(3)
	187263	Mn32O48	54%			1.38	Ia-3	9.36(9)	9.36(9)	9.369(9)
Re	196276	P2-Na0.66Mn0.77Fe0.13M0.1O2	100%	0%		2.63	P63/mmc	2.87(8)	2.87(8)	11.23(2)
	191896	Fe16Mn16O48	0.5%			2.63	Ia-3	9.38(9)	9.38(9)	9.389(9)
Ir	196276	P2-Na0.66Mn0.77Fe0.13M0.1O2	93%	9%	13%	2.02	P63/mmc	2.88(7)	2.88(7)	11.29(2)
	0	Ir2O4	2%			2.02	P42/mnm	4.48(1)	4.48(1)	3.125(5)
	290638	Mn32O48	5%			2.02	Pbca	9.39(9)	9.41(3)	9.417(7)
Pt	196276	P2-Na0.66Mn0.77Fe0.13M0.1O2	44%	0%		1.61	P63/mmc	2.86(7)	2.86(7)	11.27(7)
	187263	Mn32O48	24%			1.61	Ia-3	9.38(1)	9.38(1)	9.381(1)
	672509	Pt4	32%			1.61	Fm-3m	3.90(6)	3.90(6)	3.906(6)
Au	196276	P2-Na0.66Mn0.77Fe0.13M0.1O2	89%	3%		1.89	P63/mmc	2.86(1)	2.86(1)	11.20(4)
	33561	Fe16Mn16O48	1%			1.89	Ia-3	9.35(2)	9.35(2)	9.352(2)
	53763	Au4	5%			1.89	Fm-3m	4.05(2)	4.05(2)	4.052(2)
Tl	196276	P2-Na0.66Mn0.77Fe0.13M0.1O2	100%	10%		1.77	P63/mmc	2.87(2)	2.87(2)	11.19(3)
Pb	196276	P2-Na0.66Mn0.77Fe0.13M0.1O2	100%	10%		1.73	P63/mmc	2.88(4)	2.88(4)	11.22(5)
Bi	196276	P2-Na0.66Mn0.77Fe0.13M0.1O2	94%	0%		1.38	P63/mmc	2.88(3)	2.88(3)	11.20(6)
	182617	Na7.04Mn18O36	6%			1.38	Pbam	9.10(7)	26.22(1)	2.836(6)

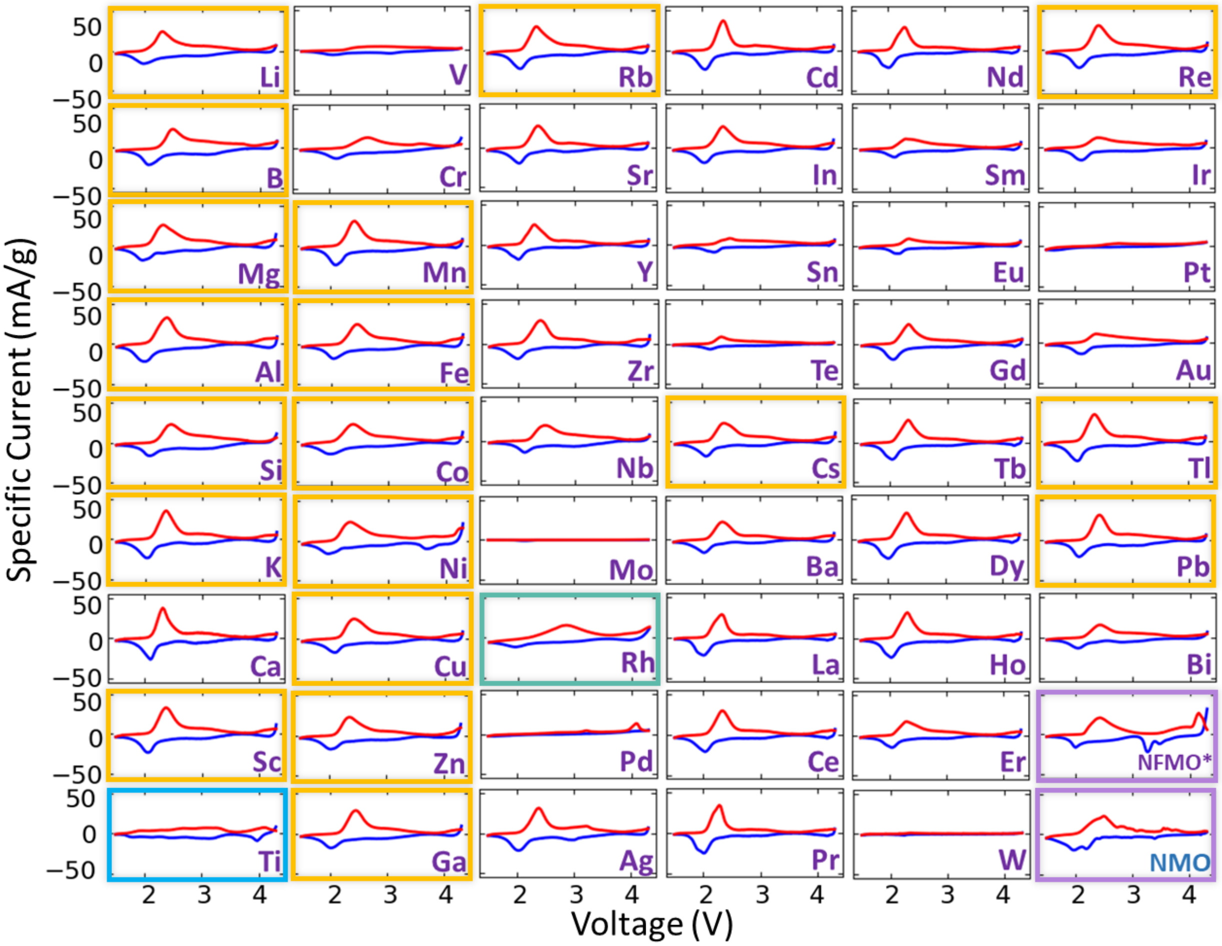

Figure S4.1 *Cyclic voltammetry plots of the HTP combinatorial cell during the first cycle of* ***set 1*** *samples, cycled within the voltage range of 1.5 V to 4.3 V vs Na/Na$^+$ at the scan rate of 0.1 V h^{-1}. The colored outlines indicate the distinct phases: pure P2 structure (yellow), P3 structure (green), tunnel structure (blue), and P2-$Na_{0.66}Fe_{0.5}Mn_{0.5}O_2$ (NFMO*) and P2/P'2-$Na_{0.66}MnO_2$ (NMO).*

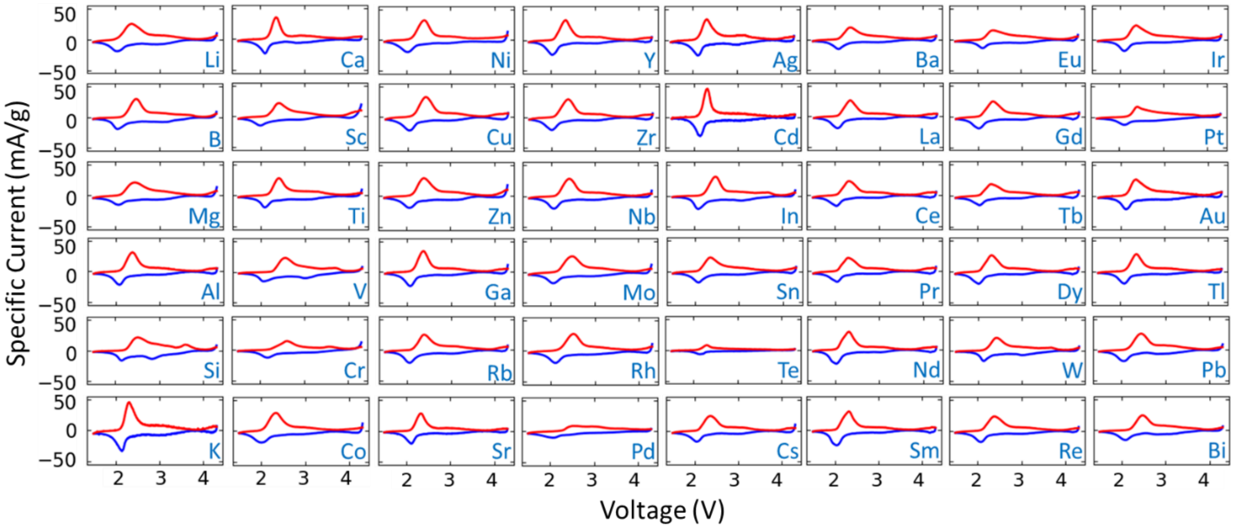

Figure S4.2 *Cyclic voltammetry plots of the HTP combinatorial cell during the first cycle of* ***set 2*** *samples, cycled within the voltage range of 1.5 V to 4.3 V vs Na/Na^{+} at the scan rate of 0.1 V h^{-1}.*

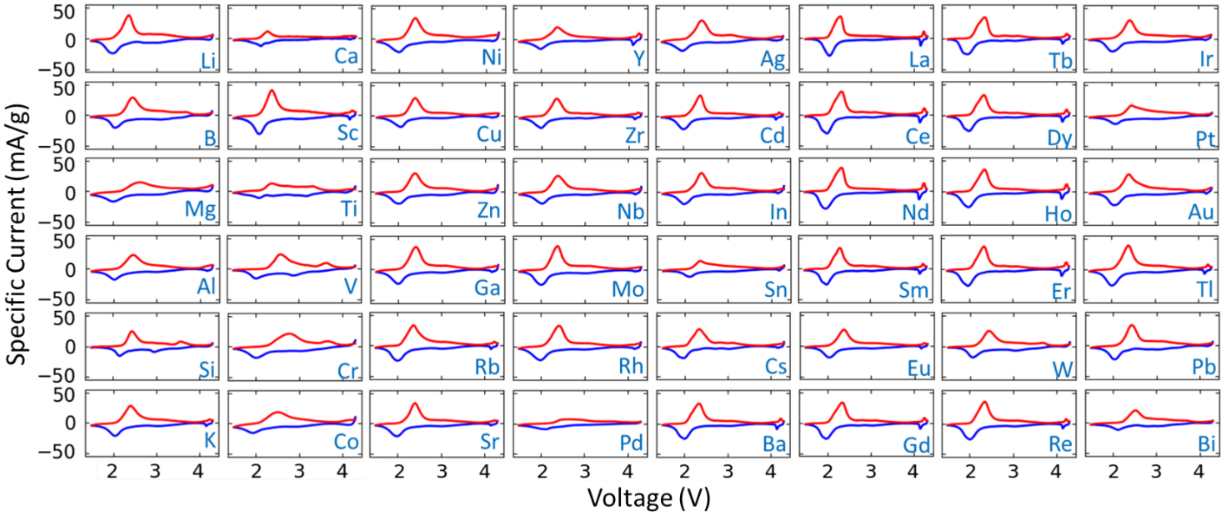

Figure S4.3 *Cyclic voltammetry plots of the HTP combinatorial cell during the first cycle of* ***set 3*** *samples, cycled within the voltage range of 1.5 V to 4.3 V vs Na/Na^{+} at the scan rate of 0.1 V h^{-1}.*

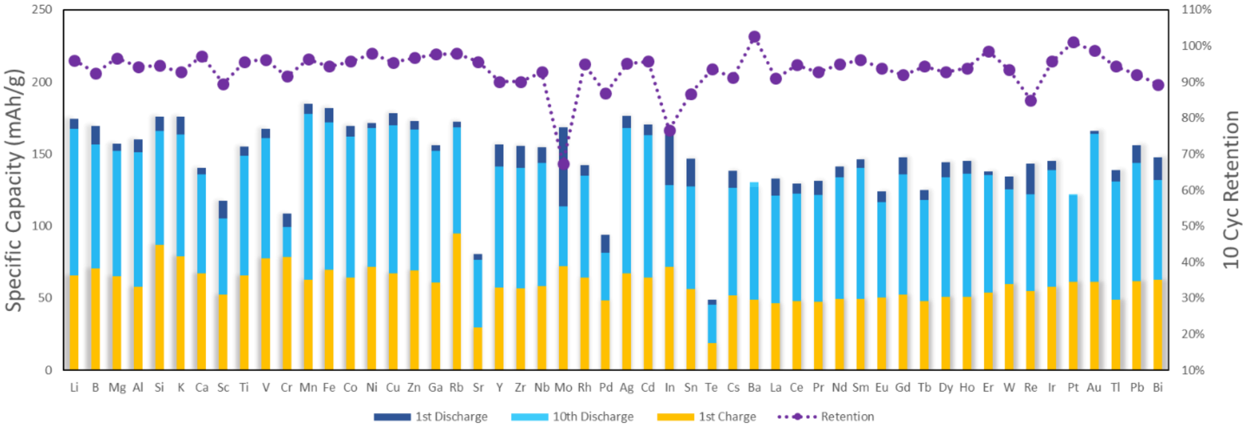

Figure S4.4 *Electrochemical properties extracted from the combinatorial cells for* ***set 2*** *samples. Specific capacities for 1*st *charge (yellow), 1*st *discharge (deep blue), and 10*th *cycle discharge (cyan) are plotted on the primary y-axis. The 10-cycle capacity retention is represented by the purple scatter plot and plotted on the secondary y-axis.*

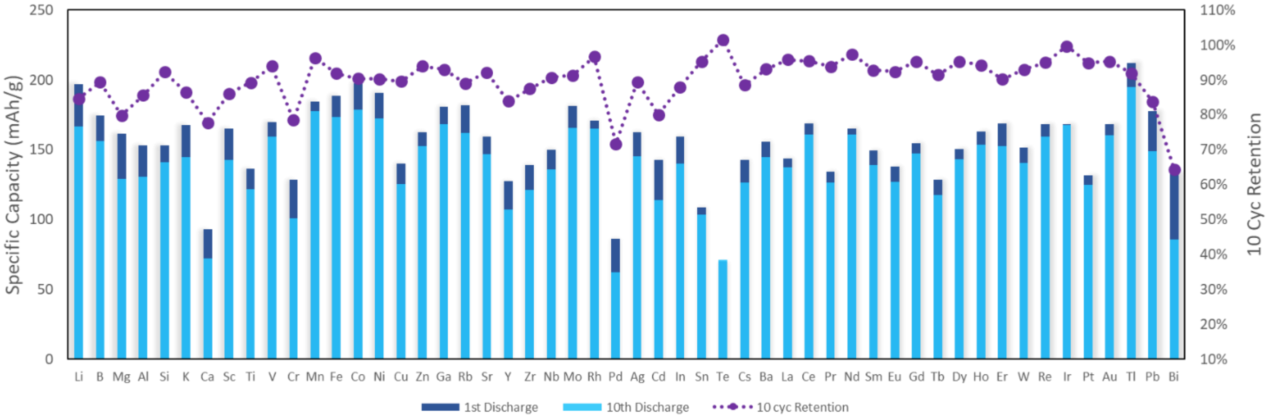

Figure S4.5 *Electrochemical properties extracted from the combinatorial cells for* ***set 3*** *samples. Specific capacities for 1*st *discharge (deep blue), and 10*th *cycle discharge (cyan) are plotted on the primary y-axis. The 10-cycle capacity retention is represented by the purple scatter plot and plotted on the secondary y-axis.*

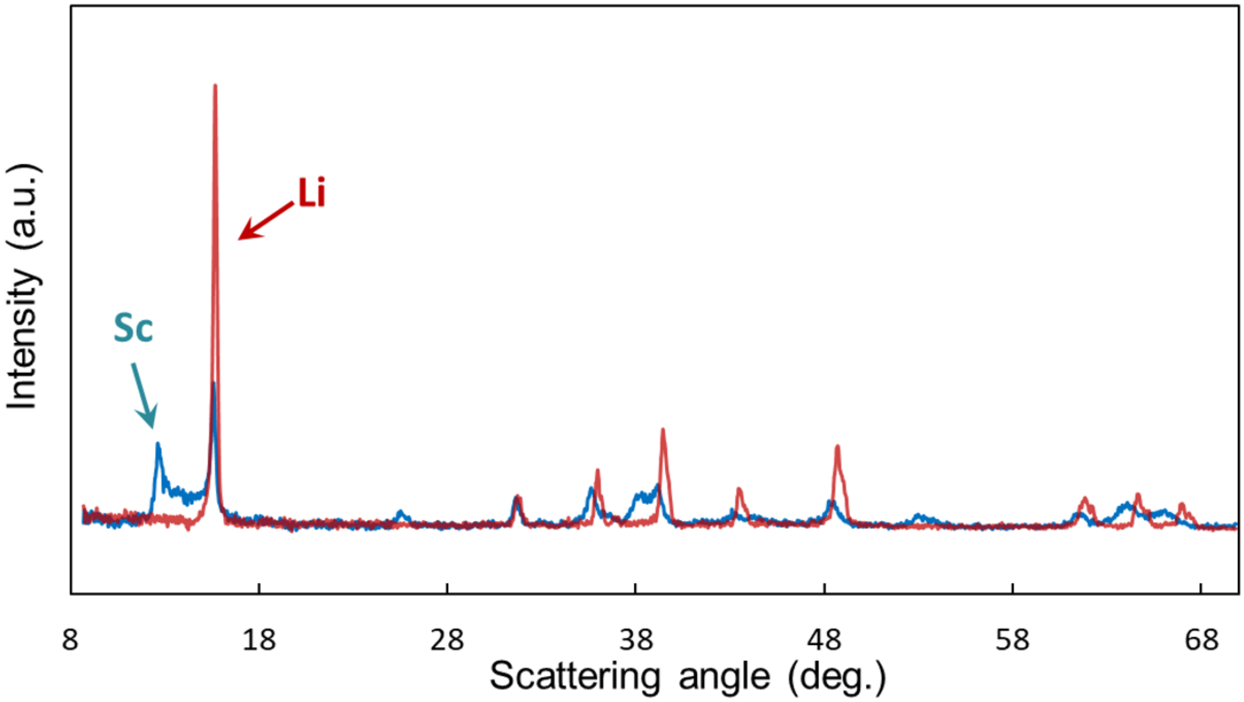

Figure S4.6 *XRD patterns of Li and Sc doped sample after TGA*

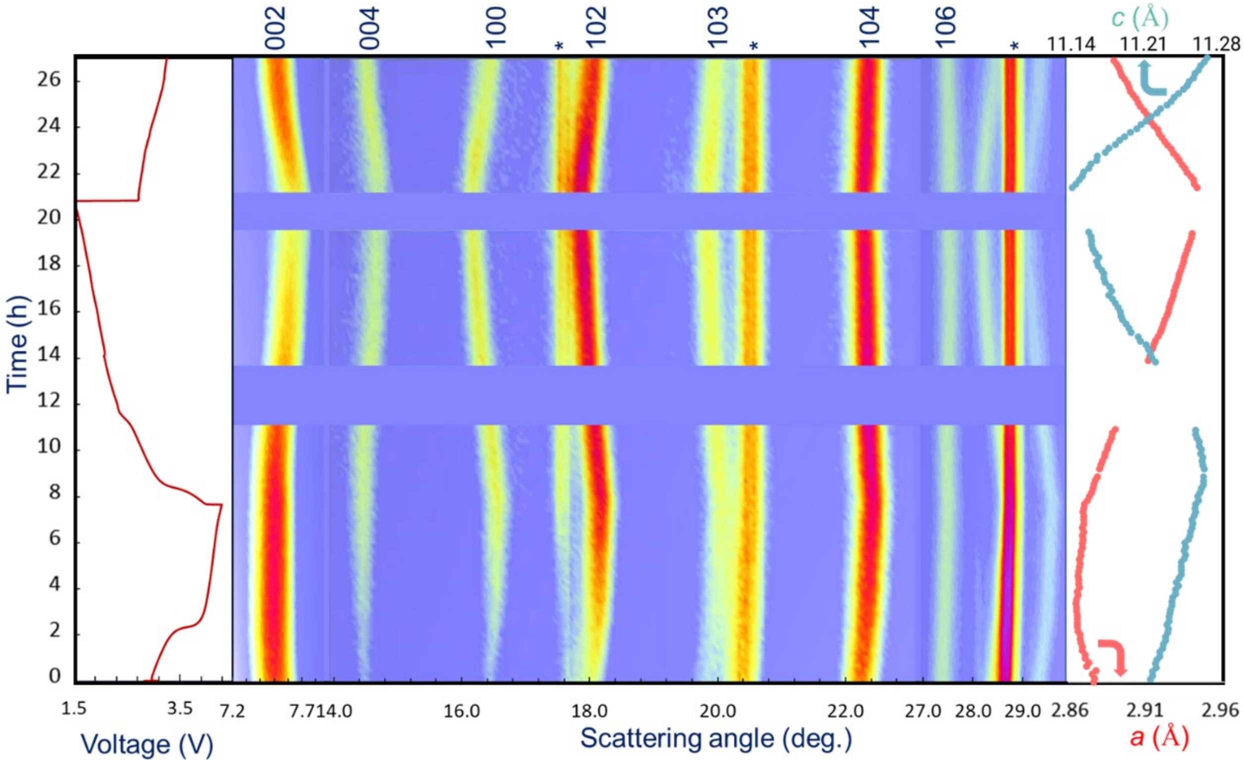

Figure S4.7 *In-situ XRD of Ga-doped* ***set 1****: $Na_{0.66}Fe_{0.13}Mn_{0.77}Ga_{0.1}O_2$*

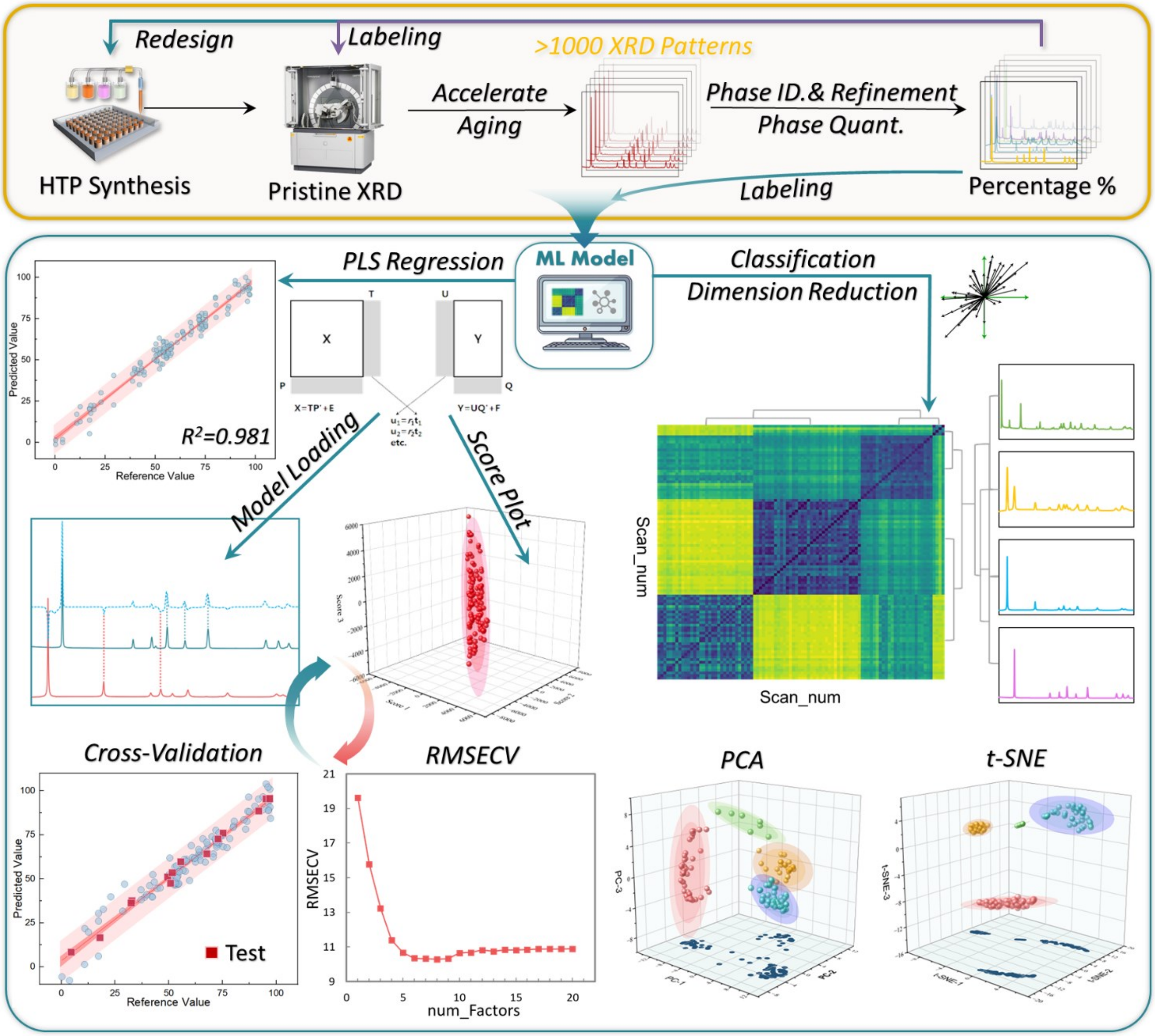

__Figure S4.8__ Workflow scheme of lab-based analysis and data-driven machine learning model.

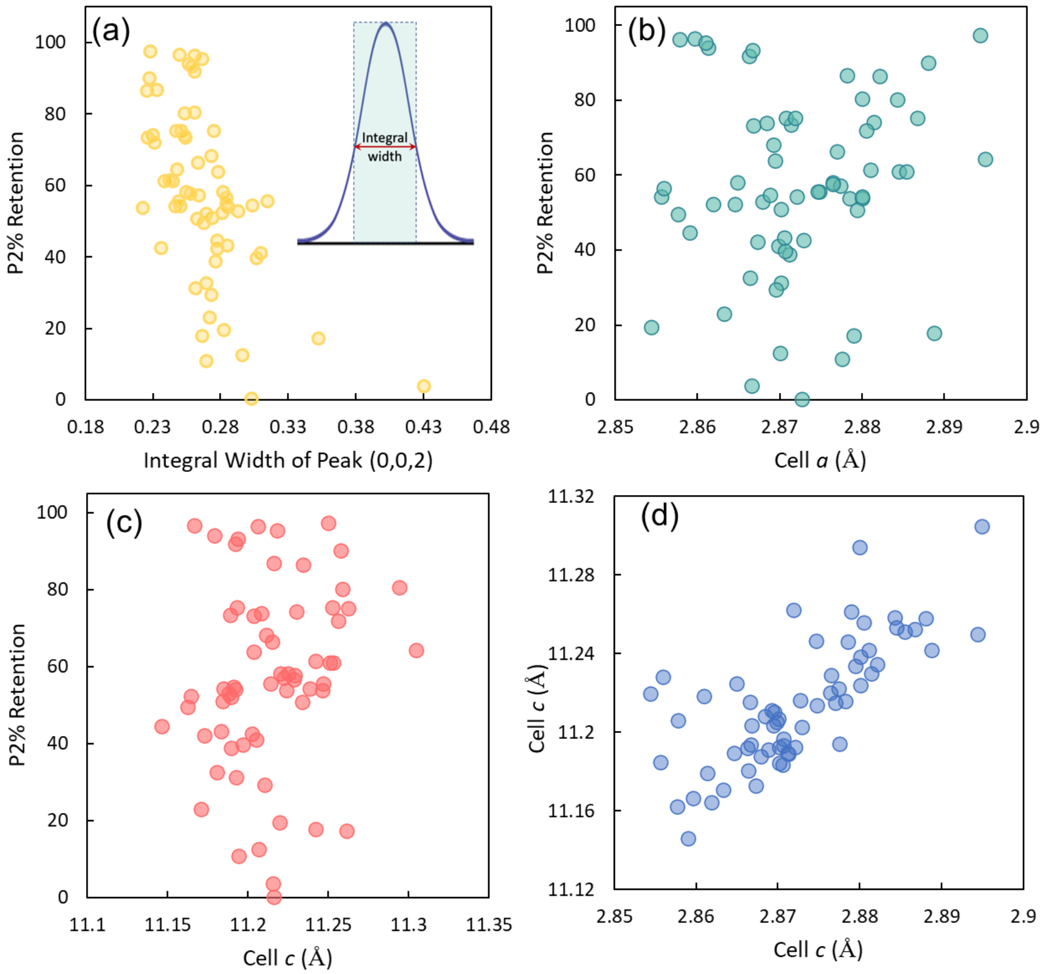

Figure S4.9 *Correlation plots of P2% retention with (a) integral width of peak (0,0,2), (b, c) lattice parameter a and c versus P2% Retention, (d) lattice parameter a and c*

Table S4.2 *Calculated XRD patterns with fine-tuned with different parameters*

Parameter	Value (Li-NFMO)	Value (Al-NFMO)
Experimental data	96.4%	56.6%
Calculated Profile	94.12%	64.30%
U (+100%)	89.71%	57.97%
V (+100%)	102.26%	88.71%
W (+100%)	94.10%	65.82%
a (+1%)	76.28%	52.44%
c (+0.2%)	106.01%	75.56%

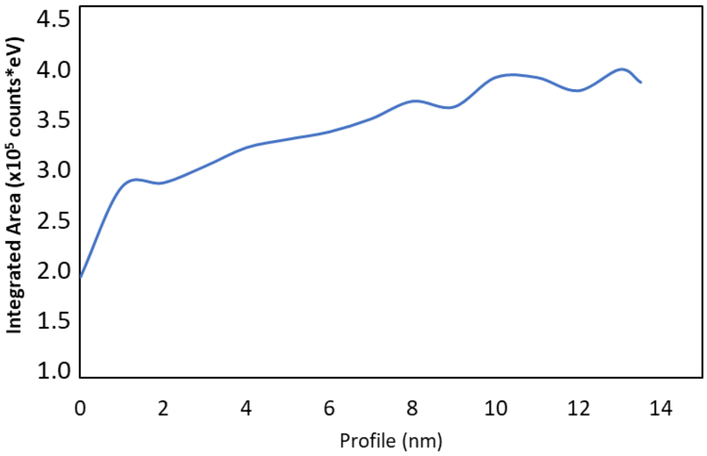

Figure S4.10 *XPS result of Fe integrated area from surface to bulk*

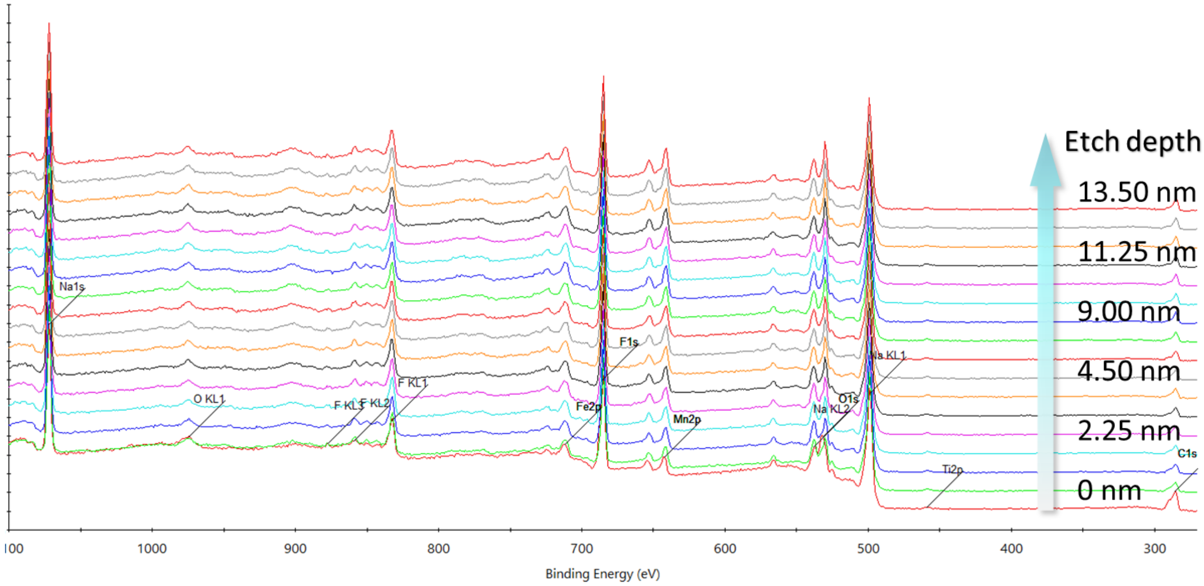

Figure S4.11 *Comprehensive XPS scan under different etching level.*

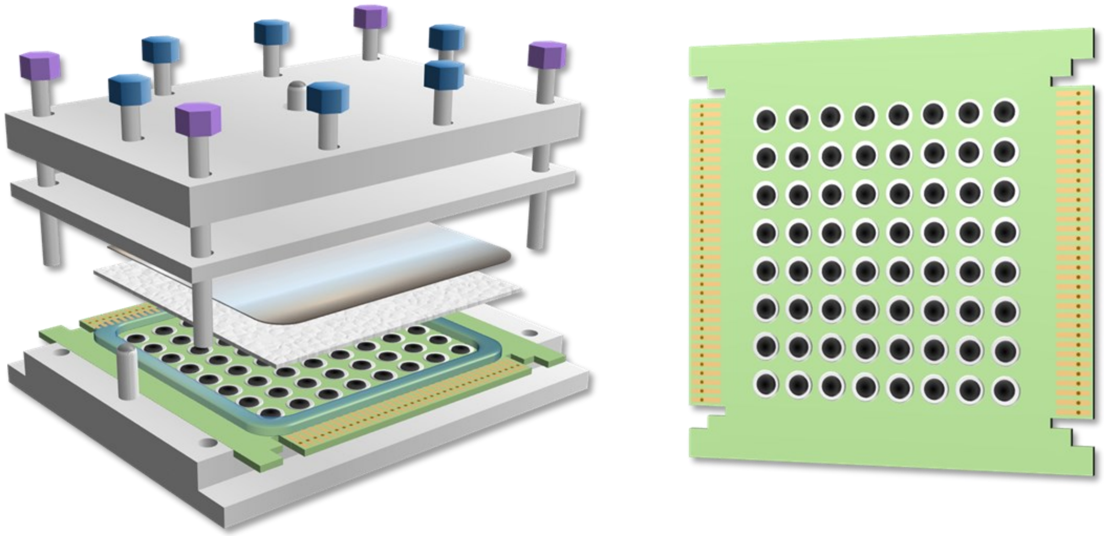

Figure S4.12 *Combinatorial cell for electrochemistry analysis and lab-built PCB for high throughput cathodes.*

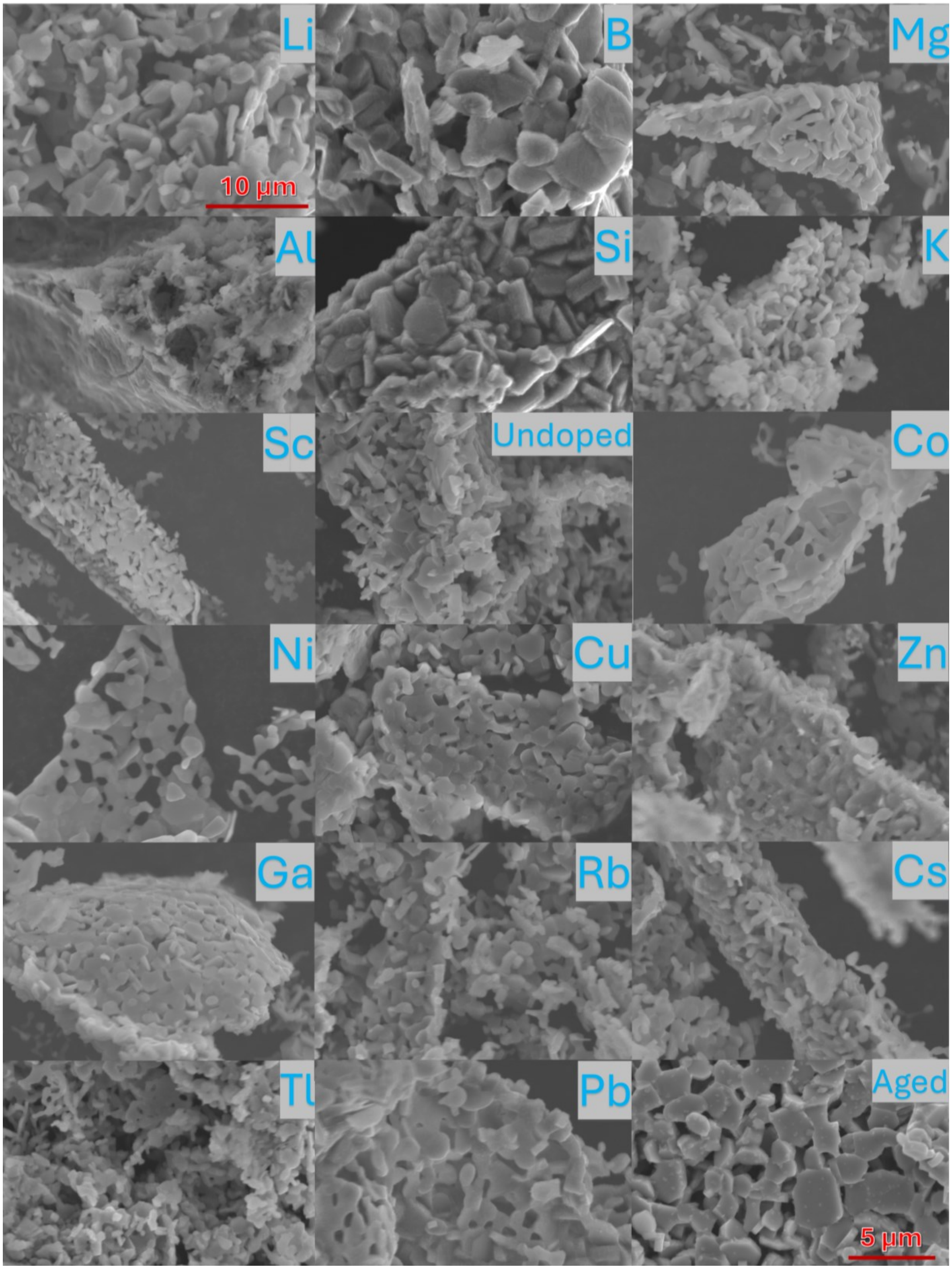

Figure S4.13 *SEM image of various doped* ***set 1*** *samples. All the images share the same scale shown for the Li-doped sample, except the undoped aged samples shown in the bottom right corner where a 5 µm bar is shown.*

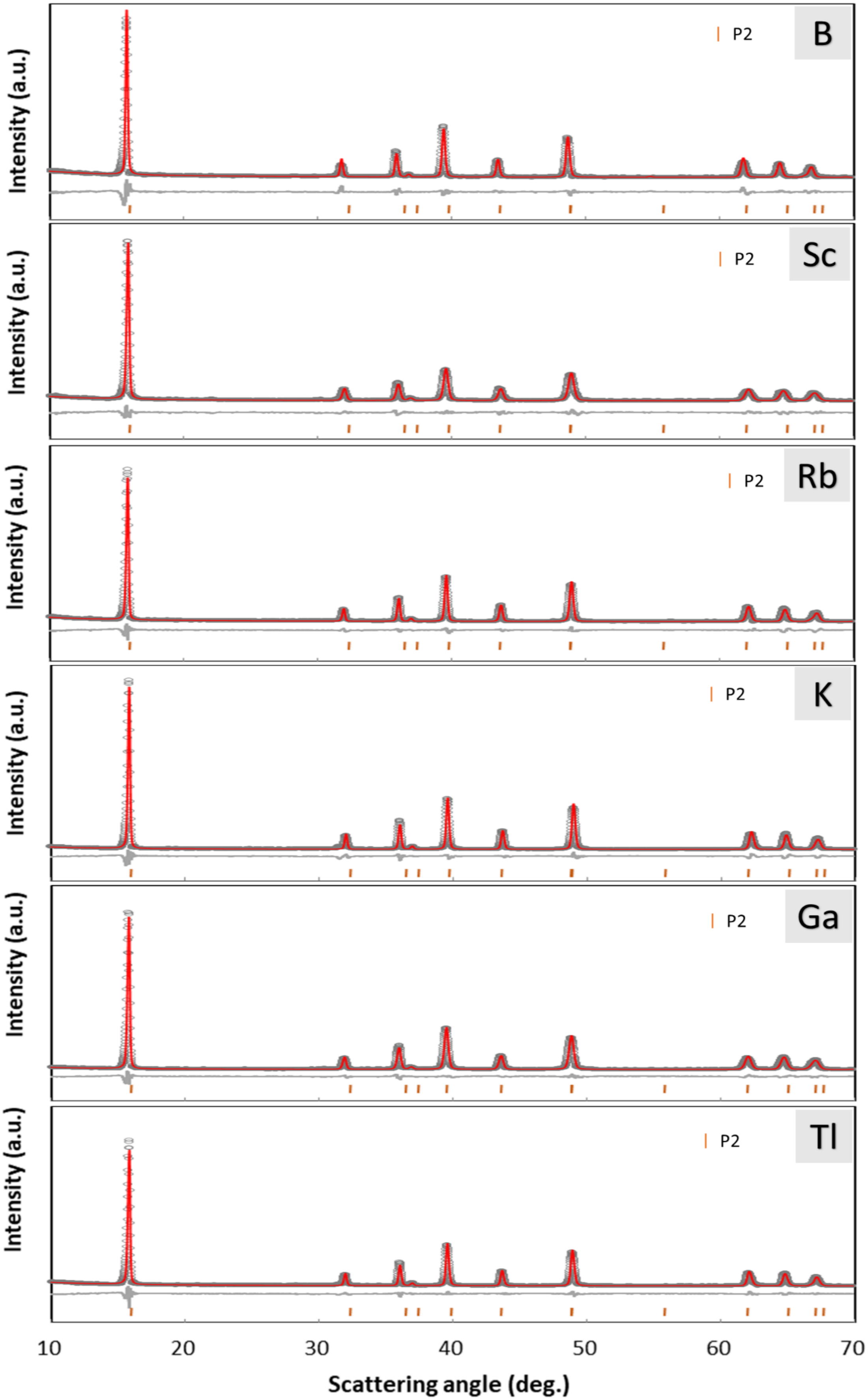

Figure S4.14 *XRD patterns and refinement of various doped* ***set 1*** *samples.*

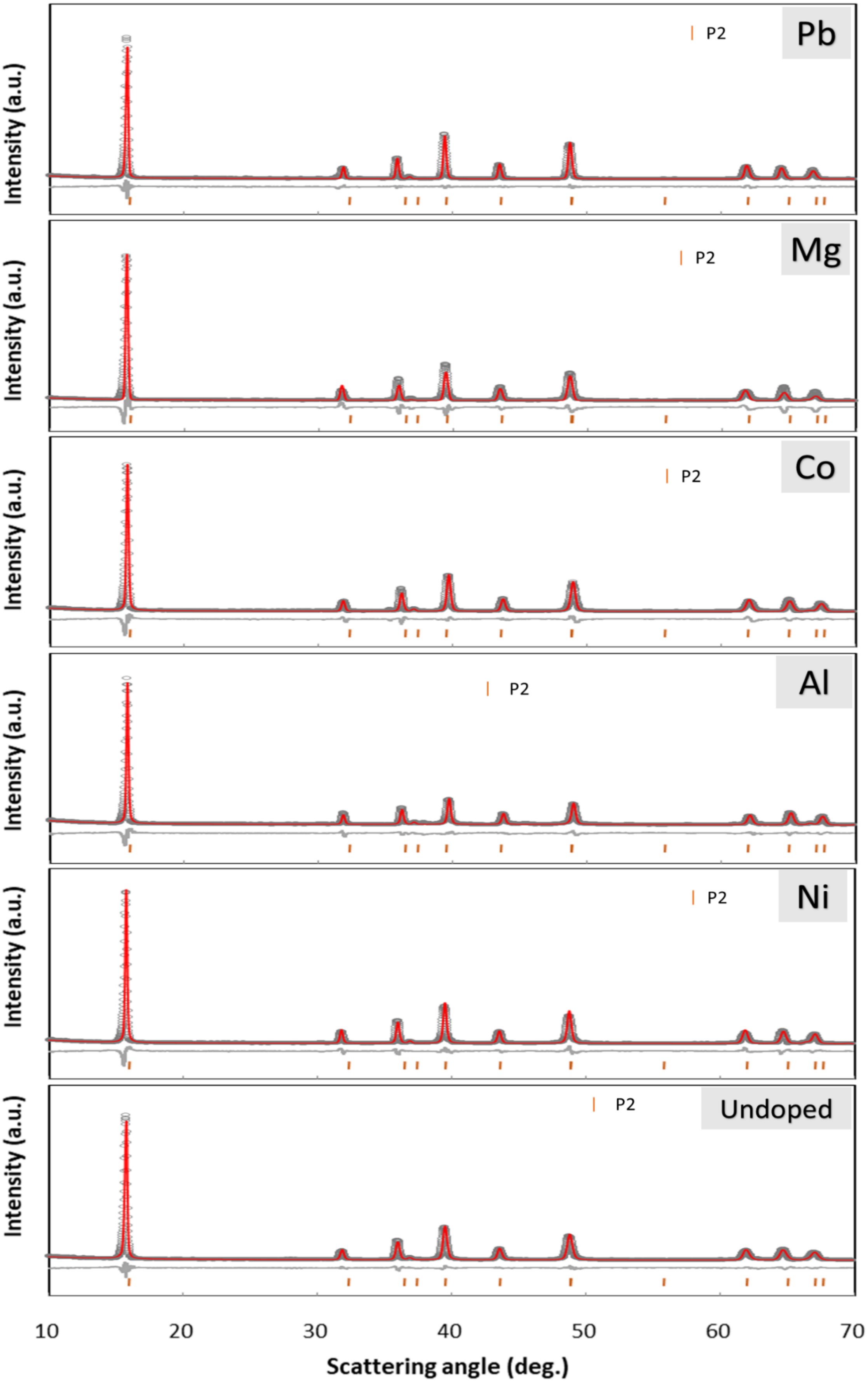

Figure S4.15 *XRD patterns and refinement of various doped **set 1** samples.*

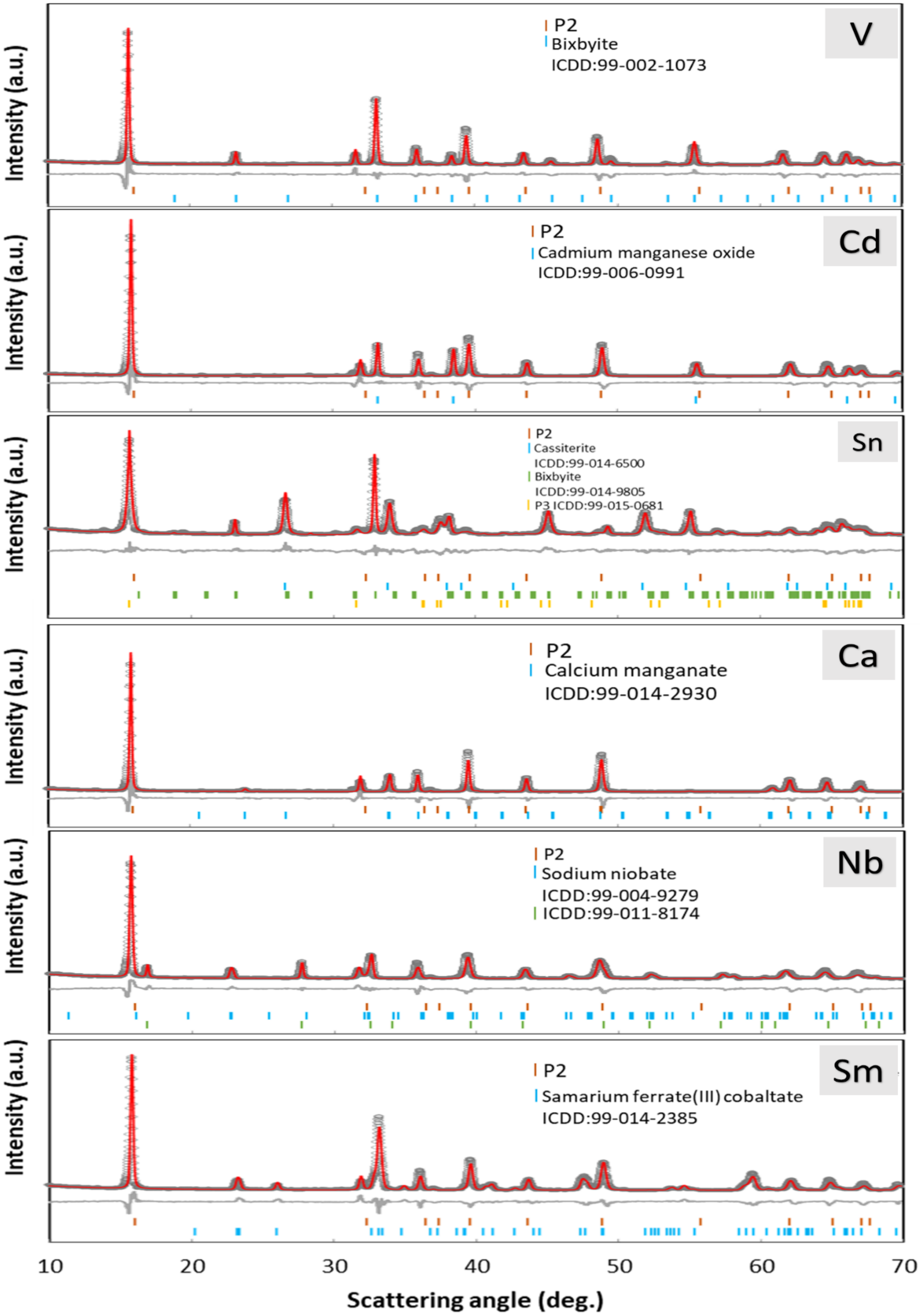

Figure S4.16 *XRD patterns and refinement of various doped* ***set 1*** *samples shown multiple phase fitting*

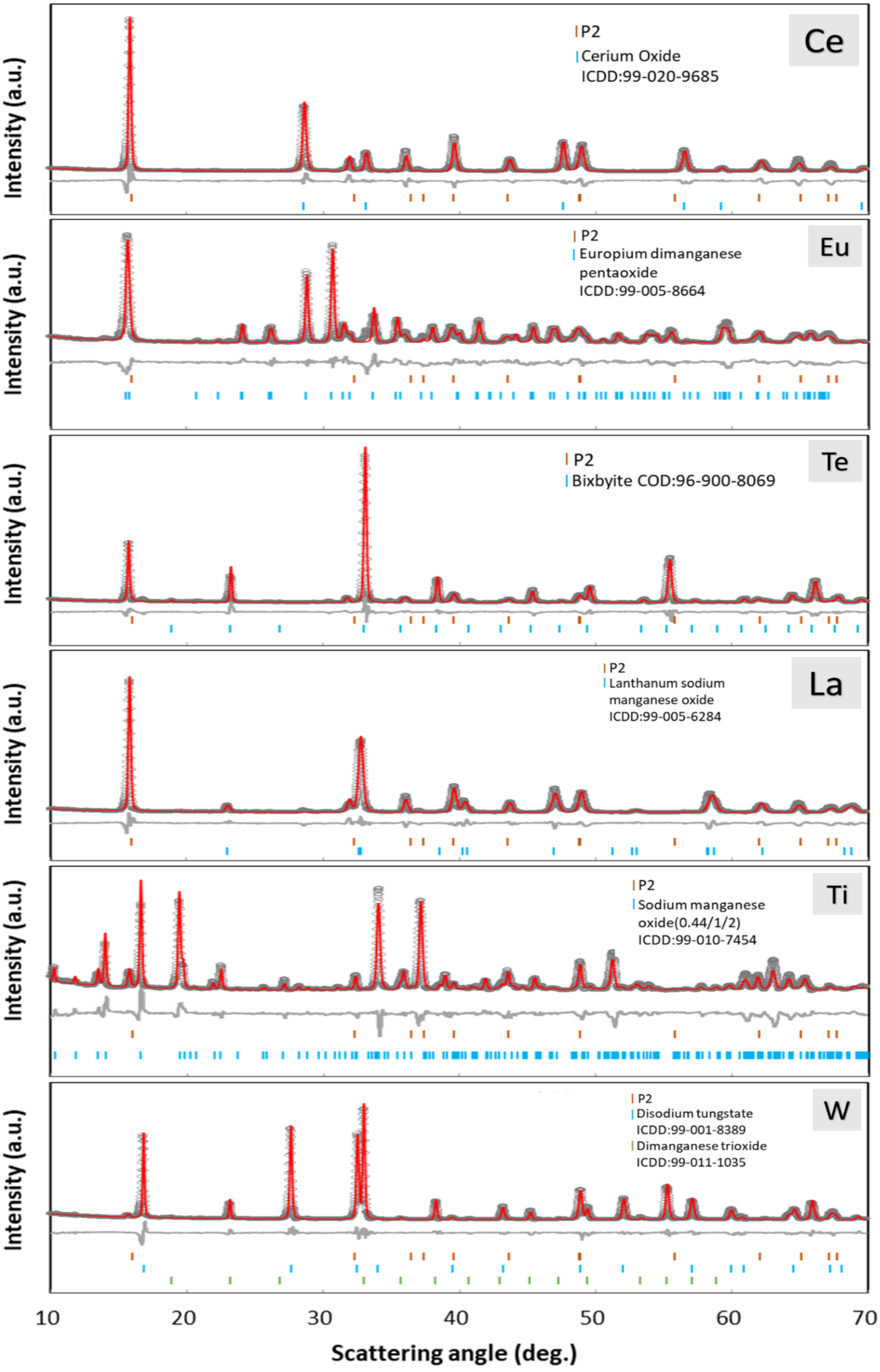

***Figure S4.17** XRD patterns and refinement of various doped **set 1** samples shown multiple phase fitting.*

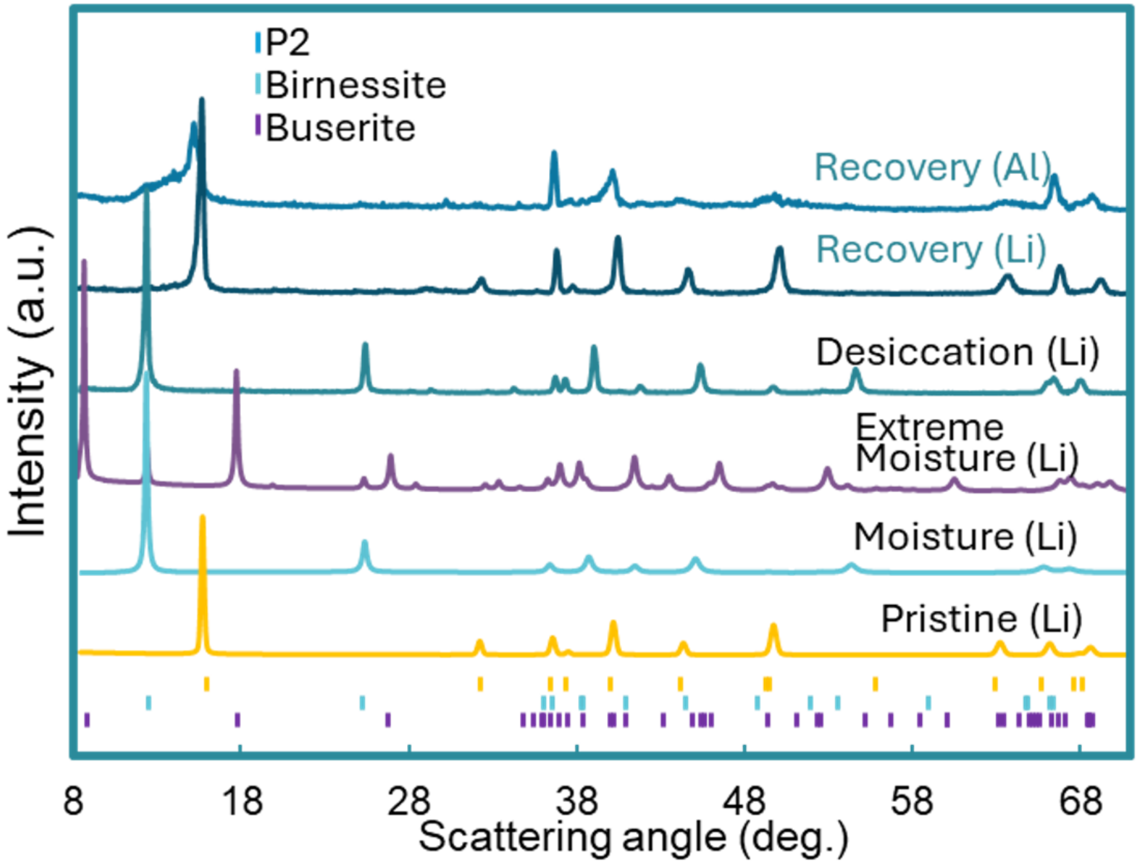

Figure S4.18 *Enlarged XRD patterns for Li and Al-doped samples, shown in* ***Figure 4.4****.*

Table S4.3 *Solution prepared for various dopant reagents*

Element	Dopant reagent	Solvent
Li	Lithium nitrate	H_2O
B	Boric acid	H_2O
Na	Sodium nitrate	H_2O
Mg	Magnesium nitrate hexahydrate	H_2O
Al	Aluminum nitrate monohydrate	H_2O
Si	Tetraethyl orthosilicate	EtOH
K	Potassium nitrate	H_2O
Ca	Calcium nitrate tetrahydrate	H_2O
Sc	Scandium (III) nitrate hydrate	H_2O
Ti	Titanium (IV) butoxide	EtOH
V	Ammonium metavanadate	HCl/H_2O
Cr	Chromium (III) nitrate monohydrate	H_2O
Mn	Manganese (II) nitrate	H_2O
Fe	Iron (III) nitrate monohydrate	H_2O
Co	Cobalt (II) nitrate	H_2O
Ni	Nickel (II) nitrate hexahydrate	H_2O
Cu	Copper (II) nitrate hemi(pentahydrate)	H_2O
Zn	Zinc nitrate hexahydrate	H_2O
Ga	Gallium (III) nitrate hydrate	H_2O
Rb	Rubidium nitrate	H_2O
Sr	Strontium nitrate	H_2O
Y	Yttrium (III) nitrate hexahydrate	H_2O
Zr	Zirconium dinitrate oxide hydrate	H_2O
Nb	Ammonium niobate(V) oxalate hydrate	H_2O
Mo	Ammonium molybdate (para)tetrahydrate	NH_4OH/H_2O
Rh	Rhodium (III) nitrate hydrate	H_2O

Element	Dopant reagent	Solvent
Rh	Rhodium (III) nitrate hydrate	H_2O
Pd	Palladium (II) nitrate hydrate	HCl
Ag	Silver nitrate	H_2O
Cd	Cadmium nitrate tetrahydrate	H_2O
In	Indium (III) nitrate hydrate	H_2O
Sn	Tin (II) chloride	H_2O
Cs	Cesium nitrate	H_2O
Ba	Barium nitrate	H_2O
La	Lanthanum (III) nitrate hexahydrate	H_2O
Pr	Praseodymium (III) nitrate hydrate	H_2O
Nd	Neodymium (III) nitrate hexahydrate	H_2O
Sm	Samarium (III) nitrate hexahydrate	H_2O
Eu	Europium nitrate pentahydrate	H_2O
Gd	Gadolinium nitrate hexahydrate	H_2O
Tb	Terbium nitrate hexahydrate	H_2O
Dy	Dysprosium nitrate pentahydrate	H_2O
Ho	Holmium nitrate pentahydrate	H_2O
Er	Erbium nitrate pentahydrate	H_2O
W	Tungsten (VI) oxide	NH_4OH/H_2O
Re	Ammonium perrhenate	H_2O
Ir	Iridium chloride hydrate	H_2O
Pt	Platinum (IV) chloride	H_2O
Au	Gold (III) chloride trihydrate	H_2O
Tl	Thallium nitrate pentahydrate	H_2O
Pb	Lead (II) nitrate	H_2O
Bi	Ammonium bismuth citrate	H_2O

4.8 References

(1) Yabuuchi, N.; Kubota, K.; Dahbi, M.; Komaba, S. Research Development on Sodium-Ion Batteries. *Chemical Reviews* **2014**, *114* (23), 11636–11682.

(2) Hwang, J.-Y.; Myung, S.-T.; Sun, Y.-K. Sodium-Ion Batteries: Present and Future. *Chemical Society Reviews* **2017**, *46* (12), 3529–3614.

(3) Chayambuka, K.; Mulder, G.; Danilov, D. L.; Notten, P. H. L. Sodium-Ion Battery Materials and Electrochemical Properties Reviewed. *Advanced Energy Materials* **2018**, *8* (16), 1800079.

(4) Feng, J.; Luo, S.; Cai, K.; Yan, S.; Wang, Q.; Zhang, Y.; Liu, X. Research Progress of Tunnel-Type Sodium Manganese Oxide Cathodes for SIBs. *Chinese Chemical Letters* **2022**, *33* (5), 2316–2326.

(5) Delmas, C.; Fouassier, C.; Hagenmuller, P. Structural Classification and Properties of the Layered Oxides. *Physica B+C* **1980**, *99* (1), 81–85.

(6) Liu, H.; Deng, W.; Gao, X.; Chen, J.; Yin, S.; Yang, L.; Zou, G.; Hou, H.; Ji, X. Manganese-Based Layered Oxide Cathodes for Sodium Ion Batteries. *Nano Select.* **2020**, *1* (2), 200–225.

(7) Han, M. H.; Gonzalo, E.; Singh, G.; Rojo, T. A Comprehensive Review of Sodium Layered Oxides: Powerful Cathodes for Na-Ion Batteries. *Energy & Environmental Science* **2014**, *8* (1), 81–102.

(8) Zhao, C.; Wang, Q.; Yao, Z.; Wang, J.; Sánchez-Lengeling, B.; Ding, F.; Qi, X.; Lu, Y.; Bai, X.; Li, B.; Li, H.; Aspuru-Guzik, A.; Huang, X.; Delmas, C.; Wagemaker, M.; Chen, L.; Hu, Y.-S. Rational Design of Layered Oxide Materials for Sodium-Ion Batteries. *Science* **2020**, *370* (6517), 708–711.

(9) Yabuuchi, N.; Kajiyama, M.; Iwatate, J.; Nishikawa, H.; Hitomi, S.; Okuyama, R.; Usui, R.; Yamada, Y.; Komaba, S. P2-Type Nax[Fe1/2Mn1/2]O2 Made from Earth-Abundant Elements for Rechargeable Na Batteries. *Nature Materials* **2012**, *11* (6), 512–517.

(10) Mortemard de Boisse, B.; Carlier, D.; Guignard, M.; Bourgeois, L.; Delmas, C. P2-NaxMn1/2Fe1/2O2 Phase Used as Positive Electrode in Na Batteries: Structural Changes Induced by the Electrochemical (De)Intercalation Process. *Inorganic Chemistry* **2014**, *53* (20), 11197–11205.

(11) Pang, W. K.; Kalluri, S.; Peterson, V. K.; Sharma, N.; Kimpton, J.; Johannessen, B.; Liu, H. K.; Dou, S. X.; Guo, Z. Interplay between Electrochemistry and Phase Evolution of the P2-Type Nax(Fe1/2Mn1/2)O2 Cathode for Use in Sodium-Ion Batteries. *Chemistry of Materials* **2015**, *27* (8), 3150–3158.

(12) McCalla, E.; Jia, S. Topology to Improve Battery Technology. *Nature Sustainability* **2022**, *5* (3), 181–182.

(13) Duffort, V.; Talaie, E.; Black, R.; Nazar, L. F. Uptake of CO2 in Layered P2-Na0.67Mn0.5Fe0.5O2: Insertion of Carbonate Anions. *Chemistry of Materials* **2015**, *27* (7), 2515–2524.

(14) Talaie, E.; Duffort, V.; Smith, H. L.; Fultz, B.; Nazar, L. F. Structure of the High Voltage Phase of Layered P2-Na2/3−z[Mn1/2Fe1/2]O2 and the Positive Effect of Ni Substitution on Its Stability. *Energy & Environmental Science* **2015**, *8* (8), 2512–2523.

(15) Jia, S.; Counsell, J.; Adamič, M.; Jonderian, A.; McCalla, E. High-Throughput Design of Na–Fe–Mn–O Cathodes for Na-Ion Batteries. *Journal of Materials Chemistry* **2022**, *10* (1), 251–265.

(16) Jia, S.; Yao, E.; Peng, R.; Jonderian, A.; Abdolhosseini, M.; McCalla, E. Chemical Speed Dating: The Impact of 52 Dopants in Na–Mn–O Cathodes. *Chemistry of Materials* **2022**, *34* (24), 11047–11061.

(17) Zhao, C.; Ding, F.; Lu, Y.; Chen, L.; Hu, Y.-S. High-Entropy Layered Oxide Cathodes for Sodium-Ion Batteries. *Angewandte Chemie International Edition* **2020**, *59* (1), 264–269.

(18) Chen, T.; Ouyang, B.; Fan, X.; Zhou, W.; Liu, W.; Liu, K. Oxide Cathodes for Sodium-Ion Batteries: Designs, Challenges, and Perspectives. *Carbon Energy* **2022**, *4* (2), 170–199.

(19) Xu, H.; Yan, Q.; Yao, W.; Lee, C.-S.; Tang, Y. Mainstream Optimization Strategies for Cathode Materials of Sodium-Ion Batteries. *Small Structures* **2022**, *3* (4), 2100217.

(20) Shi, C.; Wang, L.; Chen, X.; Li, J.; Wang, S.; Wang, J.; Jin, H. Challenges of Layer-Structured Cathodes for Sodium-Ion Batteries. *Nanoscale Horizons.* **2022**, *7* (4), 338–351.

(21) Potts, K. P.; Grignon, E.; McCalla, E. Accelerated Screening of High-Energy Lithium-Ion Battery Cathodes. *ACS Applied Energy Materials* **2019**, *2* (12), 8388–8393.

(22) McCalla, E.; Parmaklis, M.; Rehman, S.; Anderson, E.; Jia, S.; Hebert, A.; Potts, K.; Jonderian, A.; Adhikari, T.; Adamič, M. Combinatorial Methods in Advanced Battery Materials Design. *ACS Applied Energy Materials* **2021**, 1–12.

(23) Adhikari, T.; Hebert, A.; Adamič, M.; Yao, J.; Potts, K.; McCalla, E. Development of High-Throughput Methods for Sodium-Ion Battery Cathodes. *ACS Combinatorial Science* **2020**, *22* (6), 311–318.

(24) Jonderian, A.; Jia, S.; Yoon, G.; Cozea, V. T.; Galabi, N. Z.; Ma, S. B.; McCalla, E. Accelerated Development of High Voltage Li-Ion Cathodes. *Advanced Energy Materials* **2022**, *12* (40), 2201704.

(25) Viswanatha, R.; Kishore, B.; Bharath, U.; Munichandraiah, N. Communication—Electrochemical Investigation of Plate-Like Na2/3Fe1/2Mn1/2O2 for Sodium Ion Cathode. *Journal of the Electrochemical Society* **2018**, *165* (2), A263.

(26) Kumakura, S.; Tahara, Y.; Kubota, K.; Chihara, K.; Komaba, S. Sodium and Manganese Stoichiometry of P2-Type Na2/3MnO2. *Angewandte Chemie International Edition* **2016**, *55* (41), 12760–12763.

(27) Jia, S.; Kumakura, S.; McCalla, E. Unravelling Air/Moisture Stability of Cathode Materials in Sodium Ion Batteries: Characterization, Rational Design, and Perspectives. *Energy & Environmental Science* **2024**.

(28) Zuo, W.; Qiu, J.; Liu, X.; Ren, F.; Liu, H.; He, H.; Luo, C.; Li, J.; Ortiz, G. F.; Duan, H.; Liu, J.; Wang, M.-S.; Li, Y.; Fu, R.; Yang, Y. The Stability of P2-Layered Sodium Transition Metal Oxides in Ambient Atmospheres. *Nature Communications* **2020**, *11* (1), 3544.

(29) Boyd, S.; Dhall, R.; M. LeBeau, J.; Augustyn, V. Charge Storage Mechanism and Degradation of P2-Type Sodium Transition Metal Oxides in Aqueous Electrolytes. *Journal of Materials Chemistry A* **2018**, *6* (44), 22266–22276.

(30) Li, X.; Shen, X.; Zhao, J.; Yang, Y.; Zhang, Q.; Ding, F.; Han, M.; Xu, C.; Yang, C.; Liu, H.; Hu, Y.-S. O3-NaFe(1/3–x)Ni1/3Mn1/3AlxO2 Cathodes with Improved Air Stability for Na-Ion Batteries. *ACS Applied Materials & Interfaces* **2021**, *13* (28), 33015–33023.

(31) Steiner, T. The Hydrogen Bond in the Solid State. *Angewandte Chemie International Edition* **2002**, *41* (1), 48–76.

(32) Jiang, J.; He, H.-C.; Cheng, C.; Yan, T.; Xia, X.; Ding, M.; He, L.; Chan, T.-S.; Zhang, L. Improving Structural and Moisture Stability of P2-Layered Cathode Materials for Sodium-Ion Batteries. *ACS Applied Energy Materials* **2022**, *5* (1), 1252–1261.

(33) Chen, X.; Li, N.; Kedzie, E.; McCloskey, B. D.; Tang, H.; Tong, W. High-Capacity P2-Type NaxLi0.25Mn0.75O2 Cathode Enabled by Anionic Oxygen Redox. *Journal of the Electrochemical Society* **2019**, *166* (16), A4136.

(34) Lee, J.-W.; Park, W. B.; Lee, J. H.; Singh, S. P.; Sohn, K.-S. A Deep-Learning Technique for Phase Identification in Multiphase Inorganic Compounds Using Synthetic XRD Powder Patterns. *Nature Communications* **2020**, *11* (1), 86.

(35) Lombardo, T.; Duquesnoy, M.; El-Bouysidy, H.; Årén, F.; Gallo-Bueno, A.; Jørgensen, P. B.; Bhowmik, A.; Demortière, A.; Ayerbe, E.; Alcaide, F.; Reynaud, M.; Carrasco, J.; Grimaud, A.; Zhang, C.; Vegge, T.; Johansson, P.; Franco, A. A. Artificial Intelligence Applied to Battery Research: Hype or Reality? *Chemical Reviews* **2022**, *122* (12), 10899–10969.

(36) Suzuki, Y. Automated Data Analysis for Powder X-Ray Diffraction Using Machine Learning. *Synchrotron Radiation News* **2022**, *35* (4), 9–15.

(37) Suzuki, Y.; Hino, H.; Hawai, T.; Saito, K.; Kotsugi, M.; Ono, K. Symmetry Prediction and Knowledge Discovery from X-Ray Diffraction Patterns Using an Interpretable Machine Learning Approach. *Scientific Reports* **2020**, *10* (1), 21790.

(38) Dong, R.; Zhao, Y.; Song, Y.; Fu, N.; Omee, S. S.; Dey, S.; Li, Q.; Wei, L.; Hu, J. DeepXRD, a Deep Learning Model for Predicting XRD Spectrum from Material Composition. *ACS Applied Materials & Interfaces* **2022**, *14* (35), 40102–40115.

(39) Wold, S.; Sjöström, M.; Eriksson, L. PLS-Regression: A Basic Tool of Chemometrics. *Chemometrics and Intelligent Laboratory Systems* **2001**, *58* (2), 109–130.

(40) Abdi, H. Partial Least Squares Regression and Projection on Latent Structure Regression (PLS Regression). *WIREs Computational Statistics* **2010**, *2* (1), 97–106.

(41) Hewat, A.; David, W. I. F.; Eijck, L. van. Hugo Rietveld (1932–2016). *Journal of Applied Crystallography* **2016**, *49* (4), 1394–1395.

(42) Song, J.; Xiao, B.; Lin, Y.; Xu, K.; Li, X. Interphases in Sodium-Ion Batteries. *Advanced Energy Materials* **2018**, *8* (17), 1703082.

(43) Xu, J.; Han, Z.; Jiang, K.; Bai, P.; Liang, Y.; Zhang, X.; Wang, P.; Guo, S.; Zhou, H. Suppressing Cation Migration and Reducing Particle Cracks in a Layered Fe-Based Cathode for Advanced Sodium-Ion Batteries. *Small* **2020**, *16* (3), 1904388.

(44) Wang, K.; Yan, P.; Sui, M. Phase Transition Induced Cracking Plaguing Layered Cathode for Sodium-Ion Battery. *Nano Energy* **2018**, *54*, 148–155.

(45) Guo, S.; Li, Q.; Liu, P.; Chen, M.; Zhou, H. Environmentally Stable Interface of Layered Oxide Cathodes for Sodium-Ion Batteries. *Nature Communications* **2017**, *8* (1), 135.

(46) Li, X.; Xu, J.; Li, H.; Zhu, H.; Guo, S.; Zhou, H. Synergetic Anion–Cation Redox Ensures a Highly Stable Layered Cathode for Sodium-Ion Batteries. *Advanced Science* **2022**, *9* (16), 2105280.

(47) Yu, L.; Chang, Y.-X.; Liu, M.; Feng, Y.-H.; Si, D.; Zhu, X.; Wang, X.-Z.; Wang, P.-F.; Xu, S. O3-Type Na0.95Ni0.40Fe0.15Mn0.3Ti0.15O2 Cathode Materials with Enhanced Storage Stability for High-Energy Na-Ion Batteries. *ACS Applied Materials & Interfaces* **2023**, *15* (19), 23236–23245.

(48) Mu, L.; Hou, Q.; Yang, Z.; Zhang, Y.; Rahman, M. M.; Kautz, D. J.; Sun, E.; Du, X.-W.; Du, Y.; Nordlund, D.; Lin, F. Water-Processable P2-Na0.67Ni0.22Cu0.11Mn0.56Ti0.11O2 Cathode Material for Sodium Ion Batteries. *Journal of the Electrochemical Society* **2019**, *166* (2), A251.

(49) Tang, K.; Huang, Y.; Xie, X.; Cao, S.; Liu, L.; Liu, H.; Luo, Z.; Wang, Y.; Chang, B.; Shu, H.; Wang, X. Electrochemical Performance and Structural Stability of Air-Stable Na0.67Ni0.33Mn0.67-xTixO2 Cathode Materials for High-Performance Sodium-Ion Batteries. *Chemical Engineering Journal* **2020**, *399*, 125725.

(50) Yoda, Y.; Kubota, K.; Kuroki, K.; Suzuki, S.; Yamanaka, K.; Yaji, T.; Amagasa, S.; Yamada, Y.; Ohta, T.; Komaba, S. Elucidating Influence of Mg- and Cu-Doping on Electrochemical Properties of O3-Nax[Fe,Mn]O2 for Na-Ion Batteries. *Small* **2020**, *16* (50), 2006483.

(51) Boivin, E.; House, R. A.; Marie, J.-J.; Bruce, P. G. Controlling Iron Versus Oxygen Redox in the Layered Cathode Na0.67Fe0.5Mn0.5O2: Mitigating Voltage and Capacity Fade by Mg Substitution. *Advanced Energy Materials* **2022**, *12* (30), 2200702.

(52) Zhou, Y.-N.; Wang, P.-F.; Zhang, X.-D.; Huang, L.-B.; Wang, W.-P.; Yin, Y.-X.; Xu, S.; Guo, Y.-G. Air-Stable and High-Voltage Layered P3-Type Cathode for Sodium-Ion Full Battery. *ACS Applied Materials & Interfaces* **2019**, *11* (27), 24184–24191.

(53) Yuan, S.; Yu, L.; Qian, G.; Xie, Y.; Guo, P.; Cui, G.; Ma, J.; Ren, X.; Xu, Z.; Lee, S.-J.; Lee, J.-S.; Liu, Y.; Ren, Y.; Li, L.; Tan, G.; Liao, X. P2-Type Moisture-Stable and High-Voltage-Tolerable Cathodes for High-Energy and Long-Life Sodium-Ion Batteries. *Nano Letters* **2023**, *23* (5), 1743–1751.

(54) Yabuuchi, N.; Hara, R.; Kubota, K.; Paulsen, J.; Kumakura, S.; Komaba, S. A New Electrode Material for Rechargeable Sodium Batteries: P2-Type Na2/3[Mg0.28Mn0.72]O2 with Anomalously High Reversible Capacity. *Journal of Materials Chemistry A* **2014**, *2* (40), 16851–16855.

(55) Li, X.-L.; Wang, T.; Yuan, Y.; Yue, X.-Y.; Wang, Q.-C.; Wang, J.-Y.; Zhong, J.; Lin, R.-Q.; Yao, Y.; Wu, X.-J.; Yu, X.-Q.; Fu, Z.-W.; Xia, Y.-Y.; Yang, X.-Q.; Liu, T.; Amine, K.; Shadike, Z.; Zhou, Y.-N.; Lu, J. Whole-Voltage-Range Oxygen Redox in P2-Layered Cathode Materials for Sodium-Ion Batteries. *Advanced Materials* **2021**, *33* (13), 2008194.

(56) Lee, S.; Wook Doo, S.; Soo Jung, M.; Gwon Lim, S.; Kim, K.; Tae Lee, K. Direct Observation of the In-Plane Crack Formation of O3-Na 0.8 Mg 0.2 Fe 0.4 Mn 0.4 O 2 Due to Oxygen Gas Evolution for Na-Ion Batteries. *Journal of Materials Chemistry A* **2021**, *9* (24), 14074–14084.

Chapter 5 Discussion, Perspectives, and Future Work

In this thesis, we presented a comprehensive workflow for utilizing a high-throughput system to investigate layered oxide cathodes for SIBs. **Chapter 1** underscores the urgency and significance of developing advanced energy storage materials amid escalating energy demands and the ongoing environmental crisis. Traditional trial-and-error methods have proven inadequate for the extensive research and development needed in battery materials, and computational efforts to date have been largely retrospective. Thus, we introduced a high-throughput system to bridge this gap. In Section 1.1.3, we demonstrated that by 2030, the demand for battery markets, particularly for electric vehicles (EVs) and energy storage systems (ESS), will be over 3100 GWh.[1] The widespread adoption of EVs and ESS can significantly reduce dependence on and consumption of traditional fossil fuels, while enhancing the efficiency of renewable energy utilization, such as wind and solar power. Additionally, we compare LIBs and SIBs, discussing the latter's advantages and disadvantages. The advantages of SIBs include abundant resource availability, environmental friendliness, a diverse range of transition metal selections and combinations, smaller Stokes radius and desolvation energy in electrolytes, the use of aluminum foil as an anode current collector instead of copper foil, and improved safety and temperature tolerance.[2–4] These benefits are crucial for addressing the dual challenges of rising energy demand and environmental sustainability. Nonetheless, enhancing the electrochemical properties—such as specific capacity, energy density, and cycle life—remains essential for SIBs to become competitive with LIBs.

Cathode materials are pivotal in the development of SIBs. Layered oxides stand out as the most promising candidates for commercialization due to their exceptional electrochemical properties, diverse compositional combinations, and high tunability. In Section 1.4, we outlined the main challenges impeding the progress of layered oxides.[5] Subsequent chapters demonstrate how we integrated high-throughput investigation to tackle the following issues: **(1) Jahn-Teller distortion**, which can disrupt the symmetry of the octahedral configuration, cause distortion of transition metal layers, and compromise structural integrity, is addressed in Chapters 2 and 3, **(2) Phase transitions** during cycling can accelerate structural degradation and significantly limit the cycle life of battery materials; these challenges are explored in Chapters 2, 3, and 4, **(3) Transition metal dissolution**, which diminishes the electrode stability in electrolyte, reduces the activity of cathode materials, undermines long-term cycling performance, and raises safety concerns, is another critical issue we examine in Chapter 4, and **(4) The air/moisture stability** of these materials is crucial at every stage of battery production and affects handling costs, addressed in Chapters 2, 3, and 4. Importantly, each of these challenges is closely related to the compositional design of layered oxides. By leveraging high-throughput methodologies, we aim to optimize the composition and enhance the performance of these cathode materials, thereby advancing the development of SIBs.

The development of battery materials frequently employs comparative research methodologies, wherein benchmark samples are utilized to gauge the improvements of novel materials.[6,7] This approach facilitates the determination of whether a specific dopant or composition exhibits superior performance. Despite the significant attention garnered by Na-Fe-Mn-O layered materials over recent decades[8–12], there remains a notable lack of systematic and rational guidance on composition design. Comparing data across the existing literature is challenging due to inconsistencies and conflicts arising from researchers reporting diverse precursors, sintering conditions (including temperature and heating rates), and electrochemical protocols (such as varied cut-off voltages). These disparities complicate the comparison of results across different laboratories, thereby impeding the efficiency of comparative studies.

For synthesis conditions, some researchers use solid-state reactions, where the homogeneity and particle size of the precursors are crucial; better homogeneity often results in improved morphology and superior cathode materials.[13–15] Achieving high homogeneity can be particularly challenging, with some reports require days of ball milling, which is inefficient and energy-intensive. Temperature is also critical for cathode synthesis. Some studies employ very high temperatures, exceeding 1000°C, to achieve higher crystallinity of particles, leading to better electrochemical properties, especially improved cycle life.[16] However, high temperatures can accelerate sodium loss and increase energy consumption. Additionally, quenching can influence cathode performance, but its effects are not universally beneficial, and this is not typically scalable. In electrochemical studies, the voltage window is a critical parameter. Generally, a narrower voltage window results in reduced capacity due to limited Na^+ (de)-intercalation, but it often enhances cyclability by avoiding irreversible phase transitions. For instance, Delmas et al. compared the retention of $Na_xMn_{1/2}Fe_{1/2}O_2$ under different cycling voltages.[17] At a voltage window of 1.5-3.8 V, the material exhibited a capacity of 120 mAh/g with 91% retention after 50 cycles. Conversely, at a voltage window of 1.5-4.3 V, the material achieved a higher capacity of 185 mAh/g but only 60% retention after 50 cycles. Additionally, the scan rate can affect specific capacity comparisons, with higher scan rates typically resulting in lower capacity due to kinetic limitations and increased overpotential.[18] These variations in electrochemical conditions across different studies complicate and often obscure direct comparisons.

These challenges underscore the critical importance of high-throughput methodologies, which enable better control of the myriad variables involved in battery material synthesis and testing. By standardizing conditions, high-throughput approaches can provide more reliable and comparable data, ultimately expediting the development of optimized battery materials.

In **Chapter 2**, we investigated the Gibbs' triangle of the Na-Mn-Fe-O pseudoternary system and determined the stable phase distribution as a function of compositions after sintering at 850°C. Despite all being layered oxides, they occupy different structures: P2 prefers high manganese with Na contents of $x = 0.5\text{-}0.7$ in Na_xMO_2; P3 is stable in the Fe/Mn $\approx$ 1 region with Na contents of $x = 0.7\text{-}0.95$; and O3 prefers regions with high iron and high sodium contents (0.75-0.90). In **Chapter 3**, we explored high-throughput doping into $Na_{0.66}MnO_2$ and identified various phase preferences induced by doping. The most active phases were P2 and P'2, the latter exhibiting Jahn-Teller distortion. **Chapter 4** extended our investigation to the doping effects within the Na-Mn-Fe-O system, focusing particularly on the surface stability such as transition metal dissolution. Despite these findings, several intriguing phenomena require further discussion. For instance, why is there no single-phase layered oxides in the binary system explored in **Chapter 2**? What accounts for the different preferred compositions of P2, P3, and O3 phases? Additionally, why is Fe dissolution more severe than Mn dissolution, and how to mitigate the issue? These questions highlight the complexity of the system and the need for continued investigation to fully understand the underlying mechanisms.

In our study, no single phase of layered oxides was identified in the pseudo binary Na-Fe-O or Na-Mn-O systems; instead, single phases were only observed in ternary regions. The stabilization of a layer of transition metal octahedra (TMO_6) is essential for forming layered oxides. For instance, the $NaFeO_2$ composition can form two distinct structures: β-$FeNaO_2$ (orthorhombic) and α-$NaFeO_2$ (O3, hexagonal).[19] Despite sharing the same composition, these structures exhibit significant differences. β-FeNaO2 consists of tetrahedral FeO_4 and NaO_4, which are electrochemically inactive. Conversely, α-$NaFeO_2$ is composed of octahedral NaO_6 and FeO_6. The conversion temperature from α-$NaFeO_2$ to β-$FeNaO_2$ is approximately 750°C[20], which explains why we obtained the inactive β-FeNaO2 in this study. According to crystal field theory (CFT)[21], the stability of Fe^{3+} (d^5) in octahedral versus tetrahedral sites can be assessed using octahedral-site stabilization energy (OSSE)[22], derived from the difference in crystal field stabilization energies (CFSE)[23] between these configurations, shown in **Table 5.1**. For Fe^{3+} (d^5), the OSSE is zero, indicating that the conversion from octahedral to tetrahedral is facile. This explains the difficulty in obtaining O3 $NaFeO_2$ at 850 °C. However, with 20% substitution of Mn into $NaFeO_2$, O3 structures such as $Na_{0.8}Mn_{0.2}Fe_{0.8}O_2$ can be stabilized at 850 °C. Thus, Mn substitution enhances the octahedral-site stabilization energy of Fe, highlighting Mn's critical role in stabilizing the O3 structure.

***Table 5.1** Crystal field stabilization energies (CFSE) for octahedral and tetrahedral geometries at high spin configurations. Assumed crystal field splitting parameter $\Delta_{tet} = 4/9\ \Delta_o$.*[21,23]

d-electrons	Octahedral	Tetrahedral	OSSE
d^0, d^5, d^{10}	0	0	0
d^1, d^6	0.4 Δ_o	0.27 Δ_o	0.13 Δ_o
d^2, d^7	0.8 Δ_o	0.53 Δ_o	0.27 Δ_o
d^3, d^8	1.2 Δ_o	0.36 Δ_o	0.84 Δ_o
d^4, d^9	0.6 Δ_o	0.18 Δ_o	0.42 Δ_o

This low transformation energy also elucidates several phenomena, such as the irreversible migration of Fe into the Na^+ layer[24], which introduces significant overpotential, and the greater propensity for Fe dissolution compared to Mn, as discussed in **Chapter 4**. Mn^{4+} (d^3) has a high OSSE of 0.84 Δ_o, indicating its stability in octahedral sites. However, both Fe^{4+} and Mn^{3+} are d^4 with an OSSE of 0.42 Δ_o and are prone to Jahn-Teller distortion, making them less stable in octahedral sites. Consequently, during cycling, Fe^{4+} is less stable at high voltages, while Mn^{3+} is less stable at low voltages, suggesting that a narrower cut-off voltage range can enhance stability as discuss earlier. Addressing Fe dissolution involves modifying the neighboring chemical environment of FeO_6. Ceder et al. demonstrated the dependency of Fe dissolution on composition and configuration using DFT calculations, as shown in **Figure 5.1**.[25] Isolated octahedral Fe exhibits a high migration energy of approximately 0.7 eV to tetrahedral sites, but Fe migration is facilitated when Fe clusters form. The dopants identified in **Chapter 4**, improved TM dissolution resistance, by altering Fe migration energy and thus reducing Fe dissolution into the electrolyte. Future research can integrate DFT calculations to gain further insights into the effects of doping on TM dissolution.

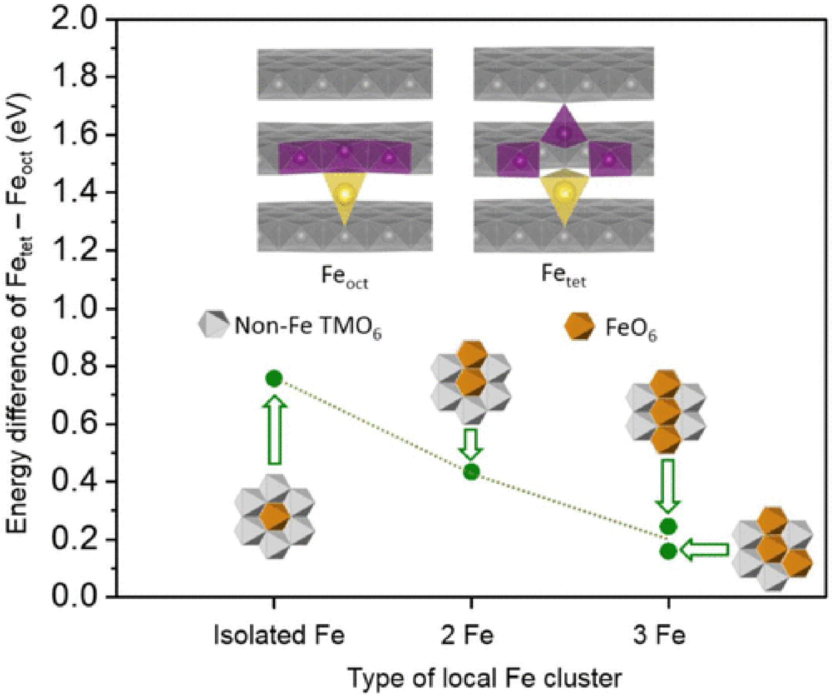

Figure 5.1 *Calculated energy penalty for Fe migration from an octahedral site in the TM layer to a tetrahedral site in the Na layer of* $NaTMO_2$*. Reproduced with permission from ref.* [25].

The Na-Mn-O binary materials present more complex scenarios. In **Chapter 2**, we did not achieve a pure P2-$Na_{0.66}MnO_2$ phase after slow cooling from 850°C; instead, we obtained a mixture of P2 and P'2 phases due to Jahn-Teller distortion (JTD)[16]. However, with as little as 5% Fe substitution, a pure P2 phase was stabilized, indicating that Fe effectively suppresses JTD. In **Chapter 3**, we further experimented by quenching $Na_{0.66}MnO_2$ from 650 °C and 500 °C, resulting in single-phase P'2 and P2 materials, respectively. This finding is intriguing as it demonstrates that JTD can be manipulated by quenching temperature. Typically, quenching stabilizes high-temperature phases by rapidly cooling the material, often in seconds. At elevated temperatures, the Jahn-Teller distortion of Mn^{3+} is triggered by high thermal energy, which breaks the degenerate orbitals and stabilizes the system energy by elongating bonds along the z-axis, thereby reducing lattice symmetry.[26] This local distortion of MnO_6 can accumulate and propagate throughout the entire transition metal layer, transforming the hexagonal P2 structure into an orthorhombic P'2 structure, a phenomenon known as cooperative Jahn-Teller distortion (CJTD)[16]. However, during cooling, further oxidation can occur, where oxygen uptake creates vacancies in the structure, partially oxidizing Mn^{3+} to Mn^{4+}. Consequently, a pure P2-$Na_{0.66}Mn_{0.9}\square_{0.1}O_2$ phase (where □ represents vacancies) is formed.[16] The presence of vacancies is crucial for relaxing lattice strain and disrupting the cooperative effect, thus suppressing JTD.

Chapter 3 identified various dopants at 10% that effectively suppress JTD, including Li, Mg, Fe, Co, Ni, Zn, and Ga. Additionally, considering the substitution level of dopant X in $Na_{0.66}Mn_{1-y}X_yO_2$, a series of local cation ratios can be calculated as $y = 1/(3n)$, where n represents the number of hexagonal rings of Mn, as illustrated **Figure 5.2**. For instance, at a doping content of $y = 1/9$, significant influence on the overall structure is observed. This ratio is close to the Fe content in the optimal $Na_{0.59}Fe_{0.13}Mn_{0.87}O_2$ composition from **Chapter 2**. Some well-studied materials that follow these ratios include $Na_{2/3}Mn_{2/3}Ni_{1/3}O_2$[27] and $NaFe_{1/3}Mn_{1/3}Ni_{1/3}O_2$[28]. Future work can adopt similar ratios such as 1/9, 1/12, and 1/15 for doping levels, providing valuable insights for material design. This approach will help to identify the effective compositions for achieving improved performance and stability in sodium-ion batteries.

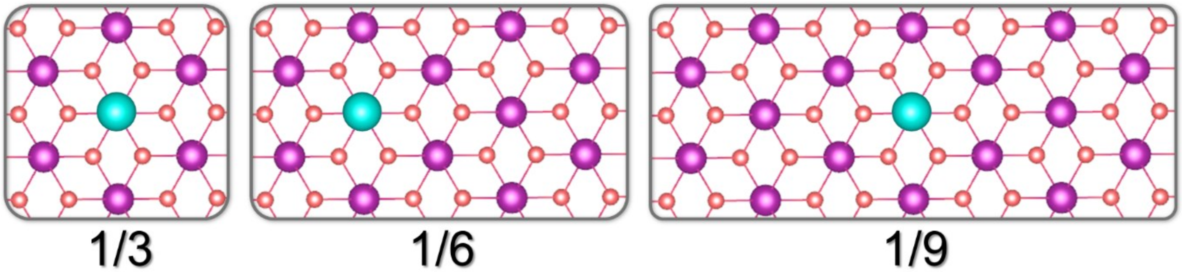

Figure 5.2 *The averaged local structure of various doping levels of* $Na_{0.66}Mn_{1-y}X_yO_2$*, considering homogeneous distribution. However, the low doping level and long range interaction is hard to establish the superstructure. Mn: purple spheres; X: the dopant shown in turquoise.*

In **Chapter 2**, we explore a large solid-solution region between Fe and Mn. Notably, naturally occurring manganese ores frequently contain iron, often in the form of mixtures such as bixbyite, highlighting the inherent similarities and chemical affinities between Fe and Mn.[29] As previously discussed, Mn can stabilize the octahedral site energy of Fe, while Fe can mitigate the JTD of Mn^{3+}, thereby enhancing structural stability. This mutual enhancement is evident in both metals. The formation of layered materials is more readily achieved in regions with high Mn content compared to regions with high Fe content, resulting in a distinct triangular region as illustrated in **Figure S2.6**. In the layered oxides $Na_x[Fe^{3+}_yMn^{3+}_{(x-y)}]Mn^{4+}_{(1-x)}O_2$, manganese exists in both the Mn^{3+} and Mn^{4+} oxidation states, whereas iron can only be stabilized as Fe^{3+} due to the high oxidizing power of Fe^{4+} (which can oxidize Mn^{3+} to Mn^{4+}). Consequently, with the substitution of Fe, the proportion of Mn^{4+} increases to maintain charge neutrality. However, Mn^{4+} has a higher cationic potential[30], as shown in **Figure 2.6**, which shifts the phase preference from P2 to O3 materials. Therefore, P2 materials are more stable in high Mn regions, while O3 materials are favored in high Fe regions. To address this issue, we can consider incorporating dopants with low ionic potentials, such as Li, Cu, and Mg, to facilitate the formation of high iron content materials.

P3 materials, positioned between the P2 and O3 regions as shown in **Figure 2.6** and **Figure S2.5**, present a challenge for cationic potential predictions. We hypothesize that P3 materials can be categorized into two types of subphases, either closer to P2 or O3. Future work could involve doping studies on P3 materials to investigate their potential conversion into P2 or O3 based on the cationic potential of the dopants. Exploring high sodium content P3 materials with various dopants may offer intriguing avenues for further research.

Another important yet often overlooked aspect of composition design is the control of Na content and Na loss. Achieving precise Na content and correct metal stoichiometry requires meticulous management of Na loss. As illustrated in **Figure S2.6**, sodium loss behavior is closely related to the TM composition and can indicate the stable phase regions. Typically, Na loss occurs above 627 °C[31]. However, we know the Na loss in materials with the same initial Na content can vary strongly, even though all samples are sintered at the same temperature and duration, and have comparable surface areas. For example, it is evident that materials with high Fe content experience significant Na loss, and no Na-rich (Na > Fe) phase can be stabilized at 850°C, particularly due to the very low octahedral site stabilization energy (OSSE) of Fe^{3+}. Consequently, stabilizing Fe^{3+} in octahedral sites at high temperatures proves challenging. The high-Fe O3 materials obtained in this study consistently show Na content below 1.0, even when higher Na stoichiometry is initially used. This indicates that these O3 materials are thermodynamically more stable with a slight Na deficiency (0.75-0.90). This Na deficiency also contributes to the improved air stability observed in these materials. As demonstrated in **Figure S2.14**, the XRD patterns of Na-deficient O3 materials remain stable, with no significant structural degradation after six months of dry air storage. In contrast, other O3 materials with more Na content undergo severe structural degradation under similar conditions. This stability can be attributed to the reduced Na^+-Na^+ repulsion in Na-deficient O3 materials, which improves the Na^+ site energy and suppresses Na dissolution. Despite this, HTP-XPS results (**Figure 2.5**) still reveal significant amounts of Na_2CO_3 on the surface, as evidenced by the shift of the (003) peak in **Figure S2.14** towards lower angles. This surface phenomenon does not lead to structural degradation in XRD. Previous studies, such as those by Sun et al., have also noted that slight Na deficiency can enhance the air stability of O3 materials.[32] Thus, precise control of Na content can be significant for O3 materials, though it is often underemphasized in many studies.

On the other hand, P2 materials with Na deficiency also exhibit high electrochemical performance. This improvement can be partly attributed to the increased interslab distance *c*, which facilitates Na diffusion, as illustrated in **Figure 2.5**. Regarding the air stability of P2 materials, previous work by Zuo has identified a critical Na content threshold. Lower Na^+ content can facilitate easier water insertion, leading to diminished moisture stability.[33] However, critical contents can vary with TM compositions. Future research could benefit from high-throughput studies to explore how varying Na contents influence different properties, especially air stability.

Furthermore, we turn our attention to the potential of machine learning (ML) in advancing battery research. **Chapter 4** details our initial attempt to apply ML techniques to XRD data, an idea that emerged from the accelerated aging studies presented in **Chapters 3** and **4**. In these studies, we analyzed hundreds of XRD patterns of aged materials, identifying significant changes and phase transitions due to air aging, as shown in **Figures 3.10** and **4.4**. The changes in XRD patterns correlate well with air stability, as XRD patterns reflect the physical structure of the materials.

Each crystal structure produces a unique XRD pattern, which can theoretically be deciphered back to its real-world structure through detailed Rietveld refinement. Despite this, our exploratory data analysis using properties extracted from XRD patterns—such as peak positions, areas, and ratios—did not reveal strong correlations with air stability. However, we believed that certain latent features within the XRD patterns might still indicate the air stability.

We then applied machine learning algorithms[35–37], including principal component analysis (PCA), t-distributed stochastic neighbor embedding (t-SNE), and partial least squares regression (PLSR). These algorithms enable pattern recognition by automatically identifying latent features without predefined parameters, a technique widely used in related fields like computer vision, anomaly detection, and cheminformatics.[38] By using XRD scans as inputs, we trained the ML models to discern patterns that discriminate the air stability of materials. Encouragingly, our models were able to predict air stability effectively using only the XRD scans of pristine samples before degradation. This success highlights the potential of integrating ML with high-throughput studies to enhance materials design, data processing, and laboratory automation. Future work may focus on expanding the use of ML algorithms in high-throughput research, potentially revolutionizing how we approach materials design and analysis, as demonstrated by several research groups.[36,39,40]

As noted earlier, even for materials with identical compositions, reports from different research labs can vary significantly due to differences in sample precursors, sintering protocols, and electrochemical test conditions. Consequently, relying solely on data from various research papers for machine learning can be problematic and unreliable. Such an approach may lead to high prediction errors for electrode material properties, diminishing the usefulness of the insights generated. High-throughput computation has shown promise in advancing machine learning studies for battery research.[41] However, these models often struggle with the complexities of real-world scenarios. For instance, DFT-based computation models are highly sensitive to the physical structural models used. During battery cycling, structural changes and evolutions occur continuously, challenging the static nature of first-principles approaches. Moreover, the high computational cost of first-principles methods limits their ability to address the dynamic complexities of battery materials. In contrast, our high-throughput methodologies offer a lower-cost, high-efficiency alternative, providing practical and real-world battery data. This approach demonstrates significant potential for machine learning applications in battery research, highlighting its ability to adapt and deliver valuable insights while managing real-world complexities.

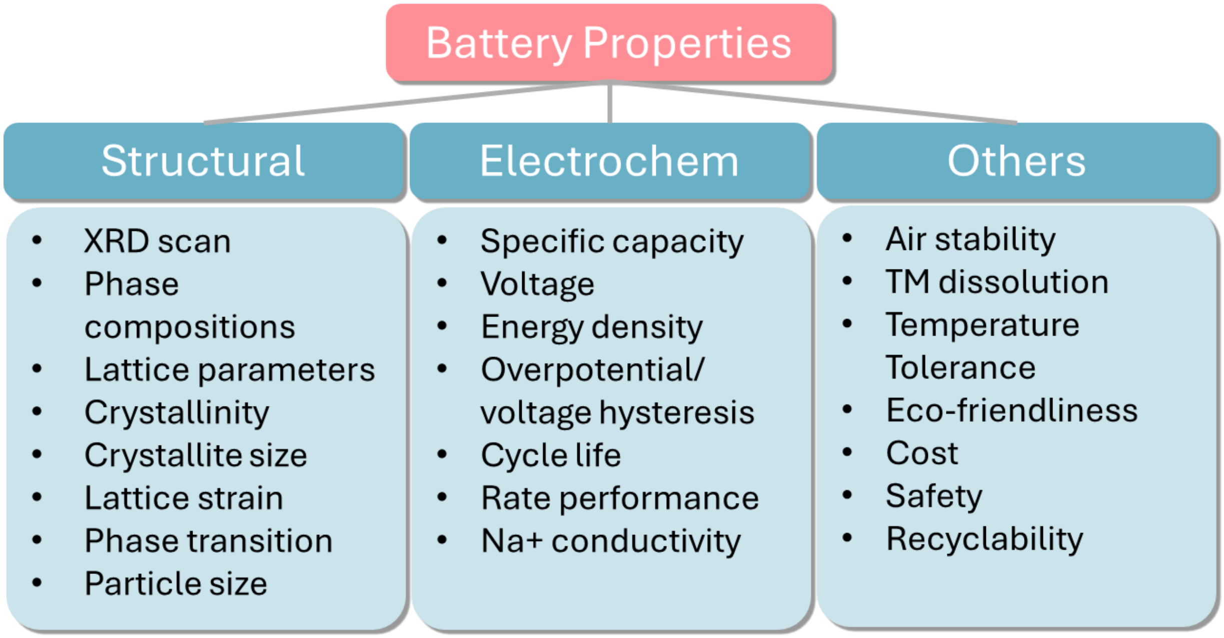

Figure 5.3 *Major battery properties can be used to train the machine learning models.*

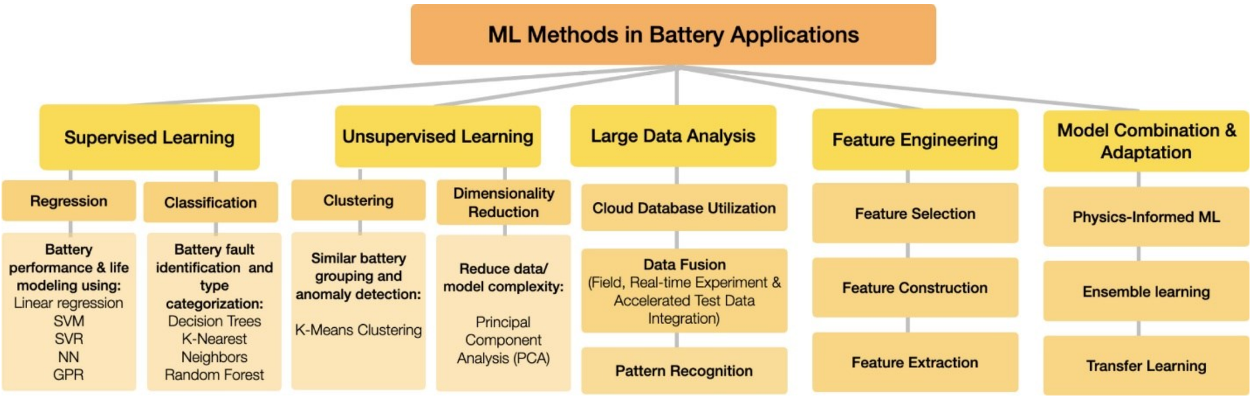

Figure 5.4 *Machine learning methods and key steps for battery research. Reproduced with permission from ref.* [35].

Here, we outline several perspectives for advancing ML/AI-assisted high-throughput research in battery technology. Key characteristics for electrode material optimization and machine learning methods applicable to battery material research are summarized in **Figures 5.3** and **5.4**. Future work can follow a multi-stage approach to integrate ML models into high-throughput methodologies for battery research:

Stage 1: Initially, we can use electrochemical data from CV and structural data from XRD as inputs for property predictions. This stage involves applying traditional machine learning models and feature engineering to predict various properties (such as battery lifetime, air stability, and etc.) based on these inputs.

Stage 2: In this stage, the model is trained with both composition and sintering conditions to predict a range of structural and electrochemical properties, such as crystal structure, specific capacity, and cycle life. Advanced machine learning models, including ensemble learning techniques, can be employed to enhance the accuracy of these predictions on high dimensional data.

Stage 3: At this stage, we can process and generate sequence data, such as XRD patterns and CV curves directly, using deep learning approaches like recurrent neural networks (RNNs). This will enable more complex and dynamic modeling of the data.

Stage 4: Finally, machine learning can guide the synthesis of new materials by optimizing synthesis conditions and compositions to achieve excellent electrochemical properties. Techniques such as Bayesian optimization or transformer models can be utilized to fine-tune these processes.

This thesis demonstrated the application of these methodologies in the Na-Mn-Fe-O pseudoternary system and high-throughput doping studies. Moving forward, we could expand our research to explore a broader range of metal combinations, including high-entropy materials such as with over five transition metals, potentially involving thousands of compositional combinations. This expansion will enable a more comprehensive understanding of complex material systems and their electrochemical properties. Additionally, integrating advanced machine learning techniques could further optimize material design and synthesis, accelerating the development of high-performance sodium-ion batteries. The studies presented in this thesis highlight a promising and foundational approach for advancing sodium-ion battery research.

5.1 Reference

(1) Bernhart, W. *Rising demand for lithium-ion batteries may lead to shortages in raw material supply*. Roland Berger. https://www.mynewsdesk.com/rolandberger/pressreleases/rising-demand-for-lithium-ion-batteries-may-lead-to-shortages-in-raw-material-supply-3173780 (accessed 2024-07-11).

(2) Liu, T.; Zhang, Y.; Jiang, Z.; Zeng, X.; Ji, J.; Li, Z.; Gao, X.; Sun, M.; Lin, Z.; Ling, M.; Zheng, J.; Liang, C. Exploring Competitive Features of Stationary Sodium Ion Batteries for Electrochemical Energy Storage. *Energy & Environmental Science* **2019**, *12* (5), 1512–1533.

(3) Hirsh, H. S.; Li, Y.; Tan, D. H. S.; Zhang, M.; Zhao, E.; Meng, Y. S. Sodium-Ion Batteries Paving the Way for Grid Energy Storage. *Advanced Energy Materials* **2020**, *10* (32), 2001274.

(4) Yabuuchi, N.; Kubota, K.; Dahbi, M.; Komaba, S. Research Development on Sodium-Ion Batteries. *Chemical Reviews* **2014**, *114* (23), 11636–11682.

(5) Su, H.; Jaffer, S.; Yu, H. Transition Metal Oxides for Sodium-Ion Batteries. *Energy Storage Materials* **2016**, *5*, 116–131.

(6) Kim, N.; Shamim, N.; Crawford, A.; Viswanathan, V. V.; Sivakumar, B. M.; Huang, Q.; Reed, D.; Sprenkle, V.; Choi, D. Comparison of Li-Ion Battery Chemistries under Grid Duty Cycles. *Journal of Power Sources* **2022**, *546*, 231949.

(7) Zhao, Y.; Jossen, A. Comparative Study of Parameter Identification with Frequency and Time Domain Fitting Using a Physics-Based Battery Model. *Batteries* **2022**, *8* (11), 222.

(8) Thorne, J. S.; Dunlap, R. A.; Obrovac, M. N. Structure and Electrochemistry of NaxFexMn1-xO2 ($1.0 \leq x \leq 0.5$) for Na-Ion Battery Positive Electrodes. *Journal of the Electrochemical Society* **2012**, *160* (2), A361.

(9) Sharma, N.; Gonzalo, E.; Pramudita, J. C.; Han, M. H.; Brand, H. E. A.; Hart, J. N.; Pang, W. K.; Guo, Z.; Rojo, T. The Unique Structural Evolution of the O3-Phase Na2/3Fe2/3Mn1/3O2 during High Rate Charge/Discharge: A Sodium-Centred Perspective. *Advanced Functional Materials* **2015**, *25* (31), 4994–5005.

(10) Lu, X.; Wang, Y.; Liu, P.; Gu, L.; Hu, Y.-S.; Li, H.; Demopoulos, G. P.; Chen, L. Direct Imaging of Layered O3- and P2-NaxFe1/2Mn1/2O2 Structures at the Atomic Scale. *Physical Chemistry Chemical Physics* **2014**, *16* (40), 21946–21952.

(11) Singh, G.; Acebedo, B.; Cabanas, M. C.; Shanmukaraj, D.; Armand, M.; Rojo, T. An Approach to Overcome First Cycle Irreversible Capacity in P2-Na2/3[Fe1/2Mn1/2]O2. *Electrochemistry Communications* **2013**, *37*, 61–63.

(12) Yabuuchi, N.; Kajiyama, M.; Iwatate, J.; Nishikawa, H.; Hitomi, S.; Okuyama, R.; Usui, R.; Yamada, Y.; Komaba, S. P2-Type Nax[Fe1/2Mn1/2]O2 Made from Earth-Abundant Elements for Rechargeable Na Batteries. *Nature Materials* **2012**, *11* (6), 512–517.

(13) Zhang, B.; Dugas, R.; Rousse, G.; Rozier, P.; Abakumov, A. M.; Tarascon, J.-M. Insertion Compounds and Composites Made by Ball Milling for Advanced Sodium-Ion Batteries. *Nature Communications* **2016**, *7* (1), 10308.

(14) Hassanzadeh, N.; Sadrnezhaad, S. K.; Chen, G. Ball Mill Assisted Synthesis of Na3MnCO3PO4 Nanoparticles Anchored on Reduced Graphene Oxide for Sodium Ion Battery Cathodes. *Electrochimica Acta* **2016**, *220*, 683–689.

(15) Lu, H.; Ai, F.; Jia, Y.; Tang, C.; Zhang, X.; Huang, Y.; Yang, H.; Cao, Y. Exploring Sodium-Ion Storage Mechanism in Hard Carbons with Different Microstructure Prepared by Ball-Milling Method. *Small* **2018**, *14* (39), 1802694.

(16) Kumakura, S.; Tahara, Y.; Kubota, K.; Chihara, K.; Komaba, S. Sodium and Manganese Stoichiometry of P2-Type Na2/3MnO2. *Angewandte Chemie International Edition* **2016**, *55* (41), 12760–12763.

(17) Mortemard de Boisse, B.; Carlier, D.; Guignard, M.; Bourgeois, L.; Delmas, C. P2-NaxMn1/2Fe1/2O2 Phase Used as Positive Electrode in Na Batteries: Structural Changes Induced by the Electrochemical (De)Intercalation Process. *Inorganic Chemistry* **2014**, *53* (20), 11197–11205.

(18) Chen, J.; Zhong, S.; Zhang, X.; Liu, J.; Shi, S.; Hu, Y.; Wu, L. High Performance of Hexagonal Plates P2-Na2/3Fe1/2Mn1/2O2 Cathode Material Synthesized by an Improved Solid-State Method. *Materials Letters* **2017**, *202*, 21–24.

(19) Kuganathan, N.; Kelaidis, N.; Chroneos, A. Defect Chemistry, Sodium Diffusion and Doping Behaviour in NaFeO2 Polymorphs as Cathode Materials for Na-Ion Batteries: A Computational Study. *Materials* **2019**, *12* (19), 3243.

(20) Grey, I. E.; Li, C. New Silica-Containing Ferrite Phases in the System NaFeO2 SiO2. *Journal of Solid State Chemistry* **1987**, *69* (1), 116–125.

(21) *Crystal Field Stabilization Energy*. Chemistry LibreTexts. https://chem.libretexts.org/Bookshelves/Inorganic_Chemistry/Supplemental_Modules_and_Websites_(Inorganic_Chemistry)/Crystal_Field_Theory/Crystal_Field_Stabilization_Energy (accessed 2024-08-04).

(22) Manthiram, A. A Reflection on Lithium-Ion Battery Cathode Chemistry. *Nature communications* **2020**, *11* (1), 1550.

(23) *Octahedral vs. Tetrahedral Geometries*. Chemistry LibreTexts. https://chem.libretexts.org/Bookshelves/Inorganic_Chemistry/Supplemental_Modules_and_Websites_(Inorganic_Chemistry)/Crystal_Field_Theory/Octahedral_vs._Tetrahedral_Geometries (accessed 2024-08-04).

(24) Talaie, E.; Duffort, V.; Smith, H. L.; Fultz, B.; Nazar, L. F. Structure of the High Voltage Phase of Layered P2-Na2/3−z[Mn1/2Fe1/2]O2 and the Positive Effect of Ni Substitution on Its Stability. *Energy & Environmental Science* **2015**, *8* (8), 2512–2523.

(25) Li, X.; Wang, Y.; Wu, D.; Liu, L.; Bo, S.-H.; Ceder, G. Jahn–Teller Assisted Na Diffusion for High Performance Na Ion Batteries. *Chemistry of Materials* **2016**, *28* (18), 6575–6583.

(26) Asl, H. Y.; Manthiram, A. Reining in Dissolved Transition-Metal Ions. *Science* **2020**, *369* (6500), 140–141.

(27) Zhang, Y.-Y.; Zhang, S.-J.; Li, J.-T.; Wang, K.; Zhang, Y.-C.; Liu, Q.; Xie, R.-S.; Pei, Y.-R.; Huang, L.; Sun, S.-G. Improvement of Electrochemical Properties of P2-Type Na2/3Mn2/3Ni1/3O2 Sodium Ion Battery Cathode Material by Water-Soluble Binders. *Electrochimica Acta* **2019**, *298*, 496–504.

(28) Jeong, M.; Lee, H.; Yoon, J.; Yoon, W.-S. O3-Type NaNi1/3Fe1/3Mn1/3O2 Layered Cathode for Na-Ion Batteries: Structural Evolution and Redox Mechanism upon Na (de) Intercalation. *Journal of Power Sources* **2019**, *439*, 227064.

(29) Tangstad, M. Chapter 7 - Manganese Ferroalloys Technology. In *Handbook of Ferroalloys*; Gasik, M., Ed.; Butterworth-Heinemann: Oxford, 2013; pp 221–266.

(30) Zhao, C.; Wang, Q.; Yao, Z.; Wang, J.; Sánchez-Lengeling, B.; Ding, F.; Qi, X.; Lu, Y.; Bai, X.; Li, B.; Li, H.; Aspuru-Guzik, A.; Huang, X.; Delmas, C.; Wagemaker, M.; Chen, L.; Hu, Y.-S. Rational Design of Layered Oxide Materials for Sodium-Ion Batteries. *Science* **2020**, *370* (6517), 708–711.

(31) Kobertz, D. Vaporization Studies on Sodium Oxide. *Calphad* **2019**, *64*, 327–333.

(32) Sun, Y.; Wang, H.; Meng, D.; Li, X.; Liao, X.; Che, H.; Cui, G.; Yu, F.; Yang, W.; Li, L.; Ma, Z.-F. Degradation Mechanism of O3-Type NaNi1/3Fe1/3Mn1/3O2 Cathode Materials During Ambient Storage and Their In Situ Regeneration. *ACS Applied Energy Materials* **2021**, *4* (3), 2061–2067.

(33) Zuo, W.; Qiu, J.; Liu, X.; Ren, F.; Liu, H.; He, H.; Luo, C.; Li, J.; Ortiz, G. F.; Duan, H.; Liu, J.; Wang, M.-S.; Li, Y.; Fu, R.; Yang, Y. The Stability of P2-Layered Sodium Transition Metal Oxides in Ambient Atmospheres. *Nature Communications* **2020**, *11* (1), 3544.

(34) H. Han, M.; Sharma, N.; Gonzalo, E.; C. Pramudita, J.; A. Brand, H. E.; Amo, J. M. L. del; Rojo, T. Moisture Exposed Layered Oxide Electrodes as Na-Ion Battery Cathodes. *Journal of Materials Chemistry A* **2016**, *4* (48), 18963–18975.

(35) Nozarijouybari, Z.; Fathy, H. K. Machine Learning for Battery Systems Applications: Progress, Challenges, and Opportunities. *Journal of Power Sources* **2024**, *601*, 234272.

(36) Thakkar, P.; Khatri, S.; Dobariya, D.; Patel, D.; Dey, B.; Singh, A. K. Advances in Materials and Machine Learning Techniques for Energy Storage Devices: A Comprehensive Review. *Journal of Energy Storage* **2024**, *81*, 110452.

(37) Wei, Z.; He, Q.; Zhao, Y. Machine Learning for Battery Research. *Journal of Power Sources* **2022**, *549*, 232125.

(38) Theodoridis, S.; Koutroumbas, K. *Pattern Recognition*; Elsevier, 2006.

(39) Szymanski, N. J.; Rendy, B.; Fei, Y.; Kumar, R. E.; He, T.; Milsted, D.; McDermott, M. J.; Gallant, M.; Cubuk, E. D.; Merchant, A.; Kim, H.; Jain, A.; Bartel, C. J.; Persson, K.; Zeng, Y.; Ceder, G. An Autonomous Laboratory for the Accelerated Synthesis of Novel Materials. *Nature* **2023**, *624* (7990), 86–91.

(40)Sanchez-Lengeling, B.; Aspuru-Guzik, A. Inverse Molecular Design Using Machine Learning: Generative Models for Matter Engineering. *Science* **2018**, *361* (6400), 360–365.

(41) Jain, A.; Hautier, G.; Moore, C. J.; Ping Ong, S.; Fischer, C. C.; Mueller, T.; Persson, K. A.; Ceder, G. A High-Throughput Infrastructure for Density Functional Theory Calculations. *Computational Materials Science* **2011**, *50* (8), 2295–2310.

Chapter 6 Conclusion

In this thesis, we successfully developed and implemented the high-throughput (HTP) methodologies, marking the first application of these techniques to the investigation of sodium-ion battery cathode materials. The focus was on promising and environmentally benign layered oxides. In our study of the Na-Fe-Mn-O pseudoternary system, we established a comprehensive HTP workflow, encompassing sol-gel inspired HTP synthesis with a throughput of 64 samples over 3 days, alongside various HTP characterizations employing XRD, XPS, ICP-OES, and CV. This approach enabled a systematic examination of the correlations between composition, crystal structure, electrochemistry, and air stability. Within this pseudoternary system, we identified a substantial solid-solution region comprising over 50 single-phase samples of P2, P3, and O3 layered oxides, many of which are marked as first-reported. Our investigation also resolved numerous contradictions in the existing literature, clarifying stable phase compositions, phase relationships, cationic calculations for new P3 materials, and XPS peak assignments. These systematic elucidations provide a more robust framework for material design. Notably, the higher manganese and slightly sodium-deficient material of P2-$Na_{0.59}Fe_{0.13}Mn_{0.87}O_2$ demonstrated superior battery performance, achieving 206 mAh/g and a specific energy of 504 Wh/kg, but exhibiting mediocre air stability. We extended our research through HTP doping studies on $Na_{0.66}Mn_{0.9}M_{0.1}O_2$ with 52 different dopants to further enhance air stability. This extensive doping study successfully incorporated 20 various dopants into Na-Mn-O materials, including previously unexplored elements such as Si, Sc, Ga, Rb, Rh, Cs, Re, and Tl. Our results indicated that the dopants significantly influenced various properties, including structural preferences (P2, P’2, P3, and tunnel structures), electrochemical performance (ranging from 40 to 200 mAh/g, with certain dopants triggering oxygen redox), and air stability (with phase retention varying from 0% to 99%

after accelerated aging). We further expanded the HTP doping study to the more complex Na-Fe-Mn-O system, investigating structural stability, battery performance, air stability, and transition metal dissolution to address surface stability. Additionally, machine learning techniques provided critical insights into enhancing air stability by analyzing factors such as lattice parameters, particle sizes, and lattice strains.

Collectively, these studies underscore the revolution potential from traditional trial-and-error method towards high-throughput synthesis, combinatorial doping, and machine learning in advancing sodium-ion battery cathode materials. The high-throughput design of layered oxide materials resolved longstanding ambiguities in phase behaviors, identified novel high-energy-density compositions, and demonstrated promising air/moisture stability. Extensive doping studies elucidated the structural and electrochemical benefits of specific dopants, offering a framework for rational material design. Machine learning-driven analysis further refined our understanding of the relationship between material properties and performance, particularly in air/moisture stability. Additionally, we outlined a blueprint for future ML/AI-assisted high-throughput methodologies to further accelerate material screening and optimization. These comprehensive insights lay a robust foundation for future research, driving the development of high-performance sodium-ion battery cathodes.